LEAN BLOWOUT SENSITIVITIES OF COMPLEX LIQUID FUELS

A Dissertation
Presented to
The Academic Faculty

by

Nicholas Andrew Rock

In Partial Fulfillment
of the Requirements for the Degree
Doctor of Philosophy in the
School of Aerospace Engineering

Georgia Institute of Technology
August 2019

LEAN BLOWOUT SENSITIVITIES OF COMPLEX LIQUID FUELS

Approved by:

Dr. Tim Lieuwen, Advisor
School of Aerospace Engineering
Georgia Institute of Technology

Dr. Joseph Oefelein
School of Aerospace Engineering
Georgia Institute of Technology

Dr. Jerry Seitzman
School of Aerospace Engineering
Georgia Institute of Technology

Dr. Med Colket
Senior Fellow
United Technologies Research Center

Dr. Suresh Menon
School of Aerospace Engineering
Georgia Institute of Technology

Date Approved: March 29, 2019

“The Lord spake unto me, saying: … my grace is sufficient for the meek, that they shall take no advantage of your weakness; And if men come unto me I will show unto them their weakness. I give unto men weakness that they may be humble; and my grace is sufficient for all men that humble themselves before me; for if they humble themselves before me, and have faith in me, then will I make weak things become strong unto them.”

Ether 12:26-27

ACKNOWLEDGEMENTS

Many people have contributed to this work that I would like to deeply thank for their guidance and support. First, I would like to thank my advisor, Professor Tim Lieuwen. In all of my interactions with him, Tim has consistently pushed me to excel and has inspired me to be a more dedicated graduate student. Tim has a contagious passion for his work that has been very influential in helping me to find so much fulfillment in combustion research. Everyone who knows Tim is impressed by his leadership, energy, and cheerful nature. I am touched by the efforts that Tim, and his wife Rinda, have made to ensure that everyone within the Combustion Lab community feels welcome. They have spent numerous hours working with students individually and planning lab outings to build camaraderie within the group. Second, I would like to thank Professor Jerry Seitzman, who I consider to be a second advisor. The lessons that I have learned from him about studying problems deeply and considering them from every possible angle have been invaluable. I would also like to directly thank my committee members, Professor Lieuwen, Professor Seitzman, Professor Menon, Professor Oefelein, and Dr. Med Colket for their guidance in this process.

I am very grateful for the U.S. Federal Aviation Administration Office of Environment and Energy through ASCENT, for funding this research. I also gratefully acknowledge the ideas and insights of numerous colleagues, including Randal McKinney, Jeff Cohen, Jeff Lovett, Med Colket, Tim Edwards, Joshua Heyne, Nagi Gebraeel, and Kamran Paynabar. The unique expertise of each of these people has complemented my work and has greatly expedited its completion.

I would like to acknowledge my family and friends for their support throughout this process. My parents particularly have taught me that hard work and perseverance are the only way to accomplish anything meaningful in life. I would not be the person I am today without them. I also want to acknowledge my wonderful sisters, Ashley and Jasmin. Regardless of the challenges that I faced, they have consistently been a great source of my happiness. I am very grateful for the support of my angelic fiancé, Mallory. She has helped me to find meaning in my work and inspires me every day to be a better person.

Lastly, I would like to thank a number of key individuals from the Georgia Tech Combustion Lab for the profound impact that they have had on my Ph.D. experience. I would especially like to thank Ben Emerson for his inspired insights and leadership. I have tremendous respect for both Ben's competence as a scientist and also the quality of his character. Everyone who knows Ben feels like they are his best friend. I appreciate the efforts of Anna Hotle, Ianko Chterev, David Wu, and Bobby Noble in training me when I was a new graduate student. I have been very fortunate to work closely with a great group of graduate students during my time at Georgia Tech, including Tim Cook, Alex Miller, Chris Douglas, Nick Magina, Luke Humphrey, Alex Miltner, Sai Kaza, Alex Steinbrenner, Travis Smith, Angie Zhang, Subodh Adhikari, Dan Fries, Vedanth Nair, Matt Sirignano, Raghul Manosh Kumar, Brandon Sforzo, Tom Pritchard, Tony John, Sukruth Somappa, and Henderson Johnson. Whether we worked together in classes, studied for qualifying exams, or ran late night experiments, I deeply appreciate your help. Lastly, I am indebted to Hanna Ek and Debolina Dasgupta. I feel honored to call you my friends and have always been impressed by how much you are able to accomplish. You will do great things in the world.

TABLE OF CONTENTS

ACKNOWLEDGEMENTS **iv**

LIST OF TABLES **viii**

LIST OF FIGURES **ix**

LIST OF SYMBOLS AND ABBREVIATIONS **xxv**

SUMMARY **xxix**

CHAPTER 1. Introduction **1**
1.1 Motivation **1**
1.2 Premixed Gaseous Lean Blowout Studies **5**
1.2.1 Blowoff Dynamics: Stage 1 10
1.2.2 Blowoff Dynamics: Stage 2 in Premixed Bluff-Body Stabilized Flames 12
1.2.3 Blowoff Dynamics: Stage 2 in Premixed Swirl Stabilized Flames 21
1.3 Nonpremixed Gaseous Lean Blowout Studies **23**
1.4 Liquid Fueled Lean Blowout Studies **26**

CHAPTER 2. Experimental overview **34**
2.1 Facility **34**
2.2 Fuel Screening Procedure **39**
2.3 Operating Conditions **42**
2.4 Fuels **45**
2.5 Characterization of Preferential Vaporization Potential **50**
2.6 CH* Chemiluminescence **53**
2.7 Photomultiplier Tube (PMT) Measurements **56**
2.8 Acoustic Measurements **58**
2.9 Planar Measurements **58**

CHAPTER 3. Data Analysis Techniques **60**
3.1 Hierarchical Non-negative Garrote Regression **60**
3.2 Edge Detection of CH* Chemiluminescence Images **65**
3.3 PMT Thresholding **66**

CHAPTER 4. Fuel Screening **73**
4.1 Lean Blowout Results **73**
4.2 Physical Property Correlations **77**
4.3 Chemical Composition and Kinetic Property Correlations **82**
4.4 Preferential Vaporization **86**
4.5 Regression Analysis **92**
4.6 Fuel Screening Summary **97**

CHAPTER 5. Characterization of the Flame, Flow Field, and Acoustics **99**
5.1 Flame Characterization **99**

5.2 Flow Field Characterization 106
5.3 Acoustics Characterization 110
5.4 Flame, Flow, and Acoustics Summary 115

CHAPTER 6. Near-Blowoff Dynamics 117
6.1 Flame Leading Edge Location and Velocity 117
6.2 Onset of "events" 122
6.3 Extinction Behaviors Under Near LBO Conditions 125
6.4 Re-ignition Behaviors Under Near LBO Conditions 133
6.5 Near LBO Dynamics Summary 136

CHAPTER 7. Concluding Remarks 138
7.1 Summary of Contributions 138
7.2 Applications for Alternative Jet Fuel Certification, OEMs, and Engine Operators 146
7.3 Recommendations for Future Work 148

APPENDIX A. S-Curve: Nonmonotonic Bulkhead Temperature Dependence 150

APPENDIX B. Complete Set of Fuel Screening Correlation Plots 155
B.1 300 K Plots 156
B.2 450 K Plots 161
B.3 550 K Plots 167

APPENDIX C. Near-Blowoff Dynamics Plots with Adjusted Thresholds 174

APPENDIX D. Re-ignition Image Sequences 176

APPENDIX E. V_{up} Probability Density Functions 214

REFERENCES 218

LIST OF TABLES

Table 2-1:	Relevant characteristic time scales.	45
Table 2-2:	Chemical composition and physical property summary of the fuels, as detailed in Ref. [129]. The smoke point of the High TSI fuel was determined using the TSI constants of Mensch et al. [134, 135] (i.e., a=4.07, b=-4.8). The virtual smoke point of Haas et al. [136] is reported below for n-dodecane. The kinematic viscosities at 313 K for fuels C-7, C-8, and C-9 are estimated by Opacich et al. [137].	49
Table 2-3:	Fuels used for the detailed measurements. Acoustic and PMT measurements were taken for each of these fuels, whereas CH* chemiluminescence videos were acquired for the fuels with an asterisk.	55
Table 2-4:	Conditions where PMT measurements (A, B) and CH* chemiluminescence videos (C, D) were acquired.	55
Table 4-1:	Correlation coefficient table depicting the correlations between fuel properties and blowout boundaries, following Burger et al. [96]. Green highlighting accentuates coefficients greater than |±0.5|.	76
Table 4-2:	Variable groups that were used for the Hierarchical Non-negative Garrote Regression.	94

LIST OF FIGURES

Figure 1.1:	Timeline and forecasting of oil production, taken from [7].	2
Figure 1.2:	Conceptual illustration of the blowoff process in premixed systems, adapted from [34].	10
Figure 1.3:	Conceptual illustration of the physics limiting LBO across different combustion regimes.	31
Figure 2.1:	Image (a) and schematic (b) of the experimental combustor.	35
Figure 2.2:	Air preparation and routing diagram.	35
Figure 2.3:	Bulkhead instrumentation placement schematic.	37
Figure 2.4:	Schematic of the swirler and fuel injector configuration.	37
Figure 2.5:	Photograph of the fuel cart used to supply fuel for these experiments.	38
Figure 2.6:	Time history of temperature and fuel flow rate during a series of blowout measurements, illustrating the blowout measurement procedure.	39
Figure 2.7:	Engine inlet conditions and regions where primary figures of merit correspond to the flight operating range. The stars represent conditions for data acquisition. Taken from [9].	43
Figure 2.8:	Relationship between T_{50} (i.e., the temperature at which 50% of the liquid volume had vaporized) and derived cetane number for investigated fuels.	46
Figure 2.9:	Distillation characteristics of Jet-A POSF 10325 determined by the boiling point temperature as a function of the liquid volume recovered by the ASTM D86 method. Insets are direct photographs of five distillation cuts collected for each of the 20% volume samples.	51
Figure 2.10:	Schematic of the PMT configuration and the corresponding viewing angles. Taken from [143].	57
Figure 2.11:	PMT placement and associated distances to the test section. The image on the left is a side view of the combustor and the right image represents a top down view of the combustor.	57

Figure 3.1: Conceptual illustration of the leave-one-out cross-validation procedure. The green groups represent the fuels used for the training data and the red groups represent the fuels used as the test data. 63

Figure 3.2: Conceptual threshold selection illustration. I_v represents an indicator of blowout proximity and P_{FS} governs flame stability. Taken from [17]. 68

Figure 3.3: PMT time series at a 450 K air inlet temperature (left) and a 300 K air inlet temperature (right). The upper and lower thresholds are represented by the orange and yellow dashed lines, respectively. The fuel is A-2 (Jet-A). 69

Figure 3.4: Equivalence ratio dependence of the average event frequency and duration as blowout is approached at a 450 K air inlet temperature (left) and 300 K air inlet temperature (right). The fuel is A-2 (Jet-A) in both instances. 69

Figure 3.5: Equivalence ratio dependence of the event frequency and duration as blowout is approached for a single 450 K air inlet temperature case (left) and the CDF of the event frequency (right). The orange line in the right plot represents 10% probability that an event will cause blowout and the corresponding equivalence ratio is marked by the yellow data point. The fuel is A-2 (Jet-A). 71

Figure 3.6: PMT time series at a 450 K air inlet temperature. A segment of the time series that includes a single LBO precursor event is shown on the left. This plot indicates how the duration of an LBO precursor event was defined. The complete time series, with indicators for the recording times corresponding to ϕ_{event} and ϕ_{LBO}, is shown on the right. The fuel is A-2 (Jet-A). 72

Figure 4.1: Percent differences in the blowout equivalence ratio between each fuel and A-2. Error bars represent 95% confidence intervals. 74

Figure 4.2: Dependence of the percent difference in blowout equivalence ratio from A-2 upon T_{10}. The data is compared at a bulkhead temperature of 500 K. 79

Figure 4.3: Dependence of the percent difference in blowout equivalence ratio from A-2 upon T_{50}. The data is compared at a bulkhead temperature of 500 K. 79

Figure 4.4: Dependence of the percent difference in blowout equivalence ratio from A-2 upon T_{90}. The data is compared at a bulkhead temperature of 500 K. 79

Figure 4.5: Average equivalence ratio at blowout versus percentage of A-2 fuel composition for A-2/C-1 blends. Blue symbols represent 300 K data, red symbols represent 450 K data, and yellow symbols represent 550 K data. Error bars represent the RMS of daily 95% confidence intervals. See Figure B. 1 for more details on uncertainties of the blended fuels. 81

Figure 4.6: Dependence of the percent difference in blowout equivalence ratio from A-2 upon the percentage of aromatics in each fuel. The data is compared at a bulkhead temperature of 550 K. 83

Figure 4.7: Dependence of the percent difference in blowout equivalence ratio from A-2 upon the derived cetane number. The data is compared at a bulkhead temperature of 500 K. 84

Figure 4.8: Dependence of the percent difference in blowout equivalence ratio from A-2 upon the derived cetane number. The data is compared at a bulkhead temperature of 550 K. 86

Figure 4.9: Dependence of the percent difference in blowout equivalence ratio from A-2 upon the derived cetane number. The data is compared at a bulkhead temperature of 640 K. 86

Figure 4.10: DCN values across the distillation range for fuels A-2 and A-3 (a), and A-2, S1, and S2 (b). 88

Figure 4.11: Dependence of $\%\phi$ from A-2 upon the 20% DCN. The data is compared at a bulkhead temperature of 500 K and has a correlation coefficient of -0.74. 89

Figure 4.12: Dependence of $\%\phi$ from A-2 upon the 20% DCN. The data is compared at a bulkhead temperature of 550 K and has a correlation coefficient of -0.91. 90

Figure 4.13: Dependence of $\%\phi$ from A-2 upon the 20% DCN. The data is compared at a bulkhead temperature of 640 K and has a correlation coefficient of -0.95. 90

Figure 4.14: $\%\phi$ from A-2 at all three air inlet temperatures. The C-1/C_7H_{16} and C-1/$C_{12}H_{26}$ fuels are designed to accentuate preferential vaporization effects. 91

Figure 4.15: Regression coefficients determined by the Hierarchical Non-negative Garrote method. 94

Figure 4.16: Regression coefficients determined by the Hierarchical Non-negative Garrote method when the 20% DCN is used for the fuels where it is available. 96

Figure 5.1: Instantaneous camcorder images of the A-2 flame at the 300 K (left), 450 K (center), and 550 K (right) air inlet temperatures. 99

Figure 5.2: Instantaneous OH-PLIF images with overlaid PIV vectors. Fuel A-2 is burning at an air inlet temperature of 450 K and an equivalence ratio of 0.45. The dotted green line represents zero velocity stagnation contours. 100

Figure 5.3: Four successive OH-PLIF images with overlaid PIV vectors. Fuel A-2 is burning at an air inlet temperature of 450 K and an equivalence ratio of 0.45. The dotted green line represents zero velocity stagnation contours. These images show evidence of flame burning in the central recirculation zone. 101

Figure 5.4: Instantaneous OH-PLIF images with overlaid PIV vectors. Fuel A-2 is burning at an air inlet temperature of 450 K during a blowout transient. The dotted green line represents zero velocity stagnation contours. 102

Figure 5.5: Four successive OH-PLIF images with overlaid PIV vectors. Fuel A-2 is burning at an air inlet temperature of 450 K shortly before the flame blew out. The dotted green line represents zero velocity stagnation contours. These images show that the flame quickly extinguished when it was transported into the central recirculation zone. 103

Figure 5.6: Six successive OH-PLIF images with overlaid PIV vectors. Fuel A-2 is burning at an air inlet temperature of 450 K and an equivalence ratio of 0.45. The dotted green line represents zero velocity stagnation contours. These images show evidence of local extinction and re-ignition. 104

Figure 5.7: Detailed view of five successive OH-PLIF images with overlaid PIV vectors. Fuel A-2 is burning at an air inlet temperature of 450 K during a blowout transient. The red circles surround a vortex in the outer shear layer that is believed to cause local extinction. 105

Figure 5.8: Detailed view of five successive OH-PLIF images with overlaid PIV vectors. Fuel A-2 is burning at an air inlet temperature of 450 K during a blowout transient. The red circles surround a helical vortex in the inner shear layer that is believed to cause local extinction. 105

Figure 5.9: Instantaneous (left) and time-averaged (right) reacting velocity field for fuel A-2 at 345 kPa, 450 K, and a global equivalence ratio of 0.45. Color represents out of plane velocity. White lines denote locations with zero axial velocity and black lines represent the jet core. The arrow in the top left indicates a 25 m/s velocity vector for reference. 106

Figure 5.10: Central recirculation zone boundaries (solid lines) and jet cores (dashed lines) for the time averaged flow fields from fuels A-2, C-1, and C-5. (450 K air temperature, 345 kPa pressure, and ϕ=0.45) 107

Figure 5.11: Central recirculation zone boundaries (left) and jet cores (right) for the time averaged flow fields from a stable burning A-2 case, a non-reacting case, and a blowout transient A-2 case. Uncertainty bounds are represented by 10% and 90% probability contours. They are calculated by the probability of reverse flow on the left and the probability that the axial velocity is greater than two thirds of the average jet core velocity on the right. (450 K air temperature, 345 kPa pressure) 109

Figure 5.12: RMS of the dynamic pressure plotted as a function of (ϕ - ϕ_{LBO}). This RMS pressure is plotted as a percentage of the mean combustor pressure and has been averaged over the 10 cases for each fuel. These measurements were taken at a 300 K air inlet temperature. 111

Figure 5.13: RMS of the dynamic pressure plotted as a function of (ϕ - ϕ_{LBO}). This RMS pressure is plotted as a percentage of the mean combustor pressure and has been averaged over the 10 cases for each fuel. These measurements were taken at a 450 K air inlet temperature. 112

Figure 5.14: RMS of the dynamic pressure plotted as a function of (ϕ - ϕ_{LBO}). This RMS pressure is plotted as a percentage of the mean combustor pressure and has been averaged over the 10 cases for each fuel. These measurements were taken at a 550 K air inlet temperature. 113

Figure 5.15: FFTs of a dynamic pressure time series taken during a transient blowout process. Fuel C-5 is burning with an air inlet temperature of 550 K. These plots are shown in 5 second intervals as blowout is approached. The top plot is furthest from blowout and the bottom plot is nearest LBO. 114

Figure 5.16: RMS of the dynamic pressure plotted as a function of T_{50}. This RMS pressure is plotted as a percentage of the mean combustor pressure. The RMS pressure values in the left plot were calculated using the entire time series and have been averaged over the 10 cases for each fuel. The RMS pressure values in the plot on the right represent the RMS of the average lines in Figure 5.14, within the interval $0.11 \geq \phi - \phi_{LBO} \geq 0$. These measurements were taken at a 550 K air inlet temperature. The error bars represent 95% confidence intervals. 114

Figure 6.1: Instantaneous CH* chemiluminescence images taken of the flame during both stable (left) and "stage 1" (center and right) conditions. A-2 (Jet-A) is burning in each of these images at 450 K. 118

Figure 6.2: Twelve successive CH* chemiluminescence images taken during an LBO precursor event near blowoff. The star denotes the most upstream spatial location of luminosity. N-dodecane is burning in these images at 450 K. 118

Figure 6.3: Twelve successive CH* chemiluminescence images taken during an LBO precursor event near blowoff. The star denotes the most upstream spatial location of luminosity. A-2 (Jet-A) is burning in these images at 450 K. 119

Figure 6.4: Average 450 K PDF of v_{up} at condition B for A-2 and C-1. The axial flow velocity PDFs U_{Total} and U_{CRZ} are also shown. 122

Figure 6.5: Equivalence ratio at which blowoff occurs, ϕ_{LBO}, plotted against the equivalence ratio where events initiate, ϕ_{event}. Results are included at both air inlet temperatures. 123

Figure 6.6: (ϕ_{event} - ϕ_{LBO}) plotted against the DCN at 450 K (a) and T_{90} at 300 K (b). The 20% DCN for fuel S2 is used here due to its potential for preferential vaporization. 125

Figure 6.7: Average duration of the LBO precursor events, τ_{event}, plotted against T_{50} (a) and T_{90} (b). The error bars represent a combined uncertainty based on 95% confidence intervals and adjusting the double thresholds by ± 5%. (Condition B) 127

Figure 6.8: Average percentage of time in the near-blowoff stages ($\phi_{event} > \phi > \phi_{LBO}$) constituted by extinction, $\%\tau_{ext}$, plotted against T_{50} (a) and T_{90} (b). The error bars represent a combined uncertainty based on 95% confidence intervals and adjusting the double thresholds by ± 5%. (Condition B) 128

Figure 6.9: Average duration of the LBO precursor events, τ_{event}, (a) and the percentage of time in the near-blowoff stages ($\phi_{event} > \phi > \phi_{LBO}$) constituted by extinction, $\%\tau_{ext}$ (b). These condition A results are plotted against T_{90} and the DCN, respectively. The 20% DCN for fuel S2 is used here due to its potential for preferential vaporization. 129

Figure 6.10: Average duration of the LBO precursor events, τ_{event}, plotted against T_{50} (a) and T_{90} (b). These τ_{event} values represent the average event duration in the final second before LBO. The error bars represent a combined uncertainty based on 95% confidence intervals and adjusting the double thresholds by ± 5%. (Condition D) 131

Figure 6.11: Average percentage of time in the near-blowoff stages ($\phi_{event} > \phi > \phi_{LBO}$) constituted by extinction, $\%\tau_{ext}$, plotted against T_{50} (a) and T_{90} (b). These $\%\tau_{ext}$ values represent the average extinction percentage in the final second before LBO. The error bars represent a combined uncertainty based on 95% confidence intervals and adjusting the double thresholds by ± 5%. (Condition D) 132

Figure 6.12: Average duration of the LBO precursor events, τ_{event}, (a) and the $\%\tau_{ext}$ (b) in the final second before LBO. These condition C results are plotted against T_{90} and the DCN, respectively. The 20% DCN for fuel S2 is used here due to its potential for preferential vaporization. 133

Figure 6.13: $\%v_{up}$ < -30 m/s at condition C (a) and condition D (b). The 450 K data is plotted against the DCN and the 300 K data is plotted against T_{90}. Since the role of preferential vaporization on re-ignition is unclear, both the 20% DCN and the DCN based on the entire fuel composition are shown for fuel S2. Error bars represent 95% confidence intervals. 135

Figure A.1: Dependence of bulkhead temperature on the equivalence ratio at blowout for fuel C-4. Orange symbols represent 300 K data, green symbols represent 450 K data, and blue symbols represent 550 K data. The different marker types represent data from separate days that the experiment was run. 151

Figure A.2: Dependence of bulkhead temperature on the equivalence ratio at blowout for fuel A-2. Orange symbols represent 300 K data, green symbols represent 450 K data, and blue symbols represent 550 K data. The different marker types represent data from separate days that the experiment was run. 152

Figure A.3: R^2 value of the blowout equivalence ratio dependence on bulkhead temperature, as a function of the mass accumulated in the Quartz Crystal Microbalance test. 153

Figure A.4: R^2 value of the blowout equivalence ratio dependence on bulkhead temperature, as a function of the maximum deposit thickness measured by the JFTOT at 285 154

Figure A.5: R^2 value of the blowout equivalence ratio dependence on bulkhead temperature, as a function of the H/C ratio. 154

Figure B. 1: Average differences in the blowout equivalence ratio between each fuel and A-2. Error bars represent the RMS of daily 95% confidence intervals. 156

Figure B. 2: Dependence of the percent difference in blowout equivalence ratio from A-2 upon the kinematic viscosity. The data is compared at a bulkhead temperature of 500 K. 156

Figure B. 3: Dependence of the percent difference in blowout equivalence ratio from A-2 upon the surface tension. The data is compared at a bulkhead temperature of 500 K. 157

Figure B. 4: Dependence of the percent difference in blowout equivalence ratio from A-2 upon the fuel density. The data is compared at a bulkhead temperature of 500 K. 157

Figure B. 5: Dependence of the percent difference in blowout equivalence ratio from A-2 upon the H/C ratio. The data is compared at a bulkhead temperature of 500 K. 158

Figure B. 6: Dependence of the percent difference in blowout equivalence ratio from A-2 upon the molecular weight. The data is compared at a bulkhead temperature of 500 K. 158

Figure B. 7: Dependence of the percent difference in blowout equivalence ratio from A-2 upon the lower heating value. The data is compared at a bulkhead temperature of 500 K. 159

Figure B. 8: Dependence of the percent difference in blowout equivalence ratio from A-2 upon the percentage of aromatics in the fuel. The data is compared at a bulkhead temperature of 500 K. 159

Figure B. 9: Dependence of the percent difference in blowout equivalence ratio from A-2 upon the percentage of iso-paraffins in the fuel. The data is compared at a bulkhead temperature of 500 K. 160

Figure B. 10: Dependence of the percent difference in blowout equivalence ratio from A-2 upon the smoke point. The data is compared at a bulkhead temperature of 500 K. 160

Figure B. 11: Dependence of the percent difference in blowout equivalence ratio from A-2 upon the radical index. The data is compared at a bulkhead temperature of 500 K. 161

Figure B. 12: Dependence of the percent difference in blowout equivalence ratio from A-2 upon T_{90}. The data is compared at a bulkhead temperature of 550 K. 161

Figure B. 13: Dependence of the percent difference in blowout equivalence ratio from A-2 upon T_{50}. The data is compared at a bulkhead temperature of 550 K. 162

Figure B. 14: Dependence of the percent difference in blowout equivalence ratio from A-2 upon T_{10}. The data is compared at a bulkhead temperature of 550 K. 162

Figure B. 15: Dependence of the percent difference in blowout equivalence ratio from A-2 upon the kinematic viscosity. The data is compared at a bulkhead temperature of 550 K. 163

Figure B. 16: Dependence of the percent difference in blowout equivalence ratio from A-2 upon the surface tension. The data is compared at a bulkhead temperature of 550 K. 163

Figure B. 17: Dependence of the percent difference in blowout equivalence ratio from A-2 upon the fuel density. The data is compared at a bulkhead temperature of 550 K. 164

Figure B. 18: Dependence of the percent difference in blowout equivalence ratio from A-2 upon the H/C ratio. The data is compared at a bulkhead temperature of 550 K. 164

Figure B. 19: Dependence of the percent difference in blowout equivalence ratio from A-2 upon the molecular weight. The data is compared at a bulkhead temperature of 550 K. 165

Figure B. 20: Dependence of the percent difference in blowout equivalence ratio from A-2 upon the lower heating value. The data is compared at a bulkhead temperature of 550 K. 165

Figure B. 21: Dependence of the percent difference in blowout equivalence ratio from A-2 upon the percentage of iso-paraffins in the fuel. The data is compared at a bulkhead temperature of 550 K. 166

Figure B. 22: Dependence of the percent difference in blowout equivalence ratio from A-2 upon the smoke point. The data is compared at a bulkhead temperature of 550 K. 166

Figure B. 23: Dependence of the percent difference in blowout equivalence ratio from A-2 upon the radical index. The data is compared at a bulkhead temperature of 550 K. 167

Figure B. 24: Dependence of the percent difference in blowout equivalence ratio from A-2 upon T_{90}. The data is compared at a bulkhead temperature of 640 K. 167

Figure B. 25: Dependence of the percent difference in blowout equivalence ratio from A-2 upon T_{50}. The data is compared at a bulkhead temperature of 640 K. 168

Figure B. 26: Dependence of the percent difference in blowout equivalence ratio from A-2 upon T_{10}. The data is compared at a bulkhead temperature of 640 K. 168

Figure B. 27: Dependence of the percent difference in blowout equivalence ratio from A-2 upon the kinematic viscosity. The data is compared at a bulkhead temperature of 640 K. 169

Figure B. 28: Dependence of the percent difference in blowout equivalence ratio from A-2 upon the surface tension. The data is compared at a bulkhead temperature of 640 K. 169

Figure B. 29: Dependence of the percent difference in blowout equivalence ratio from A-2 upon the fuel density. The data is compared at a bulkhead temperature of 640 K. 170

Figure B. 30: Dependence of the percent difference in blowout equivalence ratio from A-2 upon the H/C ratio. The data is compared at a bulkhead temperature of 640 K. 170

Figure B. 31: Dependence of the percent difference in blowout equivalence ratio from A-2 upon the molecular weight. The data is compared at a bulkhead temperature of 640 K. 171

Figure B. 32: Dependence of the percent difference in blowout equivalence ratio from A-2 upon the lower heating value. The data is compared at a bulkhead temperature of 640 K. 171

Figure B. 33: Dependence of the percent difference in blowout equivalence ratio from A-2 upon the percentage of aromatics in the fuel. The data is compared at a bulkhead temperature of 640 K. 172

Figure B. 34: Dependence of the percent difference in blowout equivalence ratio from A-2 upon the percentage of iso-paraffins in the fuel. The data is compared at a bulkhead temperature of 640 K. 172

Figure B. 35: Dependence of the percent difference in blowout equivalence ratio from A-2 upon the smoke point. The data is compared at a bulkhead temperature of 640 K. 173

Figure B. 36: Dependence of the percent difference in blowout equivalence ratio from A-2 upon the radical index. The data is compared at a bulkhead temperature of 640 K. 173

Figure C. 1: $\%v_{up}$ < -30 m/s at 450 K plotted against the DCN. These results are shown using slightly lower thresholds than the values used in Section 6.4. Since the role of preferential vaporization on re-ignition is unclear, both the 20% DCN and the DCN based on the entire fuel composition are shown for fuel S2. Error bars represent 95% confidence intervals. 175

Figure C. 2: $\%v_{up}$ < -30 m/s at 450 K plotted against the DCN. These results are shown using slightly higher thresholds than the values used in Section 6.4. Since the role of preferential vaporization on re-ignition is unclear, both the 20% DCN and the DCN based on the entire fuel composition are shown for fuel S2. Error bars represent 95% confidence intervals. 175

Figure D. 1 Twelve successive CH* chemiluminescence images taken during an LBO precursor event. The star denotes the most upstream spatial location of luminosity. A-2 is burning in these images with an air inlet temperature of 450 K. 176

Figure D. 2 Twelve successive CH* chemiluminescence images taken during an LBO precursor event. The star denotes the most upstream spatial location of luminosity. A-2 is burning in these images with an air inlet temperature of 450 K. 177

Figure D. 3 Twelve successive CH* chemiluminescence images taken during an LBO precursor event. The star denotes the most upstream spatial location of luminosity. A-2 is burning in these images with an air inlet temperature of 450 K. 178

Figure D. 4 Twelve successive CH* chemiluminescence images taken during an LBO precursor event. The star denotes the most upstream spatial location of luminosity. A-2 is burning in these images with an air inlet temperature of 450 K. 179

Figure D. 5 Twelve successive CH* chemiluminescence images taken during an LBO precursor event. The star denotes the most upstream spatial location of luminosity. A-2 is burning in these images with an air inlet temperature of 450 K. 180

Figure D. 6 Twelve successive CH* chemiluminescence images taken during an LBO precursor event. The star denotes the most upstream spatial location of luminosity. A-2 is burning in these images with an air inlet temperature of 450 K. 181

Figure D. 7 Twelve successive CH* chemiluminescence images taken during an LBO precursor event. The star denotes the most upstream spatial location of luminosity. A-2 is burning in these images with an air inlet temperature of 450 K. 182

Figure D. 8 Twelve successive CH* chemiluminescence images taken during an LBO precursor event. The star denotes the most upstream spatial location of luminosity. A-2 is burning in these images with an air inlet temperature of 450 K. 183

Figure D. 9 Twelve successive CH* chemiluminescence images taken during an LBO precursor event. The star denotes the most upstream spatial location of luminosity. A-2 is burning in these images with an air inlet temperature of 450 K. 184

Figure D. 10 Twelve successive CH* chemiluminescence images taken during an LBO precursor event. The star denotes the most upstream spatial location of luminosity. A-2 is burning in these images with an air inlet temperature of 450 K. 185

Figure D. 11 Twelve successive CH* chemiluminescence images taken during an LBO precursor event. The star denotes the most upstream spatial location of luminosity. A-2 is burning in these images with an air inlet temperature of 450 K. 186

Figure D. 12 Twelve successive CH* chemiluminescence images taken during an LBO precursor event. The star denotes the most upstream spatial location of luminosity. A-2 is burning in these images with an air inlet temperature of 450 K. 187

Figure D. 13 Twelve successive CH* chemiluminescence images taken during an LBO precursor event. The star denotes the most upstream spatial location of luminosity. A-2 is burning in these images with an air inlet temperature of 450 K. 188

Figure D. 14 Twelve successive CH* chemiluminescence images taken during an LBO precursor event. The star denotes the most upstream spatial location of luminosity. A-2 is burning in these images with an air inlet temperature of 450 K. 189

Figure D. 15 Twelve successive CH* chemiluminescence images taken during an LBO precursor event. The star denotes the most upstream spatial location of luminosity. A-2 is burning in these images with an air inlet temperature of 450 K. 190

Figure D. 16 Twelve successive CH* chemiluminescence images taken during an LBO precursor event. The star denotes the most upstream spatial location of luminosity. C-1 is burning in these images with an air inlet temperature of 450 K. 191

Figure D. 17 Twelve successive CH* chemiluminescence images taken during an LBO precursor event. The star denotes the most upstream spatial location of luminosity. C-1 is burning in these images with an air inlet temperature of 450 K. 192

Figure D. 18 Twelve successive CH* chemiluminescence images taken during an LBO precursor event. The star denotes the most upstream spatial location of luminosity. C-1 is burning in these images with an air inlet temperature of 450 K. 193

Figure D. 19 Twelve successive CH* chemiluminescence images taken during an LBO precursor event. The star denotes the most upstream spatial location of luminosity. C-1 is burning in these images with an air inlet temperature of 450 K. 194

Figure D. 20 Twelve successive CH* chemiluminescence images taken during an LBO precursor event. The star denotes the most upstream spatial location of luminosity. C-1 is burning in these images with an air inlet temperature of 450 K. 195

Figure D. 21	Twelve successive CH* chemiluminescence images taken during an LBO precursor event. The star denotes the most upstream spatial location of luminosity. C-1 is burning in these images with an air inlet temperature of 450 K.	196
Figure D. 22	Twelve successive CH* chemiluminescence images taken during an LBO precursor event. The star denotes the most upstream spatial location of luminosity. C-1 is burning in these images with an air inlet temperature of 450 K.	197
Figure D. 23	Twelve successive CH* chemiluminescence images taken during an LBO precursor event. The star denotes the most upstream spatial location of luminosity. C-1 is burning in these images with an air inlet temperature of 450 K.	198
Figure D. 24	Twelve successive CH* chemiluminescence images taken during an LBO precursor event. The star denotes the most upstream spatial location of luminosity. C-1 is burning in these images with an air inlet temperature of 450 K.	199
Figure D. 25	Twelve successive CH* chemiluminescence images taken during an LBO precursor event. The star denotes the most upstream spatial location of luminosity. N-dodecane is burning in these images with an air inlet temperature of 450 K.	200
Figure D. 26	Twelve successive CH* chemiluminescence images taken during an LBO precursor event. The star denotes the most upstream spatial location of luminosity. N-dodecane is burning in these images with an air inlet temperature of 450 K.	201
Figure D. 27	Twelve successive CH* chemiluminescence images taken during an LBO precursor event. The star denotes the most upstream spatial location of luminosity. N-dodecane is burning in these images with an air inlet temperature of 450 K.	202
Figure D. 28	Twelve successive CH* chemiluminescence images taken during an LBO precursor event. The star denotes the most upstream spatial location of luminosity. N-dodecane is burning in these images with an air inlet temperature of 450 K.	203
Figure D. 29	Twelve successive CH* chemiluminescence images taken during an LBO precursor event. The star denotes the most upstream spatial location of luminosity. N-dodecane is burning in these images with an air inlet temperature of 450 K.	204

Figure D. 30 Twelve successive CH* chemiluminescence images taken during an LBO precursor event. The star denotes the most upstream spatial location of luminosity. N-dodecane is burning in these images with an air inlet temperature of 450 K. 205

Figure D. 31 Twelve successive CH* chemiluminescence images taken during an LBO precursor event. The star denotes the most upstream spatial location of luminosity. N-dodecane is burning in these images with an air inlet temperature of 450 K. 206

Figure D. 32 Twelve successive CH* chemiluminescence images taken during an LBO precursor event. The star denotes the most upstream spatial location of luminosity. N-dodecane is burning in these images with an air inlet temperature of 450 K. 207

Figure D. 33 Twelve successive CH* chemiluminescence images taken during an LBO precursor event. The star denotes the most upstream spatial location of luminosity. S2 is burning in these images with an air inlet temperature of 450 K. 208

Figure D. 34 Twelve successive CH* chemiluminescence images taken during an LBO precursor event. The star denotes the most upstream spatial location of luminosity. S2 is burning in these images with an air inlet temperature of 450 K. 209

Figure D. 35 Twelve successive CH* chemiluminescence images taken during an LBO precursor event. The star denotes the most upstream spatial location of luminosity. S2 is burning in these images with an air inlet temperature of 450 K. 210

Figure D. 36 Twelve successive CH* chemiluminescence images taken during an LBO precursor event. The star denotes the most upstream spatial location of luminosity. S2 is burning in these images with an air inlet temperature of 450 K. 211

Figure D. 37 Twelve successive CH* chemiluminescence images taken during an LBO precursor event. The star denotes the most upstream spatial location of luminosity. S2 is burning in these images with an air inlet temperature of 450 K. 212

Figure D. 38 Twelve successive CH* chemiluminescence images taken during an LBO precursor event. The star denotes the most upstream spatial location of luminosity. S2 is burning in these images with an air inlet temperature of 450 K. 213

Figure E. 1 PDFs of v_{up} for A-2, C-1, n-dodecane, and S2 at 450 K, taken as ϕ-$\phi_{LBO}\rightarrow 0$. The axial flow velocity PDFs U_{Total} and U_{CRZ} are also shown. 214

Figure E. 2 PDFs of v_{up} for A-2, C-1, n-dodecane, and S2 at 450 K, taken as ϕ-$\phi_{LBO}\approx 0.025$. The axial flow velocity PDFs U_{Total} and U_{CRZ} are also shown. 215

Figure E. 3 PDFs of v_{up} for A-2, C-5, n-dodecane, and S2 at 300 K, taken as ϕ-$\phi_{LBO}\rightarrow 0$. 215

Figure E. 4 PDFs of v_{up} for A-2 at 450 K, taken as ϕ-$\phi_{LBO}\rightarrow 0$. The axial flow velocity PDFs U_{Total} are also shown. 216

Figure E. 5 PDFs of v_{up} for C-1 at 450 K, taken as ϕ-$\phi_{LBO}\rightarrow 0$. The axial flow velocity PDFs U_{Total} are also shown. 216

Figure E. 6 PDFs of v_{up} for n-dodecane at 450 K, taken as ϕ-$\phi_{LBO}\rightarrow 0$. The axial flow velocity PDFs U_{Total} are also shown. 217

Figure E. 7 PDFs of v_{up} for S2 at 450 K, taken as ϕ-$\phi_{LBO}\rightarrow 0$. The axial flow velocity PDFs U_{Total} are also shown. 217

LIST OF SYMBOLS AND ABBREVIATIONS

CDF	Cumulative distribution function
D	Characteristic length scale
d	Shrinkage factor
Da	Damköhler number
DCN	Derived cetane number
20/100% DCN	20% DCN for the six fuels where measurements are available and the DCN based on the entire fuel composition for the remaining fuels
DeZ	Dezubay number
FFT	Fast Fourier transform
FS	Full scale
H/C	Hydrogen to carbon ratio
I	Identity matrix
IQT	Ignition quality tester
k	Index relating to groups of variables
LBO	Lean blowout
LHV	Lower heating value
m	Number of experimental days
MW	Molecular weight
n	Direction normal to the flame front, sample size
P	Mean pressure
p	Instantaneous pressure, number of variables
PDF	Probability density function

$p_{i,j}$	Number of data points in the 50 K bulkhead temperature window for each fuel on a given experimental day
Ri	Radical index
RMS	Root mean square
R^2	R-squared value
S_d	Flame displacement speed
$s_{i,j}$	Standard deviation corresponding to each fuel and experimental day
SP	Smoke point
T	Temperature
t	Time
T_{10}	10% boiling point temperature
T_{50}	50% boiling point temperature
T_{90}	90% boiling point temperature
U	Mean velocity
u	Instantaneous velocity
U_{CRZ}	PDF of axial flow velocity in the central recirculation zone
U_{Total}	Axial flow velocity PDF based on the total measurement domain
v_n	Incoming reactant velocity in the direction normal to the flame front
v_{up}	Velocity of x_{up} between successive images
$\%v_{up}<\text{-}30\ m/s$	Percentage of LBO precursor events where v_{up} is less than -30 m/s
X	Input variable matrix
x	Position
x_{up}	Most upstream spatial location where luminosity is detected
Y	Output variable vector
β	Regression coefficients

β^{HNNG}	Hierarchical Non-negative Garrote regression coefficients
β^{OLS}	Ordinary least squares regression coefficients
β^{ridge}	Ridge regression coefficients
Δx_{up}	Difference in x_{up} between successive images
$\Delta\phi$	Difference in lean blowout equivalence ratio between a given fuel and the reference fuel, A-2
ε	Alternating unit tensor, a small value
ϵ	Regression error
λ	Tuning parameter
ν	Kinematic viscosity
ρ	Density
σ	Surface tension
$\sigma_{\Delta\phi,i}$	Uncertainty in $\Delta\phi$ for each fuel
τ_{chem}	Characteristic chemical time
τ_{evap}	Characteristic evaporation time
τ_{event}	Average duration of LBO precursor events
$\%\tau_{ext}$	Percentage of time in $\phi_{event} > \phi > \phi_{LBO}$ interval constituted by extinction
τ_{flow}	Characteristic flow time
$\tau_{flow,D/U}$	Characteristic flow time scale based on the nozzle exit diameter and velocity
$\tau_{flow,res}$	Combustor residence time
τ_{ign}	Characteristic ignition time
ϕ	Equivalence ratio
$\%\phi$	Percent difference in lean blowout equivalence ratio between a given fuel and the reference fuel, A-2
ϕ_{event}	Equivalence ratio at which LBO precursor events begin

ϕ_{LBO} Lean blowout equivalence ratio

ω Vorticity

$\odot$ Element-wise vector product

SUMMARY

Lean blowout is a process whereby a previously stable flame is either extinguished or advected out of its combustor. In aviation applications, blowout is a direct threat to passenger safety and it therefore sets operational limits on a combustor. Understanding the blowout problem is a key prerequisite to the deployment of alternative aviation fuels, as these fuels are expected to have comparable flame stability characteristics as traditional jet fuels. In order for a new jet fuel to be certified, it must satisfy a series of performance criteria, one of which is lean blowout. Although much research has been done to understand lean blowout in premixed gaseous combustors, fewer studies have investigated this phenomenon in liquid fueled systems. Furthermore, the liquid blowout studies that do exist have often come to different conclusions, as part of the researchers argue that blowout is limited by fuel vaporization characteristics and the others conclude that chemical properties control the blowout physics. Consequently, the effect that different fuel physical and chemical properties have on the stability of spray flames remains a scientific unknown. This knowledge gap hinders the ability of chemists to develop optimized fuels and raises the risk that a prospective fuel will fail the certification process, thereby discouraging potential investors. The objective of this work is to identify the fuel properties that govern lean blowout and to characterize their effect on the physics involved in the blowout process.

The blowout performance of 18 different liquid fuels were experimentally compared in an aircraft relevant combustor. The methodology that was used clearly demonstrated differences in the fuel-air ratio at blowout between fuels. Identifying the fuel properties that are responsible for these fuel-air ratio differences is challenging for three

primary reasons. First, the fuel properties themselves are often correlated with each other, making it difficult to isolate which properties actually limit lean blowout. Second, the sensitivity of blowout to fuel physical properties is likely to change with combustor operating conditions, as differences in air inlet temperature can significantly affect droplet evaporation rates. Third, some of the fuels have unique preferential vaporization characteristics which can cause the combustion chemistry to vary as the droplets evaporate. In other words, local fuel properties may not represent the characteristics based on the entire composition of the fuel. A number of approaches were used in this work to address each of these issues. Custom fuels were introduced that were specifically designed to decouple interrelated fuel properties and to accentuate the significance of preferential vaporization on lean blowout. Additionally, the experiments were repeated at 3 different air inlet temperatures: 300 K, 450 K, and 550 K. These different temperatures are intended to vary the effect of fuel physical properties. Lastly, a multiple linear regression analysis was performed to determine the relative contributions of each of the fuel properties on the lean blowout equivalence ratio. This regression was performed using a machine learning technique that accounted for correlations between variables and eliminated insignificant variables from consideration.

This work additionally seeks to characterize the effect of fuel properties on the processes that precede blowout of the flame, thereby providing an explanation for why certain fuel properties govern lean blowout boundaries. It is motivated by prior work on gaseous systems, showing that the blowout phenomenon is a culmination of several intermediate processes, initiating with local extinction of reactions (“stage 1”), followed by large scale flame and flow disruption (“stage 2”), finally leading to blowout. By

quantifying the time variation of flame luminosity and extinction “events” as a function of blowout proximity, it was demonstrated that similar local extinction processes are operative in and lead to blowout in spray flames. In addition, high speed imaging was used to analyze the space-time evolution of the most upstream point of the flame near blowout. Fast motion of these points upstream relative to the flow velocity were interpreted as flame re-ignition. These re-ignition processes become manifest when the stability of the flame is severely threatened by local extinction and often allow for recoveries that extend flame burning. Specific fuel properties were shown to have a clear effect on a flame’s propensity for extinction and re-ignition.

CHAPTER 1. INTRODUCTION

1.1 Motivation

Conventional jet fuel is a refined fraction of crude oil that is selected to have the appropriate freeze point and distillation characteristics to avoid phase changes at high altitude. As of 2007, the global aviation demand required the consumption of 177 million gallons of jet fuel each day, with 40% of this usage coming from the United States [1]. The dependence of global transportation on oil has historically made it the most coveted resource in world trade. For example, in 2006, oil exports constituted 13% of world trade expenditures [2]. This consumption rate can only be expected to continue increasing, as the global energy demand is projected to double by 2050 [3]. Since oil is a finite resource, this creates problems in terms of forecasting the limits of its supply. Scholars are divided about the imminent risk of oil reserve depletion [4-7]. However, most predict that between the years 2030-2070 the demand for oil will begin to exceed its supply [4, 7]. A range of asymmetric predictions for this oil production peak, along with estimates for when the world's petroleum reserves will be exhausted, are shown in Figure 1.1.

Climate change is another key issue that pressures the transportation industry to improve its existing technology. Reports estimate that by the year 2100, the average global temperature will increase 2-11.5 degrees Fahrenheit [8]. Other deleterious ecological effects are expected to result from climate change, including an estimated 7-23 inch rise in the average sea level, increased forest fires, droughts, heat waves, and diminished forest populations.

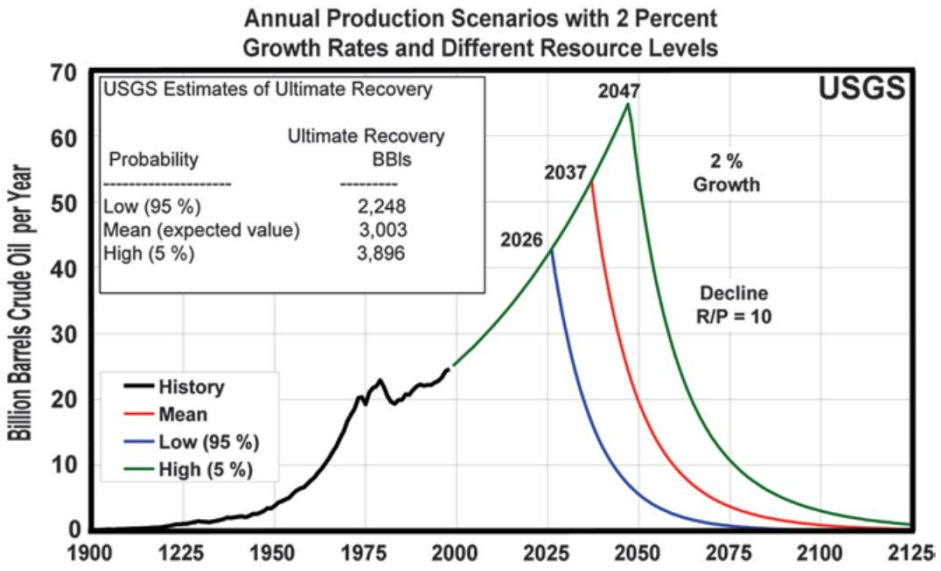

Figure 1.1: Timeline and forecasting of oil production, taken from [7].

Aviation contributes to climate change through a variety of ways, including greenhouse gas emissions, ozone production, and contrail formation. 9-11% of the United States' greenhouse gas output comes from aviation [9, 10], and the high altitude conditions where airplanes operate cause their pollutant emissions to be especially harmful [9, 11]. For example, NO_x emissions in the lower stratosphere and upper troposphere lead to ozone production, which has a significant global warming effect [8]. Furthermore, soot emissions from aircraft engines are dangerous because they reduce air quality, are a health hazard, and promote the formation of contrails that also raise the global temperature [12].

These concerns over global climate change, air quality, and flexibility in fuel sourcing continue to motivate interest in alternative jet fuels. Alternative fuels mitigate the oil supply issue and their low aromatic content [13] greatly reduces soot emissions in comparison with conventional jet fuels [11]. Although aromatics have the benefit of enhancing seal swelling capacity, they are generally an undesirable jet fuel compound [14].

In addition to promoting soot formation [15], aromatics lower the H/C ratio of the fuel, which increases greenhouse gas emissions [8] and generally lowers the heating value.

However, the fuel certification process is a major hurdle toward the broader implementation of alternative fuels. The process is costly, time consuming, and may not be ultimately successful, which adds significant risk for potential suppliers [9]. In addition to a host of physical properties, certification depends upon the fuel's impact on engine operational characteristics, including altitude re-light, cold start, and lean blowout. Lean blowout is a process whereby a previously stable flame can no longer be sustained in a combustor. It manifests itself as either the complete extinction of the flame or the advection of the flame out of the combustor. The sensitivity of lean blowout to different fuel properties makes understanding the relationship between fuel properties and flame stability a scientific imperative for expediting the fuel certification process.

Independent of its relevance for implementing alternative fuels, lean blowout is a major concern for the broader aviation industry because it is a significant threat to passenger safety. In the event that an engine does blow out, its propulsive capacity is lost and a difficult high altitude relight process is required to restore engine operation. Lean blowout is most likely to occur in practice either during transients (i.e., rapid accelerations, rapid decelerations, or sudden changes in external aerodynamic conditions) [16-18] or as an engine's fuel-air ratio is decreased while slowing the plane down before landing [9, 19]. Engine control systems avoid these issues by operating engines in a quasi-steady state manner [20] and keeping the fuel-air ratio well above the lean blowout limit. However, these strategies limit engine performance, reduce available operating ranges, and increase NO_x emissions. Ideally, engines would operate at the leanest conditions that are safely

achievable in order to reduce thermal NO_x. Furthermore, selecting appropriate engine operating conditions is complicated by the fact that the lean blowout limit is not precisely known [17]. Developing a deeper understanding of the physics associated with the lean blowout process is a prerequisite for achieving improvements in these areas. The objective of this work is to identify the fuel properties that govern lean blowout and to characterize their effect on the physics involved in the blowout process.

The manner in which fuel properties influence blowout is a strong function of the degree of vaporization of the fuel and its degree of mixing with air. Chemical kinetic rates, ignitability, fuel-air mixing quality, atomization, and the vaporization characteristics of a fuel can all influence blowoff limits. Although each of these factors are involved in the blowoff phenomenon, a smaller number of these physical processes may be dominantly responsible for controlling the blowoff fuel-air ratio. This dominant limiting process depends on the type of combustion system and the operating conditions. For example, gaseous premixed, gaseous nonpremixed, and liquid fueled systems can all have different fuel property sensitivities. Furthermore, the blowout boundaries of these different systems are also sensitive to the air inlet temperature, as this can amplify or suppress certain physical processes. Therefore, blowoff will be discussed individually from the perspective of gaseous premixed (Section 1.2), gaseous nonpremixed (Section 1.3), and liquid fueled combustors (Section 1.4) in order to prepare the reader for the content of this thesis.

Combustor geometry considerations become important because they influence the flow field involved in the flameholding process. As incoming reactant velocities in gas turbine combustors can be 100+ times greater than the turbulent flame speed [21], recirculation zones are used to slow the approach flow down and enhance the flame speed

by heating incoming reactants with hot products [14]. These hot recirculating products also provide a constant ignition source for the incoming mixture [21]. Two common techniques for creating these recirculation zones are swirling the incoming flow to promote the vortex breakdown process and introducing a blockage in the flow using a bluff-body. Details about the flame stabilization physics associated with both of these approaches will be discussed in Sections 1.2.2 and 1.2.3.

1.2 Premixed Gaseous Lean Blowout Studies

In purely premixed and pre-vaporized systems, blowout is a kinetically limited phenomenon, controlled by the relative balance of chemical rates and fluid mechanic time scales, i.e., a Damköhler number.

$$Da = \frac{\tau_{flow}}{\tau_{chem}} \tag{1.1}$$

Beginning with DeZubay [22], many correlations have been proposed in the literature to predict lean blowoff limits. DeZubay's correlation has since been modified slightly to account for air inlet temperature effects, and the accepted form is shown below [23].

$$DeZ = \frac{U * 10^4}{P^{0.95} D^{0.85} T^{1.2}} \tag{1.2}$$

It is essentially a ratio between a flow time (~U/D) and a chemical time (~PT). Correlations proposed by other researchers are similar in form and all relate back to the basic Damköhler

number relationship [22-27]. These scalings are effective at predicting lean blowout limits under a variety of different pressures, temperatures, and combustor geometries.

Open debate continues within the combustion community about the chemical time scale that should be used in the Damköhler number relationship. Different phenomenological ideas have been put forth in the literature for the details, including (1) well-stirred or perfectly stirred reactor (PSR) descriptions for the recirculating flow field [28-31], (2) autoignition scaling based upon the relative time that reactants are exposed to hot products in shear layers [32, 33], and (3) aerodynamic straining, where shear layer stabilized flames can only withstand certain levels of flame stretch before extinguishing [27, 34-36]. The different controlling kinetic scalings identified in these theories, i.e., the blowout time scale of a PSR, the autoignition time scale and the extinction stretch rate, can have quite different sensitivities to fuel composition, through both kinetic and, in the latter case, differential diffusion effects. However, determining which of these parameters is governing is complicated by the fact that they are often somewhat correlated with each other.

The autoignition based scaling was originally developed by Zukoski in his 1954 PhD thesis [32]. Zukoski concluded that the key region for flame stabilization is the combusting shear layer that separates the recirculation zone behind a bluff-body from the incoming reactants. A subequent study by Zukoski and Marble [33] concluded that flame stability depends on the amount of time that the fresh reactants spend in this combusting shear layer. In this model, blowoff occurs when the fresh gas spends insufficient time in the shear layer for ignition to occur. Heulskamp et al. [26] synthesized a wide range of bluff-body blowoff data available in the literature and found that the Damköhler number

scalings were most effective when the ignition delay time of the fuel was used as the chemical time. Potter and Wong came to a different conclusion when they performed a study very similar to that of Zukoski and Marble, but with a different fuel [37]. They found that for a similar geometry combustor and flameholder, the critical flame stability time was almost identical with that determined by Zukoski and Marble. Considering that different fuels were compared in both studies, they concluded that the key chemical time scale must depend on something like the flame speed, which is similar between hydrocarbon fuels, rather than the autoignition time which varies greatly between hydrocarbons.

Other researchers have questioned [34, 38] whether this ignition based model is physically realizable. The main issue is that it describes a mechanism of interaction between hot recirculating products and incoming reactants that can't occur for a continuous flame sheet. Premixed flames serve as a boundary between reactants and products, and they can only interact at holes in the flame. However, detailed PIV and CH-PLIF measurements by Foley [39] showed that the mixing of hot products with incoming reactants upstream of the flame attachment point was critical for flame stability.

Longwell et al. [28] viewed the recirculation zone behind a bluff-body as a well-stirred reactor. They argue that the high heat release rates inside of the recirculation zone can only be attained by homogeneous combustion. In this model, flame stability depends on the residence time within this homogeneously combusting region. In other words, the flame blows out when the mass flow rate of the incoming reactants exceeds the consumption speed of this homogeneous mixture. Others who supported this well-stirred reactor model include Blust et al. [29], Williams et al. [30], and Kundu et al. [31], although the latter two groups modified the flame stability condition to be a budget between heat

gained by the recirculation zone through combustion and lost by igniting incoming reactants. The results of Kundu et al. [31] showed support for this model as the lean blowoff velocity increased linearly with the recirculation zone strength. Furthermore, using a few of the fuels that were considered in this work, the experimental well-stirred reactor results of Stachler et al. [40] showed that the derived cetane number (DCN) was the fuel property that correlated best with lean blowout boundaries. It will be shown later that multiple liquid fueled studies have come to the same conclusion. However, support for the well-stirred reactor model has weakened as detailed diagnostics measurements show no evidence of reactions in the recirculation zone, except very near blowoff [41, 42]. In a review paper on flamelet structures, Driscoll [42] cites a number of papers which conclude that strong recirculation zones cause the flame to extinguish before reactions can occur homogeneously over a broad spatial region.

Yamaguchi et al. [35] were the first to suggest an extinction based blowoff mechanism. Both this group and Pan and Ballal [43] postulated that excessive stretch rates near the end of the bluff-body recirculation zone cause the flame to extinguish in this region. Once this occurs, the flame blows out shortly thereafter. Zhang et al. [38] experimentally tested the blowoff limits of swirl stabilized flames fueled by a range of H_2/CH_4 mixtures with very different diffusivities. They showed that extinction/re-ignition processes precede blowoff and begin at different equivalence ratios for each of the fuels. The Damköhler number, calculated using the inverse of the extinction stretch rate for the chemical time scale, was able to account for the fuel composition dependence on the rate at which these extinction/re-ignition processes occurred. However, the extinction/re-ignition rate did not have a consistent dependence between fuels on the Damköhler number

when the residence time of a well-stirred reactor or the ratio of the premixed flame thickness and laminar flame speed was used as the chemical time scale. Further support for the extinction model came from a study by Stwalley and Lefebvre [44], which tested lean blowoff boundaries using a variety of irregularly shaped flameholders. Many of the shapes that they used included notches that were intended to disrupt the flame stabilizing shear layers. They found that flameholder shape had little effect on the recirculation zone size but shapes which disrupted the shear layers always led to diminished flame stability. According to the well-stirred reactor and ignition models, increased shear layer stretch rates should not promote blowoff as long as the recirculation zone strength and size are maintained.

Foley [39] examined the flame attachment process in detail for a shear layer stabilized flame. Although the extinction stretch rate correlated well with lean blowout boundaries, detailed flame stretch measurements were much lower than the extinction stretch rate and actually decreased as the equivalence ratio was reduced. Evidence of a stabilizing edge flame with increasing velocity near blowoff caused him to conclude that blowoff likely occurs when the local flow speed is greater than the edge flame speed, rather than local extinction resulting from excessive stretch rates.

Having considered the processes that control blowoff, consider next the dynamics of flames as they approach blowoff. In premixed systems, it is known that flames go through multiple stages as blowoff is approached. As summarized in Shanbhogue et al. [34], the flame first passes through “stage 1” on the route to blowoff, where local extinction occurs on the flame, but the flame overall resembles its features from well-stabilized conditions. Local extinction manifests itself as holes that develop in the flame sheet. These

holes can either heal or grow larger before re-igniting. Moreover, the flame can persist indefinitely under such conditions, as long as the fraction of extinguished flame does not exceed some critical limit. As the flame is brought closer to blowoff it passes into "stage 2", where large scale flame and flow disruption occurs, manifested as clear changes in behavior, including large scale flame flapping, entrainment and subsequent burning of reactants into the wake, and permanent extinction of the flame downstream. Finally, the ultimate blowoff event occurs. Figure 1.2 shows a conceptual illustration of these points. The details of the dynamical processes that ultimately result in complete blowout of the flame, including the "stage 1" and "stage 2" processes, will now be discussed.

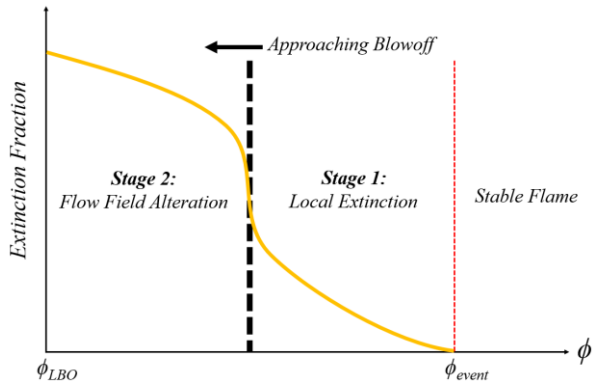

Figure 1.2: Conceptual illustration of the blowoff process in premixed systems, adapted from [34].

1.2.1 Blowoff Dynamics: Stage 1

Stage 1 of the blowout process is characterized by the initiation of local extinction processes in a flame that essentially maintains the same shape and structure as a stable burning flame. Whether these flame holes grow or heal depends on their edge flame velocity. Growing flame holes can cause regions of the flame to extinguish that would otherwise have continued burning. Once initiated, flame holes can also correct themselves,

as they create a passageway for mixing between hot products and reactants that can increase their edge flame velocity sufficiently for recovery [34, 45]. Nair and Lieuwen [46] observed these localized extinction processes in planar measurements taken from bluff-body stabilized flames. They found that the fraction of images that contained these local extinction processes increased as blowoff was approached. Furthermore, they showed a causal relationship between the instantaneous stretch rate exceeding the extinction stretch rate value and these local extinction processes. Smith et al. [47] also observed local extinction, manifested as breaks in the reaction rate contours of an otherwise stable flame, in an LES simulation of a bluff-body stabilized flame approaching blowoff.

Flames are able to operate indefinitely during this "stage 1" of blowoff because re-ignition processes follow local extinction. Researchers have shown that non-periodic oscillations, ostensibly caused by extinction/re-ignition processes of the flame, occur in the time series from acoustic [17], chemiluminescence [38, 48-51], and even ion measurements [52] prior to blowoff. Each of these different measurement techniques have shown that extinction/re-ignition processes, termed LBO precursors by Muruganandam [50], increase in frequency and duration as blowout is approached. However, Muruganandam et al. [49] caution that these LBO precursors should not be viewed as complete extinction and re-ignition of the flame. They compared simultaneous chemiluminescence measurements taken using both high speed imaging and a photomultiplier tube. Although there were some instances where data from the high speed camera showed no indication of a flame, the PMT signal did not drop completely to zero prior to LBO. Therefore, a weak flame which continued burning below the detection limit of the camera existed and possibly played a role in re-igniting the flame. Furthermore, Nair and Lieuwen [46] showed that the average

stretch rate at blowoff was much lower than the extinction stretch rate, suggesting that complete blowout occurs when local extinction processes constitute a large enough fraction of the flame topology that re-ignition is no longer possible.

As noted above, studies have shown that the stability of premixed systems can be correlated with bulk ratios of inferred chemical time and residence time scales, and other parameters [33, 53-55]. Given the above points, however, it is clear that multiple kinetic processes (e.g., both extinction and re-ignition) and fluid mechanic (e.g., the fluid mechanic straining time scales appear to be different in "stage 1" and "stage 2") influence the ultimate blowoff event. Shanbhogue et al. [34] suggested that single chemical/flow time scale blowoff correlations likely capture the physics associated with the extinction processes that *happen near blowoff, and not blowoff itself- i.e., they are correlations for the onset of "stage 1*" [34]. This is an important distinction, as the flame can exist near blowoff with significant local extinction events apparently indefinitely; i.e., while extinction and blowoff are related, they are quite distinct.

Although "stage 2" has been observed in both bluff-body and swirl stabilized flames, the physics associated with each of these different flow fields is different. Therefore, "stage 2" of blowoff will be discussed in each of these configurations separately.

1.2.2 Blowoff Dynamics: Stage 2 in Premixed Bluff-Body Stabilized Flames

Flame stabilization by bluff-bodies is of interest to the combustion community because this is the flameholder used in combustor augmentors and it provides a simplified 2D geometry for studying the complex blowoff problem. The blowoff "stage 2" process for bluff-body stabilized flames involves a range of flow features varying, and sometimes

alternating, between the reacting and non-reacting flow fields. It is understood that for sufficiently high Reynolds numbers, the non-reacting flow behind a bluff-body will form into a periodic-sinuous flow structure known as von Karman vortex shedding. However, the flow behind reacting bluff-bodies generally has a symmetric topology [56-58]. Nair and Lieuwen [46] demonstrated that the symmetric reacting flow structure becomes interrupted as blowoff is approached. Once the flame transitioned from "stage 1" to "stage 2", it began to resemble a von Karman vortex shedding wake. Nair and Lieuwen [46] warn, however, that the "stage 2" flow field should not be considered analogous to the non-reacting flow field. This is because the "stage 2" flame intermittently takes the shape of both a sinuous vortex shedding wake and two shear layers that are distorted independently of each other. In other words, even in "stage 2" the flow field alternates between its reacting and non-reacting form.

The nature of this flow field transition can be understood by considering the vorticity transport equation.

$$\frac{\partial \omega_i}{\partial t} + u_j \frac{\partial \omega_i}{\partial x_j} = \omega_j \frac{\partial u_i}{\partial x_j} - \omega_i \frac{\partial u_j}{\partial x_j} + \frac{1}{\rho^2} \varepsilon_{ijk} \frac{\partial \rho}{\partial x_j} \frac{\partial p}{\partial x_k} + \nu \frac{\partial^2 \omega_i}{\partial x_j \partial x_j} \tag{1.3}$$

The same equation can be written in vector form as:

$$\frac{\partial \vec{\omega}}{\partial t} + (\vec{u} \cdot \nabla)\vec{\omega} = (\vec{\omega} \cdot \nabla)\vec{u} - \vec{\omega}(\nabla \cdot \vec{u}) + \frac{1}{\rho^2} \nabla\rho \times \nabla p + \nu \nabla^2 \vec{\omega} \tag{1.4}$$

The physics represented by this equation can be dissected by discussing each of these terms individually. The two terms on the left hand side of the equation constitute the material time derivative of vorticity. They represent the spatio-temporal changes in vorticity. The first term on the right hand side is the vortex stretching and bending term. This term does not produce vorticity, it simply modifies vorticity that already exists in the flow. The second term on the right hand side of the equation is the flow dilatation term. Flow dilatation in reacting flows is caused by the gas expansion produced by chemical heat release. This term is a clear vorticity sink in combustion applications. The third term on the right hand side represents the baroclinic mechanism of vorticity production. It is caused by the misalignment of pressure and density gradients in the flow which create a torque that produces vorticity. This is very common in combustion applications where a pressure gradient is required to drive the flow and a density gradient of a different orientation is caused by the temperature increase across the flame. Although the exact nature of this mechanism depends on the flame temperature and position, for most conditions experienced by bluff-body stabilized flames this term produces vorticity that rotates in the opposite direction of the vorticity produced by the boundary layer on the bluff-body. In other words, it is generally a vorticity sink that tends to stabilize the flow. The strength of this baroclinic mechanism is related to the pressure and density ratios across the flame [34]. The fourth term on the right hand side represents the viscous diffusion of vorticity. The chemical heat release in reacting flows raises the gas temperature and therefore the kinematic viscosity of the gas, thereby enhancing the viscous diffusion of vorticity [34]. The terms that play the largest role in stabilizing the flow and suppressing the von Karman vortex shedding behavior are the dilatation term and the baroclinic torque term.

Multiple researchers have performed studies which isolate the effects of the baroclinic and dilatation terms on the flow dynamics of bluff-body stabilized flames. Erickson and Soteriou [58] simulated bluff-body stabilized flames with varying reactant temperatures and flame speeds. As the density ratio across the flame is directly related to the ratio of the product to reactant temperatures, this process essentially varied the baroclinic vorticity production and dilatation. They have shown that as the temperature ratio approaches unity, the initiation of the von Karman vortex shedding behavior moves upstream towards the bluff-body. In other words, as the reactant temperature approaches the flame temperature, the initially stable wake develops a convective instability that eventually transitions to the absolute Bernard-von Karman instability [34, 45]. They found that for temperature ratios greater than approximately 2, the vortex shedding behavior will not be present. However, consistent with the observations of Nair and Lieuwen [46], the reacting wake possessed at least some aperiodicity for temperature ratios between 1-2, as intermittent combustion processes irregularly interrupted vortex shedding. Furthermore, they showed that for a fixed temperature ratio of 2, the oscillating vortex phenomenon could also be adjusted by changes in the flame speed. For turbulent flame speeds that are approximately 60% of the incoming reactant velocity, the flame angle increased such that the flame dynamics become decoupled from the wake dynamics and the vortex shedding behavior was again observed. Emerson et al. [59] experimentally verified these findings of Erickson and Soteriou [58]. Their data showed that bluff-body stabilized flames indeed experience greater vortex shedding as the density ratio is reduced. Furthermore, they also saw that this process was intermittent for reacting flows with sufficiently low density ratios. Emerson et al. [59] demonstrated that these decreasing density ratio trends are the result of

a supercritical Hopf bifurcation, as the intermittency of the sinusoidal motions decreased and their amplitude increased as the density ratio approached unity. Morales et al. [60] studied bluff-body flame dynamics in a combustor using three different duct geometries. A straight duct, converging (nozzle) duct, and expanding (diffuser) duct were used to vary the pressure gradient in the flow and thereby induce changes in the baroclinic vorticity mechanism. They found that the converging duct, which had the largest pressure gradient, produced the most baroclinic vorticity and had the best flame stability characteristics.

A general picture of the "stage 2" dynamics begins to emerge from these studies. As lean blowoff is approached, the temperature ratio across the flame decreases due to the lowered equivalence ratio and local extinction processes in the flame. This weakens the influence of the dilatation and baroclinic vorticity terms which are responsible for suppressing the vortex shedding behavior in reacting flows. Therefore, the flame begins experiencing an intermittent vortex shedding process that increases in amplitude and becomes less intermittent as blowoff is approached. The "stage 2" process, however, should not be mistaken as the mechanism that causes the flame to finally blowout. Khosla et al. [61] simulated the blowoff process behind bluff-body stabilized flames using two different flameholder geometries, one where von Karman vortex shedding was present and another where it was not. They showed that the blowout equivalence ratio was the same in both cases and that increased stretch rates did not seem to cause the extinction locations observed in near blowoff reaction rate contours. This discussion of the "stage 1" and "stage 2" processes will therefore be supplemented with arguments regarding what ultimately causes the flame to blowout. However, as noted by Shanbhogue and Lieuwen [34], it

should be understood that identifying the final cause of blowout remains inconclusive and is still an area of active research.

This discussion of the mechanism for complete blowout will begin by outlining the processes that are agreed upon by almost all researchers who have studied this problem using modern experimental diagnostic techniques. Under stable operation, bluff-body stabilized flames are comprised of a thin flame front that resides outside of the fluid mechanic shear layers [41, 57, 62-64]. The recirculation zone contains hot products but there is no evidence of chemical reactions in this region while the flame is far from blowoff. As the equivalence ratio decreases towards its blowoff value, the flame speed decreases accordingly and the flame moves inward to stabilize in low velocity regions in the shear layers [35, 57, 63, 64]. The flame then goes through a pinching/constricting process near the downstream end of the bluff-body recirculation zone, where it is eventually severed [34, 35, 41, 43, 57, 63]. All burning downstream of this pinching location is terminated and combustion only remains in the recirculation zone, which is sometimes referred to as the residual flame. Continued reactant entrainment cools the residual flame such that the recirculation zone eventually becomes a soup of fresh reactants, partially burned reactants, and local heat release parcels that are unable to ignite the incoming mixture [21, 35, 65]. Researchers disagree, however, on the cause of the pinching process and how reactants are entrained into the recirculation zone such that it begins burning.

Stretch induced extinction, flame speed gradients, and flame intersection arguments have all been used to explain the flame pinching process. Each of these processes is related to the decreased heat release and density ratio across the flame as blowoff is approached. Yamaguchi et al. [35] and Pan and Ballal [43] argued that the pinching process was caused

by excessive stretch rates near the downstream end of the recirculation zone. Fugger et al. [63] took OH-PLIF and CH_2O-PLIF measurements of a bluff-body stabilized flame near blowoff. They showed that under stable operation, the flame experienced the greatest flame stretch and had the largest CH_2O thickness near the shear layer attachment point. However, as blowoff was approached, the flame stretch rates were roughly the same throughout the entire measurement domain ($0.5<x/D<3.5$) and the CH_2O thickness was greatest near the pinching/constricting region. Kedia et al. [66] argued that blowoff depends on the following dynamic stability criterion

$$\left|\frac{dS_d}{dn}\right| > \left|\frac{dv_n}{dn}\right| \tag{1.5}$$

where S_d is the flame displacement speed, n is the direction normal to the flame front, and v_n is the incoming reactant velocity in the direction normal to the flame front. Using a bluff-body stabilized flame simulation, they showed that this criterion fails first at the pinching location. Khosla et al. [61] argued that the reduced recirculation zone size and decreased flame speed near blowoff cause the two shear layers to eventually intersect each other, thereby pinching the flame.

Perhaps the largest source of debate surrounding the ultimate blowout process is regarding the pathway by which reactants enter the recirculation zone. Pan and Ballal [43] took measurements of the flow pressure gradient near the end of the recirculation zone behind a bluff-body stabilized flame. They found that this pressure gradient became increasingly adverse as the equivalence ratio was decreased, something they interpreted to represent increased entrainment of cold reactants. In order to observe the entrainment

process in near-blowoff flames, Dawson et al. [41] seeded the reactants with an aerosol. Unburned reactants were first observed approximately 1.5 diameters downstream of the bluff body. No reactants were observed to enter the recirculation zone through the shear layers, however. Instead, the flame assumed an "M" shape near blowoff as reactants were first entrained in the recirculation zone by passing through the pinching location, then they were convected upstream, and finally they began burning. The partially reacting recirculation zone retracted towards the bluff-body as the flame came closer to blowing out, and the flame was completely lost once the shear layers extinguished. Kariuki et al. [62] observed infrequent holes in the shear layer flames which they believed were caused by heat losses from entrained reactants, rather than by high stretch rates. They mostly observed reactants entering the recirculation zone from its downstream pinching location, after which they were found to quench the shear layer flames by convecting into them. However, these quenching instances were not fatal for the shear layer flames, as they continued to burn until the recirculation zone had completely filled with cold reactants. A more recent study by Kariuki et al. [65] used simultaneous OH-PLIF and CH_2O-PLIF measurements to get an indication of combustion products, preheated reactants, and the flame reaction zone. Again, they found stretch induced breaks in the reaction zone to be more common downstream of the recirculation zone than in the shear layers. They observed heat release, preheated reactants (represented by CH_2O that failed to overlap with OH), and fresh reactants (regions without either OH or CH_2O) all in the recirculation zone near blowoff, although the reactants were more likely to be preheated than fresh. A final study by Kariuki et al. [67] repeated the same experiment and measurements used in their previous studies, except with an ethylene-air flame. This ethylene-air mixture had a Lewis

number greater than one, which theoretically made it more prone to stretch based extinction than the unity Lewis number methane-air mixtures that they used previously [68]. They again saw no evidence of CH_2O entering the recirculation zone through holes in the shear layers and concluded that the blowout behavior of this flame was qualitatively similar to their previously studied methane-air flame.

Chaudhuri et al. [57, 69], on the other hand, did observe stretch induced extinction in the shear layer flames and argued that this is the opening through which reactants enter the recirculation zone. They believed that blowoff occurred when the residual flame failed to reignite the shear layers. However, it should be noted that their planar measurements were only acquired at 2.5 Hz and so it is difficult to conclude how frequently these observations actually happen. Chowdhury and Cetegen [64] used simultaneous OH-PLIF and CH_2O-PLIF to study the effects of different freestream turbulence levels on bluff-body stabilized flames. They found that increasing the turbulence intensity decreased the recirculation zone length and flame stability. Velocity measurements taken simultaneously with the PLIF measurements indicate that heated reactants are indeed transported into the recirculation zone through holes near the flame attachment point in the shear layers. Furthermore, they noticed instances where the shear layer flame extinguished and stabilized briefly in the pinching region, before the shear layer re-ignited. However, entrainment of preheated reactants near the downstream end of the recirculation zone, along with the associated heat release in this region, was also observed near blowoff. These authors acknowledge that it cannot be concluded whether reactants enter the recirculation zone primarily through the shear layer or the pinching region, as their flow field measurements show evidence of both processes.

In order to validate the mechanisms developed in their previous studies [57, 69], Chaudhuri et al. repeated their experiments using the same configuration but under acoustically forced [70] and vitiated [71] conditions. In conflict with their unforced-unvitiated mechanism, the shear layers remained burning and following the pinching process the reactants entered the recirculation zone from the downstream end in both cases [70, 71]. In reference to these observations, Kariuki et al. [62] concluded that whether local extinction/reactant entrainment first happens in the shear layer or at the downstream end of the recirculation zone depends on the combustor geometry and the particular flow field involved.

1.2.3 Blowoff Dynamics: Stage 2 in Premixed Swirl Stabilized Flames

Main stage combustors usually rely on recirculation zones developed by swirling the incoming flow to stabilize flames. Swirl flames are advantageous because they are shorter, which allows for a reduced combustor length [72], and they have improved flame stability characteristics over other flameholder geometries [73]. The conversion of axial vorticity to azimuthal vorticity induces a reverse flow velocity and the vortex breakdown process ensues. Vortex breakdown is a global hydrodynamic instability that creates a stagnation point in an otherwise unobstructed flow [45], and for sufficiently high swirl numbers, a complete recirculation zone is developed. Swirl combustors are often of the dump combustor type where the flow is suddenly expanded once it enters the combustion chamber. This results in both an inner and a toroidal outer zone of recirculating hot products. In general, increased swirl levels result in a monotonic improvement in flame stability [16], as it requires extremely high swirl levels to cause the flame to blow off due to azimuthal stretch rates [74].

Characterizing the "stage 2" blowoff process in swirl flames is complicated by different degrees to which changes in the vortex breakdown process occur. Muruganandam [50] observed that as the heat release decreases near blowout, due to local extinction and entrained reactants in the inner recirculation zone, the vortex breakdown mechanism changed from a bubble type to a spiral/helical type. This helical vortex breakdown mode enhances the reverse flow velocity and transports hot products upstream that are often able to re-ignite the flame. The survival of these "stage 2" flames depends on the success of these re-ignition processes. Zhang [75] found that fuel composition has an influence on whether the vortex breakdown mode changes near blowoff. He used fuels with a range of CH_4/H_2 compositions to vary the thermal expansion across the flame. Fuels with high flame temperatures (i.e., pure methane) maintained a vortex breakdown bubble throughout the blowoff process, whereas the low flame temperature mixtures (high H_2 content, e.g., 75% H_2 25% CH_4) transitioned to a spiral vortex breakdown mode near LBO. However, the flow structures remained identical between the different compositions when burning with a fixed adiabatic flame temperature. In addition to vortex breakdown mode changes, Zhang [75] also saw large scale vortices develop and surround the central recirculation zone of flames that had locally extinguished and lifted downstream. Prakash et al. [51] used two photomultiplier tubes, one located near the dump plane and the other far downstream, to identify LBO precursors that involved vortex breakdown mode changes. They found that the duration of these LBO precursors depended more on the local condition in the flow than the amount of chemical heat release (i.e., equivalence ratio) that preceded them. Although these studies show that the flow features of swirl flames can change significantly near blowoff, it is difficult to make general inferences about heat release effects on vortex

breakdown dynamics [76]. This is because the dynamics of the vortex breakdown process are highly dependent on the combustor geometry and operating conditions involved.

Despite their practical significance, much less is known about what ultimately causes swirl flames to blow out than the bluff-body counterpart. Using simultaneous OH-PLIF and CH_2O-PLIF measurements, Manosh Kumar et al. [77] were able to isolate unburned reactants from recirculating products in the central recirculation zone of a swirl stabilized flame. They found that reactants are not entrained far into the recirculation zone and that those that are entrained are quickly consumed. This suggests that the bluff-body blowoff arguments surrounding cooling of the recirculation zone by entrained reactants may not apply to their particular swirl flame. Stöhr et al. [78] showed that the stabilization of swirl flames depends on whether the flame root remains burning. Excessive strain rates at the flame root location make it susceptible to extinguishing, and this was observed to occur even during stable operation. These researchers showed that blowout occurs in the event that the flame root fails to reignite within 2 ms of extinguishing.

1.3 Nonpremixed Gaseous Lean Blowout Studies

In nonpremixed gaseous systems, the picture is complicated by the potentially different degrees of fuel/air premixing, as well as variations in local fuel/air ratio in regions where premixing has occurred. In such cases, blowout can range between being mixing limited and kinetically limited. For example, Shih et al. [79] studied the effects of fuel-air mixedness on lean blowout limits. They found that a partially (50%) premixed flame actually blew out at a lower global equivalence ratio than a completely premixed flame.

However, a flame without any premixing had a much higher global blowout equivalence ratio than either of the other cases.

In a review article by Lyons [80], five concepts are presented to describe the stability of nonpremixed flames. They include (1) a premixed flame stabilizing the base of the nonpremixed flame, (2) stabilization by diffusion flamelets unless a critical scalar dissipation rate is exceeded, (3) turbulence intensity increasing the burning velocity at the flame leading edge, (4) transport of the flame leading edge upstream by large eddies, and (5) a partially premixed edge flame stabilizing the base of the nonpremixed flame. A few of the key studies that contributed to these models will be discussed below.

Vanquickenborne and Van Tiggelen [81], along with Kalghatgi [82], supported the premixed flame concept and argued that flame stability is maintained by a kinematic balance between the flow speed and the local flame speed. Broadwell et al. [83] used a Damköhler number argument, defined as the ratio of a mixing time to a chemical time, to predict the blowout velocity of jet flames. They argue that the root of the flame is stabilized by large vortical structures that transport hot products from the center to the edges of the jet. These hot products are then entrained back into the jet, along with fresh air, and ignite the incoming fuel supply. Blowout then occurs when the hot products and reactants are mixed so rapidly that the mixture temperature and composition descends below a critical value before ignition can occur. Roquemore et al. [84] conflated the ideas of Vanquickenborne and Van Tiggelen [81] with those of Broadwell et al. [83]. In their model, the flame is stabilized near the lip of the burner by hot recirculating fuel and products in an outer recirculation zone. However, once the flame lifts, they believe that it acts more like a premixed flame. Driscoll and Rasmussen [85] used the previously described kinematic

balance concept to develop a modified Damköhler number that was successful in scaling nonpremixed flame blowout limits. Peters and Williams [86] hypothesized that blowoff in nonpremixed flames is caused by excessive scalar dissipation rates near the flame leading edge. The role of scalar dissipation in the stability of nonpremixed flames was challenged somewhat in a study by Stärner et al. [87]. They found that the mean scalar dissipation rate counterintuitively decreased near blowout and decreases in the flame temperature were only weakly correlated with increasing scalar dissipation rates. Using advanced diagnostics techniques to measure the mixture fraction and scalar dissipation rate fields, Sutton and Driscoll [88] determined that scalar dissipation is effective in extinguishing the flame if it occurs at the location of the stoichiometric mixture fraction contour.

The near-blowoff dynamics of nonpremixed flames primarily involve the initiation of, and recovery from, flame holes. OH-PLIF measurements by Juddoo and Masri [89] showed that increasing the fuel jet velocity was accompanied by enhanced local extinction processes that eventually cause the flame to blow out. Hult et al. [90] found that the occurrence of local extinction is somewhat self-correcting, as fuel and hot products are allowed to escape through these flame holes to form partially premixed regions that can later re-ignite. Very similar studies by Juddoo and Masri [89] and Steinberg et al. [91], identified two mechanisms whereby the flame can recover from local extinction. First, flame holes can heal through edge flame propagation, and second, growing kernels that initiated upstream can advect and re-ignite downstream regions of the flame. Steinberg et al. [91] argue that the vast majority of extinction recoveries are caused by edge flame propagation. However, Juddoo and Masri [89] conclude that re-igition through advected

kernels becomes increasingly significant as blowout is approached, and eventually becomes the dominant recovery mechanism very near blowout.

A significant difference in the near-blowoff behavior between gaseous premixed and nonpremixed flames is that nonpremixed flames lift off the burner, with a liftoff height that grows as blowoff is approached. In contrast, bluff-body stabilized premixed flames permanently extinguish downstream, with this extinction region retracting toward the burner exit as blowoff is approached [34]. However, both types of flames experience an unsteady process prior to complete blowout. For premixed flames this is manifested as the previously described "stage 1" and "stage 2" processes. On the other hand, nonpremixed flames lift off the burner and the flame base experiences an intermittent oscillatory behavior prior to complete extinction [84]. Chen et al. [92] observed that the lifted flame base fluctuated 20% of the liftoff height at 100-150 Hz prior to blowing out. Murugesan and Sujith [93] describe this intermittency phenomenon as a competition between extinction/re-ignition processes and acoustic oscillations. They argue that the flame lifts due to local extinction processes near the burner exit and re-stabilizes downstream. As the incoming gases regain sufficient heat, the flame again moves upstream. However, as the flame travels upstream it creates an increase in the acoustic pressure. High-amplitude periodic oscillations of the flame begin to occur, which result in new local extinction processes and a repetition of this cycle.

1.4 Liquid Fueled Lean Blowout Studies

In liquid-fueled systems, the additional physics associated with atomization and vaporization of the fuel come into play. As such, additional physical properties of the fuel

and its constituents, such as viscosity, surface tension, boiling points, and latent heats of vaporization are relevant. In addition, most liquid fuels have a complex range of constituents, implying that the gaseous vaporized fuel composition around a droplet can differ from the "average" fuel composition, due to preferential vaporization [94]. Previous work investigating the influence of liquid fuel physical properties on aircraft engine blowout performance has led to a variety of conclusions, the differences probably due to different ambient conditions under which data was taken and fuel-injector technology [55, 95-103]. These studies are discussed next.

Consider fuel-injector technology first, which strongly influences droplet sizes. Somewhat counterintuitively, Lefebvre [95] suggested that blowout characteristics become more problematic as atomization quality improves, such as with better fuel injectors. He noted that one advantage of poor mixing quality injectors is that they allow combustors to operate at much lower global fuel-air ratios than would be possible in a premixed combustor with a single, spatially uniform value of fuel-air ratio. Mellor [55] supported this conclusion and explained the phenomenon using a fuel penetration argument. However, this fuel penetration effect was only observed to be significant for fuels with lower volatility and higher viscosity than Jet-A.

Burger et al. [96] described a study with very similar approach and goals to the present work, as they looked at the effect of fuel properties on blowout. They looked at sixteen different fuels using a pressure-simplex atomizer and an in-house combustor based upon the primary zone of an Allison T63 combustor at an air inlet temperature of 310 K. They found that the easiest to vaporize fuels (those with the lowest T_{10} values, defined as the temperature at which 10% of the liquid volume had vaporized) were the most blowout

resistant. A strong correlation with the fuel density was also observed in their blowout data. However, it is difficult to provide a physical explanation for the density effect, as their data shows a much weaker dependence on other atomization related properties, such as the kinematic viscosity or Sauter mean diameter. Corporan et al. [103] also used an Allison T63 combustor to experimentally test the lean blowout limits of eight of the fuels used in the present study. Their experiment was unique in that it was performed using a full-scale engine. Rather than defining a loss of engine power as the lean blowout limit, they named it the lean operational limit because they were unsure whether the flame blew out or the compressor stalled. As the rotational speed of the compressor decreased with the fuel flow rate, i.e., as blowoff was approached, the compressor discharge temperature also decreased accordingly. Therefore, although their experiments started at an air inlet temperature of approximately 380 K before the fuel flow rate was reduced, the actual air inlet temperature was approximately 310 K at the threshold of operation. Consistent with the Burger et al. [96] study, their lean operational limits correlated best with T_{10}, and T_{50} was their strongest correlation when including the single component fuel n-dodecane. Grohmann et al. [100] similarly studied the blowout limits of multiple fuels at air inlet temperatures of both 323 K and 423 K. Their 323 K data differed qualitatively with the Burger et al. [96] results, as it showed that the most difficult to vaporize fuels were more blowout resistant. The 423 K data from the Grohmann et al. [100] study failed to correlate strongly with any fuel properties. These differences could potentially be due to fuel injector hardware, as a prefilming airblast atomizer was used in the Grohmann et al. [100] study.

Several studies have attempted to incorporate kinetic properties into scaling blowout limits for liquid fueled systems. Mellor [55] used time scale correlations, much

like the premixed Damköhler number scalings, to approach the liquid-fueled blowout problem. He used ignition delay times with a correction for droplet evaporation effects to fit predicted blowout fuel-air ratios with experimental data. Similarly, Lefebvre [95] combined an empirical expression for the weak extinction of bluff body stabilized flames with a fuel vaporization factor to predict blowout fuel-air ratios in liquid combustors. Colket et al. [104] showed that the derived cetane number (DCN), which is an inverted indicator of a fuel's ignition delay, closely correlated with blowout boundaries. A recent study by Stouffer et al. [105], using a subset of the fuels considered in the present work, also found that their data correlated best with the DCN. Using three of the fuels in this study and three single component fuels, Allison et al. [106] performed blowout experiments at an air inlet temperature of 340 K and a bulkhead temperature of 425 K. Consistent with the observations of other researchers, their data showed a trend with the DCN. However, by using Damköhler number scalings, with the ratio of the premixed flame thickness and laminar flame speed as the chemical time scale, they showed that the data followed distinct groupings. In other words, their data admitted two hypotheses.

Although recent studies [102, 104, 105] have shown a strong correlation between the DCN and blowout boundaries, this does not necessarily imply that blowout is controlled by the ignition propensity of a fuel. Due to the thermodynamic condition in which the DCN is determined in a pressurized/heated constant volume combustion chamber (Ignition Quality Tester) according to the ASTM D6890 standard, the DCN has a strong correlation with low temperature reactivity measured in a flow reactor experiment for both petroleum-derived and alternative jet fuels [107]. Nevertheless, the DCN also reflects the global combustion reactivity relevant to high-temperature chemistry (e.g. flame speed and

extinction) due to its strong sensitivity to the CH_2 chemical functional group [94]. The higher mass/mole fraction of the CH_2 chemical functional group in real and surrogate fuels, corresponding to a higher DCN value, indicates that n-paraffinic components are dominant over other molecular classes, which can enrich the radical pool effectively through the dominant thermal decomposition reactions. The use of the DCN as a global chemical kinetic indicator has been widely implemented in surrogate approaches [108-112], where both high- and low-temperature combustion behaviors of a target real fuel are successfully emulated by a surrogate mixture.

From the above points it is clear that far less general conclusions on controlling physical process for liquid fueled systems are possible than in gaseous premixed systems. This is due to the fact that the degree of atomization and vaporization is a function of injector technology and operating conditions, which controls the extent to which the blowout phenomenon is kinetically vs. mixing/physical property limited. Furthermore, while multiple different blowout mechanisms are plausible, determining their precise roles is confounded by the fact that they are often correlated with each other (e.g., see Refs. [95, 102, 107]). However, it is possible to categorize the limiting physics according to the rate of fuel-air mixing relative to the time required for chemical heat release. A conceptual schematic of this blowout grouping is shown in Figure 1.3. When fuel-air mixing occurs fast relative to the combustion chemistry, the blowout phenomenon approaches a kinetically limited premixed gaseous system. However, when chemistry happens much faster than the fuel-air mixing process, which is dependent on atomization and vaporization in liquid systems, blowout is limited by fuel-air mixing rates. It is highly likely that the majority of systems in operation lie in an intermediate zone where both kinetic and

mixing/atomization/vaporization influence the results, as evidenced by the inability of most studies to come up with completely definitive correlations when considering a broad range of fuels [34].

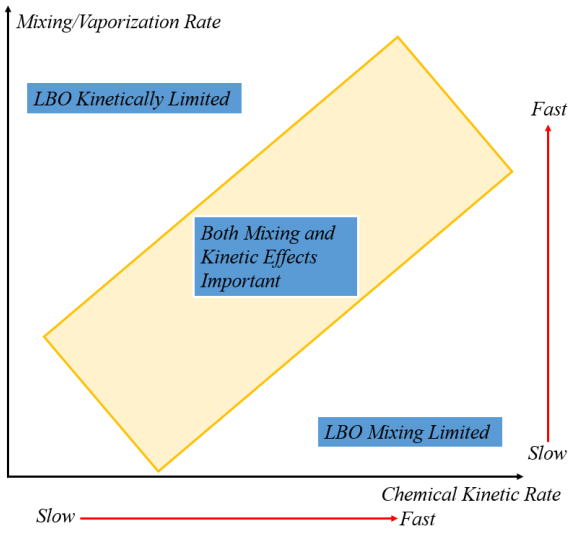

Figure 1.3: Conceptual illustration of the physics limiting LBO across different combustion regimes.

Both experiments [113-116] and simulations [117, 118] have shown that swirl-stabilized spray flames near blowoff consist of a partially premixed flame along the spray trajectory and a nonpremixed flame in the outer recirculation zone. Using simultaneous CH_2O-PLIF and OH-PLIF measurements, Yuan et al. [113] observed an "M" shaped flame with a thin OH layer that did not contain elevated levels of OH in the central recirculation zone. Therefore, the authors concluded that their particular spray flame behaved more like a nonpremixed flame that blew out as a result of increased local extinction. Evans et al. [114] took additional temperature and OH-PLIF measurements in the same Yuan et al. burner. Although they also saw minimal OH in the central recirculation zone, their measurements showed that this was a high temperature region. They concluded that the

partially premixed inner flame was highly diluted by hot products in the central recirculation zone that originated elsewhere. The LES simulation of Esclapez et al. [119] showed that the outer nonpremixed flame appeared intermittently near blowoff and formed around pockets of fuel droplets.

Although little is known about what ultimately causes lean blowout in spray flames, studies have investigated the local extinction processes that precede it. Verdier et al. [115] observed three different local extinction mechanisms in their detailed PIV and OH-PLIF data. They included (1) large stretch rates in the shear layer locally extinguishing the inner premixed flame, (2) large high velocity droplets penetrating and extinguishing the flame leading edge, and (3) disturbances in the outer nonpremixed flame caused by the sudden evaporation of droplets that extend into the outer recirculation zone. A recent LES simulation by Giusti and Mastorakos [118] matched the local extinction characteristics of detailed experimental measurements. Local extinctions in the outer flame appeared frequently and were believed to be caused by turbulent transport/mixing because they occurred at scalar dissipation rates less than the critical value. Breaks in the inner flame were rarely observed and those that did happen were caused by excessive scalar dissipation of the evaporated fuel. However, an additional study by Yuan et al. [116] showed that extinction processes in the inner flame increase in frequency as blowoff is approached. Evans et al. [114] observed that the inner flame weakened and the outer flame strengthened as the incoming air velocity was increased towards the blowout value. The LES simulation of Hasti et al. [120] showed that partially completed chemical reactions and decreased product temperatures in the central recirculation zone are indicators of a spray flame approaching blowoff.

This study was motivated by the great discrepancy amongst various authors, as discussed above. For this study, experiments were obtained with a large range of fuels with significant differences in physical properties, chemical properties, and distillation curves. The experiments were performed at multiple air preheat temperatures in order to better understand the relative roles of physical and chemical properties; this is likely the reason for the seemingly contradictory vaporization temperature sensitivities observed by past researchers [55, 95-102]. Data was obtained with several custom fuel blends that were specifically formulated in order to break the correlation between chemical and physical properties, which makes differentiation of them difficult. These efforts involved correlating both the transient dynamics near blowoff, and the actual blowoff condition itself, with fuel properties.

CHAPTER 2. EXPERIMENTAL OVERVIEW

This section describes the facility, experimental procedure, diagnostic techniques, and fuels that were used in this work. Measurements were taken using two different experimental approaches. The first were fuel screening measurements that identified blowout equivalence ratios as a function of fuel properties and the air inlet temperature. These data had a large sample size and the experiments were repeated across many different days. Second, detailed measurements were acquired that provided insight into the dynamics of the lean blowout process. Due to the difficulty involved in obtaining these measurements, a fewer number of detailed data samples were taken. Information about the fuel screening experiments is presented in Sections 2.1-2.5 and the detailed measurements are discussed in Sections 2.6-2.9.

2.1 Facility

Figure 2.1 illustrates the facility that was used for these experiments. Key components include air supply and preconditioning, fuel supply, the optically accessible pressure vessel and liner, fuel injector, and exhaust section. Each of these is detailed below.

Figure 2.2 shows a diagram of the air flow system. Compressed air at pressures up to 20 atm is heated to temperatures from 350 to 750 K. A portion of the heated air is sent to the test section and the remainder is cooled to approximately 320 K in a heat exchanger. This secondary air flows around the liner and keeps the pressure vessel structure and windows cool. Hot combustion products mix with the cooling air downstream of the test section and exit through a water cooled exhaust. A choked orifice plug of variable size is

installed at the exhaust exit in order to maintain elevated pressure in the combustion chamber. Air mass flow rates are measured using a Rosemount vortex flowmeter. The air temperature is measured 35 cm upstream of the dump plane and its value was continuously recorded during measurements. Its value typically remained within ±10 K of the nominal during a measurement. Uncertainties in air flow rate are estimated to be 2 % with a bias error of 0.1 %.

a)

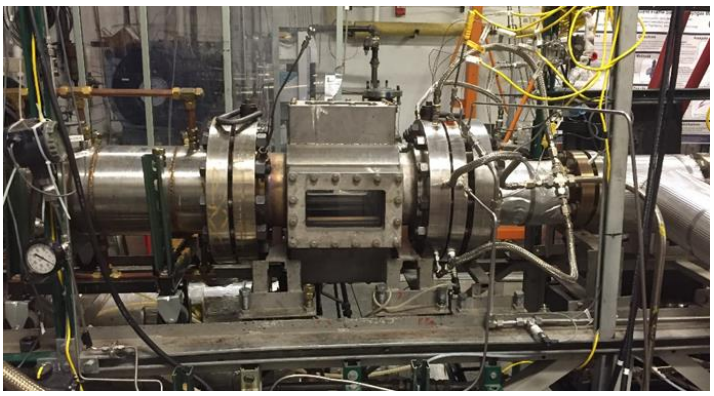

b)

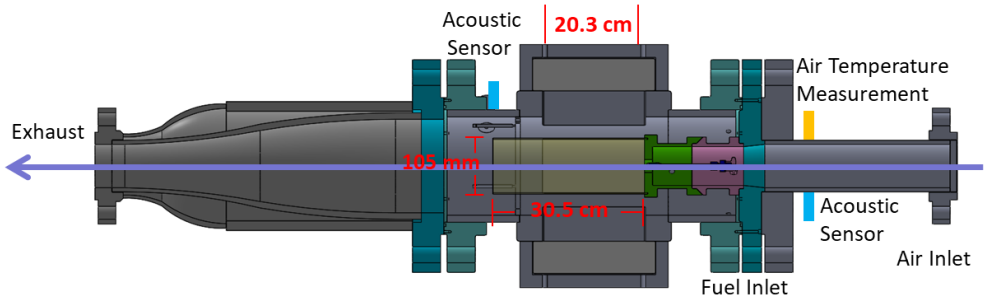

Figure 2.1: Image (a) and schematic (b) of the experimental combustor.

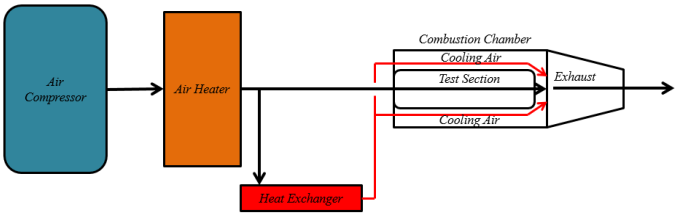

Figure 2.2: Air preparation and routing diagram.

The combustor liner consists of a 30.5 cm long, 105 mm inner diameter quartz section. The front end of the liner, or nozzle outlet, referred to as the “bulkhead” in this paper, consists of a stainless steel wall without secondary cooling passages, and is shown in Figure 2.3. This bulkhead face contains four thermocouples situated flush with the surface for monitoring bulkhead temperature, a static pressure transducer, and an ignitor. Uncertainties in combustor pressure are estimated to be 0.4% with a bias error of 0.08% FS. The pressure vessel that houses the liner has optical access on all four sides and four quartz windows with dimensions 20.3 × 10.8 × 5.1 cm (Figure 2.1).

The fuel nozzle is similar to the one described in Cohen and Rosfjord [121] and is depicted in Figure 2.4. Prior to entering the test section, the pressurized-preheated air passes through a swirler. As can be seen in Figure 2.4, air travels through two separate swirler passages. There is a pressure drop across the swirler of approximately 6.7 kPa and the air exits the nozzle with a velocity of 63 m/s, calculated using the air mass flow rate, the air density (using the air temperature measurement described above), and nozzle exit area.

Modern aircraft fuel injectors often have a hybrid design that includes two fuel circuits. The first is a prefilming airblast atomizer that sprays fuel onto a prefilming surface and relies on co-flowing air to break up the fuel into droplets. Second, a pressure atomizer is also used that sprays finely atomized droplets directly into the flow. The atomization quality of airblast atomizers is greatly impaired when the co-flow velocity is low, such as during takeoff, landing, and idle conditions [122]. However, pressure atomizers continue to perform well at these conditions and are critical for flame stabilization, as flames are most susceptible to blowout when planes prepare to land [9, 19]. Therefore, the fuel injector

used for these experiments was a pressure type atomizer. It was purchased from McMaster-Carr (product number 3178K45) and had an orifice diameter of 0.51 mm.

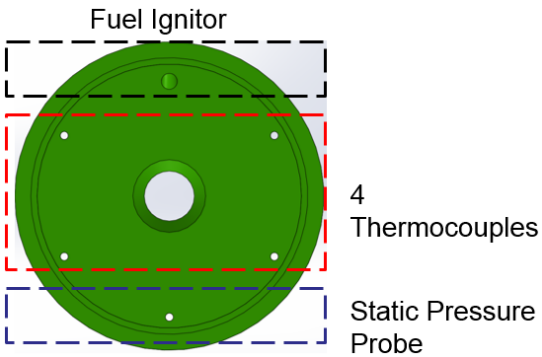

Figure 2.3: Bulkhead instrumentation placement schematic.

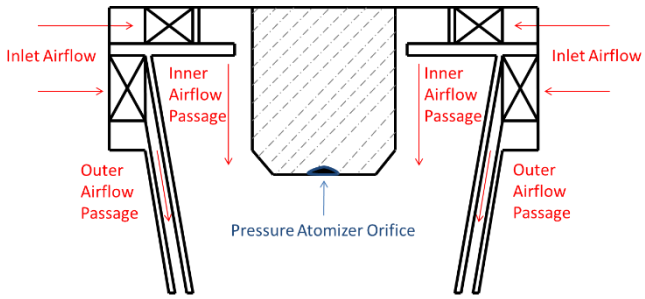

Figure 2.4: Schematic of the swirler and fuel injector configuration.

Because the focus of this study was on fuel composition influences, special consideration was given to abilities to rapidly switch between fuels. A custom fuel cart was developed and is shown in Figure 2.5, consisting of 10 cylinders, each capable of containing a different fuel. Compressed nitrogen was directed to advance the fuel of interest using electrically actuated ball valves. A ball valve corresponding to each fuel cylinder allowed for fuels to be changed easily without interrupting the experiment. The fuel cart was only operated when the cylinders were filled to at least one quarter of their total capacity. Therefore, a sufficient volume of liquid fuel was maintained between the

nitrogen-fuel interface and the fuel injector to prevent nitrogen from interfering with the fuel spray. The residence time of the fuel in the cart metering system and fuel lines upstream of the nozzle is approximately 1 minute, and the combustor was run for 5-10 minutes between fuel changes to ensure that the fuel from the prior run was purged. Fuel flow rates were initially measured using an AW-Lake positive displacement gear meter and an upgrade was later made to a Cox Turbine meter. Fuel temperatures were measured at the fuel inlet depicted in Figure 2.1 and varied between 300 and 305 K. Estimated uncertainties in overall measured fuel/air ratio are 3%.

Detailed procedures were followed to ensure that mixing between fuels was avoided. The fuel cart was loaded using separate, dedicated portable fuel safe containers for each fuel. Fuel was transferred from its respective barrel to these portable containers using dedicated fuel pumps for each fuel.

Figure 2.5: Photograph of the fuel cart used to supply fuel for these experiments.

2.2 Fuel Screening Procedure

Repeatability is a significant challenge in blowout experiments as there are many confounding variables involved. The fuel-air ratio, air inlet temperature, combustor pressure, nozzle velocity, heat transfer from the combustor hardware, acoustic fluctuations, and combustor hardware type may all influence blowout boundaries. It was intended to either fix or parametrize as many of these variables as possible. One of the more difficult variables to control is the dependence of blowout on combustor thermal state – e.g., blowout occurs at a different condition when a combustor is brought to thermal equilibrium than if it is still cold. The combustor heat transfer characteristics are difficult to control and so the bulkhead temperature (see Figure 2.3) was used as a parameter to characterize the thermal state of the combustor, as detailed next.

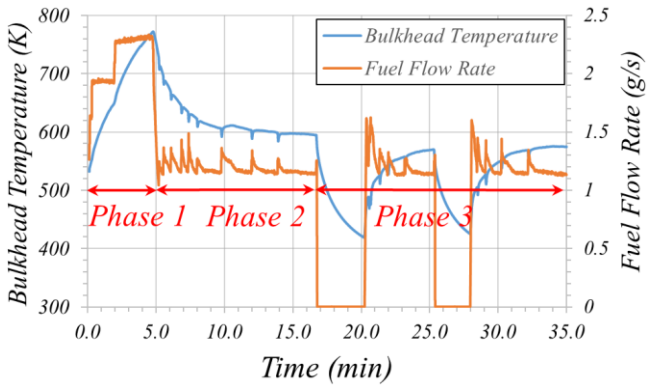

Figure 2.6: Time history of temperature and fuel flow rate during a series of blowout measurements, illustrating the blowout measurement procedure.

Figure 2.6 demonstrates the experimental procedure for a given fuel, plotting the time history of the bulkhead temperature and fuel flow rate. This procedure was adapted from previous work done by Tim Lieuwen's group [123]. The key experimental observable extracted from these data was the equivalence ratio at which the flame blew out. This value

was calculated using the minimum volume flow rate of fuel within a 5 second interval preceding LBO. The fuel specific equivalence ratio was then calculated from this volume flow rate using the density and stoichiometric fuel-air ratio for each fuel. In order to gather equivalence ratio measurements across a range of combustor thermal states (i.e., “hot”, “cold”), the experimental process included three different phases, as shown in Figure 2.6. Phase 1 is used as a heat-up period that raised the combustor to high bulkhead temperature values. This allowed blowout equivalence ratios to be measured at a super-equilibrium thermal state. Phase 1 also served the secondary purpose of operating the combustor at a high fuel flow rate to flush any previously used fuel through the system, thus ensuring that only the fuel of interest was being supplied to the combustion chamber. Once the combustor was sufficiently warm, the fuel flow rate was reduced and the procedure transitioned into Phase 2. Here, blowout equivalence ratios were gathered at high bulkhead temperatures. The fuel ramp rate was controlled by bringing the flame to a near extinction condition and then manually reducing the fuel flow rate by the smallest increments allowable until blowout occurred. The flame was then immediately re-ignited and this process was repeated while further blowout points were acquired. As Phase 2 continued, the combustor bulkhead temperature cooled, and eventually reached an equilibrium value. As such, blowout measurements were obtained for a range of combustor thermal conditions. In order to gather blowout measurements at low bulkhead temperatures, in Phase 3 the combustor was turned off and allowed to cool. Following a few minutes, the combustor was re-ignited and the blowout measurement procedure resumed. As this process continued, the combustor heated up and blowout measurements were obtained for a range of “cold” thermal conditions. In this way, blowout was measured over a range of

combustor thermal conditions. In order to avoid coking the fuel injector while terminating the fuel flow, Phase 3 was not included in the 550 K experiments.

This three phase process was then repeated for each of the fuels during an experimental operation. The fuel cart reduced the time required to consecutively test all of the fuels down to a single day – a requirement that was imposed on all runs to avoid additional uncontrolled variations in ambient conditions. This process was then repeated on other days, reversing the direction over which the fuels were tested, to verify repeatability.

Further details on these data are presented in Appendix A and a sample of the results from this procedure is shown in Figure A.1. Here the equivalence ratio at blowout is plotted as a function of the bulkhead temperature for fuel C-4. Results are shown for the three air inlet temperatures, 300 K, 450 K, and 550 K. It can be seen that blowout resistance is enhanced by an increase in either air inlet or bulkhead temperature.

Using this procedure, blowout results were quite repeatable for the majority of the fuels. By comparing day to day differences in blowout equivalence ratios at fixed bulkhead temperature intervals, the standard deviation in blowout equivalence ratio varied between 0.5-8% of the mean.

However, evidence for an additional uncontrolled variable did surface for certain fuels. Specifically, deviation in results from day to day were consistently observed for fuels A-2, A-3, C-3, C-5, C-7, and C-8, indicating additional uncontrolled variables that were a function of fuel composition. In addition, these same fuels displayed a non-monotonic dependence between the blowout fuel-air ratio and the bulkhead temperature, whereas

others showed a linear dependence. Although these issues are conceptually independent from each other, they both manifested themselves in a decrease of the correlation coefficient (quantified as the R^2 value) from a linear least squares fit of the blowout equivalence ratio vs. bulkhead temperature data. This issue is discussed in further detail in the Appendix A, see Figure A.1 and Figure A.2, but the results indicate that the average R^2 value is related to the combined percentage of aromatics and cycloalkanes in the fuel (see Figure A.3). In other words, the fuels with the lowest R^2 values had the highest percentages of ring-shaped compounds. Two potential causes of this dependence are thermal cracking of the fuel in the injector or back-heating of the fuel spray by radiation, with the latter augmented by increased soot radiation from these fuels with higher aromatic concentrations.

A key output from these results was controlling the influence of the combustor thermal state upon blowout conditions. Due to the previously discussed issues, only data that had a negatively sloped relationship between the blowout equivalence ratio and bulkhead temperature (e.g., less than 600 K for the 450 K data shown in Figure A.2) is compared in the following sections. Measured blowout results presented in Chapter 4 compare blowout trends across fuels at a fixed bulkhead temperature. Results from the 300 K, 450 K, and 550 K data sets are compared at bulkhead temperatures of 500 K, 550 K, and 640 K, respectively.

2.3 Operating Conditions

In practice, lean blowout is most likely to occur when an airplane is reducing its speed to prepare for landing [9, 19]. Figure 2.7 shows the typical engine operating pressures

and inlet air temperatures across a flight path [9]. The operating conditions for these experiments were selected to be representative of low power engine conditions where blowout is most probable. These considerations led to selecting nominal operating conditions of 345 kPa combustor pressure, a 1.3% pressure drop across the swirler, a nozzle velocity of 63 m/s, and an air inlet temperature of 450 K. In order to vary the effects of fuel physical properties on LBO results, the experiment was also run above and below this nominal temperature, at 300 K and 550 K, for the same pressure and air mass flow splits. Moreover, the study by Corporan et al. [103] demonstrated that it is important to evaluate blowout results at multiple air inlet temperatures from a practical standpoint because the compressor discharge temperature will drop as blowout is approached. The experimental operating conditions are summarized by the boxed region in Figure 2.7, where the stars represent the conditions where data was acquired.

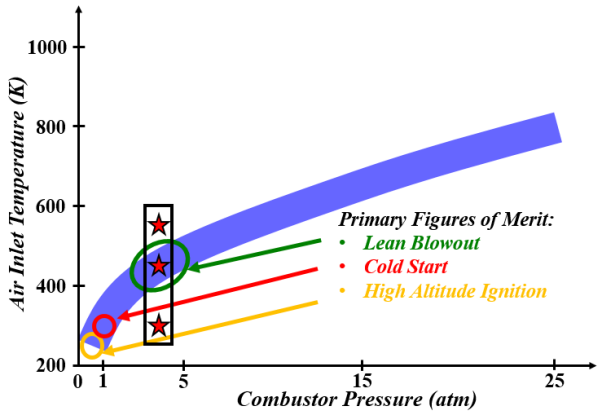

Figure 2.7: Engine inlet conditions and regions where primary figures of merit correspond to the flight operating range. The stars represent conditions for data acquisition. Taken from [9].

Although the experiments were only compared at a single operating pressure, estimates of the relevant characteristic time scales allow for inferences to be made about

the effects of pressure on lean blowout sensitivities. Measurements taken of the liquid droplet size distributions [122, 124] for the fuels used in this study showed that the Sauter Mean Diameter varied between 15-35 microns for a fuel temperature of 322 K and an atomizing gas temperature of 394 K. The Sauter Mean Diameter range increased to 18-42 microns when these measurements were repeated [125] with a fuel temperature of 280 K and an atomizing gas temperature of 259 K. Using the same combustor pressure and fuels as these referenced spray measurements , a gas temperature of 1000 K, and an initial droplet diameter of 50 microns, the LES simulation of Esclapez et al. [119] predicted a droplet evaporation time of ~5 ms. Other models for gasoline, ethanol, and diesel fuel droplets [126, 127] with an initial diameter of 24 microns predict evaporation times between 1-10 ms, with the range depending on the pressure and temperature of the combustor. These evaporation times are compared against the relevant fluid mechanic and chemical times in Table 2-1. The characteristic ignition time is calculated using the Ignitition Quality Tester conversion for the derived cetane number [128].

$$DCN = 83.99\left(\tau_{ign}[ms] - 1.512\right)^{-0.658} + 3.547 \tag{2.1}$$

As the derived cetane number for each of the fuels in this study was determined using an IQT, this equation allowed for an accurate estimate of the ignition delay time. However, it should be noted that these estimates are greater than the expected ignition delay times for pre-vaporized fuels, as the time required for atomization and vaporization of the liquid fuel is included in the IQT measurement. Although the values listed in Table 2-1 are only rough estimates, it can be seen that the characteristic ignition and evaporation times are most likely comparable at the operating conditions that were chosen in this work. However, this

may not be the case at high pressure conditions, as the droplet sizes [125] and evaporation times [126, 127] will certainly decrease as the pressure is increased. Furthermore, the enhanced fuel-air mixing rates that will be caused by the increased turbulence intensities at high pressure will likely augment the sensitivity of lean blowout to fuel chemical properties at high pressure.

Table 2-1: Relevant characteristic time scales.

τ_{evap} (ms)	$\tau_{flow,D/U}$ (ms)	$\tau_{flow,res}$ (ms)	τ_{ign} (ms)
1-10	~ 0.3	~ 6	3-18

2.4 Fuels

Fuels for this study were specifically selected to determine the influence of various fuel properties on blowout performance. Currently certified jet fuels were included as a reference to compare against. These fuels were obtained from the US Air Force as part of the National Jet Fuels Combustion Program. Extensive documentation has been published about these fuels [9, 129-131].

The standard aviation fuels JP-8, Jet-A, and JP-5 were included in this study and will be referred to by the names A-1, A-2, and A-3, respectively. Those fuels which are not currently certified are called the "C" fuels. Fuel C-1 is almost entirely composed of iso-paraffins with carbon numbers of 12 (C12) and 16 (C16) [132]. C-2 has bimodal distillation characteristics, where the aromatics evaporate first, followed by the iso-paraffins. C-3 is a high viscosity fuel composed of JP-5 and farnesane. C-4 is a mixture of the Sasol IPK alternative fuel and fuel C-1. C-5 has a low viscosity and single value boiling point

temperature. The maximum allowable aromatics percentage within the existing jet fuel specification is possessed by fuel C-8. C-9 is a fuel with a high derived cetane number that was attained by adding n-alkanes until its other fuel properties approached the boundaries of the existing jet fuel specification.

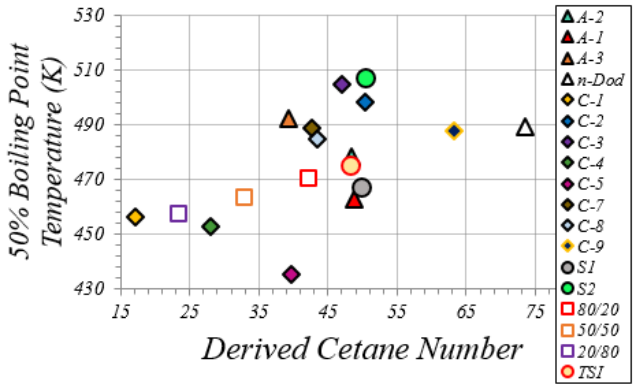

Figure 2.8: Relationship between T_{50} (i.e., the temperature at which 50% of the liquid volume had vaporized) and derived cetane number for investigated fuels.

As detailed in the Introduction, alternative fuels studies have long been plagued by the interdependence between fuel properties. For example, previous work found the 90% boiling point temperature (T_{90}), percentage of aromatics in the fuel, percentage of iso-paraffins in the fuel, and the derived cetane number to all be well-correlated with blowout boundaries [101]. This point is illustrated in Figure 2.8, where it can be seen that the derived cetane number of the studied fuels is correlated with the T_{50} value for several of the fuels. Two surrogate fuels, denoted S1 and S2, were specifically designed by Won *et al.* [94] to disrupt the correlation between physical and chemical fuel properties (However, as will be shown later, the unique preferential vaporization characteristics of these fuels make their effective DCN unclear – i.e., quantities based on average fuel properties may not capture local properties). These fuels have nearly the same derived cetane number,

threshold sooting index (TSI), molecular weight, and H/C ratio as Jet-A, but their vaporization characteristics are much different. Furthermore, n-dodecane and a high TSI fuel were used because they decoupled the correlation between the derived cetane number and aromatic content that is present in most of the other fuels [102].

Turning to the interrelationships between fuel kinetic properties, the derived cetane number is well correlated with the laminar flame speed, extinction stretch rate, and the fuel ignition delay for many of the studied fuels. Fuels C-7 and C-8 were designed to break these correlations. In particular, these fuels have essentially the same DCN but different extinction characteristics. Fuel C-7 is composed of 62% cycloalkanes, a compound exhibiting a high-temperature reactivity similar to n-alkanes but which is relatively less reactive at low temperature conditions, as captured by the ASTM derived cetane number test (ASTM D6890) [133]. Thus, a comparison of the blowout limits of fuels C-7 and C-8 to others may demonstrate the role of extinction related high-temperature flame chemistry on flame stability.

Understanding blending sensitivities is also important for fundamental and practical reasons. From a fundamental perspective, it is important to understand the linear or nonlinear influences of certain species on blowout characteristics. For example, the traditional hydrocarbon ("A") fuels contain many compounds that are not present in the synthetic ("C") fuels. From a practical perspective, the current supply of candidate alternative aviation fuels is insufficient for them to be the sole fuel source on a commercial aircraft. All potential alternative fuels would be implemented in blended proportions with a presently certified fuel, such as Jet-A. Consequently, there is great interest in

understanding blending sensitivities. For this reason, blends of A-2 and C-1 were tested in volume proportions of 80% A-2 20% C-1, 50% A-2 50% C-1, and 20% A-2 80% C-1.

Table 2-2 summarizes the chemical compositions and physical properties of each of the fuels. A detailed reference on these fuels is provided in Ref. [129].

As mentioned above, preferential vaporization can cause the fuel properties that are effective for lean blowout to be different than those based on the entire fuel composition. A key consideration in this work was the degree to preferential vaporization affects LBO boundaries. Preferential vaporization effects were accentuated by testing two fuels with identical DCNs but very different preferential vaporization characteristics. These fuels were designed by Professor Sang Hee Won at the University of South Carolina (USC). Preliminary measurements have confirmed that their actual DCNs approximate the estimated DCN values of 28. The first fuel was comprised of 91.8% C-1 and 8.2% n-heptane by volume. N-heptane has a much lower boiling point temperature (i.e., 371.6 K) than C-1 (i.e., 447.3-536.5 K). It is also much more reactive, with a DCN of 53.8 compared to the C-1 value of 17.1. Therefore, if preferential vaporization does influence lean blowout boundaries, the reactive n-heptane should vaporize first from this fuel and improve the LBO performance. The other fuel was made of 93.6% C-1 and 6.4% n-dodecane. N-dodecane has a boiling point temperature (i.e., 489.0 K) that is within the C-1 distillation range (i.e., 447.3-536.5 K). Therefore, the chemical properties of this fuel remain relatively constant across the distillation curve and preferential vaporization effects are not expected to be present.

Table 2-2: Chemical composition and physical property summary of the fuels, as detailed in Ref. [129]. The smoke point of the High TSI fuel was determined using the TSI constants of Mensch et al. [134, 135] (i.e., a=4.07, b=-4.8). The virtual smoke point of Haas et al. [136] is reported below for n-dodecane. The kinematic viscosities at 313 K for fuels C-7, C-8, and C-9 are estimated by Opacich et al. [137].

Fuel	T_{90} (K)	T_{50} (K)	T_{10} (K)	H/C	% Aromatics	% iso-Paraffins	% n-Paraffins	% Cycloalkanes	Smoke Point (mm)	DCN	MW	Ri	σ @ 300 K (mN/m)	ρ @ 288 K (kg/m^3)	ν @ 313 K (mm^2/s)	Flash Point (K)	LHV (MJ/kg)
A-1 (JP8)	506.9	462.7	437.3	2.02	13.4	39.7	26.8	20.1	28.5	48.8	151.9	0.80	23.6	779.9	1.14	315	43.2
A-2 (Jet-A)	517.6	478.4	449.8	1.94	18.7	29.5	20.0	31.9	24.0	48.3	158.6	0.75	24.6	803.2	1.31	321	43.1
A-3 (JP5)	518.8	492.6	467.2	1.90	20.6	18.1	13.9	47.4	20.0	39.2	166.1	0.67	25.5	826.8	1.57	333	42.9
80% A-2, 20% C-1	516.0	471.0	449.0	1.99	14.9	43.5	16.0	25.5	26.1	42.1	162.6	0.74	24.3	794.5	1.34	321	43.3
50% A-2, 50% C-1	513.0	464.0	449.0	2.05	9.3	64.5	10.0	16.0	29.3	32.7	168.6	0.73	23.8	781.5	1.39	323	43.5
20% A-2, 80% C-1	507.0	458.0	450.0	2.12	3.7	85.6	4.0	6.4	32.4	23.3	174.5	0.72	23.3	768.4	1.45	323	43.8
C-1	497.4	456.3	451.9	2.16	0.0	99.6	0.0	0.1	34.5	17.1	178.0	0.70	23.0	759.7	1.50	323	43.9
C-2	506.8	498.5	463.9	2.08	17.1	77.5	5.2	0.1	26.9	50.4	181.9	0.71	24.9	781.2	1.38	331	43.4
C-3	519.8	505.0	479.8	1.98	13.6	45.2	9.2	31.7	25.2	47.0	179.6	0.70	25.8	807.7	1.78	339	43.3
C-4	479.5	452.7	442.4	2.18	0.4	98.9	0.2	0.4	37.2	28.0	162.2	0.72	22.4	759.2	1.25	318	43.8
C-5	437.4	435.6	434.5	1.93	30.7	51.6	17.7	0.1	21.4	39.6	135.4	0.68	23.5	768.9	0.83	317	43.0
C-7	517.0	489.0	469.0	1.98	4.9	29.5	3.3	62.3	N/A	42.6	170.0	0.75	25.7	817.0	1.71	337	43.3
C-8	519.0	485.0	463.0	1.85	27.3	21.0	13.7	38.0	N/A	43.5	160.0	0.74	26.1	823.0	1.43	329	42.9
C-9	527.0	488.0	459.0	2.16	0.2	85.8	12.5	1.5	N/A	63.3	174.5	0.90	24.0	759.0	1.58	321	44.0
Surrogate 1	499.0	467.0	412.0	1.96	25.1	16.7	58.1	0.0	20.4	50.0	143.2	0.80	24.4	769.0	0.99	297	43.0
Surrogate 2	551.0	507.0	394.0	1.95	24.9	22.5	52.6	0.0	21.1	50.6	156.9	0.78	24.6	778.0	1.28	289	42.9
High TSI	535.7	474.9	441.8	1.91	28.8	53.7	17.6	0.0	17.6	48.4	149.3	N/A	N/A	796.2	N/A	N/A	N/A
n-Dodecane	489.0	489.0	489.0	2.17	0.0	0.0	100.0	0.0	60.0	73.5	170.3	1.00	25.0	753.0	1.29	344	44.2

2.5 Characterization of Preferential Vaporization Potential

Much of the preferential vaporization work conducted in this study was done in collaboration with Professor Sang Hee Won at the University of South Carolina (USC). The preferential vaporization potentials of six of the tested fuels have been evaluated at USC. This involved preparing distillation cuts through an ASTM D86 distillation device [138] and measuring the derived cetane number (DCN) of both the entire fuel composition, and each distillation cut, according to the ASTM D6980 standard [139]. These measurements were taken for fuels A-2, A-3, C-1, n-dodecane, S1, and S2.

The ASTM D86 distillation method requires heating a glass container (~ 250 mL) of liquid fuel with an electric heater, while determining the vaporization temperature at the top exit of the container. The vapor is then introduced to a heat exchanger tube, which is located in a chilled water bath. This chilled water is maintained at 273 K by a Cole-Parmer Polystat UX-12122-62 circulating bath and ensures that there is complete condensation of the vaporized sample by time it reaches the collection glass container. Five distillation cuts, each of ~20 % volume, of the original fuel sample are then obtained, along with their beginning and ending vapor temperatures.

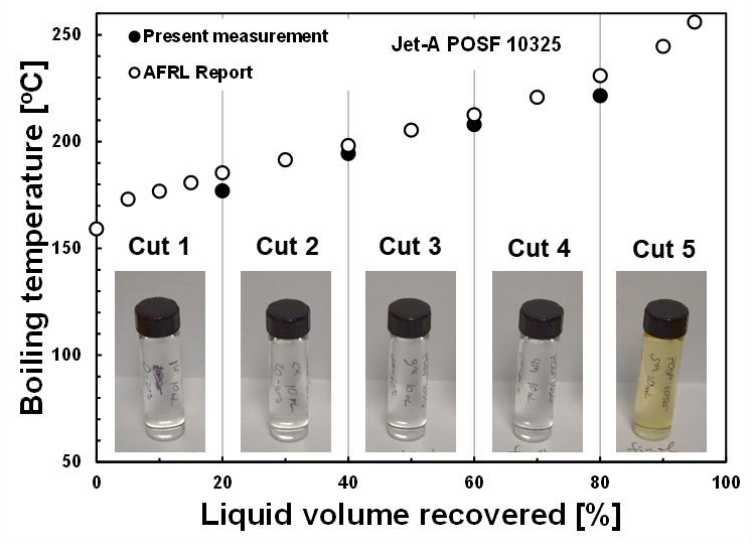

Figure 2.9: Distillation characteristics of Jet-A POSF 10325 determined by the boiling point temperature as a function of the liquid volume recovered by the ASTM D86 method. Insets are direct photographs of five distillation cuts collected for each of the 20% volume samples.

Figure 2.9 compares the measured distillation characteristics of A-2 to those reported by US Air Force Research Laboratory (AFRL) [9]. Considering that the current ASTM D86 methodology has inevitable uncertainty associated with both its configuration and the liquid volume measurement, as discussed in [140-142], the results have a maximum deviation of 9 K, which is sufficiently accurate for the present work. During the distillation measurement, the five individual distillation cuts are collected along the distillation curve by replacing the receiving container at every 20% liquid volume recovered point, as seen in the inset of Figure 2.9. Interestingly, the initial four distillation cuts of A-2 were essentially colorless, whereas the last bin sample exhibited a brownish yellow color (perhaps due to sulfur-containing species or fuel additives). Although not shown in the figure, the distillation characteristics of two other real fuels (A-3 and C-1) have been similarly produced and their distillation curve data has been compared to the results reported by AFRL.

The chemical reactivity potential of the actual fuels, as well as each of their distillation cuts, were characterized by DCN measurements performed using an ignition quality tester (IQT). The DCN is a global/relative measure of the autoignition propensity of a fuel determined by an IQT, which records ignition delay time associated with the injection of a liquid fuel sample into a heated (~ 830 K) constant volume chamber containing pressurized air at ~ 22 atm. Though cetane number variants, such as the DCN, have been historically developed for diesel applications, they have also been extensively utilized to compare the chemical kinetic reactivity potential of single fuel components, component mixtures, petroleum-derived jet fuels, alternative jet fuels, and their mixtures. Furthermore, the DCN acts as one of the Combustion Property Targets (CPT's) in the surrogate mixture formulation [108-111] to emulate the fully pre-vaporized combustion behaviors of real fuels. The DCN has a direct correlation with low-temperature reactivity due to the thermodynamic condition employed in the IQT [107], but it has also been shown that the value reflects high-temperature reactivity as well, due to the strong sensitivity of the DCN to the $(CH_2)_n$ functional group presence in the fuel [94]. A large fraction of $(CH_2)_n$ functional groups indicates the prevalence of normal-alkanes, or straight-chain alkyl groups added to cyclic compounds, that rapidly produce a highly reactive radical pool at high temperatures through oxidative pyrolysis [94, 107]. Although the relevance of low-temperature reactivity for gas turbine applications is still in debate, there is strong evidence that intermediate temperature chemistry, occurring above ~750 K, also affects radical pool development at higher pressures. Here, the DCN values of both the entire fuel composition and their distillation cuts are used as a chemical reactivity potential indicator.

2.6 CH* Chemiluminescence

The detailed measurements that were taken will now be introduced, including high speed CH* chemiluminescence videos, OH* time series from a photomultiplier tube (PMT), dynamic pressure measurements used to characterize acoustics, and OH-PLIF and stereo-PIV measurements. Fuels C-1, A-2, S2 and n-dodecane were included in the 450 K LBO videos. The same fuels were used in the 300 K high speed videos, except fuel C-1 which was exchanged for C-5. Ten fuels in total were used for the PMT and acoustic measurements and are shown in Table 2-3. The fuels labeled with an asterisk in this table are those for which CH* chemiluminescence videos were acquired. Fuels A-2, C-1, and C-5 were included in the planar measurements. The fuels which were studied further using detailed measurements were selected because they spanned the lean blowout limit range.

CH* chemiluminescence videos were taken as the blowoff process occurred. The images were acquired at 4 kHz with a 12 bit Photron SA5 camera. Each recorded video captured between 2,000-3,000 images. The camera resolution was set to 1024x1024 pixels, which resulted in a final resolution of approximately 97 μm/pixel. An AT-X M100 Tokina lens with f=100 mm and a f/D=2.8 setting was used with the camera. A 434 nm centered spectral filter with a 17 nm bandwidth was used to capture the emission from the CH* radical.

In order to record a blowoff process, a photomultiplier tube (PMT) signal was used to activate the high speed camera. Using the falling edge from a PMT signal following a blowoff event, a timing box was used to trigger the camera. A 50 μs delay was set on the timing box in order to ensure that the flame had fully extinguished before the camera began

recording. The camera was back triggered, such that it retained the images that were stored in its buffer during the viewing window preceding the receipt of the PMT signal's indication of blowoff. This procedure was repeated 2-8 times for each of the four fuels at the two different air inlet temperatures. Table 2-4 shows the conditions where chemiluminescence measurements were taken. Conditions A, B correspond to PMT measurements and conditions C, D were taken using high speed videos. Both the chemiluminescence videos and the PMT measurements were recorded during the blowout transient (ϕ-$\phi_{LBO}\rightarrow 0$). Videos were also recorded at an equivalence ratio slightly above the blowout value (ϕ-$\phi_{LBO}\approx 0.025$), in order to study the flame behavior during the pre-blowoff stages.

Table 2-3: Fuels used for the detailed measurements. Acoustic and PMT measurements were taken for each of these fuels, whereas CH* chemiluminescence videos were acquired for the fuels with an asterisk.

Fuel	T_{90} (K)	T_{50} (K)	T_{10} (K)	H/C	% Aromatics	% iso-Paraffins	% n-Paraffins	% Cycloalkanes	Smoke Point (mm)	DCN	MW	Ri	σ @ 300 K (mN/m)	ρ @ 288 K (kg/m^3)	ν @ 313 K (mm^2/s)	Flash Point (K)	LHV (MJ/kg)
A-2 (Jet-A)*	517.6	478.4	449.8	1.94	18.7	29.5	20.0	31.9	24.0	48.3	158.6	0.75	24.6	803.2	1.31	321	43.1
C-1*	497.4	456.3	451.9	2.16	0.0	99.6	0.0	0.1	34.5	17.1	178.0	0.70	23.0	759.7	1.50	323	43.9
C-4	479.5	452.7	442.4	2.18	0.4	98.9	0.2	0.4	37.2	28.0	162.2	0.72	22.4	759.2	1.25	318	43.8
C-5*	437.4	435.6	434.5	1.93	30.7	51.6	17.7	0.1	21.4	39.6	135.4	0.68	23.5	768.9	0.83	317	43.0
C-7	517.0	489.0	469.0	1.98	4.9	29.5	3.3	62.3	N/A	42.6	170.0	0.75	25.7	817.0	1.71	337	43.3
C-8	519.0	485.0	463.0	1.85	27.3	21.0	13.7	38.0	N/A	43.5	160.0	0.74	26.1	823.0	1.43	329	42.9
C-9	527.0	488.0	459.0	2.16	0.2	85.8	12.5	1.5	N/A	63.3	174.5	0.90	24.0	759.0	1.58	321	44.0
Surrogate 2*	551.0	507.0	394.0	1.95	24.9	22.5	52.6	0.0	21.1	50.6	156.9	0.78	24.6	778.0	1.28	289	42.9
High TSI	535.7	474.9	441.8	1.91	28.8	53.7	17.6	0.0	17.6	48.4	149.3	N/A	N/A	796.2	N/A	N/A	N/A
n-Dodecane*	489.0	489.0	489.0	2.17	0.0	0.0	100.0	0.0	60.0	73.5	170.3	1.00	25.0	753.0	1.29	344	44.2

Table 2-4: Conditions where PMT measurements (A, B) and CH* chemiluminescence videos (C, D) were acquired.

Condition	Equivalence Ratio	Temperature (K)	Fuels (Repeats)	Recording Time
A	$0.1>\phi-\phi_{LBO}\rightarrow 0$	450	All fuels in Table 2-3	*50 seconds*
B	$0.1>\phi-\phi_{LBO}\rightarrow 0$	300	All fuels in Table 2-3	*50 seconds*
C	$\phi-\phi_{LBO}\rightarrow 0$	450	A-2 (8), C-1 (7), n-Dodecane (7), S2 (6)	*Less than 1 sec*
D	$\phi-\phi_{LBO}\rightarrow 0$	300	A-2 (2), C-5 (3), n-Dodecane (2), S2 (2)	*Less than 1 sec*

2.7 Photomultiplier Tube (PMT) Measurements

Photomultiplier tube (PMT) measurements were used to acquire OH* chemiluminescence signals over longer time intervals than would be possible using cameras alone, allowing better estimates of event statistics near blowoff. By integrating all of the intensity in its field of view, the PMT outputted a single intensity point value taken at 10 kHz over a 50 second interval. This involved beginning the measurements at an equivalence ratio of ϕ-$\phi_{LBO}\approx$0.1 and gradually reducing the fuel flow rate until blowoff occurred. These cases are labeled conditions A (450 K) and B (300 K) in Table 2-4. The Hamamatsu H5784-04 PMT was stored inside of a box during data acquisition in order to prevent background light from interfering with the chemiluminescence measurements. Also, as shown in Figure 2.10, this box configuration allowed for easy determination of the measurement's field of view. Light was able to enter the PMT housing box through a 0.115" aperture in a bulkhead optical fiber connector. A Newport spectral filter was placed between the bulkhead connector and the PMT in order to reject emission that wasn't associated with the OH* radical. It had a center frequency of 310 nm and a half width of 10 nm. The PMT had an effective diameter of 8 mm and, based on the distances shown in Figure 2.10, the half angle at which light enters the PMT housing box through the bulkhead connector port is 6 degrees. Figure 2.11 shows images of the test section and the PMT configuration. Based on the 6 degree viewing half angle and the width of the windows providing optical access into the test section, the opening port of the PMT needed to be placed at least 533 mm away from the desired field of view. For this reason, the PMT was placed 546 mm from the outermost edge of the test section, thereby capturing all of the

luminosity that was observable in the combustor. These distances were measured prior to operation and did not change significantly during the data acquisition process.

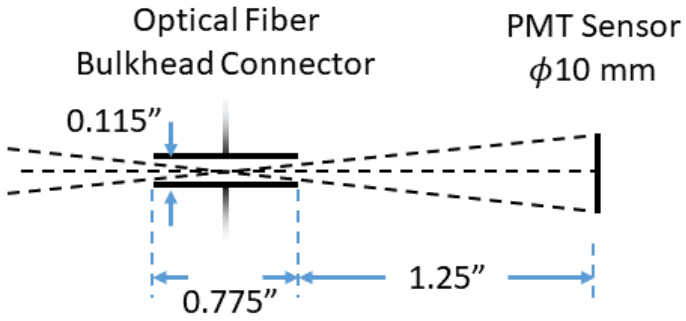

Figure 2.10: Schematic of the PMT configuration and the corresponding viewing angles. Taken from [143].

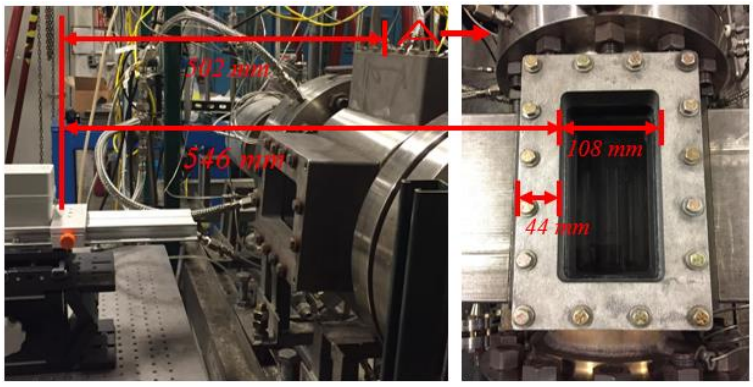

Figure 2.11: PMT placement and associated distances to the test section. The image on the left is a side view of the combustor and the right image represents a top down view of the combustor.

These PMT time series data were acquired 10 times, at both the 300 K and 450 K air inlet temperatures, for each of the ten fuels that were considered, resulting in 200 total cases that were analyzed. Data was also taken at 550 K but were there non-negligible acoustic oscillation levels (p’/P~0.7%, as opposed to 0.25% at 300 K and 450 K). This point will be discussed in more detail later in Section 5.3. Given the potential influence of

thermoacoustic coupling on blowoff, PMT results are only shown for the 300 K and 450 K data.

2.8 Acoustic Measurements

Dynamic pressure measurements were taken both upstream of the swirler, and also downstream of the test section, as shown in Figure 2.1. These measurements were acquired using Kistler Type 6023A differential pressure sensors that were mounted flush with the inner diameter of the pressure vessel piping. These piezoelectric sensors are capable of operating in temperatures up to 973 K and account for vibrations or shocks that would otherwise interfere with their measurements. The response of the sensors is temperature dependent, but the thermal sensitivity shift varies less than ± 5% over the operating temperature range. The sensors' signal is outputted in picocoulombs (pC) with a conversion factor of 1.006 pC/kPa. A Kistler Type 5181A differential charge amplifier is then used to convert the signal from picocoulombs to millivolts, in 10 mV/pC proportions. These measurements were also taken at 10 kHz over a 50 second interval. 10 repetitions of these data were taken for each fuel and air inlet temperature, resulting in 300 total acoustic time series.

2.9 Planar Measurements

Simultaneous OH-PLIF and PIV measurements were taken at 5 kHz to characterize the details of the flame and flow structure. These data were acquired at an air inlet temperature of 450 K and the nominal operating pressure of 345 kPa. Both stable burning cases (ϕ-$\phi_{LBO}\approx$0.1) and a blowout transient case were included in this data set. Data was obtained for the stable burning case with fuels A-2, C-1, and C-5. Fuel A-2 was used for

the blowout transient case. Due to allowable operating time limitations for the OH-PLIF camera intensifier, it was not possible to back trigger the planar measurements for the blowout transient case as was done for the CH* chemiluminescence videos. Therefore, this case was captured by operating the combustor on the threshold of lean blowout and then simultaneously closing the fuel valve and triggering the camera. Although this was not an authentic blowout process, fuel continued to be injected into the combustor throughout the entire series of recorded images, including after the flame blew out. Assuming that the fuel spray was not significantly altered by the fuel valve's closure, the images that were captured likely represent a blowout transient with a rapid fuel ramp rate. Details of the diagnostic techniques that were used to acquire this data can be found in these references [76, 144, 145].

CHAPTER 3. DATA ANALYSIS TECHNIQUES

This section introduces and provides details for the data analysis techniques that will be used in the following results sections. The types of analysis that will be discussed include a multiple linear regression that was applied to the fuel screening data, flame edge tracking for CH* chemiluminescence images, and thresholding of the PMT time series.

3.1 Hierarchical Non-negative Garrote Regression

A multiple linear regression analysis was performed to identify the relative contributions of each of the fuel properties on the fuel screening LBO boundaries. Obtaining regression results that both accurately represent the data and are physically meaningful depends on including only the causal variables for the problem under consideration [146]. Therefore, variable selection techniques were used to identify the most important variables for lean blowout and obtain an estimate of their regression coefficients. This problem is represented by the following equation:

$$Y_i = \sum_{j=1}^{J} X_{ij}\beta_j + \epsilon_i \tag{3.1}$$

where Y_i is an n x 1 vector of outputs, X_{ij} is an n x p matrix of input variables, β_j is a p x 1 vector of regression coefficients, and ϵ_i is the error. In this nomenclature, n represents the sample size and p is the number of variables.

The most effective variable selection approaches are those that are able to completely eliminate the influence of insignificant variables. Such approaches include the

Non-negative Garrote (NNG) method [147], Least Absolute Shrinkage and Selection Operator (LASSO) Regression [148], and Least Angle Regression (LARS) [149]. As each of these are supervised learning techniques, the results depend on appropriately chosen tuning parameters for the optimization algorithm. For example, in Breiman's [147] original Non-negative Garrote method

$$d_j(\lambda) = \arg\min_{d_j}\left(\frac{1}{2}\left\|Y_i - X_{ij}\left(\beta_j^{OLS} \odot d_j\right)\right\|^2 + \lambda\sum_{j=1}^{J} d_j\right); subject\ to\ d_j \geq 0, \forall j \qquad (3.2)$$

where "⊙" represents the element-wise vector product, the shrinkage factor, d_j, depends on the value of tuning parameter, λ, which is a required input for optimizing this equation. Therefore, obtaining a consistent solution path across a range of tuning parameters is a key variable selection issue. Yuan and Lin [150] define a consistent solution path as one that includes at least a single desirable estimate of the regression coefficients and relevant variables. By including artificial variables in their set of predictors and applying these methods to data sets with known regression coefficients, they showed that the path consistency performance of the Non-negative Garrote method is superior to other methods, provided that it receives an accurate initial estimate [150]. The ordinary least squares regression coefficients, β_j^{OLS}, are used as the initial estimate in equation (3.2).

$$\beta_j^{OLS} = \left(X_{ij}^T X_{ij}\right)^{-1} X_{ij}^T Y_i \qquad (3.3)$$

Cross-validation is among the most popular model selection techniques and was applied here to select the optimal tuning parameters. This procedure involves separating a data set into multiple groups and assigning a single group to act as test data, while the data

in the remaining groups serve as the training data. The model is developed on the training data for a single tuning parameter input (some models involve multiple tuning parameters, but only one value for each tuning parameter can be cross-validated at a time) and its error is then calculated using the test data. Cross-validation performs this training/testing process in an iterative fashion, where the testing/training sets are successively re-assigned until each portion of the data has acted as both training and test data. The mean squared error associated with the different test data sets is determined and this value represents the quality of the model developed using the inputted tuning parameter(s). This cross-validation procedure is then repeated for a range of tuning parameters and the tuning parameter(s) is selected which minimizes the mean squared error.

Determining the number of groups to use is a key consideration in cross-validation. Using a small number of groups causes large bias errors, where the estimated mean squared error of the model varies significantly with small changes in the tuning parameter(s). However, using too many groups shrinks the size of the test data and causes large variances in the calculated mean squared error [151]. Furthermore, the appropriate group size is also dependent on the size of the overall data set. For example, small data sets ($n<20$) are very sensitive to bias errors that can corrupt the cross-validation procedure. In such cases it is best to use leave-one-out cross-validation, where the group count is maximized by treating each individual sample as a group, and only one sample is used as the test data for each iteration of the procedure. Since 18 fuels were experimentally tested in this study, leave-one-out cross-validation was used to select the tuning parameters for this small data set. Figure 3.1 illustrates this procedure, where each fuel acted as an individual cross-validation

group. The groups labeled in green represent the training data and the groups in red represent the test data.

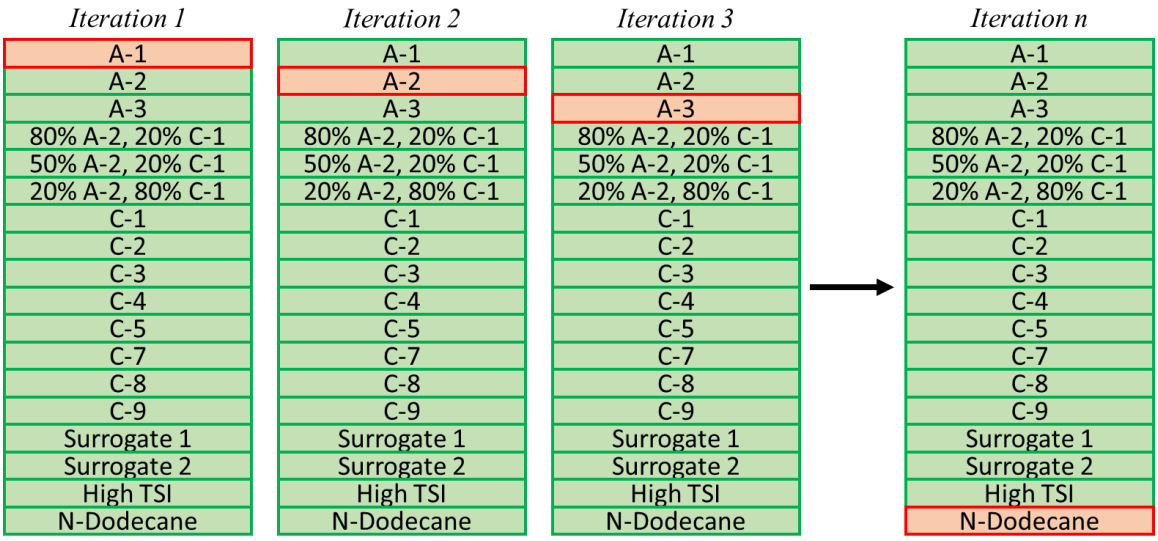

Figure 3.1: Conceptual illustration of the leave-one-out cross-validation procedure. The green groups represent the fuels used for the training data and the red groups represent the fuels used as the test data.

Correcting for inter-correlated variables is a critical variable selection issue. Each of the previously mentioned variable selection techniques have limitations in their ability to circumvent this problem. However, Paynabar et al. [146] developed a two-step process, known as the Hierarchical Non-negative Garrote method, that has been shown to perform accurate variable selection while still accounting for correlations between variables. First, important groups of variables are identified and then the individual variables within these groups are regressed in the second step. Step 1 utilizes the Group Non-negative Garrote method of Yuan and Lin [152]

$$d_k(\lambda) = \arg\min_{d_k}\left(\frac{1}{2}\left\|Y_i - \sum_{k=1}^{K}\left(\sum_{j=1+p_k(k-1)}^{p_k(k)} X_{ij}\beta_j^{OLS}\right)d_k\right\|^2 + \lambda\sum_{k=1}^{K} d_k\right);\ d_k \geq 0, \forall k \qquad (3.4)$$

where *k* represents the group number, p_k is the number of variables within each group, and d_k is the group shrinking factor. As d_k indicates the relative importance of each group of variables, this step performs variable selection at the group level. Groups with a d_k value greater than 10^{-5} advance to Step 2 in the method. As was mentioned earlier, the Non-negative Garrote method relies heavily on receiving an accurate initial estimate of the regression coefficients. The ordinary least squares estimate, used in equation (3.4), is known to have poor prediction accuracy for data sets with a small sample size [150]. In such cases, Paynabar et al. [146] recommend substituting the ridge regression coefficients for the initial estimate in equation (3.4).

$$\beta_j^{ridge} = \left(X_{ij}^T X_{ij} + \lambda I\right)^{-1} X_{ij}^T Y_i \qquad (3.5)$$

This ridge regression substitution was applied here, since n<20 for the data set under consideration. Following the approach of Yuan and Lin [150], cross-validation was applied first to equation (3.5) in order to determine the tuning parameter for the ridge regression. Using this initial estimate, equation (3.4) was cross-validated next to identify the optimal tuning parameter for the group selection step. A modified form of the Non-negative Garrote method that is not affected by correlations between individual variables is then solved in Step 2.

$$d_j(\lambda_1, \lambda_2) = \arg\min_{d_j}\left(\frac{1}{2}\left\|Y_i - X_{ij}\left(\beta_j^{ridge} \odot d_j\right)\right\|^2 + \lambda_1\|d_j\|_1 + \frac{\lambda_2}{2}\|d_j\|^2\right); d_j \geq 0, \forall j \qquad (3.6)$$

The solution to the previous equation depends on two tuning parameter, λ_1 and λ_2, where λ_2 is also used as the tuning parameter for the ridge regression coefficients, β_j^{ridge}, in equation (3.6). Therefore, the tuning parameters were chosen that minimized the mean squared cross-validation error on a solution surface. The optimization problems in equations (3.4) and (3.6) were solved using CVX, a Matlab software package for performing convex optimization [153, 154]. The final regression coefficients for the individual variables are calculated by the element-wise vector product between the shrinkage factors and β_j^{ridge} used in equation (3.6).

$$\beta_j^{HNNG} = d_j(\lambda_1, \lambda_2) \odot \beta_j^{ridge} \tag{3.7}$$

It should be noted that each of the predictor variables were standardized to have zero mean and a standard deviation of one before the Hierarchical Non-negative Garrote method was applied. However, the response variables were not centered on the mean. Instead, they were referenced to the A-2 (Jet-A) fuel, as described in Section 4.1. As noted in Table 2-2, some fuel property measurements were unavailable for certain fuels. In such cases, linear interpolation between the missing variable and its most closely correlated variable was used to provide the needed estimates for these unavailable properties in the regression analysis.

3.2 Edge Detection of CH* Chemiluminescence Images

Near blowoff, the most upstream point of the flame jumps axially back and forth, presumably associated with extinction, re-ignition, and axial convection. Two separate examples of this phenomenon that each include an LBO precursor event are shown later in

Figure 6.2 and Figure 6.3. These figures show twelve consecutive images where the most upstream luminosity point is labeled, x_{up}. Flame edge tracking techniques were used to identify x_{up} in each image. This location was determined in the following manner. First, the images were inverted in order to accentuate the flame edge. This procedure enhanced the contrast between the image background and the image area occupied by the flame. Image denoising techniques were then used in order to further sharpen the flame edge. Much of the noise was periodic due to the dim edges of these weakly burning flames being near the detection limit of the camera. Therefore, an automated filtering process developed by Sur et al. [155], that operated in the image frequency domain, was used to remove this periodic noise from the images.

A Gaussian smoothing filter with a standard deviation of four was then applied to the images in order to prevent random noise from being picked up by the edge detection algorithm. A global threshold, determined by Otsu's method [156], was then used to define the flame edge for each image. Unlike using a constant threshold value throughout all cases, this method accounted for differences in the CH* emission intensity between fuels.

3.3 PMT Thresholding

Spatially integrated measurements of filtered flame luminosity are a useful way to characterize the blowout process of a flame throughout its entire history, from stable burning to complete extinction. The same double threshold method described by Murganandam [50] was used here to identify LBO precursor events from PMT measurements. The thresholds are calculated as a fixed percentage of the moving average of the mean. The signal must descend below and recover above both thresholds in order

for a drop in intensity to be classified as an “event”. The upper threshold was 55% of the local mean and the lower threshold was 40% of the local mean for the 450 K data. The upper threshold was 65% of the local mean and the lower threshold was 50% of the local mean for the 300 K data. There is a certain level of arbitrariness in the values that were chosen for these thresholds. However, Nair and Lieuwen [17] provide some general criteria that can be used to select an appropriate threshold. These criteria will be illustrated using a figure from their paper, which is shown here as Figure 3.2, where I_v is an indicator of blowout proximity and P_{FS} is a parameter that governs the flame stability. In this study, I_v is quantified by the number of LBO precursor events per second and the equivalence ratio serves as P_{FS}. Their first criterion is that the blowoff indicator value must be much greater just before blowout than during stable operation (i.e., $I_{v,LBO} >> I_{v,safe}$). Second, I_v should increase monotonically as the equivalence ratio is reduced towards blowoff. Third, the gradient in I_v must increase near blowoff (i.e., $dI_{v,LBO}/dP_{FS} > dI_{v,safe}/dP_{FS}$). In reference to Figure 3.2, only curves 3, 4, and 5 satisfy this criterion. Fourth, the maximum gradient in I_v should not take place during stable operation or too close to blowout. Lastly, any results must not be overly sensitive to the selected threshold value. Therefore, the optimal threshold according to these criteria would be one that is situated between curves 3 and 4 in Figure 3.2. The following discussion will demonstrate that each of these criteria were satisfied in this analysis.

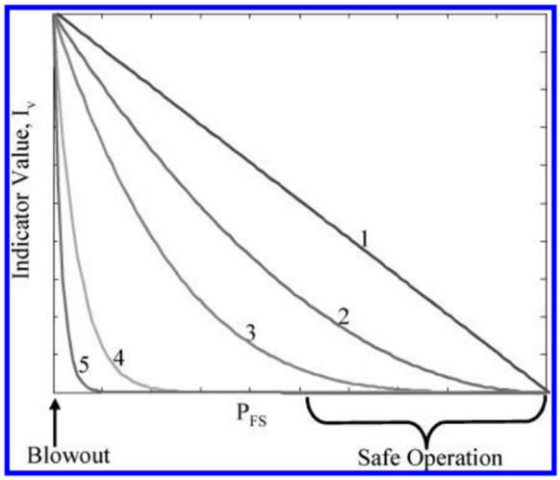

Figure 3.2: Conceptual threshold selection illustration. I_v represents an indicator of blowout proximity and P_{FS} governs flame stability. Taken from [17].

Figure 3.3 shows an example of the PMT time series and double thresholds for fuel A-2 operating at both air inlet temperatures. It is apparent that the number of threshold crossings increases near blowout. The contrast in event frequency and duration between stable operation and lean blowout, averaged across the 10 cases for each fuel, is shown in Figure 3.4. The equivalence ratio was measured in 1 second intervals as LBO was approached and the number of events in each of these intervals was counted. Similarly, the average duration of the events in each interval was determined. Consistent with criteria 1-3, the events increased approximately monotonically in frequency and duration as LBO was approached.

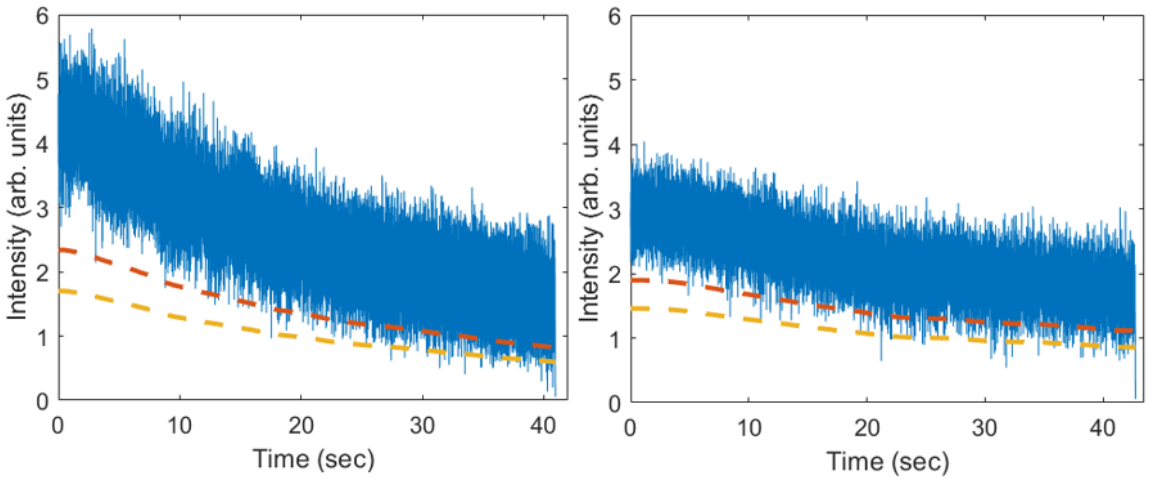

Figure 3.3: PMT time series at a 450 K air inlet temperature (left) and a 300 K air inlet temperature (right). The upper and lower thresholds are represented by the orange and yellow dashed lines, respectively. The fuel is A-2 (Jet-A).

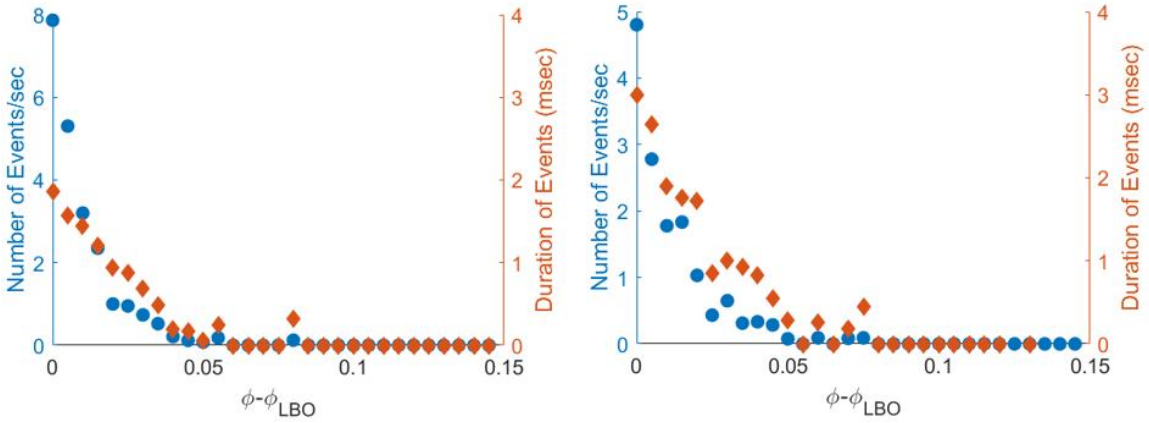

Figure 3.4: Equivalence ratio dependence of the average event frequency and duration as blowout is approached at a 450 K air inlet temperature (left) and 300 K air inlet temperature (right). The fuel is A-2 (Jet-A) in both instances.

Obtaining an accurate estimate of the equivalence ratio at which the events began, (ϕ_{event}), is required to satisfy criteria 4. LBO precursor events were occasionally observed in the high speed videos that were taken at ϕ - ϕ_{LBO}≈0.025. Although Figure 3.4 shows that the selected thresholds indeed predict that LBO precursor events will begin at equivalence ratios greater than ϕ - ϕ_{LBO}≈0.025, determining the precise value for ϕ_{event} is challenging

because the event frequency does not increase smoothly from zero to the blowoff value. In other words, the initial events that are detected may not be particularly informative about blowoff proximity because the flame is capable of returning to stable operation afterwards. The probability that registered events will be imminently followed by LBO was determined by fitting a monotonic curve to the equivalence ratio measurements and then calculating the cumulative distribution function of the event frequency. ϕ_{event} was defined for each individual run as the equivalence ratio at which the events had at least 10% probability of causing blowout, and those with lower probabilities were discarded in the subsequent analysis. This procedure for defining ϕ_{event} is illustrated in Figure 3.5, where it is applied to the 450 K time series that was shown previously in Figure 3.3. The contrast plot of the event frequency and duration is shown on the left and the corresponding event frequency CDF is shown on the right. The orange line on the right plot in Figure 3.5 represents 10% probability that events will be imminently followed by LBO and the associated equivalence ratio, ϕ_{event}, is marked by the yellow data point.

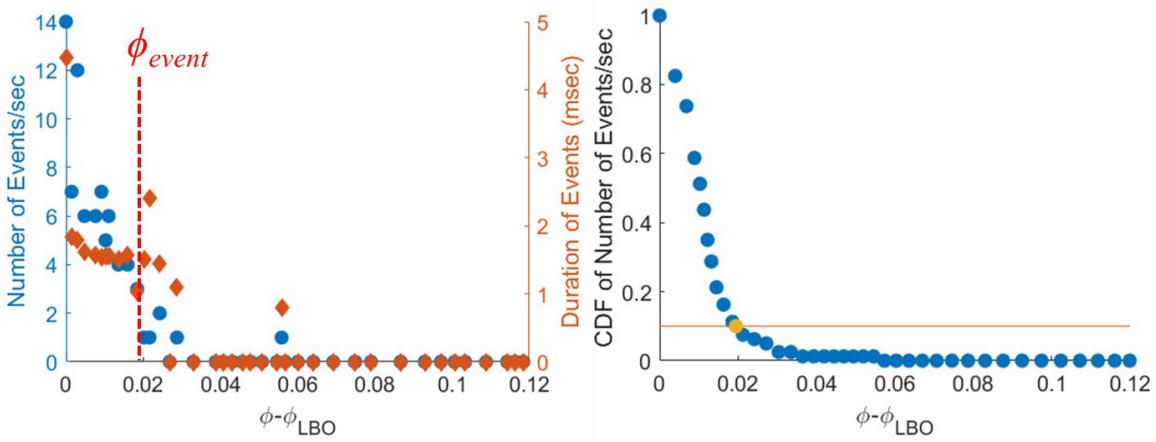

Figure 3.5: Equivalence ratio dependence of the event frequency and duration as blowout is approached for a single 450 K air inlet temperature case (left) and the CDF of the event frequency (right). The orange line in the right plot represents 10% probability that an event will cause blowout and the corresponding equivalence ratio is marked by the yellow data point. The fuel is A-2 (Jet-A).

The following information was extracted from the PMT data - the average duration of the events, τ_{event}, the equivalence ratio at which the events began (ϕ_{event}), and the percentage of burning time in the near blowoff stages ($\phi_{event} > \phi > \phi_{LBO}$) that was constituted by extinction, $\%\tau_{ext}$. Figure 3.6 uses the 450 K time series in Figure 3.3 as an example to demonstrate how the event duration and $\%\tau_{ext}$ were calculated. A small segment of the time series surrounding the 33.5 second mark, along with the upper and lower thresholds, are shown on the left in Figure 3.6. As there is only one instance in the left plot where the signal descends below and then recovers above both thresholds, a single LBO precursor event occurred within this portion of the time series. When an LBO precursor event does occur, the event duration is defined as the amount of time in which the signal remains below the upper threshold, as indicated by the red dimensions on the left plot in Figure 3.6. As the x-axes in Figure 3.6 can also be represented by the equivalence ratio, the recording time values corresponding to ϕ_{event} and ϕ_{LBO} are indicated in the complete time series shown on the right in Figure 3.6. τ_{event} represents the average duration of the events in the ($\phi_{event} >$

$\phi > \phi_{LBO}$) time interval and $\%\tau_{ext}$ represents the percentage of time in this interval that was comprised of LBO precursor events. These values were determined for each individual run and then averaged over the 10 cases for each fuel. The error bars that are shown in the plots in Sections 6.2-6.3 represent a combined uncertainty with two contributions. One is a thresholding contribution that comes from the difference between the values at the selected thresholds and those at ± 5% of the chosen thresholds. The other is a data variability contribution that was determined using 95% confidence intervals. Although the quantitative values (e.g., $\%\tau_{ext}$) do depend on the threshold that was used, the general trends in each of the following plots were very insensitive to the threshold value.

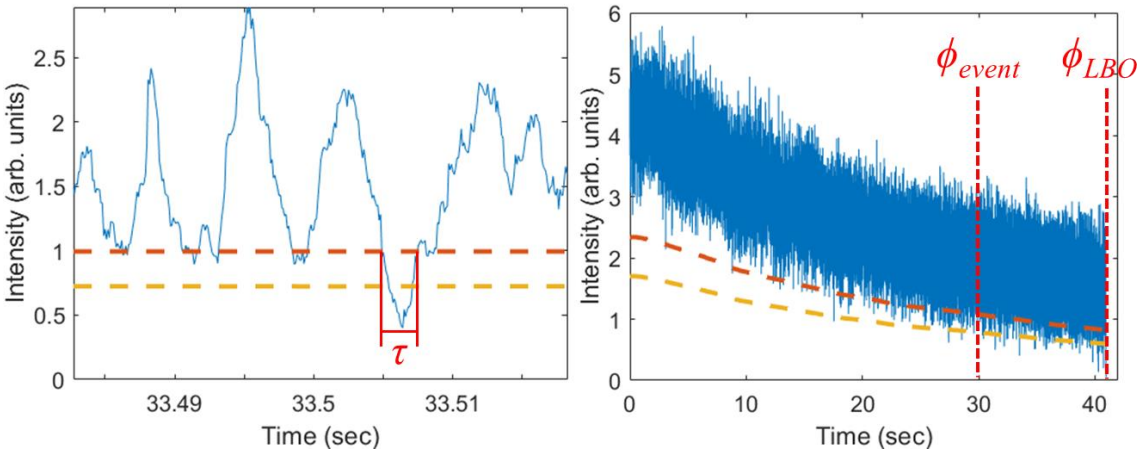

Figure 3.6: PMT time series at a 450 K air inlet temperature. A segment of the time series that includes a single LBO precursor event is shown on the left. This plot indicates how the duration of an LBO precursor event was defined. The complete time series, with indicators for the recording times corresponding to ϕ_{event} and ϕ_{LBO}, is shown on the right. The fuel is A-2 (Jet-A).

CHAPTER 4. FUEL SCREENING

The goal of this section is to understand the dependence of the lean blowout equivalence ratio on fuel properties. It will be shown that this dependence is a strong function of the air inlet temperature, as this can cause the relative significance of the physical and kinetic properties controlling LBO to change. Furthermore, it will be shown that physical and chemical properties can have a coupled effect on lean blowout, as preferential vaporization can cause the kinetic properties of a small fraction of the constituents to have a dominant effect on flame stability. Lastly, a multiple linear regression analysis was performed to accentuate the relative contributions of each of the fuel properties on LBO.

4.1 Lean Blowout Results

Blowout results were compared between 18 different fuels and were tested at three different air temperatures (300 K, 450 K, and 550 K). These blowout sensitivities are displayed as the percent difference in equivalence ratio between a given fuel and the reference fuel A-2, denoted as $\%\phi$ from A-2. This percent difference, $\%\phi$, is calculated by averaging the blowout equivalence ratios within a fixed bulkhead temperature window of 50 K, subtracting the corresponding average for A-2 from that value, dividing this difference by the average A-2 value, and then averaging these percent differences across each of the days that the experiment was performed (ranging between 3-12). This composite equivalence ratio percent difference, $\%\phi$, is the value that will be presented in the following plots.

The number of samples in the 50 K bulkhead temperature window are used to calculate 95% confidence intervals corresponding to each fuel and including all experimental days. Since results for each fuel are shown relative to the reference fuel, these 95% confidence intervals are based on the percent difference between each data point and the corresponding average A-2 value on the day that the experiment was performed. This uncertainty in the composite $\%\phi$ value for each fuel is represented by the error bars shown in Figure 4.1. Additional details about the uncertainty in $\%\phi$ are included in Appendix B.

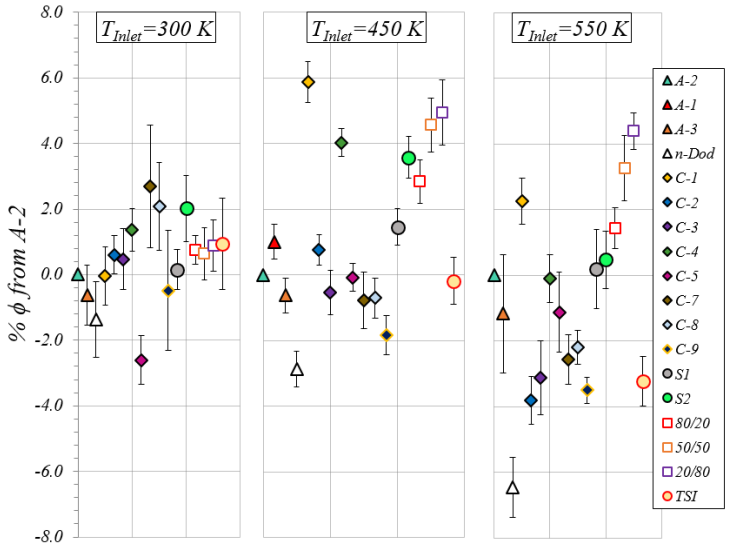

Figure 4.1: Percent differences in the blowout equivalence ratio between each fuel and A-2. Error bars represent 95% confidence intervals.

Table 4-1 provides an introduction to the plots that will be shown in the following sections. It follows the approach of Burger et al. [96] in displaying the correlation coefficients between different fuel properties and the blowout data. This is a helpful way to identify correlations between fuel properties and determine how they trend with blowout sensitivities. For example, this table shows that both the DCN and the radical index correlate with 550 K blowout equivalence ratios, with correlation coefficients of -0.76 and

-0.57, respectively (note also that these fuel properties are both correlated with each other, with a correlation coefficient of 0.77). Cells highlighted green in this table denote correlation coefficients with an absolute value greater than 0.5.

As noted in the Introduction, blowout in liquid fueled combustors is a function of both fuel physical and chemical properties. The following results sections will be organized around physical and chemical property correlations. Although many different fuel properties were investigated, the focus of the discussion will be on the fuel properties that correlated best with blowout. A complete set of plots for $\%\phi$ as a function of each of the available fuel properties, across all three air inlet temperatures, is shown in Appendix B.

Table 4-1: Correlation coefficient table depicting the correlations between fuel properties and blowout boundaries, following Burger et al. [96]. Green highlighting accentuates coefficients greater than |±0.5|.

	T_{10} (K)	T_{50} (K)	T_{90} (K)	v (mm^2/s)	σ (mN/m)	ρ (kg/m^3)	H/C	MW	LHV	% Arom.	% iso-Par.	SP (mm)	DCN	Ri
T_{50} (K)	0.27													
T_{90} (K)	-0.08	0.72												
v (mm^2/s)	0.57	0.60	0.60											
σ (mN/m)	0.41	0.77	0.45	0.45										
ρ (kg/m^3)	0.26	0.44	0.43	0.46	0.75									
H/C	0.23	-0.20	-0.24	0.11	-0.61	-0.78								
Molecular Weight	0.63	0.46	0.31	0.84	0.17	0.01	0.54							
LHV (MJ/kg)	0.41	-0.16	-0.17	0.22	-0.45	-0.69	0.95	0.55						
% Aromatics	-0.45	0.06	0.07	-0.46	0.37	0.45	-0.88	-0.68	-0.91					
% iso-Paraffins	-0.01	-0.42	-0.19	0.14	-0.70	-0.45	0.61	0.37	0.52	-0.47				
Smoke Point (mm)	0.53	-0.04	-0.30	0.09	-0.16	-0.61	0.82	0.41	0.90	-0.80	0.02			
Cetane Number	0.17	0.55	0.21	-0.07	0.48	-0.03	-0.08	-0.09	0.03	0.13	-0.57	0.21		
Radical Index	0.14	0.24	0.12	-0.09	0.06	-0.45	0.40	0.03	0.51	-0.36	-0.32	0.71	0.77	
%φ LBO (450 K)	-0.48	-0.45	-0.02	0.11	-0.66	-0.33	0.31	0.10	0.12	-0.21	0.56	-0.08	-0.79	-0.45
%φ LBO (300 K)	-0.15	0.35	0.62	0.44	0.24	0.39	-0.16	0.23	-0.18	-0.04	0.02	-0.21	-0.21	-0.18
%φ LBO (550 K)	-0.65	-0.43	-0.06	-0.25	-0.49	-0.04	-0.13	-0.29	-0.35	0.16	0.26	-0.44	-0.76	-0.57

4.2 Physical Property Correlations

Liquid fuel physical properties govern the atomization and vaporization processes required to form a combustible gas-phase fuel-air mixture. The fuel viscosity, surface tension, and density impact the atomization process. Extensive studies on the spray characteristics of these fuels have shown no correlation between fuel physical properties and droplet sizes [122, 124, 125, 157]. Although these findings de-emphasize the expected role of fuel droplet sizes on LBO, they may not be directly applicable to this study, as these measurements were taken using a different pressure atomizer design. Furthermore, efforts are underway by these authors to reduce their measurement uncertainty. The fuel boiling point temperatures are the physical properties that correlate best with blowout trends and so they are the focus of this section. The strongest correlations were seen at air inlet temperatures below the various fuel flash points. This is consistent with the findings from previous studies [96, 100], although these prior studies disagree on whether improved vaporization quality helps or hinders flame stability. This consideration was a key motivator for the 300 K air inlet temperature test point, as all fuels except S1 and S2 had flash points above this value.

The many different chemical species and compounds in jet fuels lead to a vaporization process that extends across a range of temperatures. Blowout boundaries were compared along this distillation range at T_{90}, T_{50}, and T_{10}, representing the temperatures at which 90%, 50%, and 10%, respectively, of the liquid volume had vaporized. Figure 4.2 shows the blowout equivalence ratio sensitivity to T_{10}. A linear least-squares curve fit of this data set produces a negatively sloped line, driven largely by S2 and n-dodecane. The resulting physical explanation is the same conclusion expressed by Grohmann et al. [100]

and Lefebvre [95] – i.e., that difficult to vaporize fuels may extend blowout boundaries because they create locally richer regions with locally elevated flame temperatures. However, with the exception of these two fuels, no correlation exists between T_{10} and $\%\phi$. Figure 4.3 and Figure 4.4 present plots of the dependence of $\%\phi$ upon T_{50} and T_{90}, showing a general trend that the easily vaporized fuels were more resistant to blowout. These trends are consistent with those observed by Burger et al. [96] and Corporan et al. [103]. Further insight into the physics associated with an evaporation limited blowout process can be gained from recent simulations [117, 158]. They show that when enough fuel droplets fail to evaporate, much of the fuel remains in liquid form and there is insufficient gaseous fuel to sustain combustion. The superior correlations between $\%\phi$ and the higher distillation temperatures suggest that a majority of the liquid volume must vaporize for combustion to be sustained.

Section 4.3 will detail the significant correlation of LBO to the derived cetane number. However, it is important to note here that chemical property effects may compete with physical property effects at some conditions. It is suspected that the high DCN of n-dodecane is responsible for its slight deviation from the T_{50} and T_{90} correlations that are seen with the remaining fuels. In other words, while physical properties are largely controlling at this T=300 K temperature, there are some kinetic effects which become evident with fuels that have extremely fast oxidation rates.

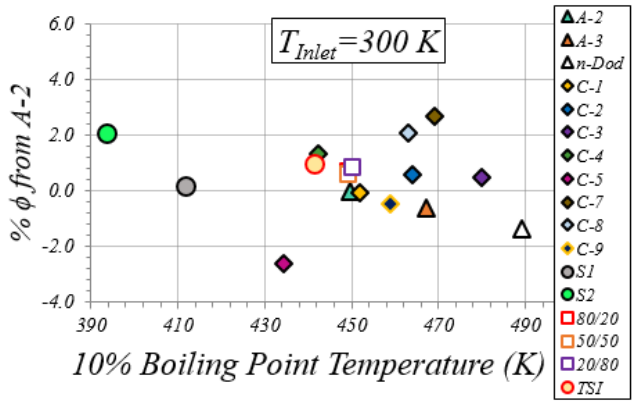

Figure 4.2: Dependence of the percent difference in blowout equivalence ratio from A-2 upon T_{10}. The data is compared at a bulkhead temperature of 500 K.

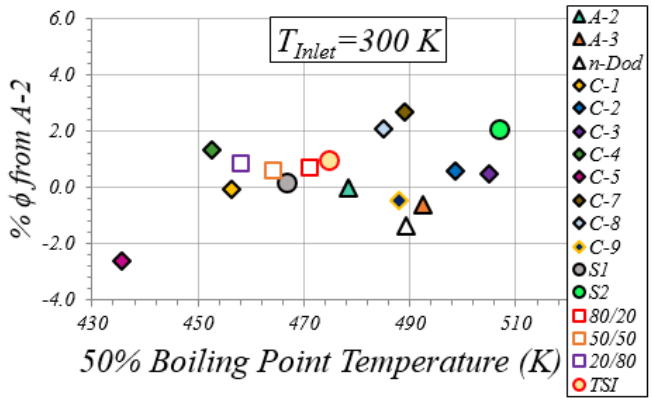

Figure 4.3: Dependence of the percent difference in blowout equivalence ratio from A-2 upon T_{50}. The data is compared at a bulkhead temperature of 500 K.

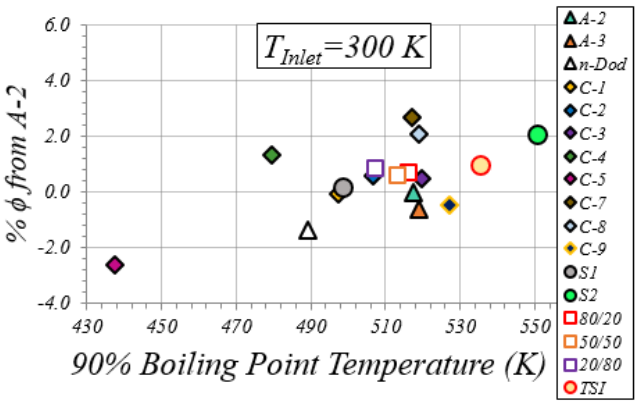

Figure 4.4: Dependence of the percent difference in blowout equivalence ratio from A-2 upon T_{90}. The data is compared at a bulkhead temperature of 500 K.

Fuel vaporization effects were much less apparent in the 450 K and 550 K data. The blowout equivalence ratio was essentially uncorrelated with T_{50} and T_{90} at these higher air inlet temperatures. Table 4-1 shows that there was perhaps some relationship between $\%\phi$ and T_{10} at 450 K and 550 K. However, the absence of a convincing physical explanation for these observed negative correlations suggests that this is caused by interrelated fuel properties, rather than representing limiting blowout physics. It will be shown later in Section 4.5 that these negative correlations with T_{10} are likely related to preferential vaporization.

Results from the blended fuels were of particular interest because they demonstrate whether a small quantity of one species can significantly influence blowout. Figure 4.5 shows the composite blowout equivalence ratio values for A-2/C-1 blends at both 300 K, 450 K, and 550 K. Within experimental uncertainty, each of the fuels essentially blew out at the same equivalence ratio at 300 K. However, at 450 K there was a clear linear trend between the percentage of A-2 in the fuel and the equivalence ratio at blowout. A potential explanation for these results is that physical properties are rate limiting at low air inlet temperatures, but at 450 K chemical property differences become manifest. Since the A-2/C-1 blends have essentially the same physical properties, they blew out at the same 300 K equivalence ratio. However, when chemical kinetic rates are the rate limiting factor, a linear average between the constituents of a mixture is sufficient to predict their blended lean blowout behavior. The 550 K results show that there are additional physics associated with fuel blending that are not present at the other air inlet temperatures. A nonlinear blending trend is observed, as demonstrated by the fact that the fuels with 20% and 50% A-2 compositions blew out at higher equivalence ratios than either complete C-1 or A-2.

Although this is an interesting discovery, the cause of this nonlinear blending relationship is unknown. It may be related to the thermoacoustic instability that is only present at 550 K, as discussed in Section 5.3. It is clear that predicting fuel blending effects on lean blowout limits is a complex problem, as blending can have no effect, a linear effect, or a nonlinear effect, depending on the air inlet temperature. It should also be noted that any plots including blended fuels should be interpreted with caution, as the linear 450 K relationship will show a correlation with any fuel property regardless of whether there is a physical basis for causality. In other words, five of the fuels are linearly related blends which may give the illusion of a correlation with a certain fuel property that would not hold if a different set of fuels were considered. Furthermore, interpreting results from the 550 K fuel blends is challenging because there are uncontrolled blending physics that are not manifest at the other temperatures. Therefore, blended fuels are not included in plots for the 450 K and 550 K data.

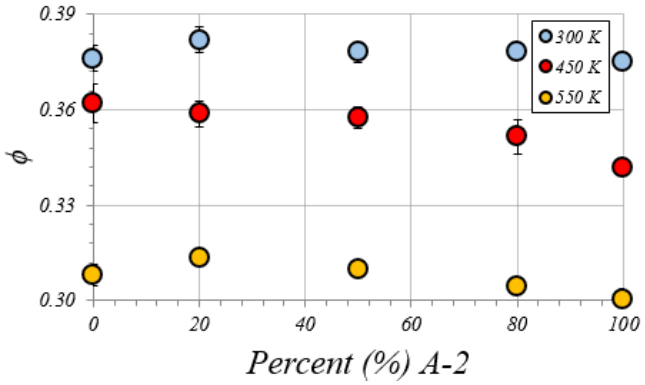

Figure 4.5: Average equivalence ratio at blowout versus percentage of A-2 fuel composition for A-2/C-1 blends. Blue symbols represent 300 K data, red symbols represent 450 K data, and yellow symbols represent 550 K data. Error bars represent the RMS of daily 95% confidence intervals. See Figure B. 1 for more details on uncertainties of the blended fuels.

4.3 Chemical Composition and Kinetic Property Correlations

Flame stability is often limited by chemical kinetics at limit combustion conditions. Chemical composition and kinetic properties govern a variety of physical processes that all influence the blowout phenomenon, such as autoignition delays, extinction stretch rates, species diffusion speeds, chemical heat release, and flame propagation speeds. Correlations between the blowout boundaries of the various fuels and their respective chemical properties are examined in this section. For space reasons, plots for all of the studied correlations will not be shown, but a few synthesis comments will be made.

First, a majority of the fuels showed correlations with the percentages of certain chemical compounds, such as aromatics or iso-paraffins. For example, Figure 4.6 shows a plot of $\%\phi$ versus the percentage of aromatics in a given fuel. However, these aromatic composition correlations do not hold when S1, S2, C-7, C-9, and n-dodecane were included. This suggests that a correlation between aromatics and another fuel property more closely related to blowout limits is driving the trend observed with some of the fuels.

The radical index [159], which has been shown to be proportional to the extinction stretch rate, was also examined. It ranks the chemical kinetic rate at which a fuel's radical pool is populated in a diffusion flame configuration. This radical production rate plays a central role in the flame heat release rate. Considering that the derived cetane number also reflects the oxidation rate of a fuel, it is expected that the radical index and DCN are inter-correlated. As shown in Table 4-1, there is some correlation between blowout and the radical index. However, other fuel properties, such as the derived cetane number, correlate better with $\%\phi$. Both the fuel molecular weight and the H/C ratio were uncorrelated with

blowout results. The derived cetane number had the highest correlation with $\%\phi$ across a range of fuels at the higher air inlet temperatures of 450 K and 550 K. For this reason, the rest of this section further analyzes DCN correlations.

It was shown in the previous section that at 300 K, blowout limits can be correlated with fuel vaporization properties, with the caveat that kinetic effects are also present for high DCN fuels. Figure 4.7 shows the 300 K blowout results plotted as a function of the derived cetane number. As expected, there was no correlation at this air temperature. Similar results were seen in the Burger et al. [96] data. However, both studies agree that while a majority of the fuels were uncorrelated with the derived cetane number at below flash point air inlet temperatures, the highest DCN fuels were still among the most difficult fuels to blowout.

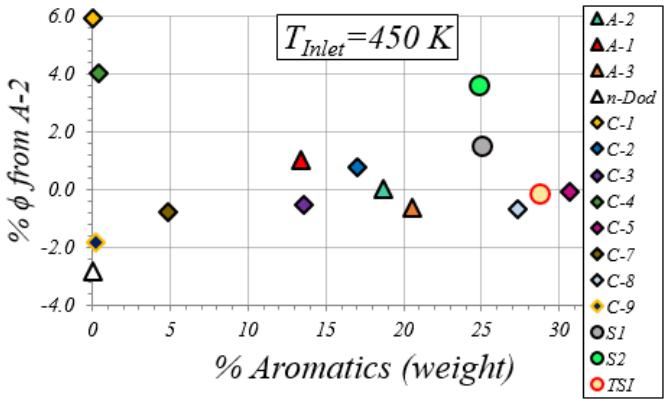

Figure 4.6: Dependence of the percent difference in blowout equivalence ratio from A-2 upon the percentage of aromatics in each fuel. The data is compared at a bulkhead temperature of 550 K.

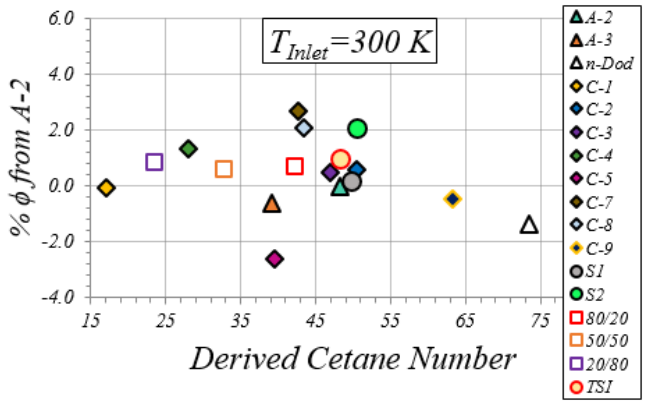

Figure 4.7: Dependence of the percent difference in blowout equivalence ratio from A-2 upon the derived cetane number. The data is compared at a bulkhead temperature of 500 K.

DCN correlations become stronger as the air inlet temperature is increased. Figure 4.8 and Figure 4.9 show the relationship between $\%\phi$ and the DCN at air inlet temperatures of 450 K and 550 K, respectively. Consistent with other studies [19, 104, 105], this was the strongest correlation with any of the fuel properties. Caution should be exercised, however, in relating the derived cetane number only to autoignition times, as studies have shown that it is also correlated with other fuel properties. In particular, fuel physical properties can influence the measurement, and they become especially impactful for high DCN fuels [94]. Furthermore, it can be seen that a few of the fuels, namely S1 and S2, didn't follow the same trend. These fuels have unique preferential vaporization characteristics [94], which is a phenomenon that occurs when the initially vaporized constituents of a multi-component fuel impact the global combustion characteristics pertinent to LBO. This perspective considers the local DCN of the constituents that vaporize at a particular temperature along the distillation curve. The most easily vaporized constituents for fuel S2 have a DCN of approximately 19, and it is the species which vaporize last that raise its DCN to the average value [94]. These unreactive, easily

vaporized constituents are likely responsible for the behavior of S1 and S2 seen in Figure 4.8 and Figure 4.9.

A natural next question is whether the autoignition time is fundamentally the relevant quantity influencing blowout, or if it is simply a surrogate for another potentially correlated kinetic quantity, such as the extinction stretch rate or laminar flame speed. Some clarity into this question comes from Burger's work [19], which showed a much stronger correlation between blowout proportionality constants and the derived cetane number (correlation coefficient=-0.71) than laminar flame speed (correlation coefficient=-0.08). Whether blowout is extinction or autoignition limited in liquid fueled systems is still open for debate. The nearly identical performance of fuel C-7 in the previous two figures, relative to other fuels with comparable derived cetane numbers, suggests that the large percentage of cycloalkanes in this fuel have little effect on its blowout performance. The merely mild correlation between the radical index and blowout equivalence ratios supports the conclusion that a fuel's autoignition propensity cannot be disregarded when conceptualizing high air inlet temperature blowout, where the local flame extinction and ignition start to appear right before lean blowout.

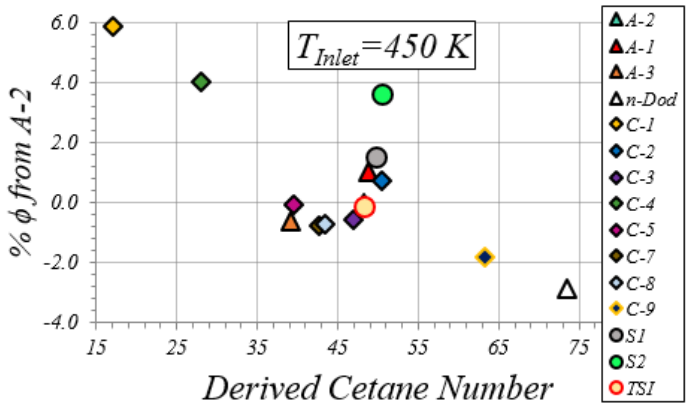

Figure 4.8: Dependence of the percent difference in blowout equivalence ratio from A-2 upon the derived cetane number. The data is compared at a bulkhead temperature of 550 K.

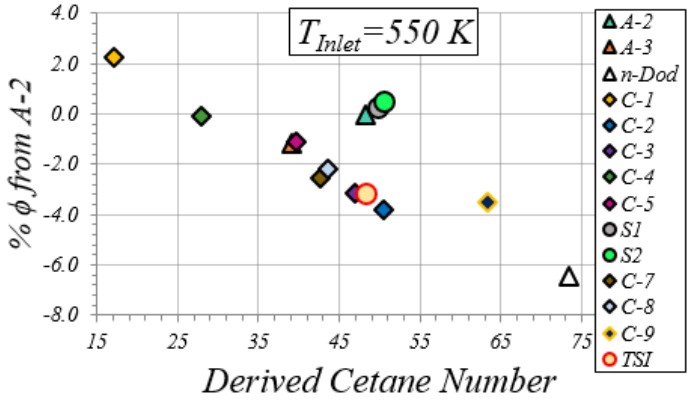

Figure 4.9: Dependence of the percent difference in blowout equivalence ratio from A-2 upon the derived cetane number. The data is compared at a bulkhead temperature of 640 K.

4.4 Preferential Vaporization

Jet fuels are comprised of many different chemical species which each have their own vaporization and kinetic characteristics. Preferential vaporization is a phenomenon that occurs when the more volatile fuel constituents are evaporated first and the less volatile constituents disproportionately remain in the liquid phase. In other words, the chemical or

reactive character of the initially vaporized fuel fraction is different than that of the original liquid fuel mixture. This can cause the effective kinetics of a jet fuel to be much different than those that would be predicted based on the entire fuel composition. As the characteristic evaporation time scale is expected to be larger than the characteristic flow time scale in this combustor (i.e., 1-10 ms vs ~0.3 ms, see Table 2-1), there is reason to believe that liquid droplets may reach the flame before completely vaporizing. The key consideration in this discussion is how the chemical reactivity of the initially vaporized constituents affects flame stability. For example, it was previously shown that the DCN is the dominant fuel property for determining lean blowout limits at high air inlet temperatures. The fact that the droplet heat-up time is expected to be comparable to the characteristic flow time (~0.3 ms) [127] raises the question of whether it is the DCN of the initially vaporized constituents that is actually responsible for governing the LBO phenomenon. Figure 4.10 illustrates these points by showing how the DCN for fuels A-2, A-3, S1, and S2 changes with the percentage of the liquid volume that has vaporized. Consider the comparison between fuels A-2 and A-3 in plot **(a)** in Figure 4.10. Although the DCN based on the entire fuel composition varies by about 10 between these fuels, the DCNs of their initially vaporized constituents are quite similar. Plot **(b)** in Figure 4.10 shows that fuel S2 has the greatest potential for preferential vaporization effects, as the DCN of the initially vaporized constituents is only 19.1, compared with the value of 50.6 based on the entire fuel composition. This potentially explains why S2 failed to follow the DCN correlation observed in Figure 4.8.

a)

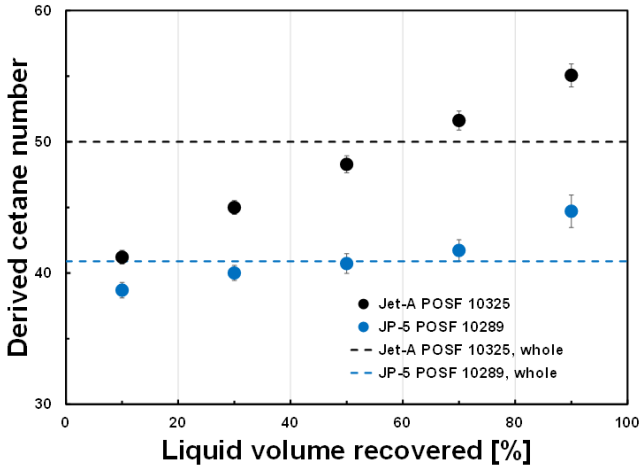

b)

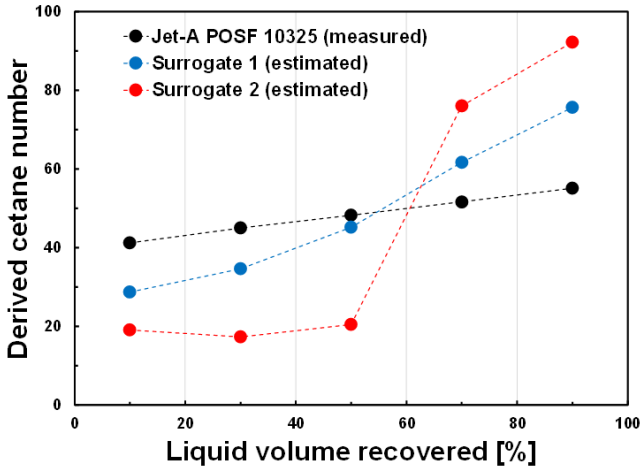

Figure 4.10: DCN values across the distillation range for fuels A-2 and A-3 (a), and A-2, S1, and S2 (b).

This investigation into the role of preferential vaporization on lean blowout boundaries was done in close collaboration with Professor Sang Hee Won at the University of South Carolina (USC). As was introduced in Section 2.5, the DCN of the initial 20% of liquid volume to vaporize was measured for six of the fuels at USC and the LBO data was taken at Georgia Tech. Figure 4.11 shows $\%\phi$ at 300 K plotted against the 20% DCN. There is a correlation coefficient of -0.74 between these two parameters and the 20% DCN seems to have a greater effect on $\%\phi$ at 300 K than the entire composition DCN, shown in Figure

4.7. However, the fact that fuels C-1 and S2 have very similar 20% DCNs and still blew out at different equivalence ratios belies the argument that preferential vaporization significantly influences LBO at 300 K. A stronger correlation coefficient of 0.83 exists between T_{90} and $\%\phi$ at 300 K for these same six fuels. It may be that preferential vaporization is less important at 300 K because very little vaporization of the liquid fuel droplets occurs before they reach the flame. Although the role of preferential vaporization on 300 K LBO behavior is unclear, there is strong evidence that it matters at the higher air inlet temperatures. Figure 4.12 and Figure 4.13 show $\%\phi$ plotted against the 20% DCN at 450 K and 550 K, respectively. These correlations are extremely strong, with a -0.91 correlation coefficient at 450 K and a -0.95 correlation coefficient at 550 K.

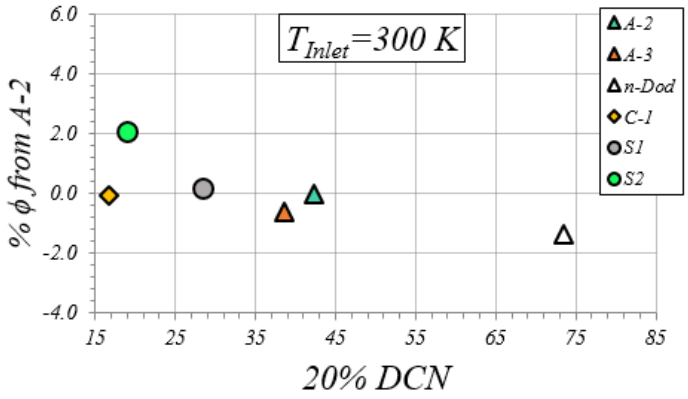

Figure 4.11: Dependence of $\%\phi$ from A-2 upon the 20% DCN. The data is compared at a bulkhead temperature of 500 K and has a correlation coefficient of -0.74.

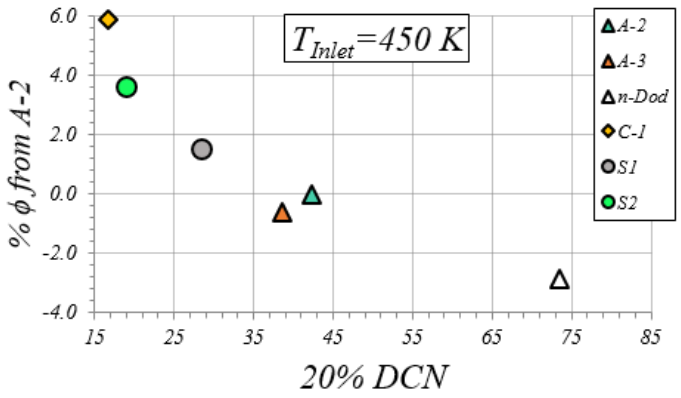

Figure 4.12: Dependence of *%ϕ* from A-2 upon the 20% DCN. The data is compared at a bulkhead temperature of 550 K and has a correlation coefficient of -0.91.

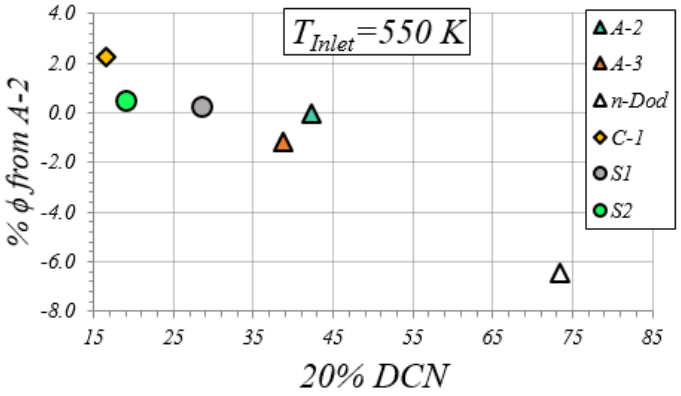

Figure 4.13: Dependence of *%ϕ* from A-2 upon the 20% DCN. The data is compared at a bulkhead temperature of 640 K and has a correlation coefficient of -0.95.

The importance of preferential vaporization on LBO boundaries was further demonstrated by testing two fuels with identical DCNs but very different preferential vaporization characteristics. These fuels were designed by Professor Sang Hee Won at the University of South Carolina (USC) and were tested at Georgia Tech. The first fuel was comprised of 91.8% C-1 and 8.2% n-heptane by volume. N-heptane has a much lower boiling point temperature (i.e., 371.6 K) than C-1 (i.e., 447.3-536.5 K). It is also much more reactive, with a DCN of 53.8 compared to the C-1 value of 17.1. Therefore, if preferential vaporization does influence lean blowout boundaries, the reactive n-heptane

should vaporize first from this fuel and improve the LBO performance. The other fuel was made of 93.6% C-1 and 6.4% n-dodecane. The chemical properties of this fuel remain relatively constant across the distillation curve, and therefore preferential vaporization effects were not expected.

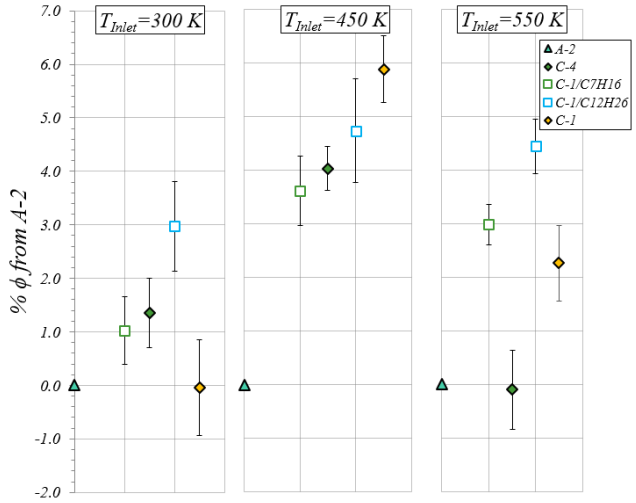

Figure 4.14: *%ϕ* from A-2 at all three air inlet temperatures. The C-1/C_7H_{16} and C-1/$C_{12}H_{26}$ fuels are designed to accentuate preferential vaporization effects.

Figure 4.14 shows a plot of the percent difference from A-2 for these two fuels, C-1, and also C-4, which has the same DCN value of 28 as the preferential vaporization fuels. Across each of the air inlet temperatures, the C-1/n-heptane fuel performed better than the C-1/n-dodecane fuel. At 300 K and 450 K, the C-1/n-heptane fuel also blew out at a lower equivalence ratio than C-4. However, both the C-1/n-heptane and C-1/n-dodecane fuels blew out at a much higher equivalence ratio than either fuel C-4 or C-1 at 550 K. The cause of these peculiar 550 K results is unknown but they are consistent with the discussion surrounding nonlinear 550 K blending in Section 4.2.

In summary, results from two fuels that were designed to accentuate preferential vaporization, along with strengthened LBO correlations using the 20% DCN, suggest that preferential vaporization does affect LBO boundaries. The evidence was strongest at 450 K, where the C-1/n-heptane fuel blew out at a lower equivalence ratio than other fuels with identical DCNs, and the 20% DCN resulted in a very strong correlation with $\%\phi$. The C-1/n-heptane fuel also blew out at the lowest equivalence ratio out of the 28 DCN fuels at 300 K. However, preferential vaporization effects at this temperature are confounded by the fact that two fuels with very similar 20% DCNs blew out at much different equivalence ratios. At 550 K, C-1/n-heptane outperformed C-1/n-dodecane and the 20% DCN led to an improved correlation with $\%\phi$. However, the fact that C-1/n-heptane and C-1/n-dodecane blew out at much higher equivalence ratios than C-4, a fuel with a matching DCN, suggests that there may be additional physics associated with 550 K fuel blending that are not being taken into account. It is also possible that the differences in the LBO performance between the C-1/n-heptane and C-1/n-dodecane fuels at 550 K is caused by something other than preferential vaporization, as preferential vaporization effects would not be expected if the liquid fuel completely vaporizes before reaching the flame.

4.5 Regression Analysis

As there wasn't a single fuel property that correlated perfectly with the data, it is believed that the combined influence of a variety of fuel properties are involved in determining the blowout equivalence ratio. Furthermore, as the fuel properties depend on the chemical structure of the fuel, they are intrinsically interrelated [95]. This creates problems when attempting to relate fuel properties with lean blowout causality, as certain fuel properties may be correlated with lean blowout boundaries that simply reflect inter-

correlations between variables and have no physical basis. Therefore, a variable selection technique was used to perform a multiple linear regression on the fuel screening data while also eliminating insignificant fuel properties from consideration.

The Hierarchical Non-negative Garrote method of Paynabar et al. [146] was applied to the fuel screening data in order to determine the relative contributions of each of the different variables on lean blowout. This is a two-step method that first identifies which groups of variables should be included in the regression and then selects the most important variables from those in the remaining groups. 15 fuel properties were used, and the data were divided into 5 groups of 3 fuel properties. These groups were chosen to include physically related sets of variables and are shown in Table 4-2. Group 1 contained the 3 boiling point temperatures, Group 2 was comprised of the physical properties related to atomization, Group 3 was based on the chemical composition and molecular weight, Group 4 involves the chemical energy of the fuel, and the properties most closely associated with chemical kinetics constitute Group 5. The A-2/C-1 blended fuels were included in this regression analysis in order to increase the sample size. Step 1 of the Hierarchical Non-negative Garrote method selected the significant groups of variables. Step 2 accounted for correlations between these variables and calculated the appropriate regression coefficients. Leave-one-out cross-validation was used to select the appropriate tuning parameters for this model.

Table 4-2: Variable groups that were used for the Hierarchical Non-negative Garrote Regression.

Group 1	Group 2	Group 3	Group 4	Group 5
T_{10}	ν (mm^2/s) 313 (K)	MW	H/C Ratio	% n-Parrafins
T_{50}	σ (mN/m) 300 K	% Aromatics	LHV (MJ/kg)	DCN
T_{90}	ρ (kg/m^3) 288 K	% iso-Paraffins	Smoke Point (mm)	Radical Index

Figure 4.15 shows the regression coefficients that were determined by the Hierarchical Non-negative Garrote method. It can be seen that T_{50} was the dominant fuel property governing LBO at 300 K and that the DCN had a secondary effect. This significant finding was postulated in Section 4.2 but was not obvious from the single variable correlations. The 450 K and 550 K regression results show that blowout is predominantly limited by the DCN and it is also influenced to a lesser extent by T_{10}.

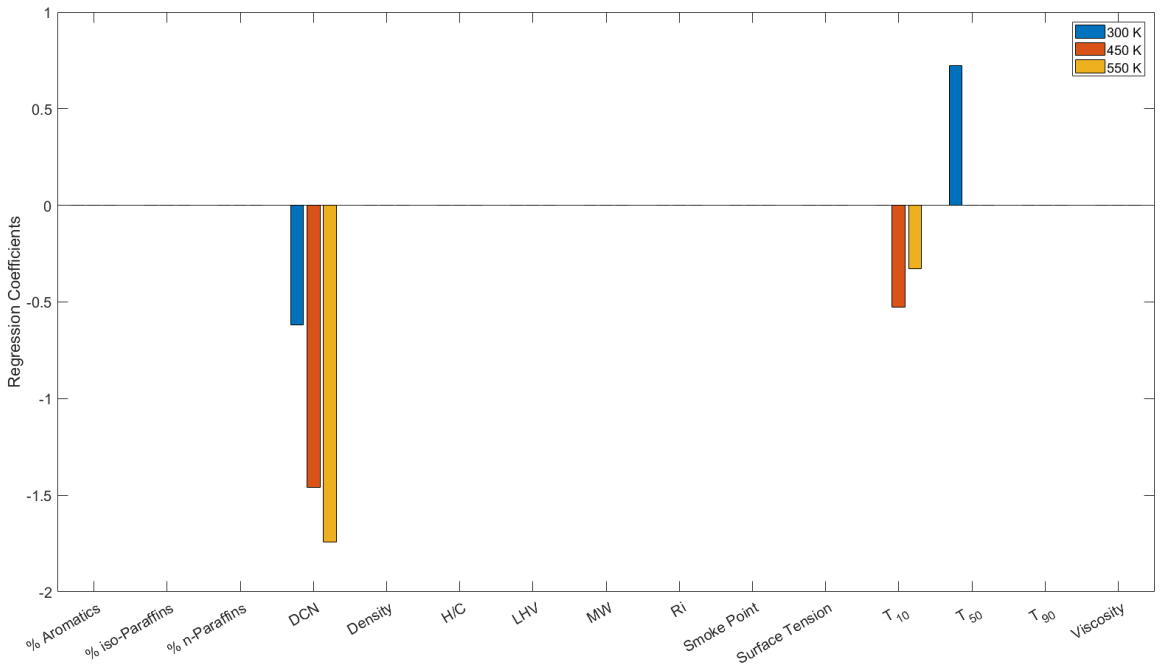

Figure 4.15: Regression coefficients determined by the Hierarchical Non-negative Garrote method.

The previous section presented evidence that preferential vaporization can cause a small fraction of initially vaporized constituents to dominate the chemical reactivity of near-blowoff flames. This raises the question of whether the T_{10} effect at 450 K and 550 K, shown in Figure 4.15, is a consequence of the regression model capturing trends in the data caused by preferential vaporization. The fuels with the lowest T_{10} values (i.e., S1 and S2) often had the greatest preferential vaporization potential and, as was introduced in Section 4.2, a reasonable physical explanation for the high air temperature data to show a negative correlation with T_{10} is lacking. Therefore, the analysis was repeated using the 20% DCN for the six fuels for which these measurements were available and the DCN values based on the entire fuel composition were used for the remaining fuels. The regression results are not expected to change significantly when only using the 20% DCN where it is available rather than for all of the fuels. This is because the fuels with the greatest preferential vaporization potential are included in the group of 6 for which the 20% DCN measurements were made. Figure 4.16 shows the updated regression results with the preferential vaporization correction. The fuel boiling point temperatures are still predicted to dominate LBO at 300 K, with the largest contribution from T_{90} and a smaller dependence on T_{50}. Again, chemical properties have a secondary effect at 300 K, as represented by the 20/100% DCN and %n-paraffins. Another interpretation of these results is that the combined influence of the fuel boiling point temperature and kinetics properties on lean blowout is such that there is not a single fuel property that is completely rate limiting at 300 K. For all intents and purposes, the 450 K lean blowout boundaries were solely dependent on the 20/100% DCN. This demonstrates that the previously shown influence of T_{10} at 450 K was simply caused by preferential vaporization. The 20/100% DCN is also

the dominant fuel property at 550 K. However, including the 20% DCN where available caused a negatively correlating dependence on T_{50} to appear. As will be discussed in Section 5.3, additional physics associated with thermoacoustic instabilities were present at 550 K that did not exist at the other air inlet temperatures. Consistent with the 550 K regression results shown here in Figure 4.16, the dynamic pressure RMS was negatively correlated with T_{50} (see Figure 5.16). Therefore, these 550 K regression coefficients are likely indicating a secondary influence of acoustic oscillations on lean blowout boundaries at 550 K.

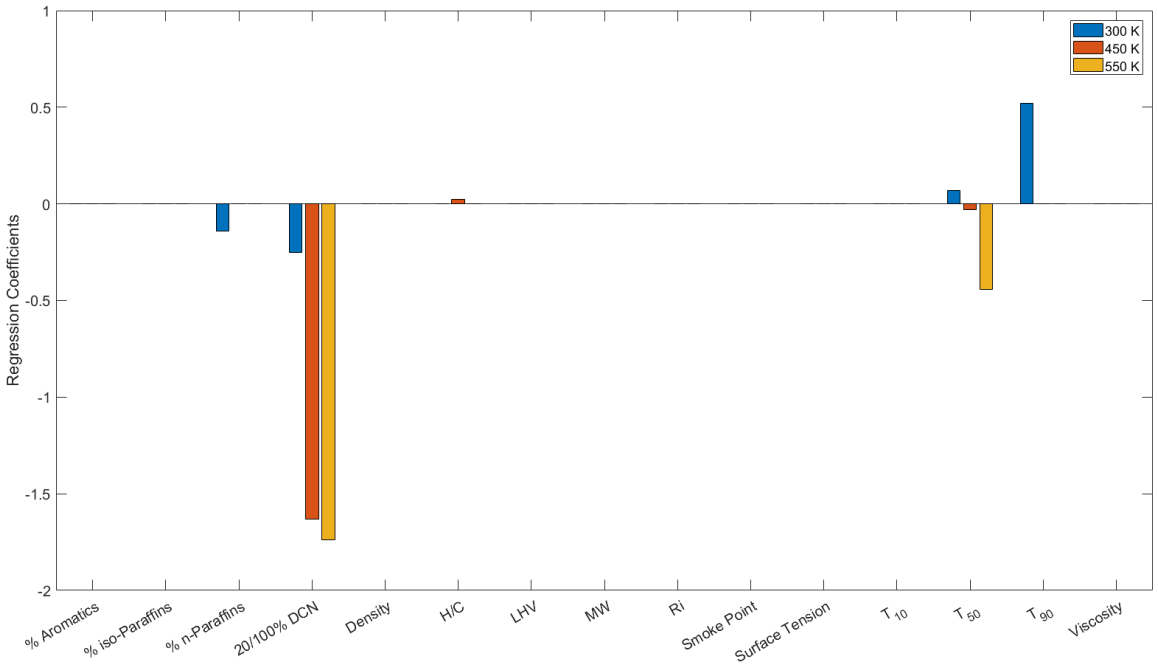

Figure 4.16: Regression coefficients determined by the Hierarchical Non-negative Garrote method when the 20% DCN is used for the fuels where it is available.

4.6 Fuel Screening Summary

This section has shown that there is not a single fuel property that governs blowout, but rather, that blowout is an operating condition dependent phenomenon. This was evident as blowout boundaries were observed to change when the experiment was conducted at different air inlet temperatures. At air inlet temperatures lower than the fuel flash point, blowout appears to be predominantly limited by fuel vaporization quality. Vaporizing the liquid fuel is especially challenging at such low air inlet temperatures. The flame will extinguish in the event that a flammable mixture fails to form, rendering fuel chemical/kinetic processes unimportant. What follows is that easily vaporized fuels are the most blowout resistant. When the experiment was repeated at air inlet temperatures of 450 K and 550 K, fuel chemical properties represented by the DCN showed the strongest relationship with blowout boundaries. Fuels that had a high derived cetane number blew out at lower equivalence ratios.

Another contribution of this work was separating interrelated fuel properties (e.g. vaporization temperatures and derived cetane numbers), which is an issue that has long plagued alternative fuels studies. This selection of fuels was carefully chosen to disrupt correlations between physical and chemical fuel properties, and also correlations between individual kinetics properties that describe different physics. For example, multiple kinetics properties correlate well with the DCN, including the laminar flame speed, autoignition delay time, and the extinction stretch rate. This motivated the use of two fuels which had the same DCN but very different stretch resistance characteristics. For the high air temperature conditions where chemistry was observed to dominate, it was found that these fuels had nearly identical blowout performance. This result, along with the absence

of an observed correlation with the radical index, suggests that for high air temperatures blowout might be limited by the autoignition propensity of a fuel rather than its extinction stretch rate. Furthermore, results from a multiple linear regression analysis showed that the DCN may have a secondary effect on LBO at 300 K, and acoustic oscillations may have a secondary influence on LBO at 550 K.

Preferential vaporization effects were found to be at least partially responsible for the failure of some fuels to fit the previously described correlations. There is the strongest support for preferential vaporization at 450 K. It is also believed to be present at 550 K, however, the data appears to include some uncontrolled physics associated with fuel blending that may have an influence on the results. At 300 K there is both supporting and negating evidence for preferential vaporization effects. This is likely due to the role that fuel physical properties are known to have on LBO boundaries at this air inlet temperature.

The effect of the flow field on the lean blowout phenomenon should not be overlooked. There is always a possibility that experimentally observed blowout boundaries are geometry specific due to differences in turbulence levels and flow structures between combustors. For this reason, flow field effects will be considered in greater detail in Chapter 5. However, the consistency between these results and those of other researchers who tested a smaller subset of these fuels suggests that fuel property effects are generally not overwhelmed by flow field differences.

CHAPTER 5. CHARACTERIZATION OF THE FLAME, FLOW FIELD, AND ACOUSTICS

Understanding the flame, flow features, and background acoustics of this combustor was necessary to isolate the cause of blowout. A key initial question was the degree to which fuel properties influence the bulk flow field and acoustics. Planar measurements, including OH-PLIF and stereo-PIV, along with dynamic pressure measurements were used to gain insight into these details.

5.1 Flame Characterization

Figure 5.1 shows an instantaneous camcorder image of the flame at each of the air inlet temperatures. The baseline fuel A-2 is shown in this figure and it can be seen that a lifted flame existed near blowoff at each of the air inlet temperatures. The flame also become progressively less sooty as the air inlet temperature was increased.

Figure 5.1: Instantaneous camcorder images of the A-2 flame at the 300 K (left), 450 K (center), and 550 K (right) air inlet temperatures.

Simultaneous OH-PLIF and PIV measurements were used to understand further details of the flame structure. Two instantaneous OH-PLIF images with overlaid PIV vectors are shown in Figure 5.2. Fuel A-2 is burning with a 450 K air inlet temperature and

a stable equivalence ratio in these images. Consistent with the observations of other researchers, Figure 5.2 illustrates a partially premixed flame that followed the fuel spray trajectory and a nonpremixed flame in the outer recirculation zone. It should be noted that fluorescence from the fuel spray and the OH radical is not clearly distinguished in these images. However, the fuel spray had a greater fluorescence emission intensity and therefore the bright red regions can be safely interpreted as fuel droplets. Large fuel droplets were observed to extend deep into the flame region, but it appears that most of the liquid fuel evaporated before reaching the flame. More fuel spray was generally observed in the bottom flame branch, as there was a slight asymmetry in the fuel injector. Interestingly, the outer recirculation zone flame was usually observed to be stronger in the upper flame branch.

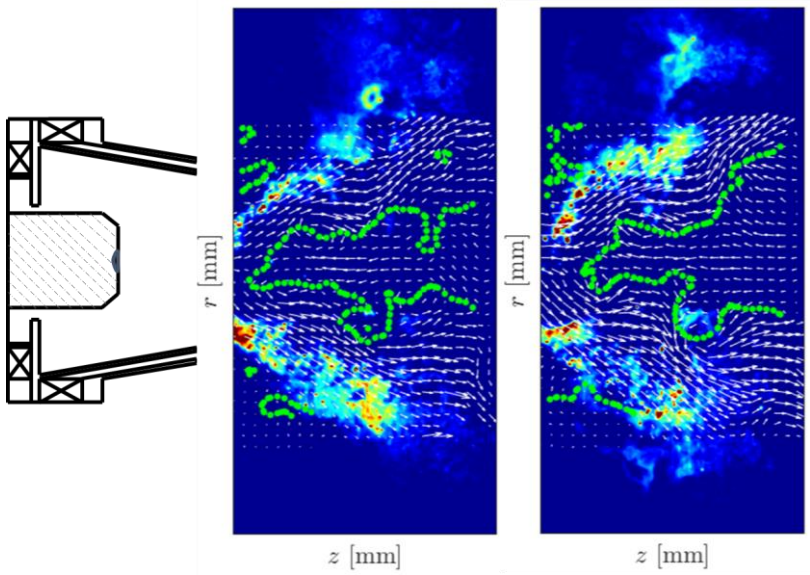

Figure 5.2: Instantaneous OH-PLIF images with overlaid PIV vectors. Fuel A-2 is burning at an air inlet temperature of 450 K and an equivalence ratio of 0.45. The dotted green line represents zero velocity stagnation contours.

One of the key contributions of these images was the insight that they provided into the flame stabilization mechanism. Figure 5.2 shows that the flame stabilized in the outer shear layer that separates the annular air jet from the outer recirculation zones. Burning was occasionally observed in the central recirculation zone, as evidenced by the image sequence shown in Figure 5.3. However, this was a rare occurrence.

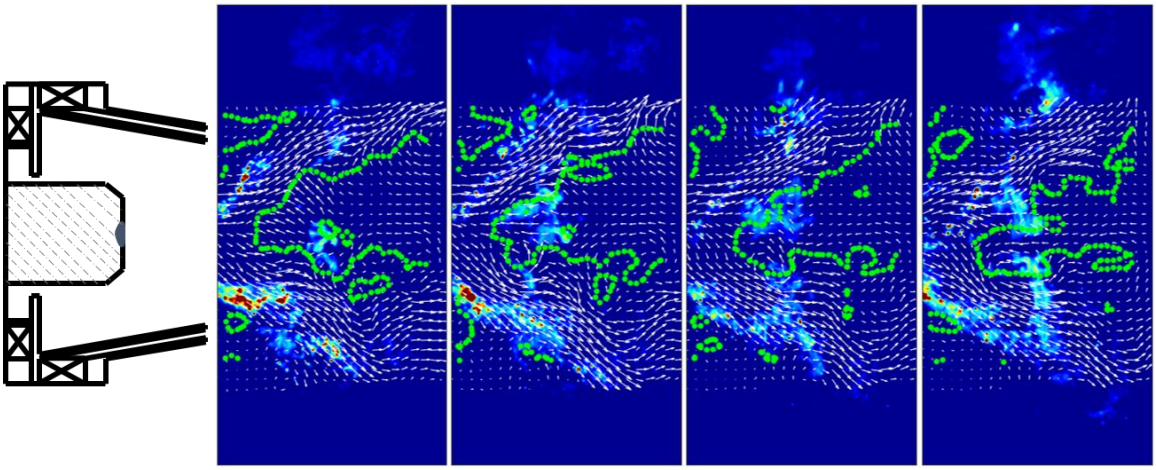

Figure 5.3: Four successive OH-PLIF images with overlaid PIV vectors. Fuel A-2 is burning at an air inlet temperature of 450 K and an equivalence ratio of 0.45. The dotted green line represents zero velocity stagnation contours. These images show evidence of flame burning in the central recirculation zone.

Details of the flame during a lean blowout transient were also studied using these same planar measurements. Instantaneous OH-PLIF images from this lean blowout case are shown Figure 5.4. The flame again stabilized in the outer shear layer for the blowout transient case. However, the partially premixed flame along the spray path was much weaker near blowoff, and very little burning happened in the outer recirculation zone. Furthermore, larger volumes of liquid fuel can be observed in these images compared with those from the stable burning case, which likely reflects delays in droplet vaporization

caused by decreased flame temperatures. In contrast with the stable burning case, it appears that a majority of the liquid fuel vaporizes after reaching the flame.

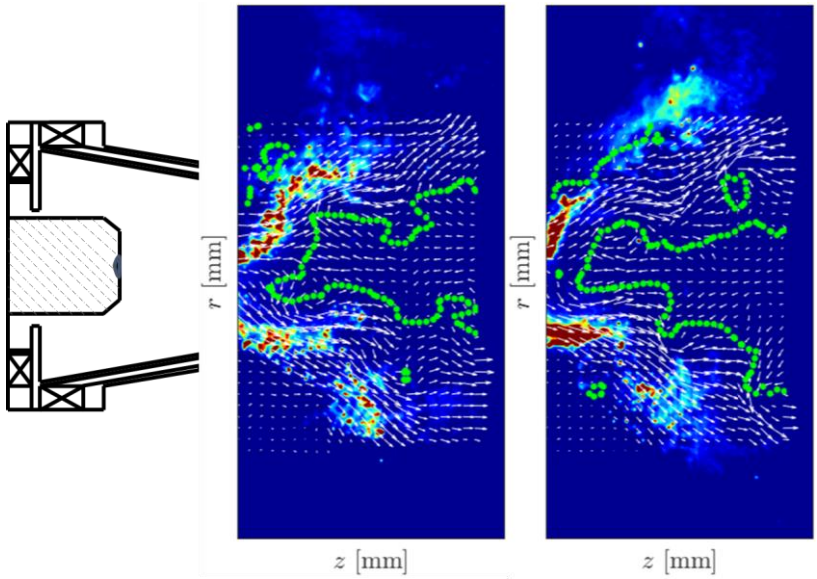

Figure 5.4: Instantaneous OH-PLIF images with overlaid PIV vectors. Fuel A-2 is burning at an air inlet temperature of 450 K during a blowout transient. The dotted green line represents zero velocity stagnation contours.

Blowout must be related to processes that decrease the temperature of the gases that surround the incoming reactants such that they can no longer be ignited. In premixed bluff-body stabilized flames, this happens when entrained reactants cool the temperature of the bluff-body recirculation zone below a critical level. Since measurements that represent entrained reactants were unavailable here, chemical reactions located in the central recirculation zone would be the best indicator that a similar mechanism causes spray flames to blow out. Figure 5.5 shows an image sequence shortly before complete blowout when a segment of the flame was transported into the central recirculation zone. Unlike premixed bluff-body stabilized flames, where reactions spread from the shear layers under stable operation to the recirculation zone as blowoff is approached, this flame segment was

quickly extinguished. This suggests that reactants do not constitute a large fraction of the central recirculation zone chemical composition and agrees well with the findings of Manosh Kumar et al. [77], who observed minimal CH_2O in the central recirculation zone of swirl-stabilized, premixed flames near blowoff. Furthermore, there was not a noticeable difference in the amount of burning in the central recirculation zone between the stable burning and transient blowout cases. It occurred infrequently in both instances.

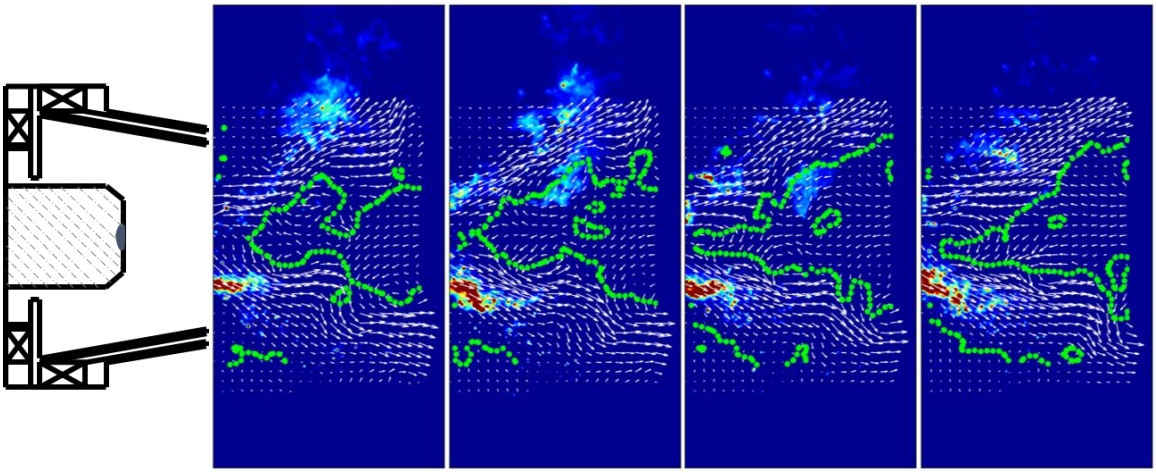

Figure 5.5: Four successive OH-PLIF images with overlaid PIV vectors. Fuel A-2 is burning at an air inlet temperature of 450 K shortly before the flame blew out. The dotted green line represents zero velocity stagnation contours. These images show that the flame quickly extinguished when it was transported into the central recirculation zone.

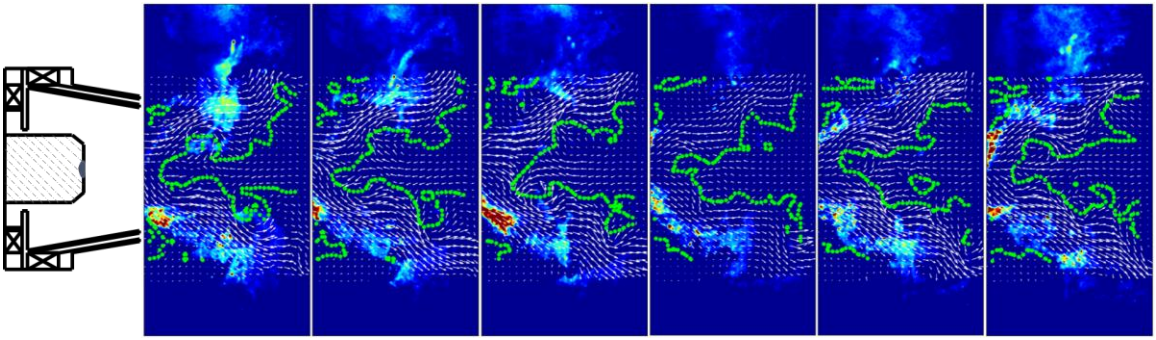

Figure 5.6: Six successive OH-PLIF images with overlaid PIV vectors. Fuel A-2 is burning at an air inlet temperature of 450 K and an equivalence ratio of 0.45. The dotted green line represents zero velocity stagnation contours. These images show evidence of local extinction and re-ignition.

It is clear from these data that LBO precursor events precede complete blowout of the flame. Even during stable operation these precursor events are prone to occur, as shown in Figure 5.6. In this image sequence the upper flame branch locally extinguishes before being re-ignited. However, these LBO precursors are more threatening to the stability of near-blowoff flames, which locally extinguish more easily and are less capable of re-igniting. Although there are many potential causes of these LBO precursors, two will be discussed in reference to the examples in Figure 5.7 and Figure 5.8, which are taken from the blowout transient case. Figure 5.7 shows an example where the flame is locally extinguished by a vortex in the outer shear layer. Since this flame stabilizes in the outer shear layer, it seems reasonable that it would be susceptible to extinction by vortices that are convected through this region. Figure 5.8 shows a separate case where the flame is extinguished by a vortex in the inner shear layer separating the annular air jet from the central recirculation zone. Previous work [160] has quantitatively shown that a helical vortex exists in this combustor and resides in the inner shear layer. It is present in most of

the available images, as evidenced by staggered vortices that convect downstream. Although this flame stabilizes in the outer shear layer, this helical vortex appears to grab part of the flame, as demonstrated by the flame being rolled up to resemble the hook-like feature in Figure 5.8. The portion of the flame that is subsequently extinguished by this vortex may have been critical for stabilizing the flame, as the entire flame branch locally extinguishes immediately afterwards. It should be noted that the absence of OH fluorescence is not necessarily evidence of local extinction. This can also be caused by burnout of the fuel, as super-equilibrium OH under near stoichiometric conditions will decay quickly when it is mixed with cold air. Therefore, a quantitative vortex tracking and flame stretch analysis would be required to rigorously characterize the local extinction processes in these planar measurements.

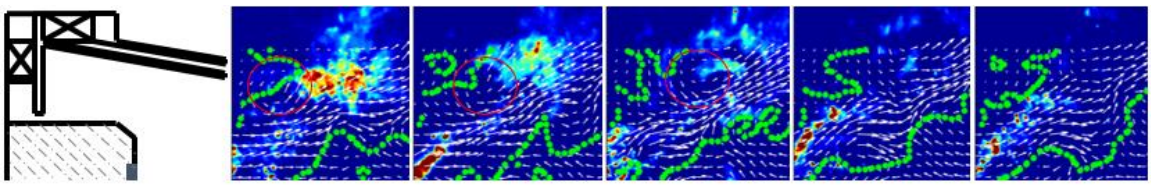

Figure 5.7: Detailed view of five successive OH-PLIF images with overlaid PIV vectors. Fuel A-2 is burning at an air inlet temperature of 450 K during a blowout transient. The red circles surround a vortex in the outer shear layer that is believed to cause local extinction.

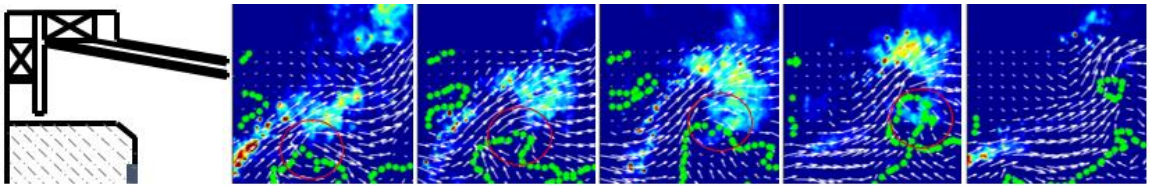

Figure 5.8: Detailed view of five successive OH-PLIF images with overlaid PIV vectors. Fuel A-2 is burning at an air inlet temperature of 450 K during a blowout transient. The red circles surround a helical vortex in the inner shear layer that is believed to cause local extinction.

5.2 Flow Field Characterization

The velocity field for the reacting flow in this combustor is shown in Figure 5.9. This data was taken using stereoscopic particle image velocimetry (sPIV) at an air inlet temperature of 450 K and an equivalence ratio of 0.45; details on the measurements and additional detailed measurements are provided in Chterev et al. [145]. Black vectors represent positive axial velocity and red vectors represent negative axial velocity. The azimuthal, or out of plane, velocity component is represented by the background color. Contour lines have been added to these plots to aid in visualizing topological flow features. The white lines represent the location of zero axial flow velocity and the black lines represent the jet core. As is expected for a swirling flow field, the flow involves both central and outer recirculation zones that are separated by a high velocity fluid jet.

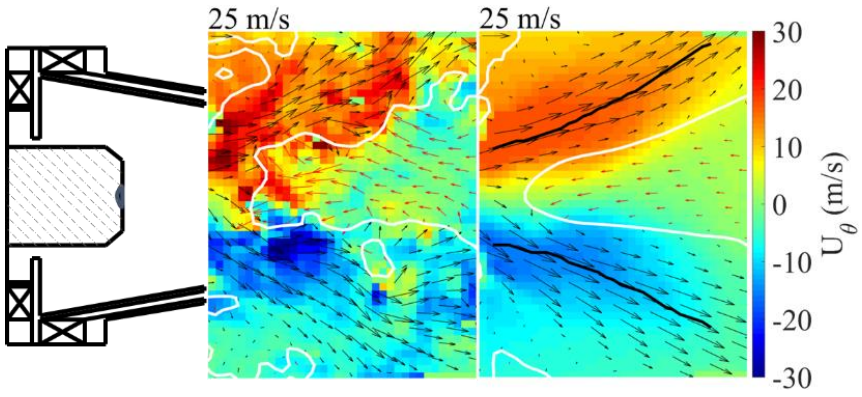

Figure 5.9: Instantaneous (left) and time-averaged (right) reacting velocity field for fuel A-2 at 345 kPa, 450 K, and a global equivalence ratio of 0.45. Color represents out of plane velocity. White lines denote locations with zero axial velocity and black lines represent the jet core. The arrow in the top left indicates a 25 m/s velocity vector for reference.

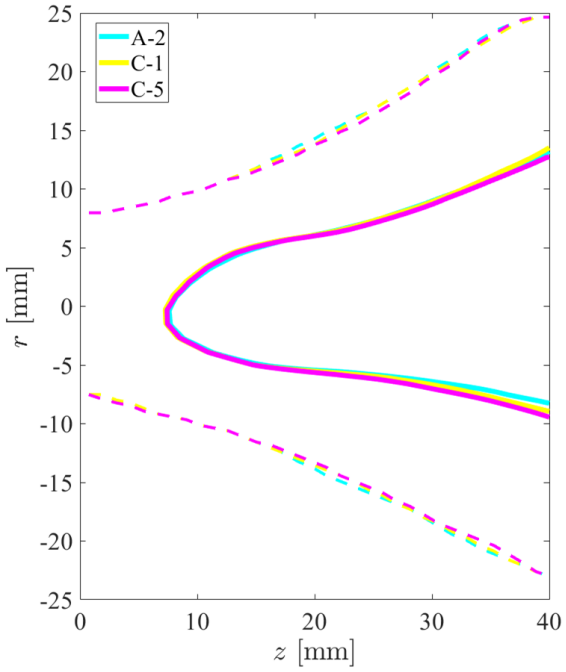

Figure 5.10: Central recirculation zone boundaries (solid lines) and jet cores (dashed lines) for the time averaged flow fields from fuels A-2, C-1, and C-5. (450 K air temperature, 345 kPa pressure, and ϕ=0.45)

Contour lines representing the average central recirculation zone boundary and jet core are compared in Figure 5.10 for three fuels with significantly different fuel properties. It can be seen that the time averaged flow features are practically identical amongst the fuels. Therefore, it can be confidently concluded that differences in blowout boundaries between fuels result from changes in the combustion process rather than the bulk flow field. The reason for this flow field similarity is likely due to the similar heating values of all the fuels, implying similar flame temperatures. If there were significant differences in flame temperature or flame stabilization locations across the fuels, it could be expected that the flow fields would be more different for reasons of gas expansion and flow inhomogeneity [75].

Large scale changes in the bulk flow features are known to immediately precede the complete blowout of premixed flames. These “stage 2” blowoff processes include the transition to a sinuous wake dominated by von Karman vortex shedding for bluff-body stabilized flames and changes in vortex breakdown modes for swirl-stabilized flames. Contour lines representing topological flow features were used to obtain information about the “stage 2” flow field of the studied spray flames. Figure 5.11 plots the average central recirculation zone contour lines on the left and the average jet core contour lines on the right for the non-reacting, stable burning A-2, and blowout transient cases. The nonlinear averaging techniques of Chterev et al. [161] were used to estimate the uncertainties in these average contour lines. The uncertainty in the central recirculation zone boundary is represented by 10% and 90% reverse flow probability contour lines. Following the approach of Ek et al. [160], the uncertainty in the jet core is denoted by contour lines representing 10% and 90% probability that the axial velocity is greater than two thirds of the average jet core velocity. It can be seen that the average non-reacting central recirculation zone is wider and begins further upstream than the reacting cases. Surprisingly, the average central recirculation zone of the blowout transient case does not approach the non-reacting case. Instead, it is almost identical with that of the stable burning flame. Two hypotheses provide explanations for the similarity between the stable burning and blowout transient average flow fields. First, this may be an artifact of the rapid fuel reduction rate that induced blowout for the transient case. The “stage 2” flow field alterations are caused by changes in heat release as the flame approaches blowout. It is possible that the fuel flow rate was ramped down so quickly that the temperature of the surrounding fluid didn’t change much between stable burning and LBO. Had an authentic

blowout process been recorded, such as those captured by the CH* chemiluminescence videos, greater differences may have been observed between these two average flow fields. Second, perhaps these flames don't transition to "stage 2" until just before blowout. A careful examination of the OH-PLIF and PIV images for the blowout transient case indicates that large scale flame flapping does occur when blowout is imminent. However, the results in Figure 5.11 suggest that these instances constitute a small fraction of the 2820 available flow field images for the blowout transient case, and the average flow field is dominated by features that mirror stable burning. It may be that the flame cannot survive long after "stage 2" begins and will blow out almost immediately afterwards.

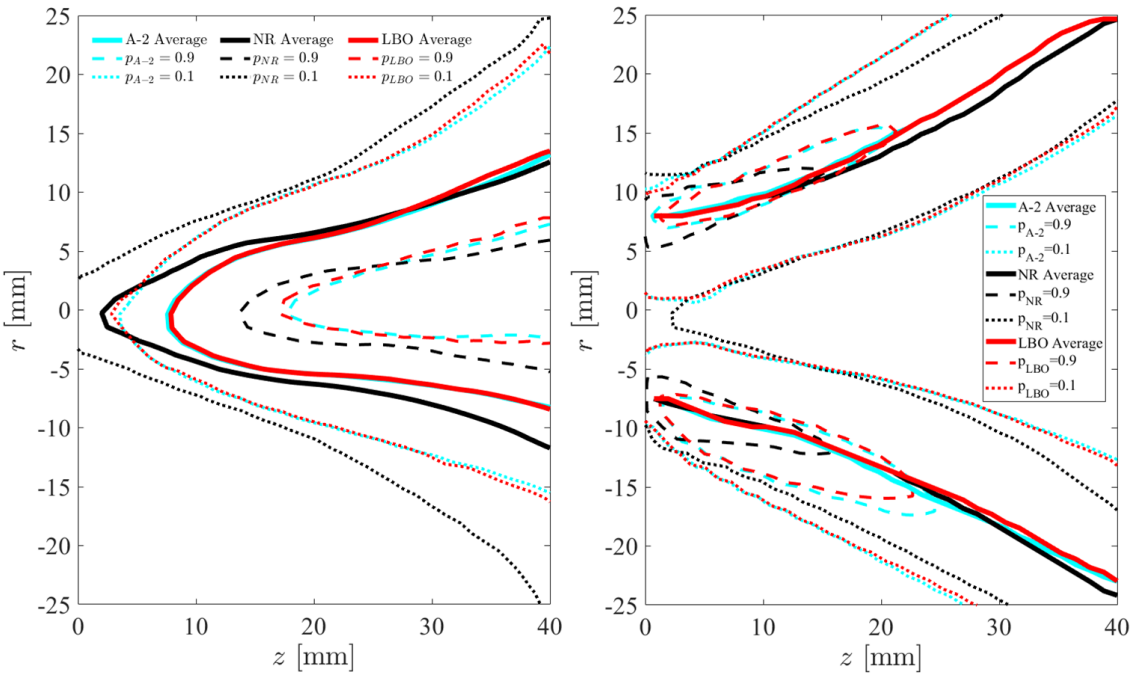

Figure 5.11: Central recirculation zone boundaries (left) and jet cores (right) for the time averaged flow fields from a stable burning A-2 case, a non-reacting case, and a blowout transient A-2 case. Uncertainty bounds are represented by 10% and 90% probability contours. They are calculated by the probability of reverse flow on the left and the probability that the axial velocity is greater than two thirds of the average jet core velocity on the right. (450 K air temperature, 345 kPa pressure)

5.3 Acoustics Characterization

Dynamic pressure measurements were taken at all three air inlet temperatures to compare the acoustic response leading up to LBO. These measurements were initiated at an approximate equivalence ratio of ϕ-ϕ_{LBO}≈0.1 and continued throughout the transient blowout process. Ten repetitions were recorded at 10 kHz for each fuel over a 50 second time interval.

Figure 5.12 shows the local RMS of the dynamic pressure plotted as a percentage of the mean pressure, %p'/P, at 300 K. %p'/P is plotted against ϕ-ϕ_{LBO}, which demonstrates how this value changes as blowout is approached. These p' values were calculated over 1 second intervals and are averaged across each of the 10 cases for a given fuel. It can be seen that throughout much of the operational history, the acoustic response was relatively constant at approximately 0.25% of the mean pressure. There is a slight increase in %p'/P just before the flame blows out. This is likely caused by low frequency pressure changes, due to LBO precursor events that increase in frequency and duration near blowoff (see Figure 3.4), rather than acoustic oscillations. These LBO precursor events will be discussed in detail in Section 6.3. Differences in fuel properties seem to have little effect on the acoustics and it is unlikely that thermoacoustics influenced the 300 K lean blowout boundaries.

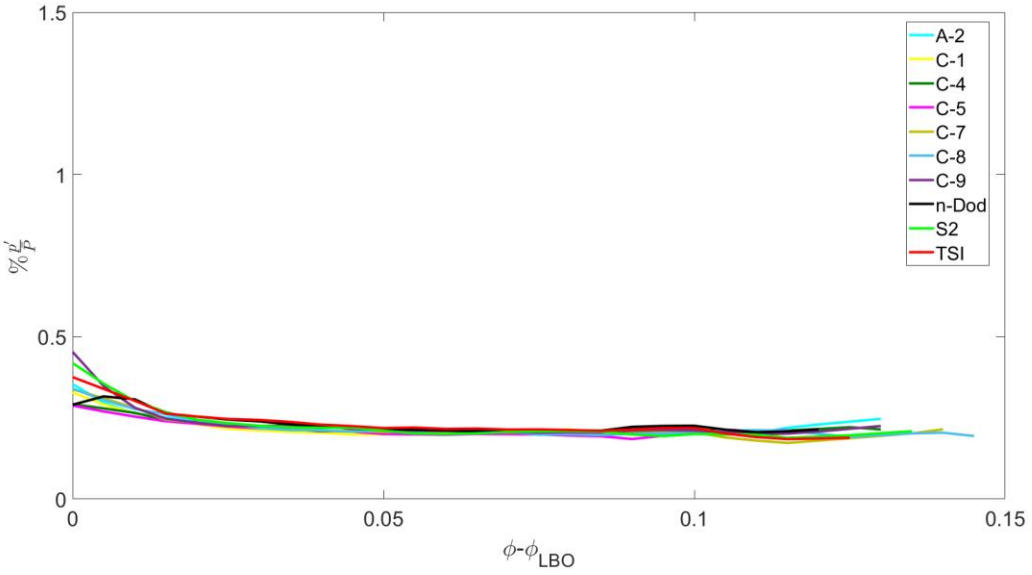

Figure 5.12: RMS of the dynamic pressure plotted as a function of (ϕ - ϕ_{LBO}). This RMS pressure is plotted as a percentage of the mean combustor pressure and has been averaged over the 10 cases for each fuel. These measurements were taken at a 300 K air inlet temperature.

Figure 5.13 shows %p'/P plotted as a function of ϕ-ϕ_{LBO} for the 450 K data. It can be seen that the acoustics were almost completely constant throughout the transient blowout process. The consistent %p'/P value of 0.25% of the mean pressure was almost identical with the 300 K acoustics, although there does appear to be less of an increase just before LBO. Again, the possibility of thermoacoustic dynamics at 450 K can be safely disregarded.

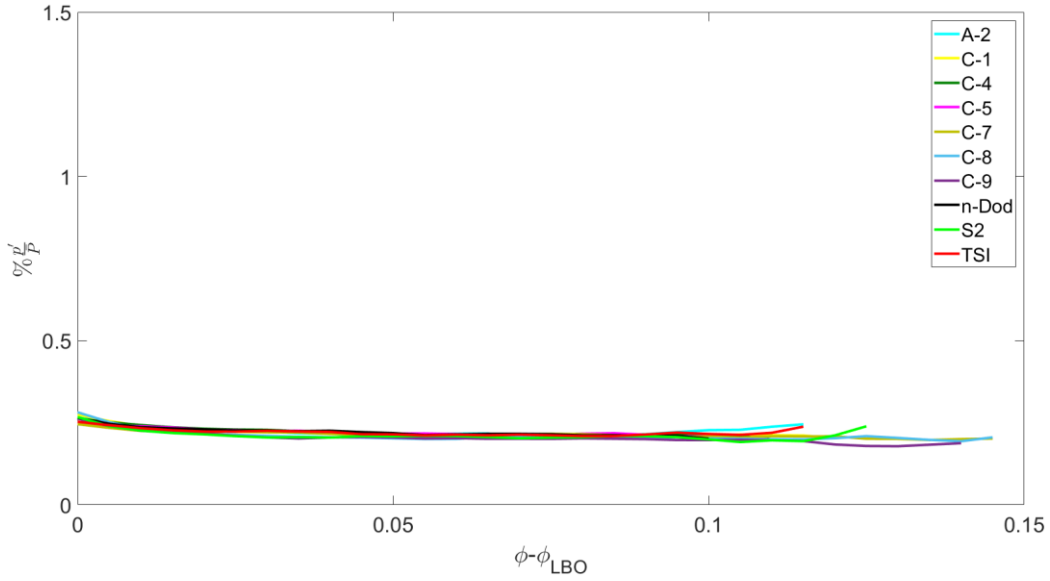

Figure 5.13: RMS of the dynamic pressure plotted as a function of (ϕ - ϕ_{LBO}). This RMS pressure is plotted as a percentage of the mean combustor pressure and has been averaged over the 10 cases for each fuel. These measurements were taken at a 450 K air inlet temperature.

Contrary to the 450 K and 300 K flames, the 550 K flames passed through a thermoacoustic instability on their way to blowout. This can be seen by considering the 550 K %p'/P versus ϕ-ϕ_{LBO} plot shown in Figure 5.14. The %p'/P values reach their peak at ϕ-ϕ_{LBO}≈0.13 and then converge to the 0.25% value where the acoustic oscillations settled at 300 K and 450 K. These observations are consistent with the findings of Unni and Sujith [162]. Their flames were initially unaffected by thermoacoustic dynamics at an equivalence ratio well away from LBO. As the equivalence ratio was reduced towards the blowout value, the flames then passed through a thermoacoustic instability. However, this instability ceased as the equivalence ratio was decreased further, and the flames experienced negligible acoustic interference before ultimately blowing out. This phenomenon is demonstrated in Figure 5.15 for the 550 K flames considered here. FFTs taken over 5 second time intervals are shown as the flame progressively approaches

blowout, where the top plot has the highest equivalence ratio and bottom plot is nearest LBO. The narrowband spectral peak at approximately 500 Hz that is apparent in the top three plots is indicative of the thermoacoustic instability in the combustor. This peak weakens in each subsequent plot until eventually there are negligible acoustic oscillations just before LBO.

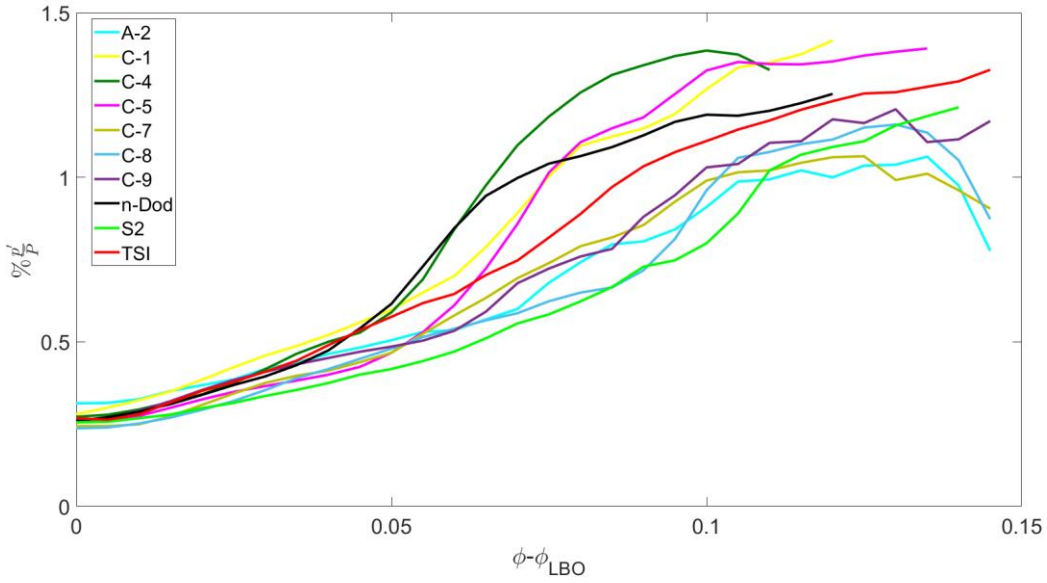

Figure 5.14: RMS of the dynamic pressure plotted as a function of (ϕ - ϕ_{LBO}). This RMS pressure is plotted as a percentage of the mean combustor pressure and has been averaged over the 10 cases for each fuel. These measurements were taken at a 550 K air inlet temperature.

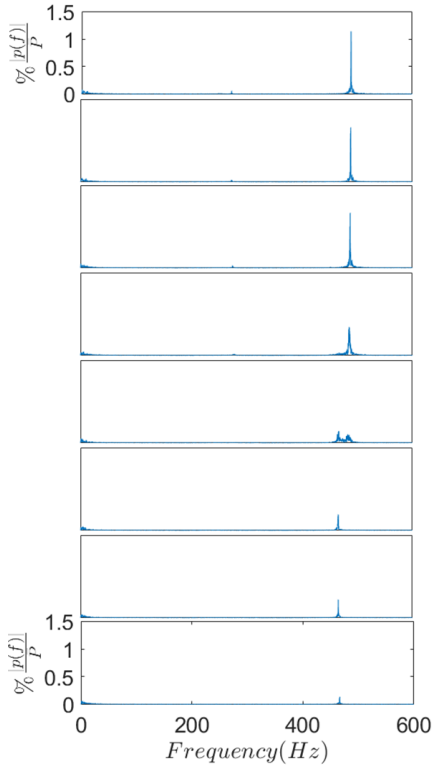

Figure 5.15: FFTs of a dynamic pressure time series taken during a transient blowout process. Fuel C-5 is burning with an air inlet temperature of 550 K. These plots are shown in 5 second intervals as blowout is approached. The top plot is furthest from blowout and the bottom plot is nearest LBO.

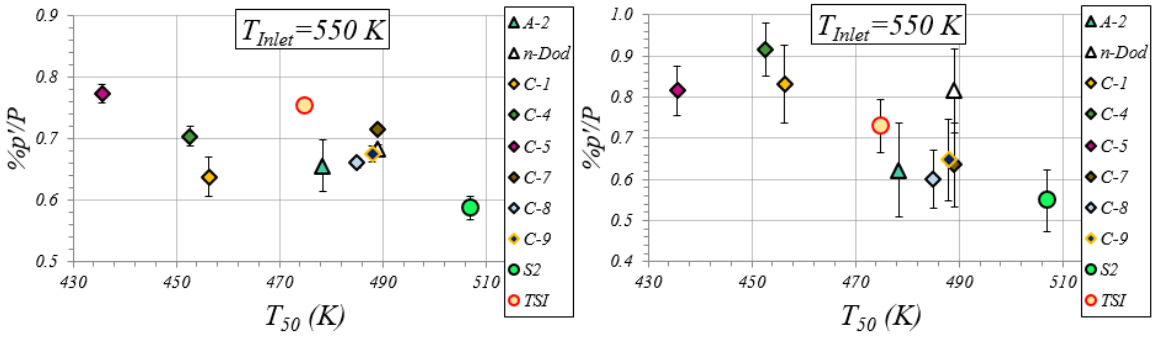

Figure 5.16: RMS of the dynamic pressure plotted as a function of T_{50}. This RMS pressure is plotted as a percentage of the mean combustor pressure. The RMS pressure values in the left plot were calculated using the entire time series and have been averaged over the 10 cases for each fuel. The RMS pressure values in the plot on the right represent the RMS of the average lines in Figure 5.14, within the interval $0.11 \geq \phi - \phi_{LBO} \geq 0$. These measurements were taken at a 550 K air inlet temperature. The error bars represent 95% confidence intervals.

The effects of fuel properties on %p'/P at 550 K were analyzed by calculating the dynamic pressure RMS over the entire 50 second time series. The plot on the left in Figure 5.16 shows these %p'/P values, based on entire individual runs, that have been averaged over each of the 10 cases for a given fuel. In order to account for differences in fuel ramp rates and burning time before LBO, the RMS of the average %p'/P lines in Figure 5.14, with equivalence ratios between $0.11 \geq \phi - \phi_{LBO} \geq 0$, are also plotted on the right in Figure 5.16. It can be seen that %p'/P ranged between 0.5-0.9%, with most fuels having values of about 0.7%. %p'/P is plotted against T_{50} in both the left and right plots in Figure 5.16, as this is the fuel property with which %p'/P is most strongly correlated in both instances. This is interesting because the Hierarchical Non-negative Garrote Regression results, shown in Figure 4.16, predicted that T_{50} would have a mild negatively correlating effect on lean blowout boundaries. Similarly, %p'/P is shown here to have a mild negative correlation with T_{50}. The most noticeable physical difference between the blowoff dynamics at 450 K and 550 K is the previously described thermoacoustic coupling. Therefore, these acoustic influences are likely responsible for the dependence of ϕ_{LBO} on T_{50} that was demonstrated by the regression analysis. However, it should be noted that these thermoacoustic dynamics are only expected to have a minor effect on lean blowout boundaries, as Figure 5.14 shows that the largest pressure oscillations have dampened by the time the flame blows out. Furthermore, the regression results in Figure 4.16 show that the 20/100% DCN is still the dominant fuel property at 550 K.

5.4 Flame, Flow, and Acoustics Summary

Planar measurements were used to characterize the flame and flow field of these near blowoff flames. OH-PLIF images with overlaid PIV vectors showed that the flames

stabilized in the outer shear layer and experienced minimal burning in the central recirculation zone. The traditional spray flame structure was observed, with a partially premixed flame that followed the fuel spray and a nonpremixed flame in the outer recirculation zone. Images taken during a blowout transient showed changes in the flame structure, including weakening of both the inner partially premixed flame and the outer nonpremixed flame, an increase in the amount of observable liquid fuel, and emerging evidence of local extinction processes.

Fuel property differences were shown to have no effect on the bulk flow features of the average flow field. These average flow features were also compared for a non-reacting, stable burning, and blowout transient case. Surprisingly, the average flow field for the blowout transient case closely resembled that during stable burning and did not approach the average non-reacting flow field. It is uncertain whether this says something about the "stage 2" dynamics of these spray flames or whether this is simply a consequence of the way that the data was taken.

Dynamic pressure measurements were used to characterize the acoustics in this combustor. Negligible acoustic oscillations were detected at the 300 K and 450 K air inlet temperatures. However, at 550 K it was shown that the flame passes through a thermoacoustic instability as the equivalence ratio is reduced towards blowout. Although the flame recovers from this instability before blowing out, significant differences were observed in the dynamic pressure RMS between fuels, which may have had an effect on the 550 K lean blowout boundaries.

CHAPTER 6. NEAR-BLOWOFF DYNAMICS

This section was motivated by a desire to correlate the transient dynamics of near-blowoff flames with fuel properties, as opposed to Chapter 4 that focused on correlating the actual blowoff condition itself. It may be that these correlations better describe the onset of "stage 1", where local extinction and re-ignition occurs. For this reason, data were obtained as part of this study for a subset of fuels and the actual blowoff process itself observed, which indicated not only the condition at which blowoff occurs but also where "stage 1" initiates. These conditions, along with quantitative measures of the extinction and re-ignition processes, were then correlated against the same fuel physical and kinetic properties. Chemiluminescence measurements taken at the conditions shown in Table 2-4 were used for these purposes.

6.1 Flame Leading Edge Location and Velocity

Videos were used to understand the spatio-temporal flame dynamics preceding complete blowout. Far from blowoff, the flame stabilized in a consistent spatial location. Figure 6.1 shows an instantaneous image of a stable flame burning at ϕ=0.41 (left). As the equivalence ratio was reduced towards the lean blowout limit, stable burning was interrupted by what appear to be extinction and re-ignition events. Two examples at ϕ=0.34 are shown in the center and right images of the same figure. Local extinction is evident in these images but there is not an immediate risk that these flames will blow out; i.e., they are in "stage 1". Following the terminology of Muruganandam [50], these temporary extinction processes will be referred to as "LBO precursor events".

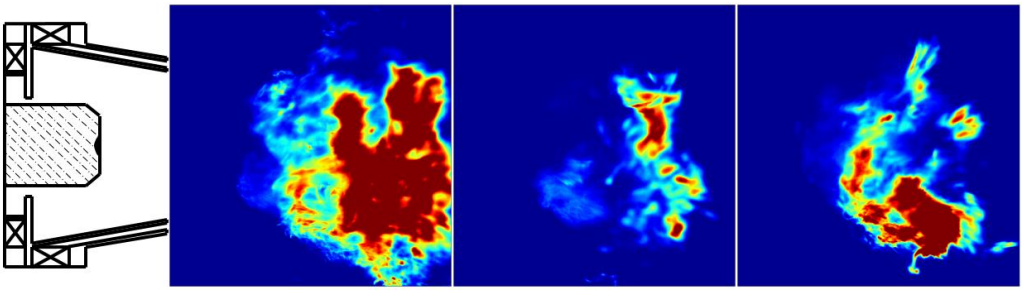

Figure 6.1: Instantaneous CH* chemiluminescence images taken of the flame during both stable (left) and "stage 1" (center and right) conditions. A-2 (Jet-A) is burning in each of these images at 450 K.

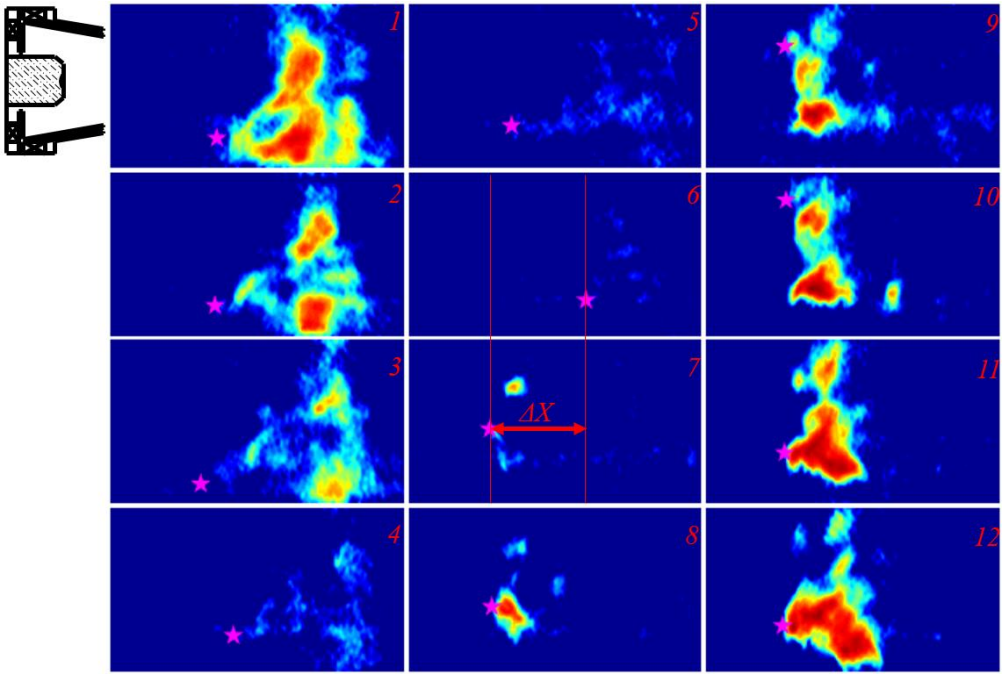

Figure 6.2: Twelve successive CH* chemiluminescence images taken during an LBO precursor event near blowoff. The star denotes the most upstream spatial location of luminosity. N-dodecane is burning in these images at 450 K.

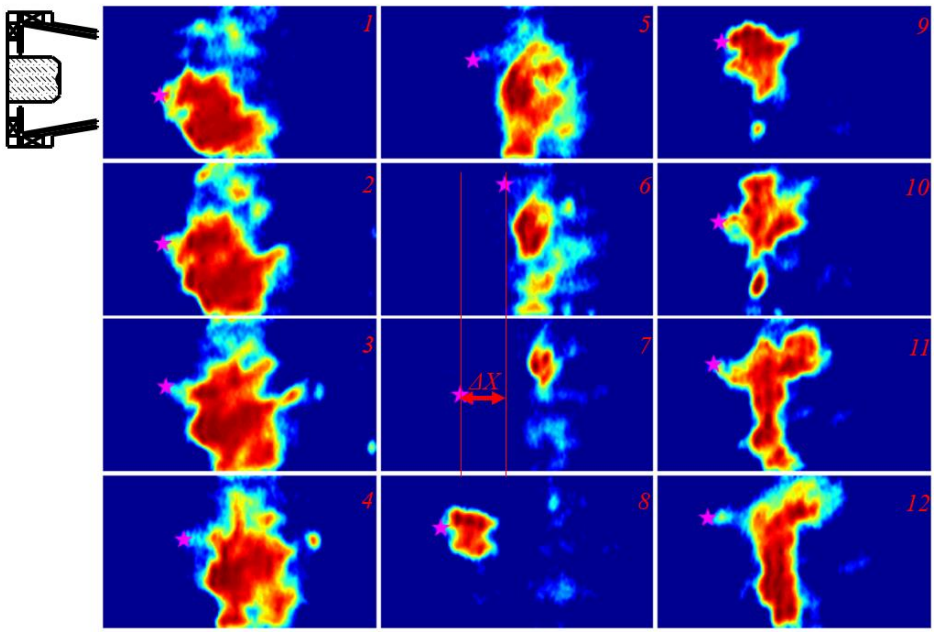

Figure 6.3: Twelve successive CH* chemiluminescence images taken during an LBO precursor event near blowoff. The star denotes the most upstream spatial location of luminosity. A-2 (Jet-A) is burning in these images at 450 K.

Near blowoff, the most upstream point of the flame jumps axially back and forth, presumably associated with extinction, re-ignition, and axial convection. Two separate examples of this phenomenon, each including an LBO precursor event, are shown in Figure 6.2 and Figure 6.3. Additional examples are included in Appendix D. An analysis of the most upstream spatial location where luminosity was detected (x_{up}) was used to characterize these LBO precursors. Section 3.2 describes the method used to determine this location.

Using this axial coordinate, x_{up}, and the time interval between images, the distance that the most upstream part of the flame travels between images, Δx_{up}, can be converted to a velocity, v_{up}. Positive velocities represent the flame either being convected downstream or extinguishing. Comparison of these flame velocities with flow velocities provides some

insight into which Δx_{up} distances may be associated with extinction and ignition. Two measured axial flow velocity PDFs are shown in Figure 6.4, obtained from stereo-PIV measurements. Both the axial flow velocity PDF based on the total measurement domain, U_{Total}, and the PDF of the axial velocities in the central recirculation zone (i.e., all spatial locations in the CRZ where the velocity is negative), U_{CRZ}, are shown. These data indicate that the peak positive flow velocity is approximately 52 m/s (see Figure 5.9 and Figure 6.4) [145]. Any forward motion of the leading luminosity point at a velocity greater than this value is interpreted as extinction.

Negative velocities represent either flame propagation, reverse flow, or re-ignition processes. Turbulent flame propagation speeds are O(1-10 m/s). The axial flow velocity measurements shown in Figure 6.4 indicate that the peak reverse flow velocity is around -30 m/s [145, 163]. This implies that v_{up} < ~-30 m/s, are potentially caused by re-ignition. However, v_{up} < ~-30 m/s can also be caused by portions of the flame appearing that were previously undetected. Therefore, instances where v_{up} < ~-30 m/s had to also coincide with an LBO precursor event in order for them to be considered a re-ignition occurrence. The LBO precursor events in these CH* chemiluminescence videos were identified by integrating the intensity in each image and applying the same double threshold method discussed previously in reference to the PMT measurements. Each of these integrated time series were standardized before the thresholds were applied to correct for intensity differences in the detected CH* emission between fuels. The images shown in Figure 6.2 and Figure 6.3 constitute an example of re-ignition. Both occurred during an LBO precursor event and the velocity of the leading edge is too great for reverse flow convection

or flame propagation. Among the identified re-ignition instances, there were v_{up} values that ranged between ~-30 m/s to ~-100 m/s.

CH* chemiluminescence videos were also acquired at an equivalence ratio slightly above the blowout value (ϕ-ϕ_{LBO}≈0.025) in order to study the flame behavior during the pre-blowoff stages. However, none of the LBO precursor events that were detected here coincided with v_{up} < ~-30 m/s. Therefore, the following discussion surrounding re-ignition will only focus on the dynamics within the blowout transient (i.e., conditions C and D where ϕ-ϕ_{LBO}→0).

A word on nomenclature - the word “re-ignition”, not “autoignition”, is used in order to reserve the latter expression for low-temperature chemistry driven chemical induction processes. In contrast, there are multiple physical processes involved in the re-ignition of a locally extinguished flame, including mixing, edge flame propagation, independently burning flame parcels, autoignition, and the contact of reactants with hot combustion products [45, 89, 164-166].

Figure 6.4 plots the average 450 K PDFs of v_{up} taken at condition C. Fuels A-2 and C-1 are overlaid on this plot, along with U_{Total} and U_{CRZ}. These flame velocity distributions were all centered at or near 0 m/s, as must be the case for a flame that is neither completely blowing off nor flashing back. Moreover, the shape of the distributions is largely insensitive to fuel type and blowout equivalence ratio. The shape of the 300 K distributions are comparable to the 450 K cases, but the negative v_{up} values are larger (i.e., the PDFs are narrower). The results for all fuels, including each of the individual runs at both temperatures, are presented in Appendix E.

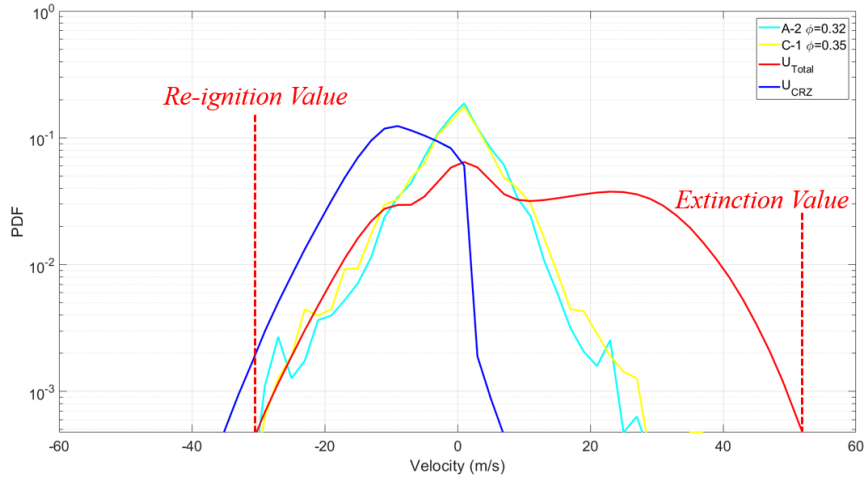

Figure 6.4: Average 450 K PDF of v_{up} at condition B for A-2 and C-1. The axial flow velocity PDFs U_{Total} and U_{CRZ} are also shown.

The following sections present results for the pre-LBO flame dynamics, such as when "events" are first observed or the fraction of time over which they occur, as a function of fuel properties.

6.2 Onset of "events"

Prior work has extensively correlated the conditions under which LBO occurs with kinetic and fluid mechanic parameters. As noted in the Introduction, it has been hypothesized that these correlations likely capture the physics associated with the extinction processes that happen near blowoff, and not blowoff itself [34]. If this hypothesis is correct, it should be expected that the same correlations that work for ϕ_{LBO} should also work for ϕ_{event}.

Figure 6.5 shows the LBO boundaries of the cases where the OH* time series were acquired, similar to the previous results shown in Chapter 4, plotted against ϕ_{event}. For reference a 1-1 is dropped in, indicating the limit where $\phi_{event} = \phi_{LBO}$. The difference

between these two equivalence ratios, (ϕ_{event} - ϕ_{LBO}), quantifies the key observations summarized in the Introduction – that blowoff is preceded by extinction– and quantifies the separation in ϕ space between when they occur. It is also important from an operational standpoint because it indicates how close a combustor can safely approach LBO with some warning that it is imminent.

It can be seen that ϕ_{event} has a nearly linear relationship to ϕ_{LBO} and the $\phi_{event} = \phi_{LBO}$ line at 300 K. The slope of the line at 450 K is slightly different, suggesting some systematic difference between ϕ_{event} and ϕ_{LBO}. Further insight into these points can be gained from Figure 6.6, which plots the dependence of (ϕ_{event} - ϕ_{LBO}) upon the DCN at 450 K and T_{90} at 300 K. Figure 6.6 shows that at 450 K, (ϕ_{event} - ϕ_{LBO}) increases for high DCN fuels, with C-9 being the largest exception. No clear correlation between (ϕ_{event} - ϕ_{LBO}) and T_{90} exists at 300 K.

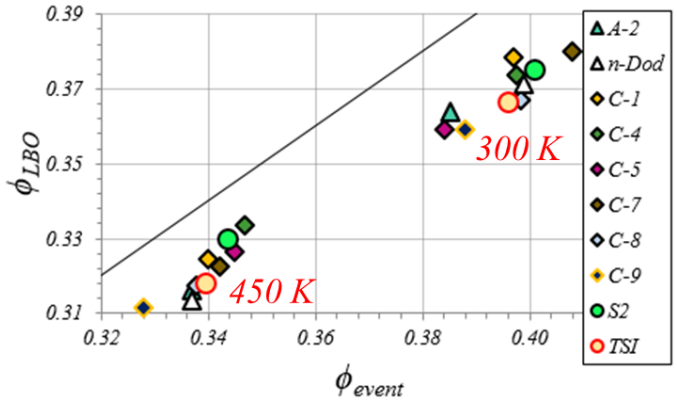

Figure 6.5: Equivalence ratio at which blowoff occurs, ϕ_{LBO}, plotted against the equivalence ratio where events initiate, ϕ_{event}. Results are included at both air inlet temperatures.

These results share similarities with the re-ignition measurements at conditions C and D, which are presented in Figure 6.13, and will be revisited in Section 6.4. It should be noted that less confidence should be placed in the ϕ_{LBO} values used in Figure 6.5 and Figure 6.6 than in the LBO boundaries shown in Chapter 4. This is because the process of acquiring PMT measurements introduced difficulties in controlling bulkhead temperatures, fuel ramp rates, and prevented more than 5 fuels from being tested on a given day. Each of these factors were well controlled, and many more samples were included, in the results from Chapter 4.

An important question raised in the introduction is the degree to which (ϕ_{event} - ϕ_{LBO}) changes with fuel properties and operating conditions. These results suggest that there is some effect but it is weak and only evident at 450 K. The fact that ϕ_{LBO} and ϕ_{event} have the same behaviors lends further support to the hypothesis outlined in the Introduction – that correlations for LBO describe the physics associated with the onset of extinction and re-ignition, “stage 1”.

a)

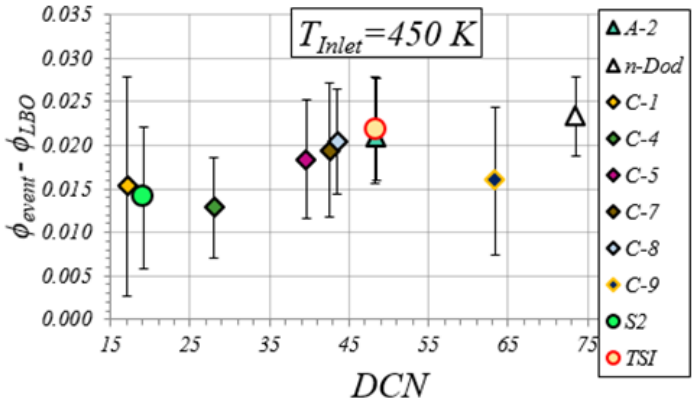

b)

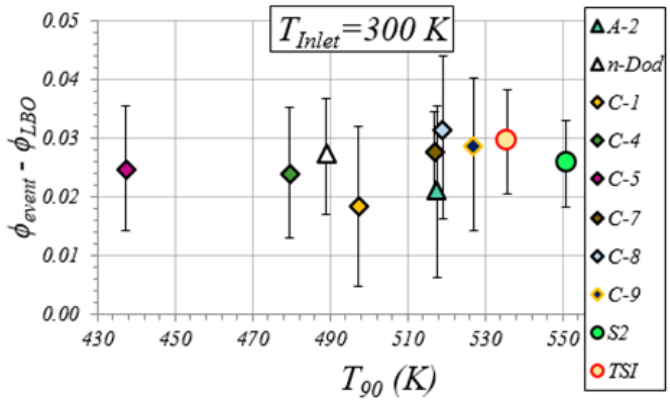

Figure 6.6: (ϕ_{event} - ϕ_{LBO}) plotted against the DCN at 450 K (a) and T_{90} at 300 K (b). The 20% DCN for fuel S2 is used here due to its potential for preferential vaporization. The error bars represent a combined uncertainty based on 95% confidence intervals and adjusting the double thresholds by ± 5%.

6.3 Extinction Behaviors Under Near LBO Conditions

This section analyzes extinction behaviors under conditions near LBO, including the effect of fuel properties. Interestingly, no instances of flame motion downstream at velocities faster than the peak flow velocity (see Figure 6.4) were observed; this indicates that the flame does not actually extinguish in some large region of space, so that the leading edge of the reaction volume jumps discontinuously downstream. Rather, "extinction events" are actually "downstream convection events". It is likely that a small region of the

flame responsible for flame stabilization extinguishes, leading to downstream convection of the flame. In contrast, the data clearly indicates the presence of the leading edge of the flame traveling upstream at velocities significantly higher than would be associated with convection or flame propagation, as discussed in the next section.

The duration of extinction events, and the extinction history of these flames in the near-blowoff stages, $\phi_{event} > \phi > \phi_{LBO}$, will now be considered. The extinction history was quantified as the percentage of time when the flame was in an extinguished condition ($\%\tau_{ext}$). Consider first the average event duration. Figure 6.7 shows the average duration of extinction events, τ_{event}, plotted against T_{50} **(a)** and T_{90} **(b)**, at 300 K. τ_{event} ranges in value from about 2-6 ms at 300 K, and Figure 6.9 **(a)** shows that it ranges from 1-2 ms at 450 K. In other words, the extinction event time interval at 450 K is less than half than at 300 K. For reference, a bulk fluid mechanic time scale associated with the nozzle exit diameter and velocity, $\tau_{flow,D/U}$, is ~O(0.3 ms). $\%\tau_{ext}$ at 300 K is plotted in Figure 6.8 as a function of T_{50} **(a)** and T_{90} **(b)**, and Figure 6.9 **(b)** shows $\%\tau_{ext}$ at 450 K. In both cases, the extinction events persist for about 0.8-1.3% of the time.

At 300 K, there is a clear correlation between τ_{event} and T_{50} (there is also a strong correlation with T_{90}, as shown in Figure 6.7 **(b)**, but the correlation is strongest here with T_{50}). Specifically, fuels that vaporized most easily have the shortest events and the fuels that were most difficult to vaporize had the longest events. Similarly, the fraction of extinction time, $\%\tau_{ext}$, is also correlated with T_{90} at 300 K. The flames of difficult to vaporize fuels remain in an extinguished condition for a greater amount of time before they blow out than easily vaporized fuels.

Much weaker correlations are seen at 450 K. τ_{event} perhaps depends on T_{90} somewhat, but the differences between fuels are minor. $\%\tau_{ext}$ is also very similar between fuels and showed no correlation with the DCN, even though ϕ_{LBO} is highly correlated with the DCN at 450 K. It is possible that C-1, the high TSI fuel, and n-dodecane experience slightly more extinction time than the other fuels, but these deviations are well within the uncertainty.

a)

b)

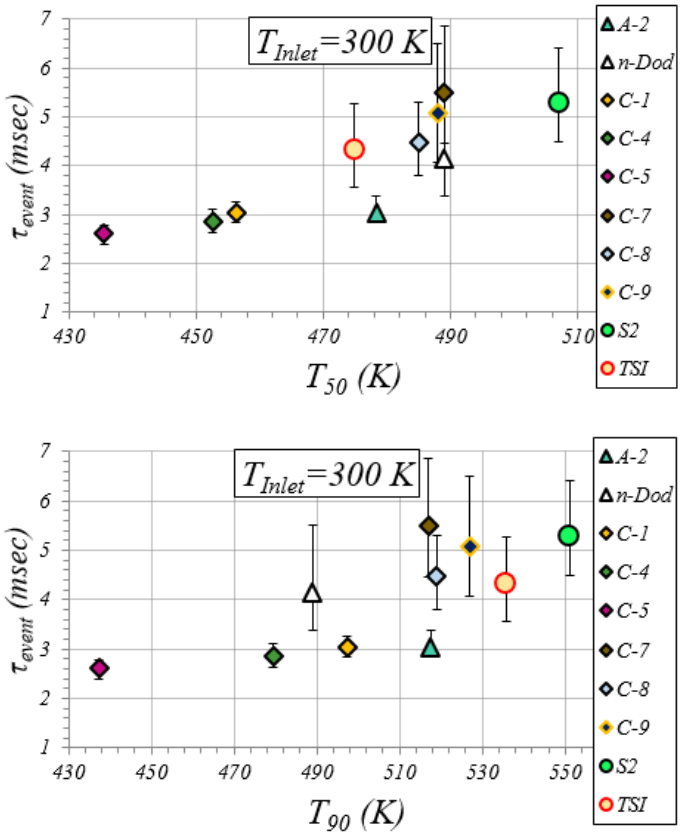

Figure 6.7: Average duration of the LBO precursor events, τ_{event}, plotted against T_{50} (a) and T_{90} (b). The error bars represent a combined uncertainty based on 95% confidence intervals and adjusting the double thresholds by ± 5%. (Condition B)

a)

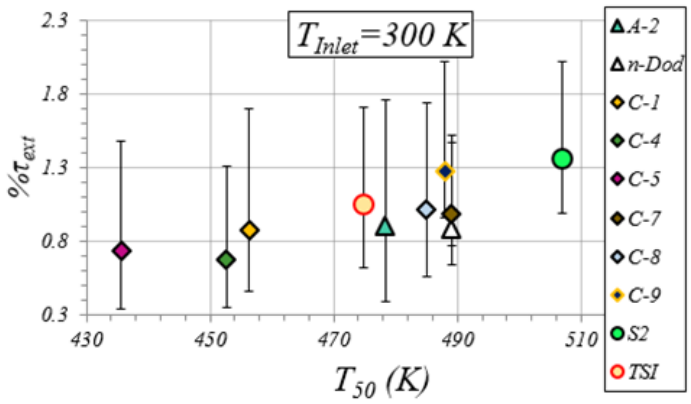

b)

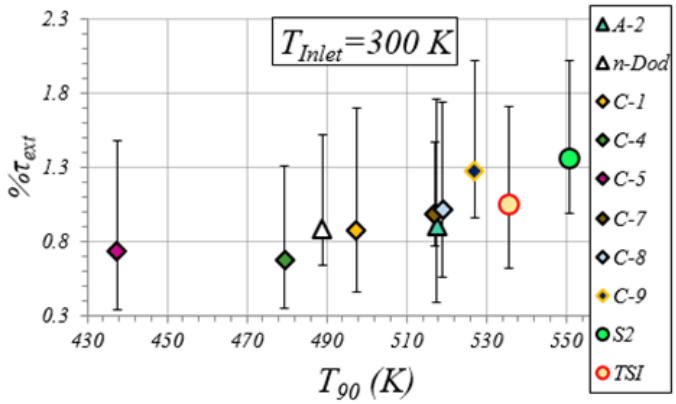

Figure 6.8: Average percentage of time in the near-blowoff stages ($\phi_{event} > \phi > \phi_{LBO}$) constituted by extinction, $\%\tau_{ext}$, plotted against T_{50} (a) and T_{90} (b). The error bars represent a combined uncertainty based on 95% confidence intervals and adjusting the double thresholds by ± 5%. (Condition B)

a)

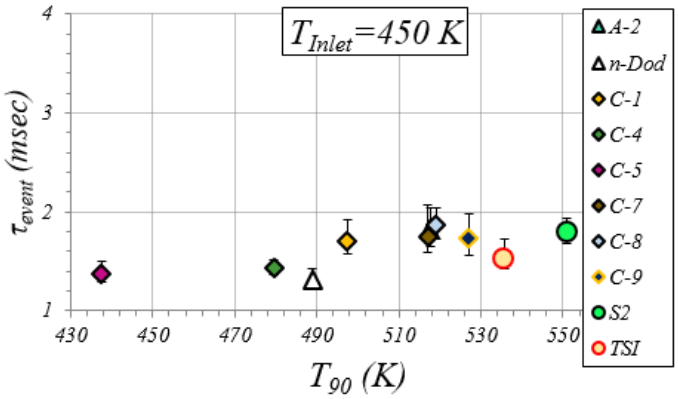

b)

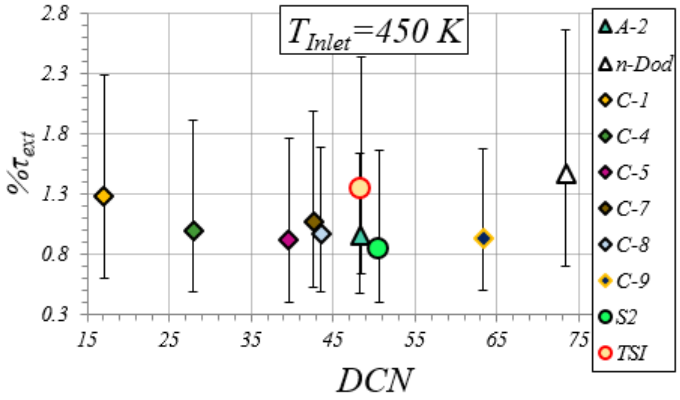

Figure 6.9: Average duration of the LBO precursor events, τ_{event}, (a) and the percentage of time in the near-blowoff stages ($\phi_{event} > \phi > \phi_{LBO}$) constituted by extinction, $\%\tau_{ext}$ (b). These condition A results are plotted against T_{90} and the DCN, respectively. The 20% DCN for fuel S2 is used here due to its potential for preferential vaporization. The error bars represent a combined uncertainty based on 95% confidence intervals and adjusting the double thresholds by ± 5%.

It is also of interest to note the similarity in ranges of the $\%\tau_{ext}$ values observed at both 300 K and 450 K, and across the fuels, all lying in the approximate range of 0.8-1.3%. There is no reason to expect that these percentages should be similar, given that ϕ_{LBO} occurs at substantially higher values at 300 K than 450 K, and that the length of extinction events is quite different as well. However, this observation provides some clues into the relationship between ϕ_{event} and ϕ_{LBO}. As noted in Shanbhogue et al.'s review [34], it is clear that flames can withstand a certain fraction of extinction but still exist indefinitely without

blowing off. However, it is also clear that the flame will blow off if the fraction of time and/or space over which extinction occurs is too large (this was referred to as the "critical extinction level" in Shanbhogue et al.'s review [34]). This is likely due to a reduction in temperature of the hot recirculating gases responsible for re-igniting the incoming mixture. What this "critical extinction value" should be is not currently understood. However, if this "critical extinction value" hypothesis is correct, then one would expect more universal behavior across operating conditions and fuel compositions right near blowoff. The fact that $\%\tau_{ext}$ has nearly the same value across all the fuels, and at both temperatures, is consistent with this idea.

However, the above results are essentially an average over the range, $\phi_{event} > \phi > \phi_{LBO}$. In order to further evaluate the above "critical extinction value" hypothesis, these values were recalculated over a much narrower range of ϕ values right on the edge of blowoff. This procedure reduces some of the averaging that is present over a broader range of equivalence ratios, but also increases the random error in the extinction event statistics, as there are fewer realizations to average over. Figure 6.10, Figure 6.11, and Figure 6.12 plot τ_{event} and $\%\tau_{ext}$ right on the edge of blowoff, $\phi_{LBO+\varepsilon} > \phi > \phi_{LBO}$, where ε ~0.002 (calculated by taking the final second of data before LBO). These figures show that even on the very edge of blowoff, extinction events are uncommon. The maximum value in $\%\tau_{ext}$ is always less than 10%, with values closer to 3-5% for most cases. Comparing these results with those in Figure 6.7, Figure 6.8, and Figure 6.9, note that the trends in τ_{event} do not change qualitatively, although there is somewhat of an increase in τ_{event} relative to its value when averaged over $\phi_{event} > \phi > \phi_{LBO}$. Similar conclusions apply for $\%\tau_{ext}$ at 450 K. However, the picture does change for $\%\tau_{ext}$ at 300 K; here we see that its value is now

appreciably higher than at 450 K and does also seem to increase with T_{50} and T_{90}. Taken together, these results suggest that the "critical extinction value" hypothesis is a helpful, but incomplete, characterization of why flames ultimately transition from local extinction to complete blowoff.

a)

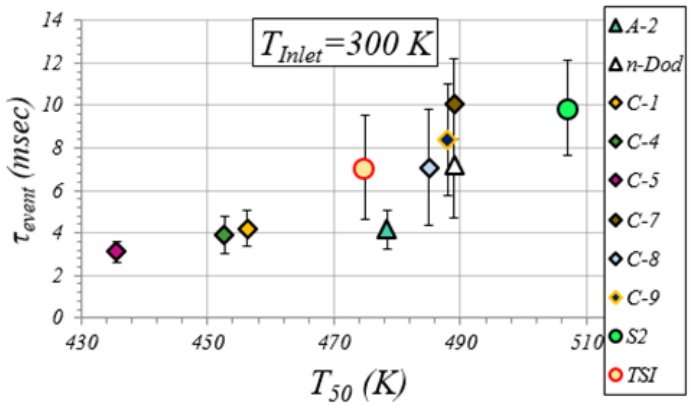

b)

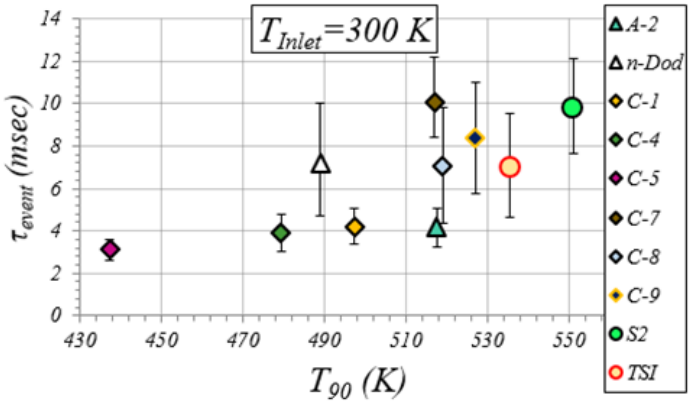

Figure 6.10: Average duration of the LBO precursor events, τ_{event}, plotted against T_{50} (a) and T_{90} (b). These τ_{event} values represent the average event duration in the final second before LBO. The error bars represent a combined uncertainty based on 95% confidence intervals and adjusting the double thresholds by ± 5%. (Condition D)

a)

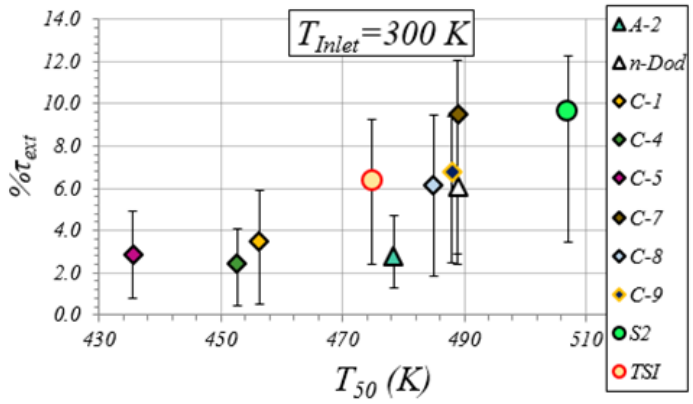

b)

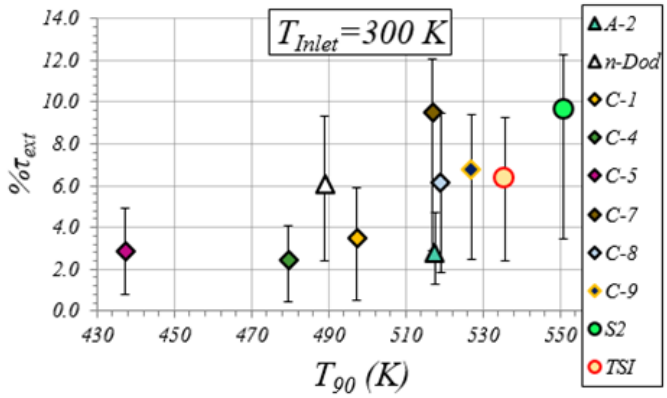

Figure 6.11: Average percentage of time in the near-blowoff stages ($\phi_{event} > \phi > \phi_{LBO}$) constituted by extinction, $\%\tau_{ext}$, plotted against T_{50} (a) and T_{90} (b). These $\%\tau_{ext}$ values represent the average extinction percentage in the final second before LBO. The error bars represent a combined uncertainty based on 95% confidence intervals and adjusting the double thresholds by ± 5%. (Condition D)

a)

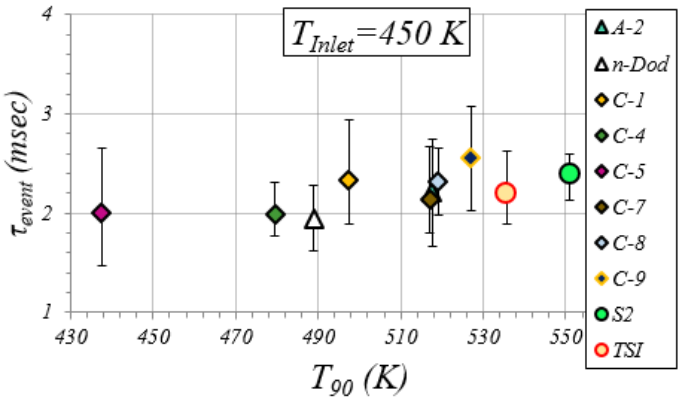

b)

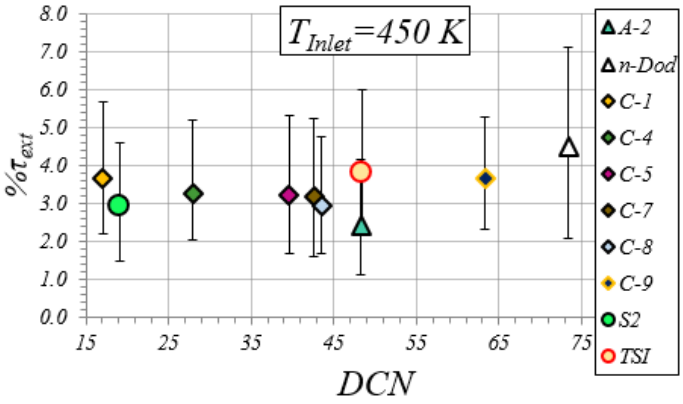

Figure 6.12: Average duration of the LBO precursor events, τ_{event}, (a) and the $\%\tau_{ext}$ (b) in the final second before LBO. These condition C results are plotted against T_{90} and the DCN, respectively. The 20% DCN for fuel S2 is used here due to its potential for preferential vaporization. The error bars represent a combined uncertainty based on 95% confidence intervals and adjusting the double thresholds by ± 5%.

6.4 Re-ignition Behaviors Under Near LBO Conditions

This section analyzes the re-ignition behaviors under conditions near LBO, including the effect of fuel properties. As noted earlier, the data clearly indicates the presence of the leading edge of the flame traveling upstream at velocities significantly higher than would be associated with convection or flame propagation. These realizations in the negative velocity tails of the v_{up} PDFs, that also satisfied the LBO precursor event criterion, were used as an indicator of the near blowoff re-ignition propensity of these fuels.

Of course, these values must be referenced against the number of extinction events that the flame must recover from. Therefore, the number of re-ignition instances in each run was normalized by the corresponding number of extinction events. Appendix C demonstrates that the plots shown in this section are not a strong function of the thresholds that were used to determine the number of extinction events.

Figure 6.13 plots the percentage of extinction events where v_{up} < -30 m/s, averaged across each of the cases for a given fuel, at conditions C **(a)** and D **(b)**. This percentage of v_{up} is plotted against the DCN and T_{90}, the fuel properties previously shown to correlate best with LBO at 450 K and 300 K, respectively (see Chapter 4). First, note that while the flame does recover from extinction events by re-ignition, this is relatively infrequent, occurring in most cases about 20-30% of the time. The peak value is around 50% for n-dodecane at 450 K, and is only observed for fuel S2 at 300 K. This indicates that with the exception of n-dodecane at 450 K, the flame recovers from the majority of extinction events through some other means than re-ignition – presumably simply upstream convection and propagation of the flame.

Consider next the fuel property sensitivity. It can be seen that high DCN fuels have a much greater propensity for re-ignition recoveries at 450 K than low DCN fuels. As each of these fuels experiences approximately the same amount of extinction at 450 K (see Figure 6.9), this is a likely explanation for the positive correlation between (ϕ_{event} - ϕ_{LBO}) and the DCN shown in Figure 6.6. Once the flame begins experiencing LBO precursor events, the operation of high DCN fuels is extended to lower equivalence ratios because these fuels are better able to recover through re-ignition. The superior LBO performance of high DCN fuels should not be limited to strictly re-ignition considerations, as Figure 6.5

also shows that these fuels also have lower ϕ_{event} values. Therefore, it appears that high DCN fuels are better able to resist blowoff by delaying the onset of LBO precursor events, and then their improved re-ignition performance allows them to survive longer once these precursor events begin to threaten the stability of the flame.

a)

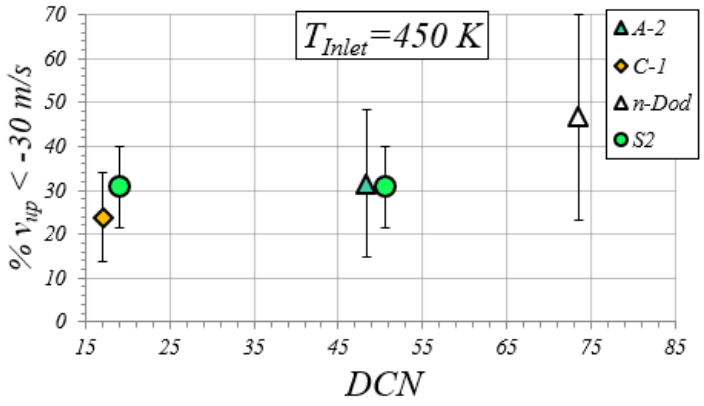

b)

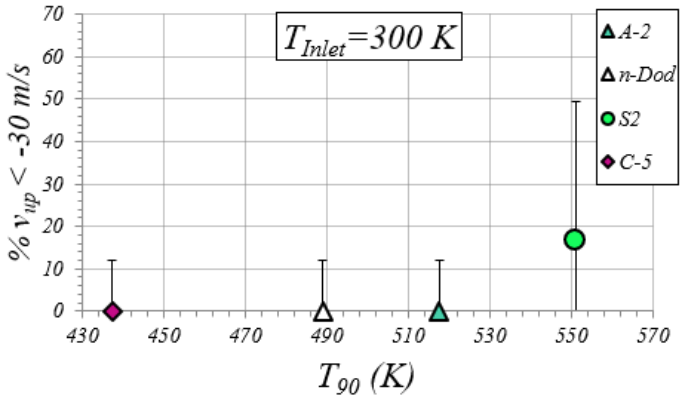

Figure 6.13: %v_{up} < -30 m/s at condition C (a) and condition D (b). The 450 K data is plotted against the DCN and the 300 K data is plotted against T_{90}. Since the role of preferential vaporization on re-ignition is unclear, both the 20% DCN and the DCN based on the entire fuel composition are shown for fuel S2. Error bars represent 95% confidence intervals.

Given that LBO is predominantly vaporization limited at 300 K, fuel property effects were not expected to be found in the re-ignition characteristics. The %v_{up} < -30 m/s values shown in Figure 6.13 **(b)** indicate that re-ignition recoveries only occurred for the

highest T_{90} fuel, S2. This is likely related to the greater susceptibility of this fuel for extinction, as was discussed previously. Furthermore, the re-ignition instances that did occur for S2 at 300 K happened infrequently. As noted above, the flame recovers from the majority of extinction events through some other means than re-ignition – presumably simply upstream convection and propagation of the flame.

6.5 Near LBO Dynamics Summary

The lean blowout process of fuels with very different chemical compositions and physical properties were compared using detailed chemiluminescence measurements. High speed videos of the CH* chemiluminescence emission were recorded for four fuels during the blowout transient. Insight was extracted from these videos by analyzing the motion of the leading luminosity point throughout the entire image sequence. Photomultiplier tube (PMT) measurements were also used to monitor chemiluminescence during the 50 seconds preceding blowoff. These measurements were taken using ten fuels and a double threshold technique was used to identify LBO precursor events. Both types of chemiluminescence measurements were taken at air inlet temperatures of 300 K and 450 K.

Clear physical differences were observed in the 300 K and 450 K near-blowoff dynamics. Fuel property differences seem to have a lesser effect on the 450 K extinction behavior, as quantified by τ_{event}, and $\%\tau_{ext}$. The amount of time that the flame spends in an extinguished condition, and the duration of its extinction events, was insensitive to fuel type. There was, however, evidence of a higher percentage of re-ignition recoveries for high DCN fuels. This finding, taken in conjunction with the lower ϕ_{event} values for high

DCN fuels, suggests that high DCN fuels more successfully resist blowoff by delaying the onset of LBO precursor events and then they are more often able to recover from these precursor events through re-ignition. The 300 K PMT analysis showed that there is a strong correlation between a fuel's boiling point temperature and the duration of its extinction history preceding LBO. Furthermore, the highest boiling point temperature fuel was also found to be more likely to experience re-ignition recoveries. A possible phenomenological explanation for lean blowout at 300 K can be developed by considering the relationship between extinction and droplet evaporation. It was observed from the simultaneous OH-PLIF and PIV measurements of the blowout transient case that most of the liquid fuel vaporizes after reaching the flame. Although these measurements were only taken at 450 K, it is expected that even less of the liquid fuel will vaporize before reaching the flame at 300 K due to the larger droplet sizes and lower surrounding gas temperature. Therefore, the liquid fuel is required to evaporate over a smaller time interval at 300 K than at the other operation conditions in order to maintain a combustible fuel-air mixture. The flame must recover quickly from any local extinction processes that occur, otherwise the subsequent reduction in surrounding gas temperature will cause droplet evaporation rates to decrease. This would result in a shortage of gaseous fuel and further extinguishing of the flame. Supporting evidence for this conceptual model comes from the fact that the high boiling point temperature fuels have longer extinction durations. Without gaseous fuel to burn, hot gases will be swept downstream until the liquid fuel sufficiently vaporizes. Since this is a slower process for high boiling point temperature fuels, these flames are more often required to re-ignite in order to re-establish a stable flame.

CHAPTER 7. CONCLUDING REMARKS

The implementation of alternative jet fuels must be preceded by an understanding of the effects of fuel property differences on combustion limit phenomena, including lean blowout, altitude relight, and cold start. Lean blowout performance is among the most important considerations for certifying new jet fuels [9], as differences in fuel physical and chemical properties likely have the greatest effect on the combustion process under near-blowout conditions. The work in this thesis has made novel contributions towards characterizing the role of fuel properties on lean blowout physics and understanding the mechanisms leading to the blowout of spray flames. This chapter includes a summary of these contributions, along with a discussion of their applications. Lastly, a set of recommendations for future work is presented.

7.1 Summary of Contributions

Determining whether differences in fuel properties affect the equivalence ratio at which flames blow out is among the most important considerations for certifying alternative jet fuels. As each of the fuels involved in this study have comparable heating values, it is not obvious that there should be differences. Furthermore, many of the earlier studies by other researchers failed to show fuel chemical property effects in lean blowout boundaries [95, 96, 98], although some of them did observe fuel physical property effects. The experimental results in this study showed clear differences in the blowout equivalence ratio with fuel type. This is likely related to the well-controlled experimental procedure that was used in this work, as the bulkhead temperature parametrization eliminated

systematic errors between runs caused by differences in the combustor hardware temperature.

After establishing that fuel effects are present, the second key contribution of this work was identifying which fuel properties govern lean blowout boundaries. This task was complicated by the variety of different conclusions that are reported in the literature for similar studies. For example, even researchers who agree that a particular fuel property is flame stability limiting often disagree on the nature of the correlation, where one researcher may show a negative correlation with LBO boundaries and others show a positive correlation with the very same fuel property. It was shown in this study that many of these issues are caused by differences in experimental operating conditions, as the relative importance of the physical and kinetic fuel properties controlling LBO change with the air inlet temperature. Experiments were performed here at three different air inlet temperatures: 300 K, 450 K, and 550 K. At 300 K, lean blowout was shown to be a vaporization limited problem. In this case, fuels with higher boiling point temperatures, specifically T_{90}, were observed to blow out more easily than those with low boiling point temperatures. At both 450 K and 550 K, blowout was observed to be kinetically limited. At these conditions, high DCN fuels blew out at lower equivalence ratios and low DCN fuels blew out at higher equivalence ratios. These conclusions are strengthened by the fact that the large number of repetitions involved, the variety of different conditions tested, and the well-explored fuel property space, constituted by the 18 different liquid fuels that were evaluated, make this the largest available data set on lean blowout sensitivities of spray flames.

Experimental results inherently have a dependence on the combustor geometry in which the data was acquired. In order for the results in this study to be applicable to real-world scenarios, consideration should also be given to additional geometrical features that are incorporated in modern aircraft combustors. These features include a hybrid fuel injector, an effusion cooled combustor liner, and dilution air jets. Adding an airblast atomizer to the fuel injector configuration would most likely cause the flame to stabilize closer to the nozzle exit [101]. This would lead to hotter gases in the outer recirculation zone and increased droplet evaporation rates. The 323 K data of Grohmann et al. [100], taken using an airblast atomizer, showed that difficult to vaporize fuels blew out at the lowest equivalence ratios. Therefore, it seems reasonable that using an airblast atomizer at a low air inlet temperature would improve the relative flame stability performance of high boiling point temperature fuels, as their liquid fuel droplets would extend further into the outer recirculation zone and heat the recirculating gases. Increased cooling of the central and outer recirculation zones would result from a combustor with dilution air jets and an effusion cooled liner. Little evidence was found from the planar measurements in this work that gases in the central recirculation zone significantly affect flame stability. However, cooling of the outer recirculation zone would weaken the outer nonpremixed flame and cause blowoff to be more sensitive to extinction of the flame along the spray trajectory. The reverse effect would take place in a combustor configuration that had a higher swirl number, as fuel and hot gases would be pulled towards the outer recirculation zone [74, 114]. Insight into whether the fuel property effects shown in this study would apply to a more realistic combustor with a similar fuel injector can be gained by considering the experimental results of Stouffer et al. [105] and Corporan et al. [103]. Both groups also

used a pressure atomizer to test a subset of the fuels in the present work. Consistent with the results in this study, the derived cetane number correlated best with the data of Stouffer et al. [105]. Their data was taken at an air inlet temperature of 394 K in a combustor with an effusion cooled liner, dilution air jets, and a different swirler configuration. The data of Corporan et al. [103] was taken in a full-scale engine at an air inlet temperature of approximately 310 K. They also found that easily vaporized fuels had the best lean blowout performance, with their data correlating most strongly with T_{50}.

Fuel blending is very important from a practical standpoint because alternative jet fuels will initially be implemented in blended proportions with traditional jet fuels. This is because the available supply of any alternative jet fuel is insufficient to meet the required demand. Three fuel blends of A-2 and C-1 were tested in 80/20, 50/50, and 20/80 proportions. These fuels had very different properties and demonstrated how a traditional jet fuel will perform when blended with an alternative fuel. The lean blowout sensitivities of these blends were also shown to be dependent on the air inlet temperature. At 300 K, the blends each blew out at approximately the same equivalence ratio. This is likely caused by each of the blends having very similar boiling point temperatures. At 450 K, there was a linear relationship between the blowout equivalence ratio and fraction of fuel C-1 that was blended with A-2, which approximately correlated with the spread in derived cetane number between these fuels. Interestingly, at 550 K a nonlinear relationship existed between the blowout equivalence ratio and the fraction of C-1 in the blend. Even though this was known to be a kinetically limited regime, the addition of 20% A-2 to C-1 caused this blend to blow out at a higher equivalence ratio than either the complete A-2 or C-1 fuels. An explanation for this observed phenomenon was not identified.

An interesting coupling between physical and chemical fuel properties, known as preferential vaporization, was also shown to influence lean blowout boundaries. Preferential vaporization occurs when a fraction of the fuel constituents evaporate quickly while the rest remain in liquid form. This can cause the chemical properties of these initially vaporized constituents to dominate the kinetics under threshold combustion conditions. Therefore, the fuel properties based on the entire fuel composition may not be as meaningful for the lean blowout problem as those of the initially vaporized fraction. Measurements of the 20% DCN were made for six of the fuels and were shown to improve the correlations with lean blowout boundaries across all of the air inlet temperatures. The greatest improvements in the correlations were observed for the kinetically limited 450 K and 550 K conditions. However, a weaker correlation between the blowout equivalence ratio and the 20% DCN was also observed at 300 K. In addition, two fuels with identical DCNs but very different potentials for preferential vaporization were also tested. The initially vaporized constituents of one of the fuels was very reactive, whereas the other fuel maintained constant kinetic properties throughout its distillation process. The fuel with the reactive front end, caused by preferential vaporization, always blew out at a lower equivalence ratio than the fuel with the constant chemical properties. These results suggest that preferential vaporization effects must be a key consideration in the design of alternative jet fuels.

Distinguishing between correlation and causality is one of the key challenges in alternative fuels studies. Because the properties of a fuel are rooted in its chemical structure, each of these properties are at least partially dependent on, and correlated with, the others [95]. This creates challenges in identifying the cause of a certain phenomenon,

such as lean blowout, as an observed correlation with a particular fuel property may be in reality caused by a different fuel property with which it is correlated. A supervised machine learning technique, known as the Hierarchical Non-negative Garrote method, was used to circumvent these variable selection challenges and perform a multiple linear regression. This method is able to account for correlations within variables and identifies the relative contributions of a smaller number of significant variables on a particular outcome. The Hierarchical Non-negative Garrote method was applied to the fuel screening data and confirmed that the DCN is indeed the fuel property that governs the 450 K lean blowout behavior, without any other fuel properties making a significant contribution. Although the regression also confirmed the findings of the single variable correlations at 300 K and 550 K, it additionally revealed fuel properties that have secondary effects on LBO that were not apparent otherwise. For example, even in the vaporization limited 300 K regime, the regression indicated that the DCN has a secondary effect. Furthermore, the DCN was shown to be the dominant fuel property at 550 K, with a secondary dependence on T_{50}. This T_{50} dependence is likely caused by thermoacoustic dynamics that are only present at 550 K, as the dynamic pressure RMS was most closely correlated with T_{50}.

Planar measurements were used to understand the details of the flame and flow structure for multiple fuel types and even during a blowout transient. As very few measurements of this kind have been published for spray flames at elevated pressure, the insights gained from these measurements were very valuable. Both under stable burning conditions and during the blowout transient, an outer shear layer stabilized flame was observed that rarely experienced burning in the central recirculation zone. This suggests a different mechanism for blowoff than the bluff-body stabilized flame case, where blowoff

occurs when reactant entrainment in the bluff-body recirculation zone cools the flame beyond a critical level. Furthermore, the bulk flow field boundaries were compared between three fuels with very different fuel properties. The average flow features of these fuels were found to be basically identical, suggesting that the flow field in this study did not change significantly with fuel composition.

Lastly, the dynamics of these flames in the near-blowoff stages were also considered. It is understood that a series of extinction and re-ignition processes precede complete blowout of the flame. These processes were quantified using chemiluminescence measurements as a function of blowoff proximity and were compared at two air inlet temperatures: 300 K and 450 K. PMT measurements were used to characterize the extinction history of these flames using a double threshold method. In addition, high speed imaging was used to analyze the space-time evolution of the most upstream point of the flame near blowoff for four of the fuels. Fast motion of these points upstream relative to the flow velocity were interpreted as flame re-ignition. It was found that local extinction processes preceding blowoff, known as LBO precursor events, increase in frequency and duration as LBO is approached. Furthermore, it was shown that 450 K flames will recover from these LBO precursors approximately 20-50% of the time by re-ignition when blowoff is imminent. Re-ignition recoveries were much rarer at 300 K. The equivalence ratio at which local extinction processes began, ϕ_{event}, was determined and compared between fuels. This allowed for the determination of $(\phi_{event} - \phi_{LBO})$, which is important from an operational standpoint because it determines how close a combustor can safely approach blowoff before passenger safety is threatened. At 300 K, $(\phi_{event} - \phi_{LBO})$ was essentially

constant between fuels. However, at 450 K (ϕ_{event} - ϕ_{LBO}) was positively correlated with the DCN.

Although previous researchers have shown correlations between lean blowout boundaries and a particular fuel property, absent from the literature is a rigorous demonstration of why these fuel properties are critical for flame stability. Therefore, the fuel properties which were shown to be lean blowout limiting were correlated with extinction and re-ignition processes that precede complete blowout of the flame. The LBO precursor event analysis showed that high boiling point temperature fuels are much more likely to experience extinction, and their extinction events happen for a longer duration, compared to low boiling point temperature fuels at 300 K. Although recoveries from these LBO precursors through re-ignition were rare at 300 K, they happened most often for the fuel which had the greatest propensity for extinction. In contrast, re-ignition was more common at 450 K, and it was found that the highest DCN fuels recovered from LBO precursors through re-ignition much more often than low DCN fuels. A much weaker correlation was observed between either the event duration or flame extinction history and fuel properties at 450 K. This suggests that extinction characteristics are essentially uniform between fuels at 450 K. Therefore, the positive correlation between (ϕ_{event} - ϕ_{LBO}) and the DCN is likely caused by re-ignition recoveries extending burning to lower equivalence ratios. It should also be noted that high DCN fuels also had lower ϕ_{event} values. Therefore, it appears that high DCN fuels are better able to resist blowoff by delaying the onset of LBO precursor events, and then their improved re-ignition performance allows them to survive longer once these precursor events begin to threaten the stability of the flame.

7.2 Applications for Alternative Jet Fuel Certification, OEMs, and Engine Operators

The findings in this thesis have value for a regulatory agency, such as the Federal Aviation Administration, because they provide helpful information for refining the jet fuel certification standards. It is suggested that the existing jet fuel specification be updated to include minimum DCN and maximum boiling point temperature limits. These limits will be beneficial for streamlining the alternative jet fuel certification process because they will improve the likelihood that a prospective fuel has sufficient flame stability performance.

These contributions also add value for Original Equipment Manufacturers (OEMs) by demonstrating the effects of fuel blending and highlighting new possibilities for high performance fuels. OEMs are primarily interested in the effect that alternative fuels will have on their engines. Therefore, understanding the physics associated with fuel blending is of great concern for them because this is the most immediate way that engines will be affected by alternative fuels. From a long-term perspective, the design of high performance fuels has the potential to greatly improve engine performance. For example, the discussion surrounding preferential vaporization illustrates that only a small fraction of reactive constituents may be necessary for maintaining flame stability. Although high DCN fuels are advantageous from a low power perspective where lean blowout must be avoided, at high power conditions it is desirable to delay the ignition of a fuel for as long as possible to avoid pre-ignition and hardware damage. Therefore, low DCN fuels are better for high power conditions because they reduce harmful emissions by allowing sufficient time for fuel-air mixing. A promising idea initially proposed by Clarence Chang of NASA is that one can potentially design a fuel with a high 20% DCN but a low DCN based on the entire

fuel composition. The high reactivity of the initially vaporized constituents would take effect near LBO and improve the likelihood that a stable flame is maintained. On the other hand, at high power conditions, where the fuel vaporizes rapidly, the low DCN of the entire fuel composition would result in improved mixing and good emissions performance. In addition, since high DCN fuels are generally high in n-paraffins, this strategy would avoid the effect of high molecular weight n-paraffins that cause waxing problems in the fuel at low temperatures.

The findings in this work can also help engine operators to ensure the safe travel of their aircraft. In a real engine, the compressor driven air mass flow rate and the equivalence ratio are coupled. Therefore, as the equivalence ratio is reduced towards blowout, the air mass flow rate and the compressor discharge temperature will decrease. It was thereby shown in the findings of Corporan et al. [103] that although the combustor may be initially operating at a high air inlet temperature, the decrease in compressor discharge temperature as the equivalence ratio is reduced can cause the flame to transition to a regime where its stability is vaporization limited. As blowout equivalence ratios are higher for low air inlet temperatures, the flame may blow out at a higher equivalence ratio than expected based on high temperature considerations. This problem will be avoided if engine operators understand the lean blowout temperature dependence. Furthermore, values of $(\phi_{event} - \phi_{LBO})$ were presented that will allow engine operators to estimate how close they can safely approach LBO.

7.3 Recommendations for Future Work

This work has shown that the governing physics of the lean blowout problem changes with the combustor air inlet temperature. At 300 K, lean blowout was observed to be vaporization limited, whereas at 450 K and 550 K lean blowout was found to be kinetically limited. Determining the exact temperature where the governing physics transitions from being dominated by vaporization to chemical kinetics would be beneficial. Since the effects of combustor pressure were not tested, repeating these experiments at high pressure conditions would complement the conclusions that were drawn about the effects of operating conditions on lean blowout. It would be interesting to know whether the combustor pressure also causes a change in the sensitivity of lean blowout to fuel properties and if the observed air temperature dependence is influenced by the combustor pressure. As the fuel droplet evaporation rates will likely increase with the combustor pressure, it may be that lean blowout is no longer vaporization limited for a high pressure-300 K operating condition and instead is governed by the secondary dependence on the DCN at 300 K. Extending this data set to a variety of combustor pressures would also provide insight into combustor geometry effects on lean blowout, as a more complete set of operating conditions would allow for a direct comparison with the existing data sets in the literature.

Characterizing the dynamics near-blowoff was one of the novel contributions of this work. However, the quantified flame re-ignition behavior was a high variance process. Therefore, it would be beneficial to gather a larger number of CH* chemiluminescence videos to reduce the uncertainty. Furthermore, 10 PMT samples were gathered at both the 300 K and 450 K air temperatures for each of the ten fuels for which these measurements

were taken, in contrast to the hundreds of fuel screening data points. Therefore, an increased number of PMT data samples would also be helpful for solidifying the reported conclusions.

The LBO precursors that precede the lean blowout process were quantified by applying a double threshold technique to PMT measurements. These thresholds were calculated based on a percentage of the moving average of the signal, and this percentage was determined according to a set of published thresholding criteria [17]. The conclusions that were drawn from this analysis could be strengthened by selecting these thresholds in a statistically rigorous way, such as using machine learning techniques.

Although much progress has been made towards characterizing fuel property effects on lean blowout, there is still a great deal of work that must be done towards understanding a mechanism for blowoff in spray flames. It is recommended that the detailed planar measurements that were taken are rigorously analyzed to draw quantitative conclusions and develop a mechanism for blowout. Furthermore, it is needful to analyze the cause of LBO precursor events. These planar measurements were only taken at 450 K. It would be beneficial to gather simultaneous OH-PLIF and PIV data at 300 K as well. This would provide insight into the effects of air inlet temperature on near-blowoff flames and their flow fields. In order for this analysis to be definitive, a rigorous technique must be developed to separate the OH-PLIF signal from the fuel spray fluorescence. Lastly, it is also unclear what effect the sudden closure of the fuel valve had on the OH-PLIF and PIV data for the blowout transient case. Therefore, it would be desirable to obtain these planar measurements during an authentic blowout transient.

APPENDIX A. S-CURVE: NONMONOTONIC BULKHEAD TEMPERATURE DEPENDENCE

This appendix details the blowout measurement approach and the sensitivity of the blowout equivalence ratio to the thermal state of the combustor. It is an extension of Section 2.2 and shows samples of the data that was acquired. As discussed previously, the combustor hardware was intentionally heated and cooled to capture blowout measurements across a range of bulkhead temperatures. Once a heating or cooling phase was completed, the fuel flow rate was gradually decreased until the flame extinguished. It was then immediately re-ignited and the process continued until an equilibrium bulkhead temperature was reached. Figure A.1 shows the resulting data for fuel C-4 at each of the three air inlet temperatures. Only a single air inlet temperature was ever tested on a given experimental day. Data from two separate days of experiments at each air inlet temperature, including six days in total, are overlaid. It can be seen that the data achieved good day-to-day repeatability and showed a linear dependence on the bulkhead temperature. Compare this plot with the corresponding data for fuel A-2, shown in Figure A.2. The data for this fuel is not repeatable and often depended non-monotonically on the bulkhead temperature, with an "S-curve" shape. Although these issues were never completely resolved, only comparing blowout equivalence ratios with a negatively sloped dependence on the bulkhead temperature (e.g., less than 600 K for the 450 K data shown in Figure A.2) prevented them from influencing the previously shown results.

The experimental measurements showed that fuel composition differences influenced both the blowout sensitivity to bulkhead temperature, and the likelihood that

results were consistent across multiple repetitions of the experiment. Fuels that are composed almost entirely of either straight chain or branched alkanes maintain the near-linear dependence upon bulkhead temperature that is observed in Figure A.1. Fuels with large quantities of aromatics and cycloalkanes often display the nonlinear behavior seen in Figure A.2. Whether a given fuel's blowout performance was repeatable was often, but not always, related to this observed "S-curve" phenomenon. For example, at a fixed bulkhead temperature there was significant scatter in the blowout equivalence ratios for fuel A-1. Yet the data for this fuel had a mostly linear dependence on the bulkhead temperature. C-2 generally followed a linear curve fit but the slope of this fit was not repeatable across different experimental days. However, the fuels which showed the greatest nonlinearity, A-2, A-3, C-3, C-5, C-7, and C-8, also had issues with repeatability. The repeatability of a given fuel was quantified using a composite R^2 value. This value was calculated by averaging the individual R^2 values for a fuel across each of the days that the experiment was performed. Data for each of the air inlet temperatures were combined in this average.

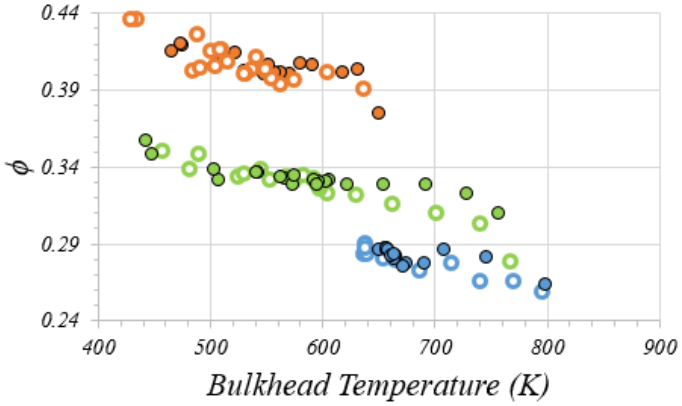

Figure A.1: Dependence of bulkhead temperature on the equivalence ratio at blowout for fuel C-4. Orange symbols represent 300 K data, green symbols represent 450 K data, and blue symbols represent 550 K data. The different marker types represent data from separate days that the experiment was run.

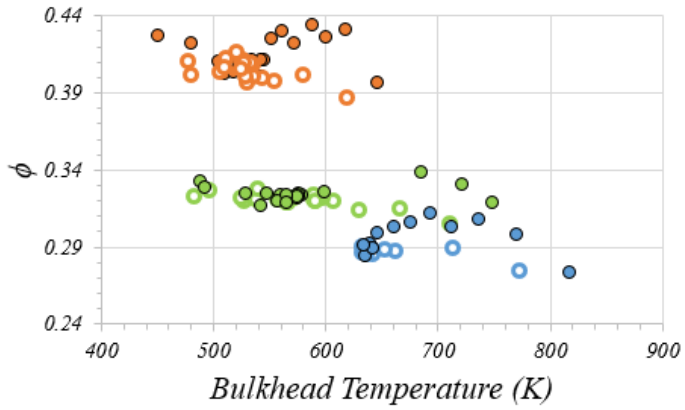

Figure A.2: Dependence of bulkhead temperature on the equivalence ratio at blowout for fuel A-2. Orange symbols represent 300 K data, green symbols represent 450 K data, and blue symbols represent 550 K data. The different marker types represent data from separate days that the experiment was run.

Two hypotheses will be presented for this "S-curve" phenomenon. First, aromatics and cycloalkanes tend to be the jet fuel-type compounds that are most prone to thermal cracking [167]. Therefore, fuels that contain these chemical structures in high quantities are more likely to begin experiencing oxidation reactions prematurely in the fuel injector, which may have some back heating due to radiation from the flame. Figure A.3 shows the dependence of the R^2 value on the amount of mass accumulated in a Quartz Crystal Microbalance test. Consistent with this hypothesis, the fuels which this measurement deemed to be the least thermally stable also had the lowest R^2 values. Furthermore, Figure A.4 shows data from the Jet Fuel Thermal Oxidation Test (ASTM 3241, JFTOT), performed at 285 C. The large deposits created by fuel C-5 are suspected to be a consequence of the very low boiling point temperature of this fuel (see Table 2-2). C-8 and A-3 showed a lesser sensitivity to the JFTOT, but the remaining fuels all appeared to be stable.

Second, certain hydrocarbon compounds promote soot formation and the subsequent flame radiation losses more than others. This could potentially result in lowered flame temperatures and back heating of the incoming fuel injector hardware; i.e., that the thermal state of the combustor is not well characterized by the bulkhead temperature alone. Zeuthen and Blunck [168] experimentally studied the radiation propensities of many of the fuels involved in the present work. They found that fuels with lower H/C ratios had the highest radiative heat losses. Figure A.5 shows the composite R^2 value plotted versus the fuel H/C ratio. It can be seen that there is only a mild correlation between these values.

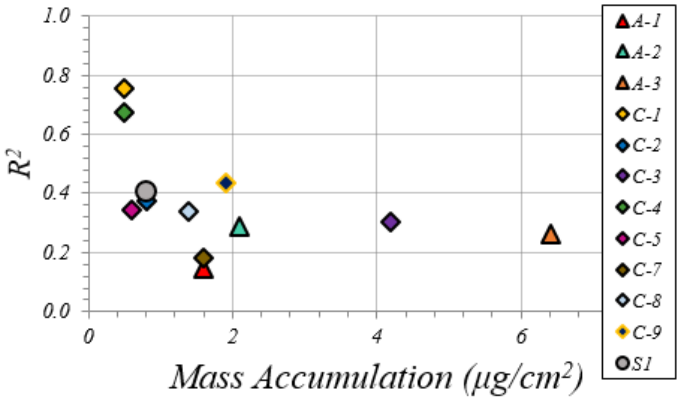

Figure A.3: R^2 value of the blowout equivalence ratio dependence on bulkhead temperature, as a function of the mass accumulated in the Quartz Crystal Microbalance test.

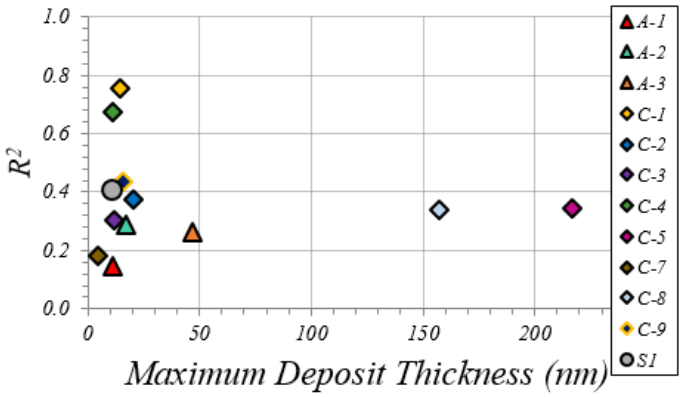

Figure A.4: R^2 value of the blowout equivalence ratio dependence on bulkhead temperature, as a function of the maximum deposit thickness measured by the JFTOT at 285 C.

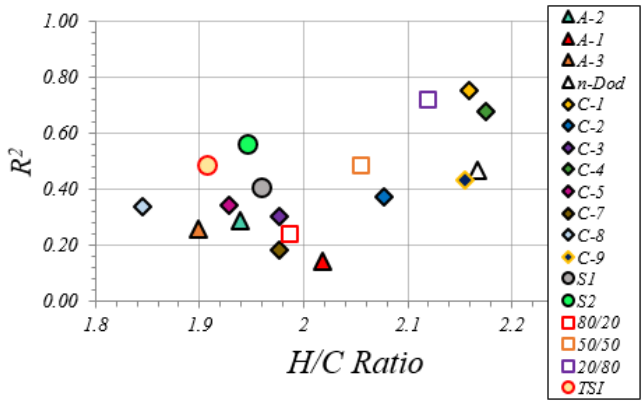

Figure A.5: R^2 value of the blowout equivalence ratio dependence on bulkhead temperature, as a function of the H/C ratio.

APPENDIX B. COMPLETE SET OF FUEL SCREENING CORRELATION PLOTS

This appendix includes the complete set of fuel screening plots, which for space reasons, could not be included in Chapter 4. The presentation of these plots will be organized around the air inlet temperature. The error bars associated with these plots were presented in Figure 4.1. These error bars were calculated using 95% confidence intervals for the day-to-day differences in the $\%\phi$ from fuel A-2. Therefore, the uncertainty associated with fuel A-2 did not make a contribution to these error bars. Alternatively, the data can be presented as the average difference in blowout equivalence ratio between a given fuel and A-2, $\Delta\phi$. The same data that was shown previously is plotted in this manner in Figure B. 1. The error bars in this figure include a contribution from each individual fuel and A-2. They are calculated using the following equation.

$$\sigma_{\Delta\phi,i} = \sqrt{\frac{1}{n-1}\left\{\sum_{j}^{m}\left(1.96\frac{s_{i,j}}{\sqrt{p_{i,j}}} + 1.96\frac{s_{A2,j}}{\sqrt{p_{A2,j}}}\right)^2\right\}} \tag{B.1}$$

where $\sigma_{\Delta\phi,i}$ is the uncertainty in $\Delta\phi$ for each fuel (excluding A-2), n is the number of fuels, m is the number of experimental days, $s_{i,j}$ is the standard deviation corresponding to each fuel and day, and $p_{i,j}$ is the number of data points in the 50 K bulkhead temperature for each fuel on a given experimental day. Uncertainties in the fuel properties can be found in the detailed reference on these fuels by Dr. Tim Edwards [129].

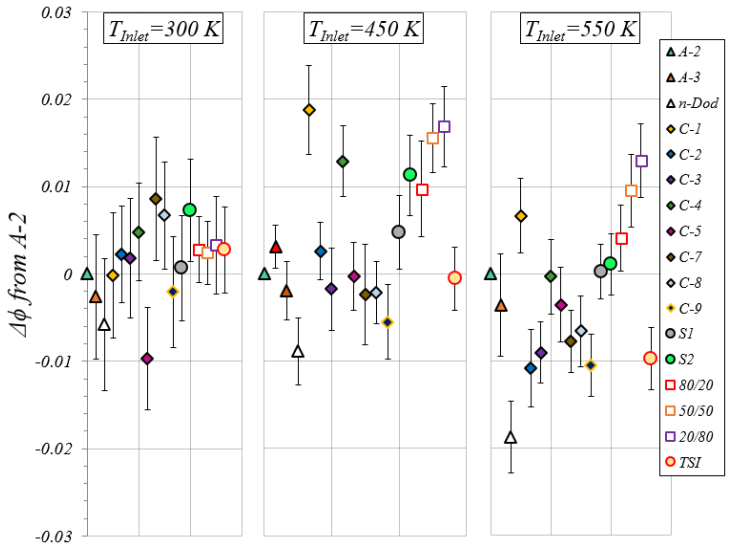

Figure B. 1: Average differences in the blowout equivalence ratio between each fuel and A-2. Error bars represent the RMS of daily 95% confidence intervals.

B.1 300 K Plots

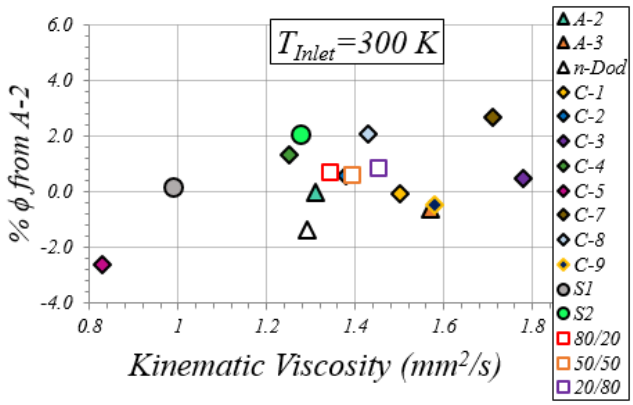

Figure B. 2: Dependence of the percent difference in blowout equivalence ratio from A-2 upon the kinematic viscosity. The data is compared at a bulkhead temperature of 500 K.

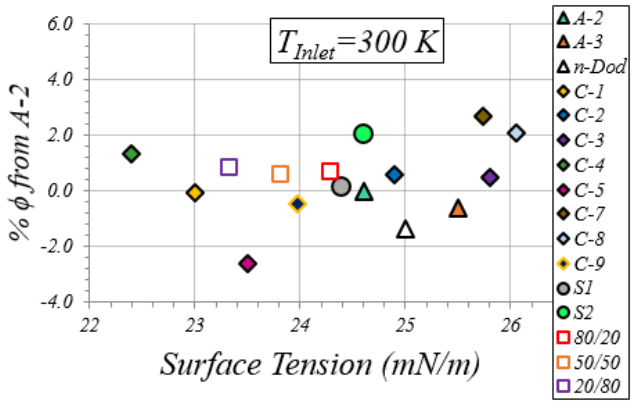

Figure B. 3: Dependence of the percent difference in blowout equivalence ratio from A-2 upon the surface tension. The data is compared at a bulkhead temperature of 500 K.

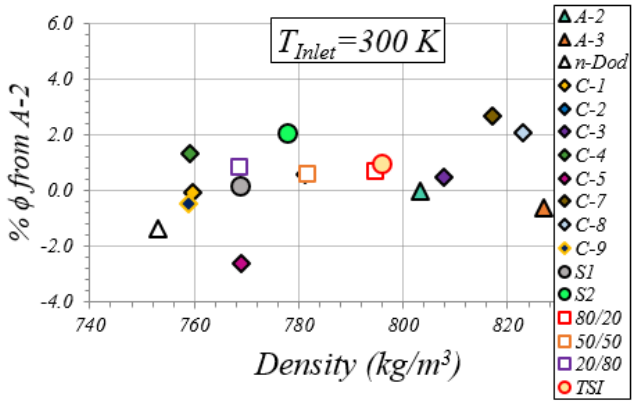

Figure B. 4: Dependence of the percent difference in blowout equivalence ratio from A-2 upon the fuel density. The data is compared at a bulkhead temperature of 500 K.

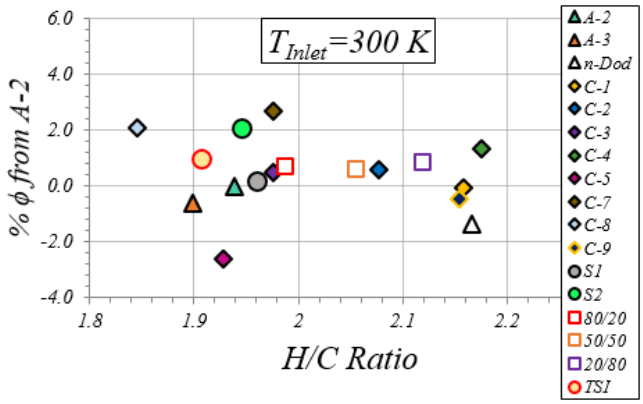

Figure B. 5: Dependence of the percent difference in blowout equivalence ratio from A-2 upon the H/C ratio. The data is compared at a bulkhead temperature of 500 K.

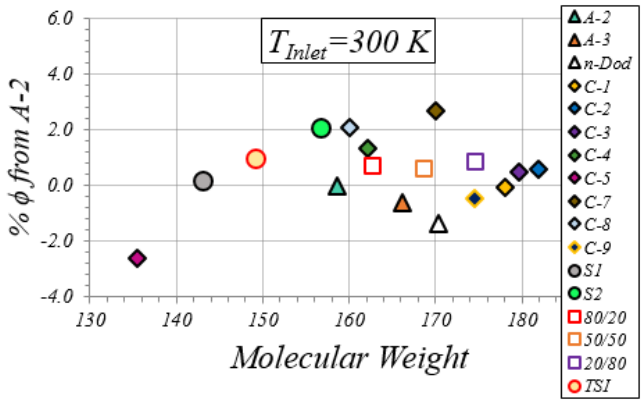

Figure B. 6: Dependence of the percent difference in blowout equivalence ratio from A-2 upon the molecular weight. The data is compared at a bulkhead temperature of 500 K.

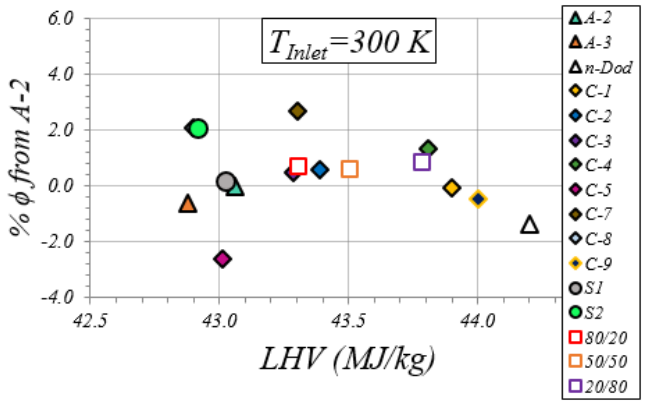

Figure B. 7: Dependence of the percent difference in blowout equivalence ratio from A-2 upon the lower heating value. The data is compared at a bulkhead temperature of 500 K.

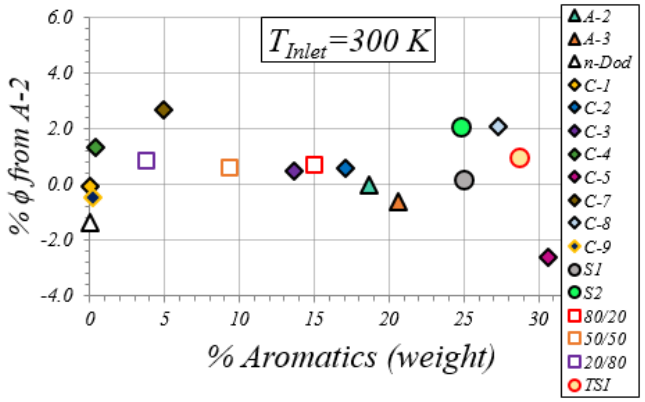

Figure B. 8: Dependence of the percent difference in blowout equivalence ratio from A-2 upon the percentage of aromatics in the fuel. The data is compared at a bulkhead temperature of 500 K.

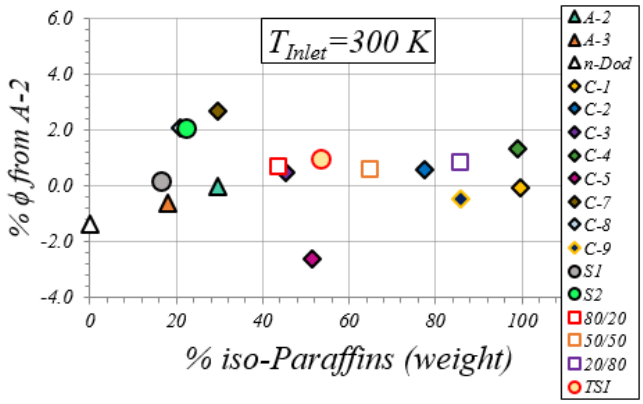

Figure B. 9: Dependence of the percent difference in blowout equivalence ratio from A-2 upon the percentage of iso-paraffins in the fuel. The data is compared at a bulkhead temperature of 500 K.

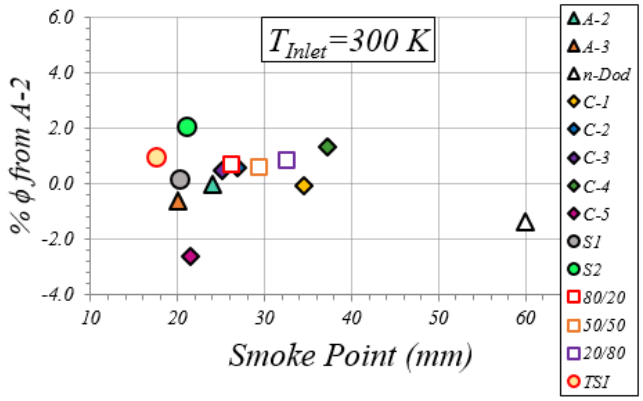

Figure B. 10: Dependence of the percent difference in blowout equivalence ratio from A-2 upon the smoke point. The data is compared at a bulkhead temperature of 500 K.

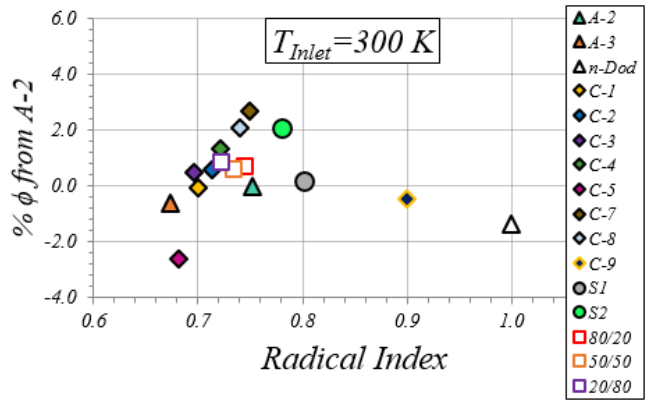

Figure B. 11: Dependence of the percent difference in blowout equivalence ratio from A-2 upon the radical index. The data is compared at a bulkhead temperature of 500 K.

B.2 450 K Plots

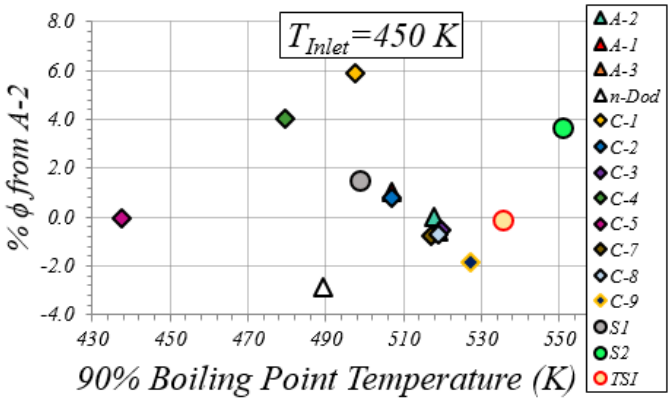

Figure B. 12: Dependence of the percent difference in blowout equivalence ratio from A-2 upon T_{90}. The data is compared at a bulkhead temperature of 550 K.

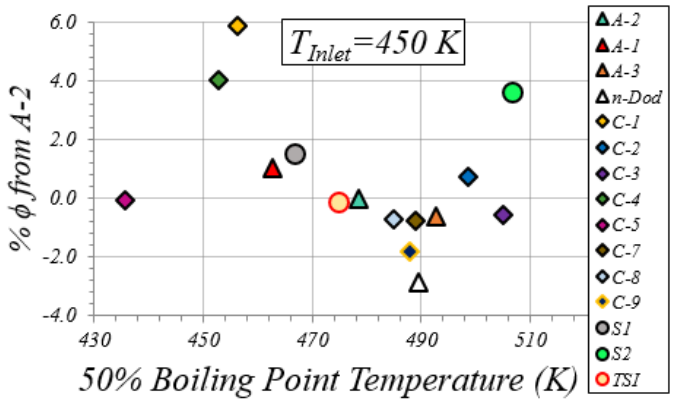

Figure B. 13: Dependence of the percent difference in blowout equivalence ratio from A-2 upon T_{50}. The data is compared at a bulkhead temperature of 550 K.

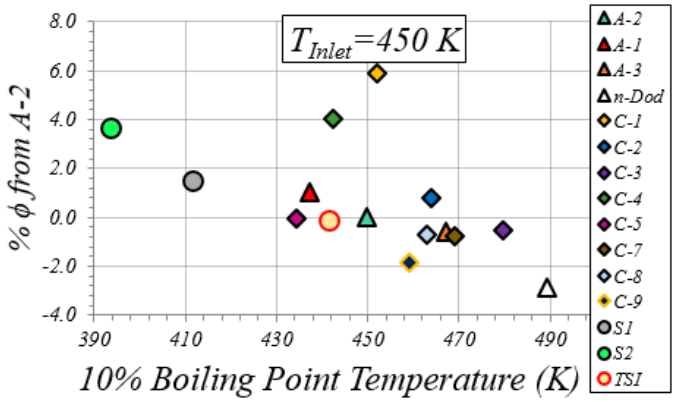

Figure B. 14: Dependence of the percent difference in blowout equivalence ratio from A-2 upon T_{10}. The data is compared at a bulkhead temperature of 550 K.

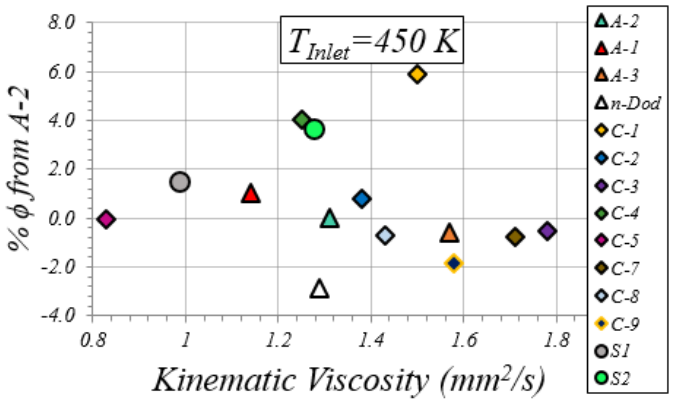

Figure B. 15: Dependence of the percent difference in blowout equivalence ratio from A-2 upon the kinematic viscosity. The data is compared at a bulkhead temperature of 550 K.

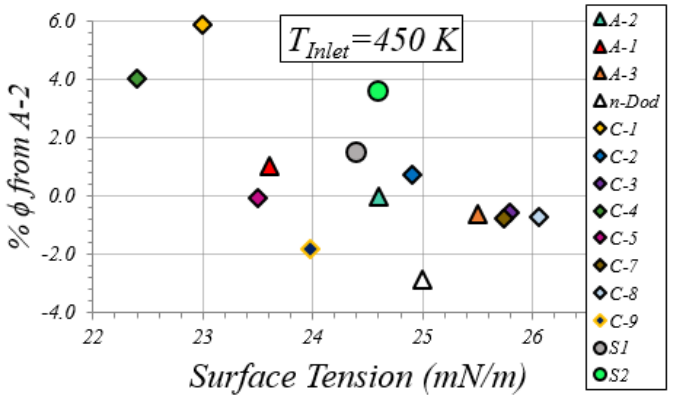

Figure B. 16: Dependence of the percent difference in blowout equivalence ratio from A-2 upon the surface tension. The data is compared at a bulkhead temperature of 550 K.

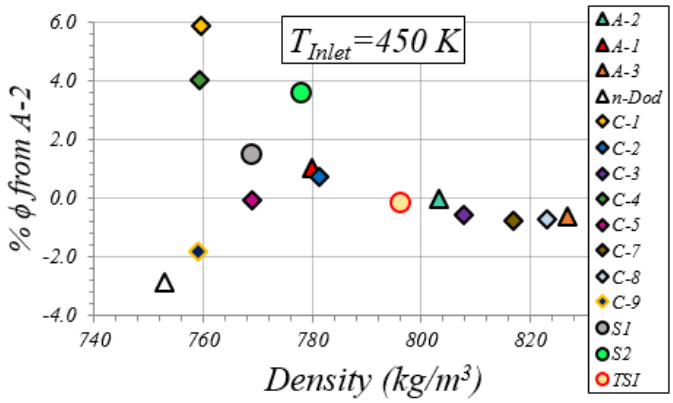

Figure B. 17: Dependence of the percent difference in blowout equivalence ratio from A-2 upon the fuel density. The data is compared at a bulkhead temperature of 550 K.

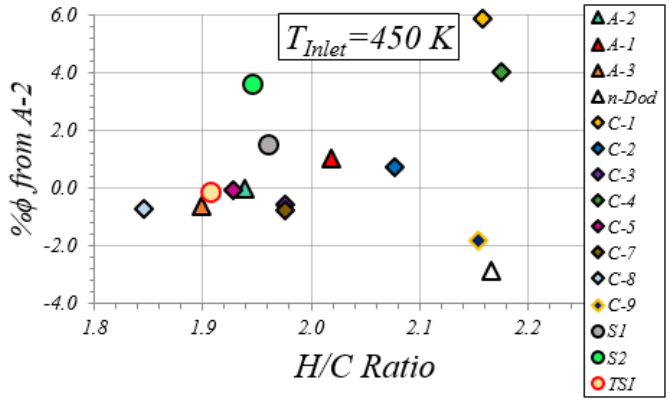

Figure B. 18: Dependence of the percent difference in blowout equivalence ratio from A-2 upon the H/C ratio. The data is compared at a bulkhead temperature of 550 K.

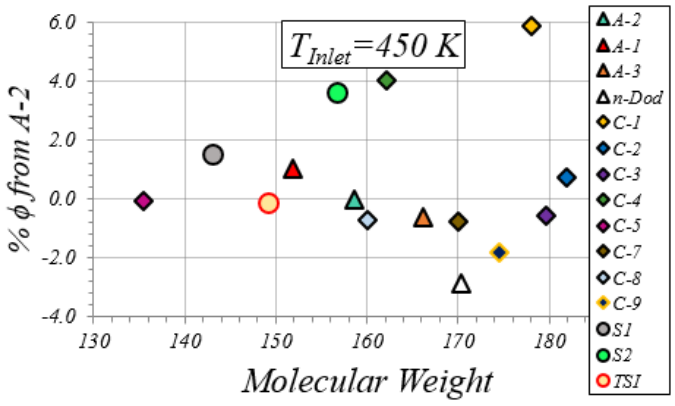

Figure B. 19: Dependence of the percent difference in blowout equivalence ratio from A-2 upon the molecular weight. The data is compared at a bulkhead temperature of 550 K.

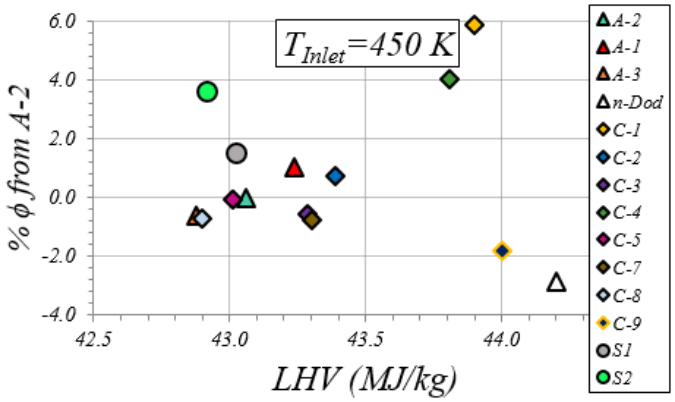

Figure B. 20: Dependence of the percent difference in blowout equivalence ratio from A-2 upon the lower heating value. The data is compared at a bulkhead temperature of 550 K.

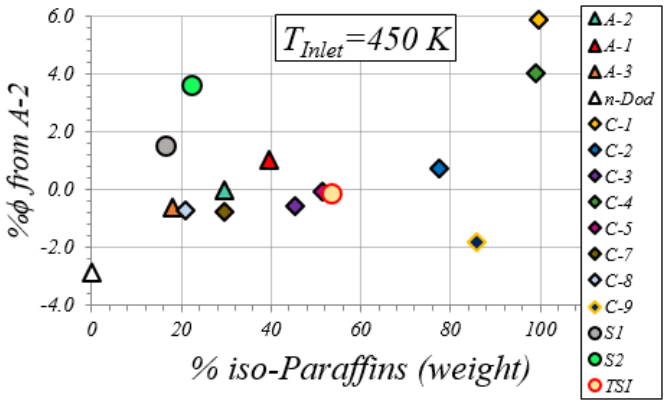

Figure B. 21: Dependence of the percent difference in blowout equivalence ratio from A-2 upon the percentage of iso-paraffins in the fuel. The data is compared at a bulkhead temperature of 550 K.

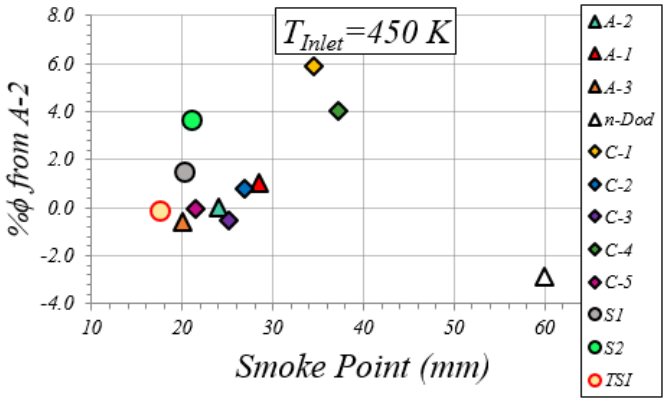

Figure B. 22: Dependence of the percent difference in blowout equivalence ratio from A-2 upon the smoke point. The data is compared at a bulkhead temperature of 550 K.

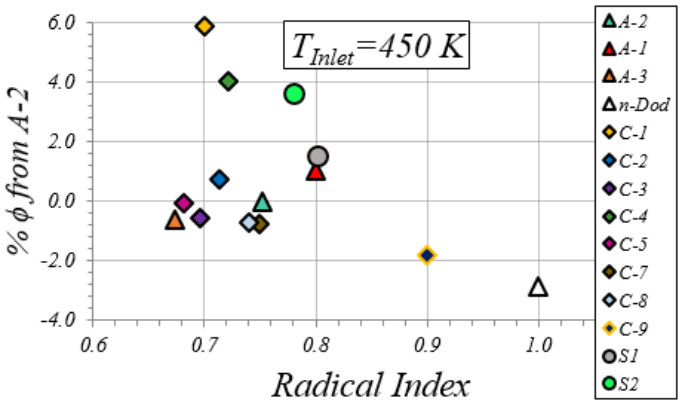

Figure B. 23: Dependence of the percent difference in blowout equivalence ratio from A-2 upon the radical index. The data is compared at a bulkhead temperature of 550 K.

B.3 550 K Plots

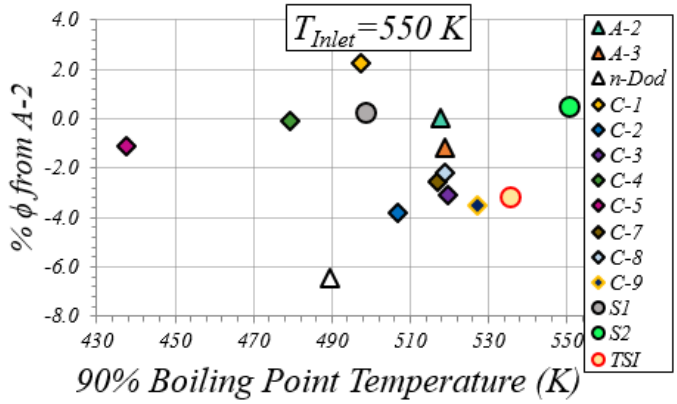

Figure B. 24: Dependence of the percent difference in blowout equivalence ratio from A-2 upon T_{90}. The data is compared at a bulkhead temperature of 640 K.

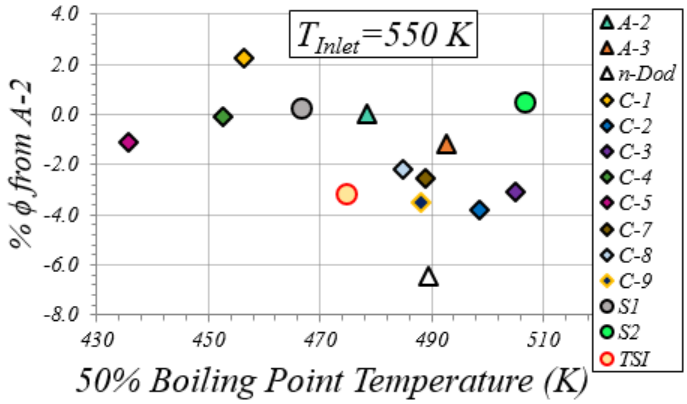

Figure B. 25: Dependence of the percent difference in blowout equivalence ratio from A-2 upon T_{50}. The data is compared at a bulkhead temperature of 640 K.

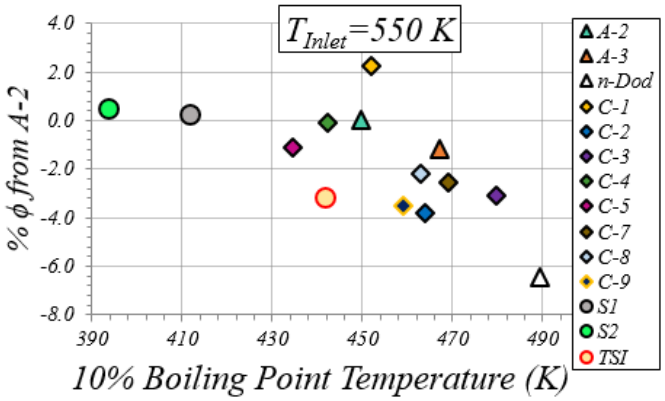

Figure B. 26: Dependence of the percent difference in blowout equivalence ratio from A-2 upon T_{10}. The data is compared at a bulkhead temperature of 640 K.

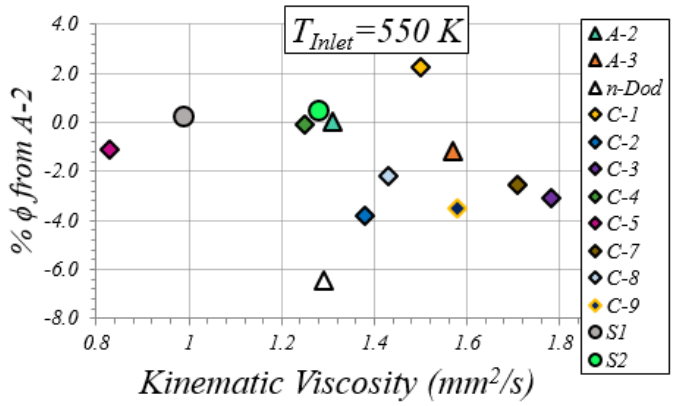

Figure B. 27: Dependence of the percent difference in blowout equivalence ratio from A-2 upon the kinematic viscosity. The data is compared at a bulkhead temperature of 640 K.

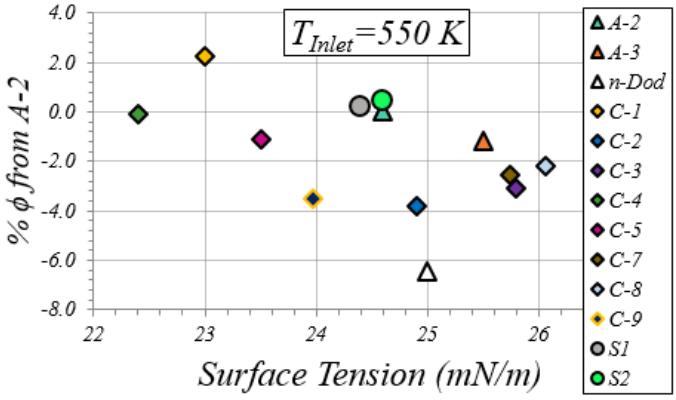

Figure B. 28: Dependence of the percent difference in blowout equivalence ratio from A-2 upon the surface tension. The data is compared at a bulkhead temperature of 640 K.

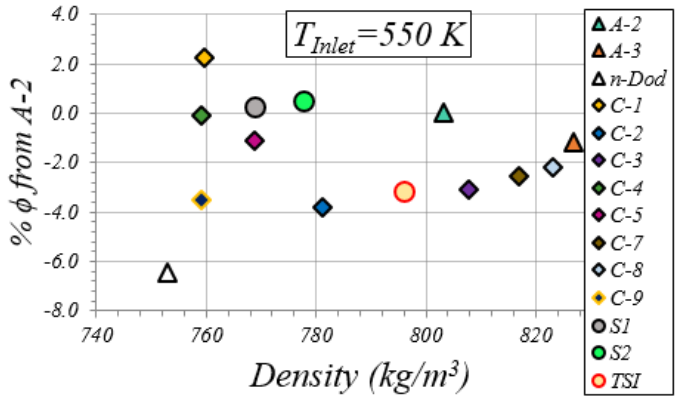

Figure B. 29: Dependence of the percent difference in blowout equivalence ratio from A-2 upon the fuel density. The data is compared at a bulkhead temperature of 640 K.

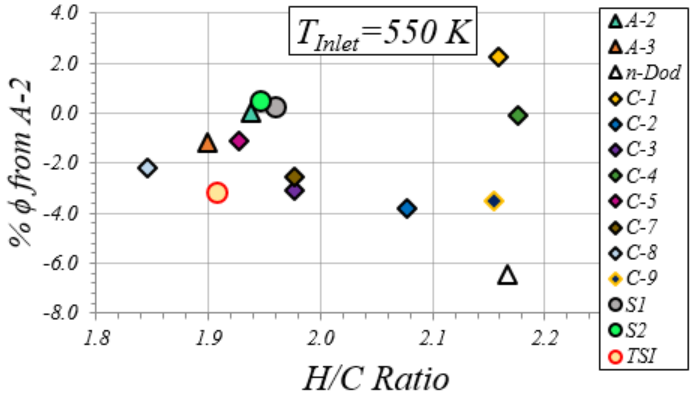

Figure B. 30: Dependence of the percent difference in blowout equivalence ratio from A-2 upon the H/C ratio. The data is compared at a bulkhead temperature of 640 K.

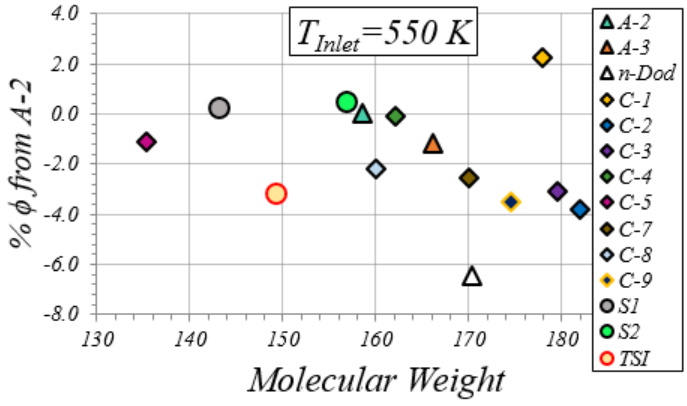

Figure B. 31: Dependence of the percent difference in blowout equivalence ratio from A-2 upon the molecular weight. The data is compared at a bulkhead temperature of 640 K.

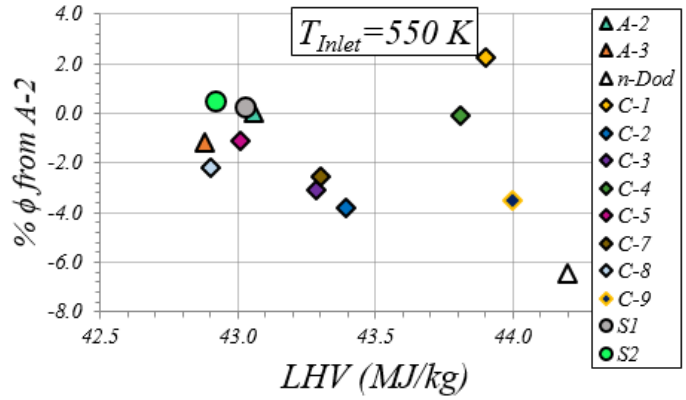

Figure B. 32: Dependence of the percent difference in blowout equivalence ratio from A-2 upon the lower heating value. The data is compared at a bulkhead temperature of 640 K.

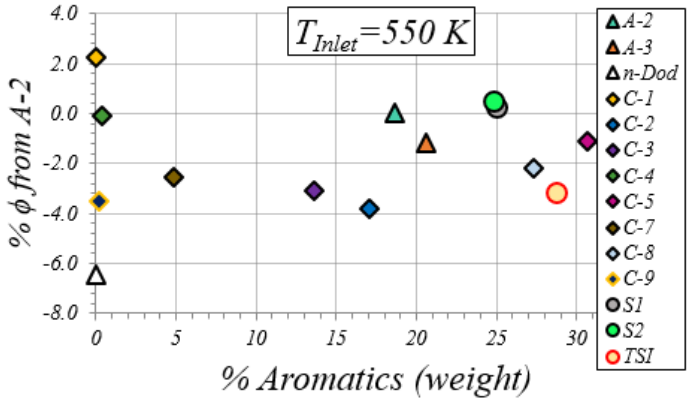

Figure B. 33: Dependence of the percent difference in blowout equivalence ratio from A-2 upon the percentage of aromatics in the fuel. The data is compared at a bulkhead temperature of 640 K.

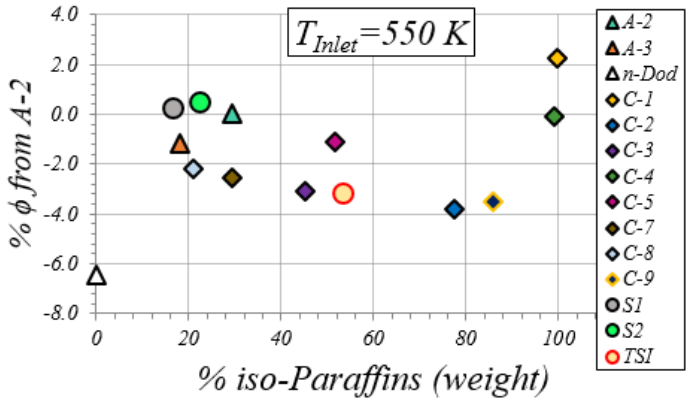

Figure B. 34: Dependence of the percent difference in blowout equivalence ratio from A-2 upon the percentage of iso-paraffins in the fuel. The data is compared at a bulkhead temperature of 640 K.

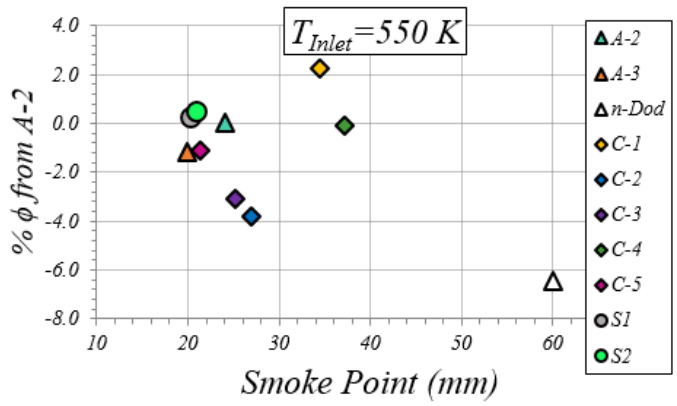

Figure B. 35: Dependence of the percent difference in blowout equivalence ratio from A-2 upon the smoke point. The data is compared at a bulkhead temperature of 640 K.

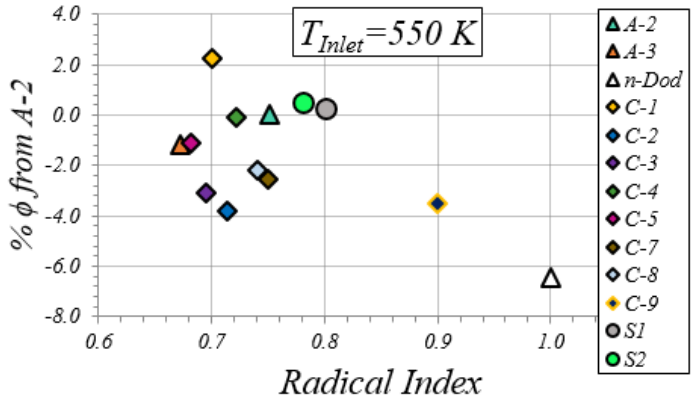

Figure B. 36: Dependence of the percent difference in blowout equivalence ratio from A-2 upon the radical index. The data is compared at a bulkhead temperature of 640 K.

APPENDIX C. NEAR-BLOWOFF DYNAMICS PLOTS WITH ADJUSTED THRESHOLDS

Since the % v_{up} < -30 m/s values shown in Section 6.4 depend on the number of LBO precursor events, they are a threshold dependent quantity. The number of these extinction events that occurred during each CH* chemiluminescence video was determined by integrating the intensity in each image and then applying the same double threshold method that was described in Section 3.3 in reference to the PMT measurements. This appendix demonstrates how the plots shown in Section 6.4 change when the double threshold values are adjusted slightly. Updated plots will only be shown for the 450 K air inlet temperature cases, as slight changes in the selected thresholds did not affect the 300 K results. It can be seen that these % v_{up} < -30 m/s plots are not a strong function of the chosen threshold. Furthermore, the $\%\tau_{ext}$ values calculated from the CH* chemiluminescence videos were comparable to those calculated from the PMT measurements, with average values ranging from 2.8-6.8% between fuels at 450 K and 1.5-7% at 300 K. The uncertainty in this analysis is driven largely by the sample size, as 2-8 CH* chemiluminescence videos were gathered for each fuel (see Table 2-4). The difficulty involved in obtaining these measurements prevented more data from being acquired.

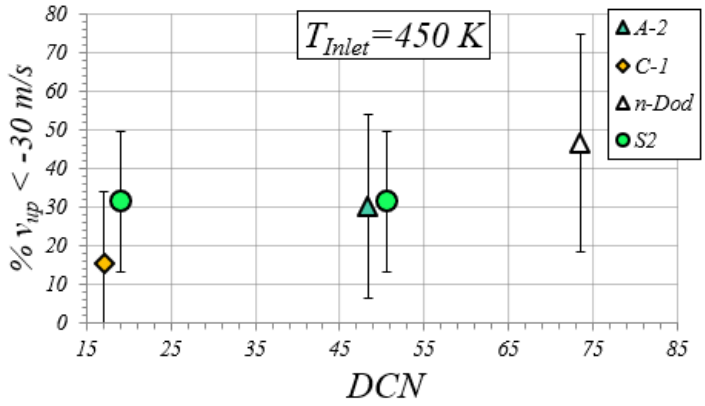

Figure C. 1: % v_{up} < -30 m/s at 450 K plotted against the DCN. These results are shown using slightly lower thresholds than the values used in Section 6.4. Since the role of preferential vaporization on re-ignition is unclear, both the 20% DCN and the DCN based on the entire fuel composition are shown for fuel S2. Error bars represent 95% confidence intervals.

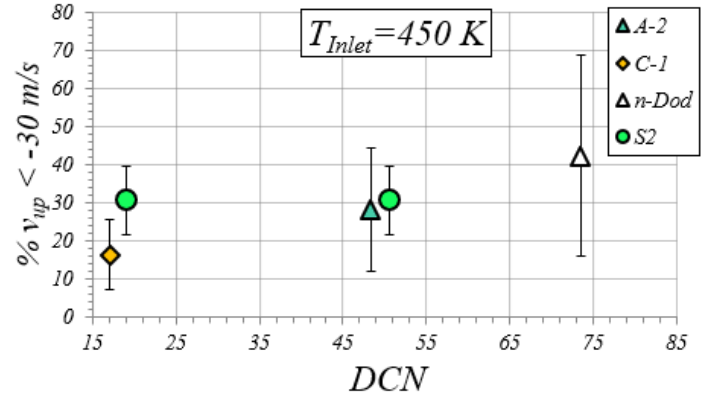

Figure C. 2: % v_{up} < -30 m/s at 450 K plotted against the DCN. These results are shown using slightly higher thresholds than the values used in Section 6.4. Since the role of preferential vaporization on re-ignition is unclear, both the 20% DCN and the DCN based on the entire fuel composition are shown for fuel S2. Error bars represent 95% confidence intervals.

APPENDIX D. RE-IGNITION IMAGE SEQUENCES

This appendix includes additional examples of re-ignition image sequences for the 450 K air inlet temperature cases. Rather than using a fixed threshold to define the flame edge, an automated technique that applied Otsu's method [156] was used to set a global threshold for each image. This procedure accounted for differences in the CH* emission intensity between fuels. The edge detection method is described in more detail in Section 3.2.

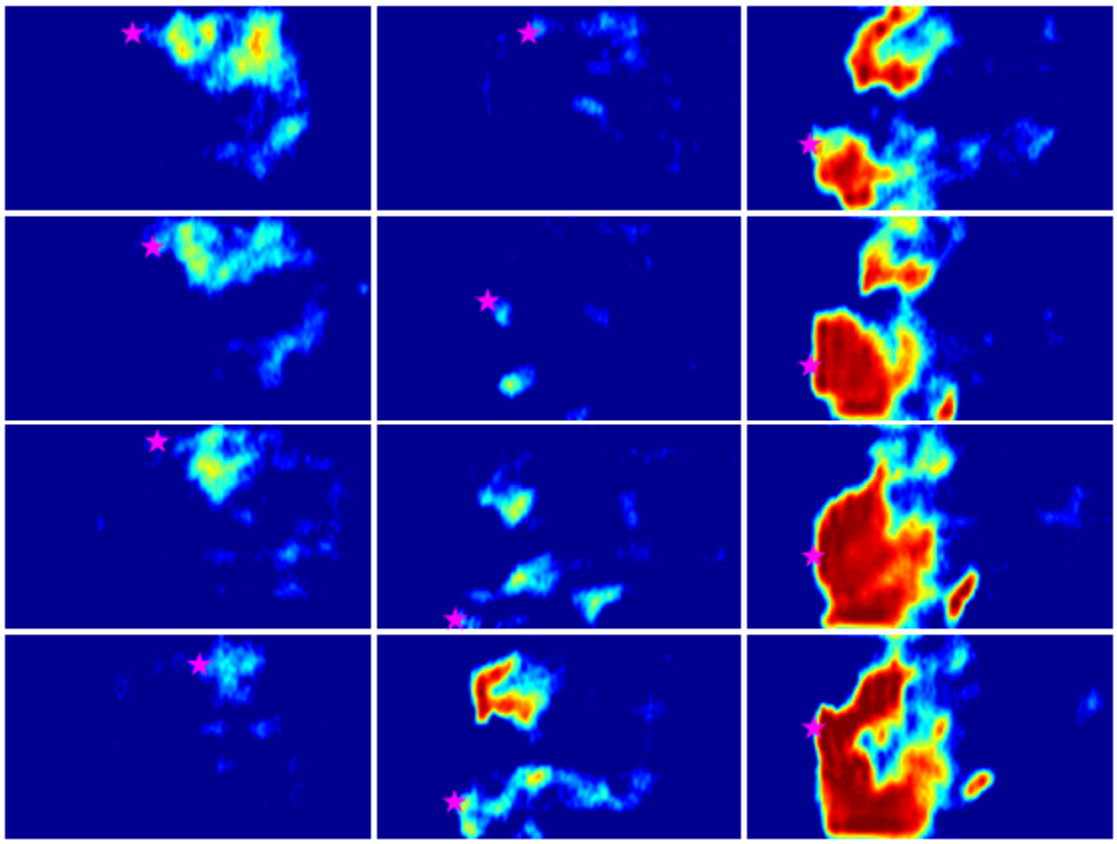

Figure D. 1: Twelve successive CH* chemiluminescence images taken during an LBO precursor event. The star denotes the most upstream spatial location of luminosity. A-2 is burning in these images with an air inlet temperature of 450 K.

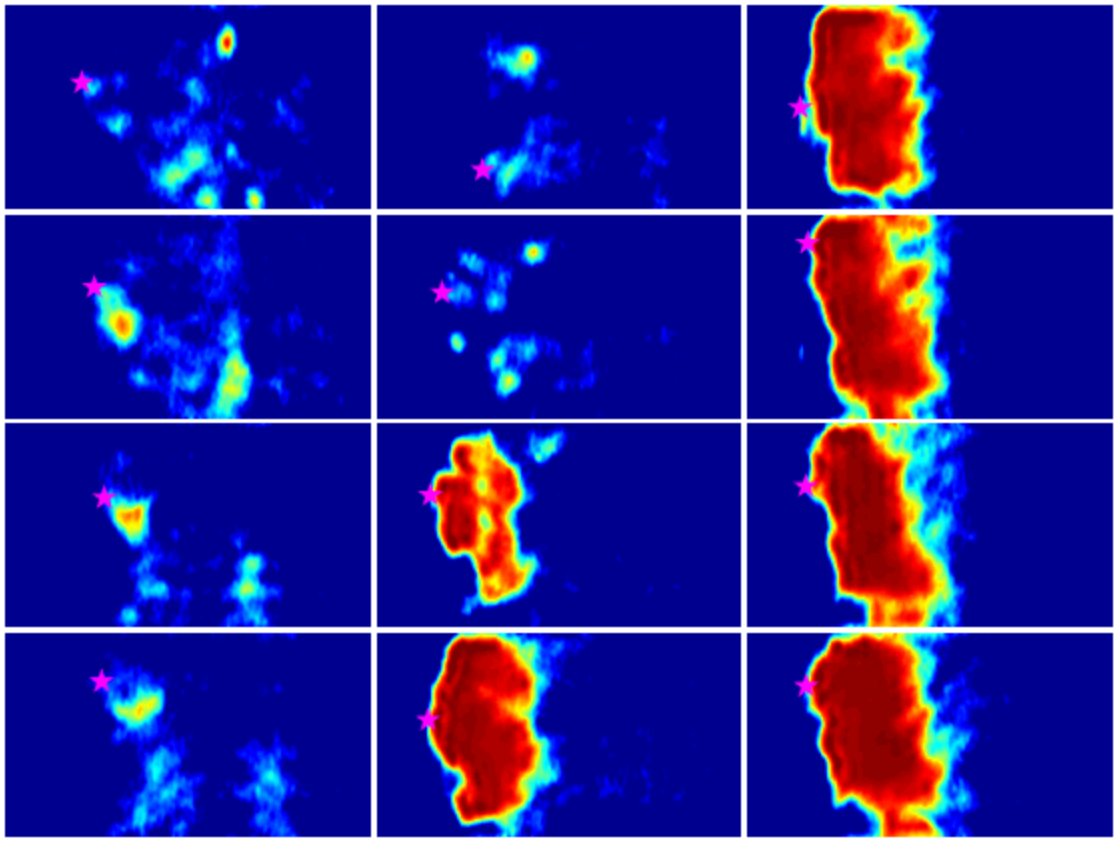

Figure D. 2: Twelve successive CH* chemiluminescence images taken during an LBO precursor event. The star denotes the most upstream spatial location of luminosity. A-2 is burning in these images with an air inlet temperature of 450 K.

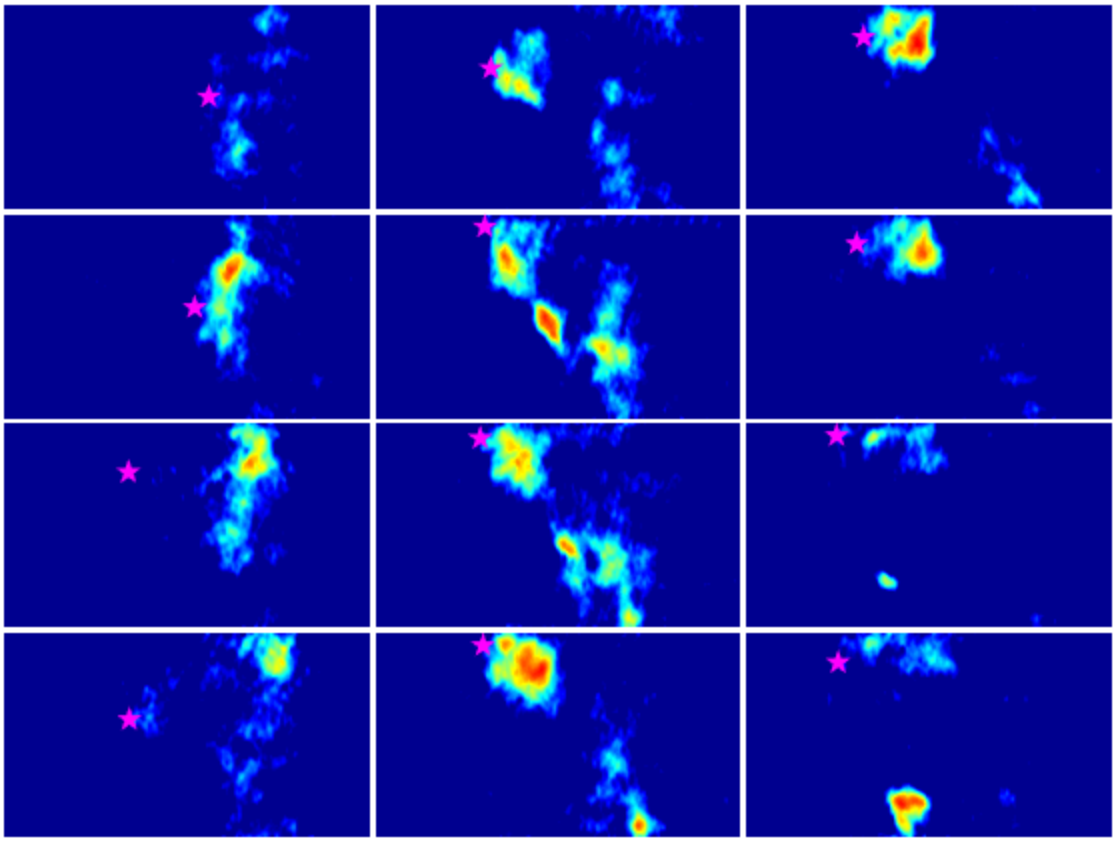

Figure D. 3: Twelve successive CH* chemiluminescence images taken during an LBO precursor event. The star denotes the most upstream spatial location of luminosity. A-2 is burning in these images with an air inlet temperature of 450 K.

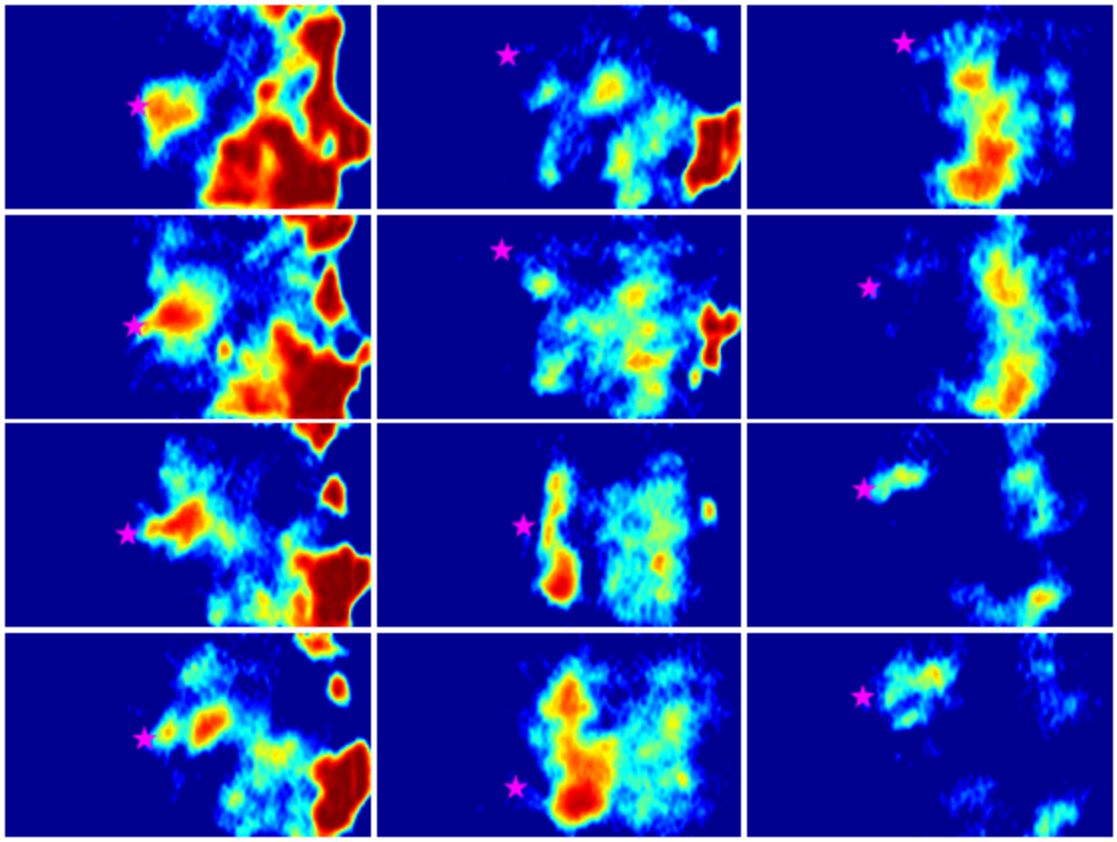

Figure D. 4: Twelve successive CH* chemiluminescence images taken during an LBO precursor event. The star denotes the most upstream spatial location of luminosity. A-2 is burning in these images with an air inlet temperature of 450 K.

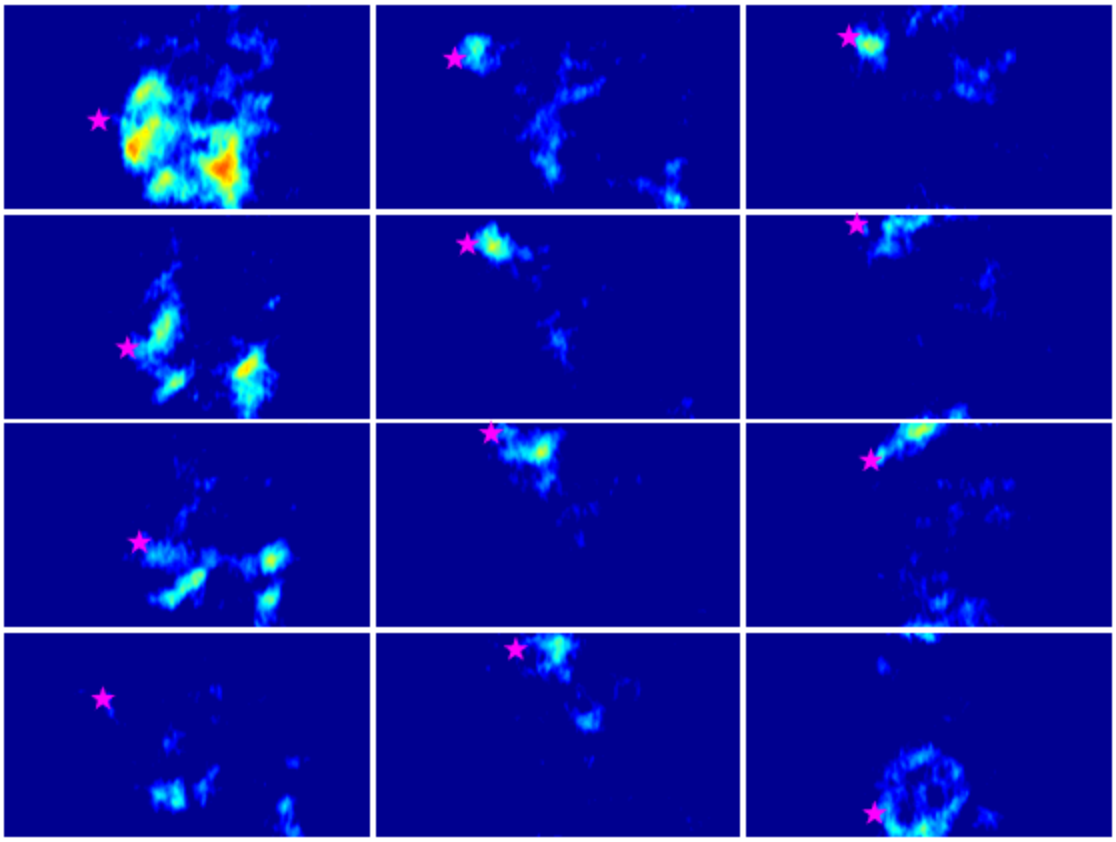

Figure D. 5: Twelve successive CH* chemiluminescence images taken during an LBO precursor event. The star denotes the most upstream spatial location of luminosity. A-2 is burning in these images with an air inlet temperature of 450 K.

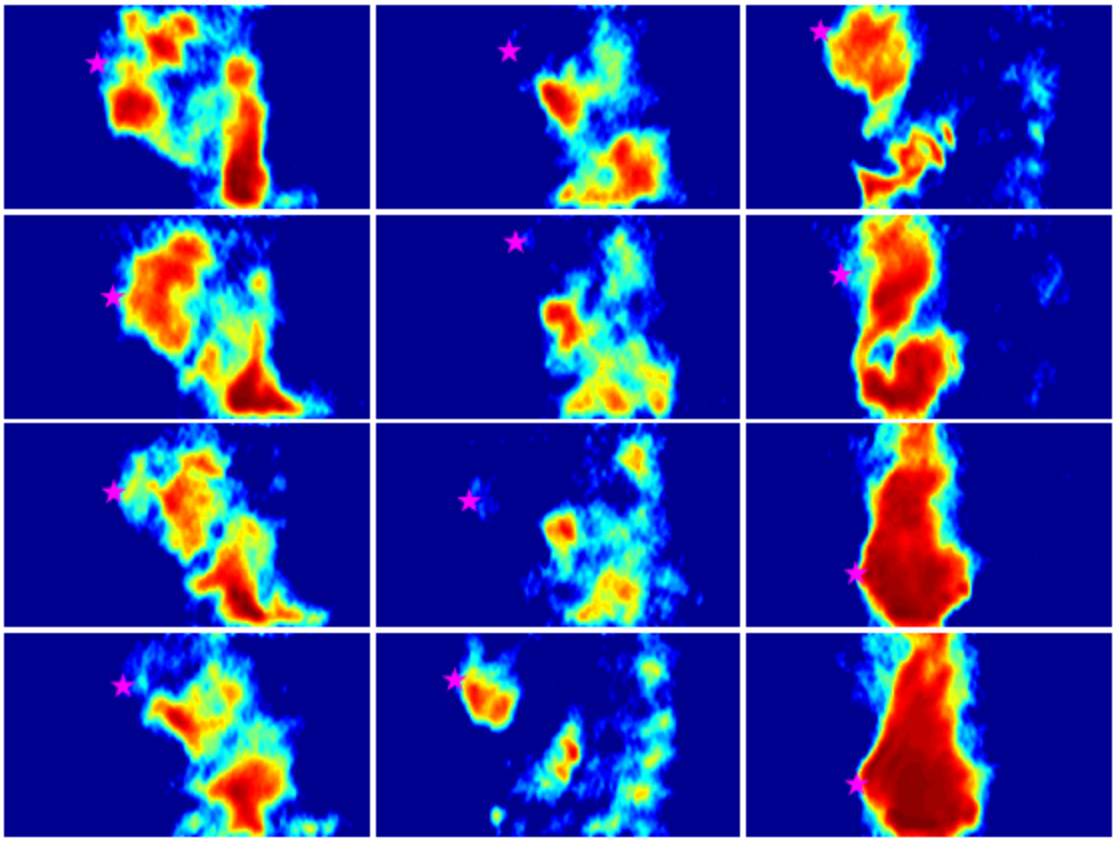

Figure D. 6: Twelve successive CH* chemiluminescence images taken during an LBO precursor event. The star denotes the most upstream spatial location of luminosity. A-2 is burning in these images with an air inlet temperature of 450 K.

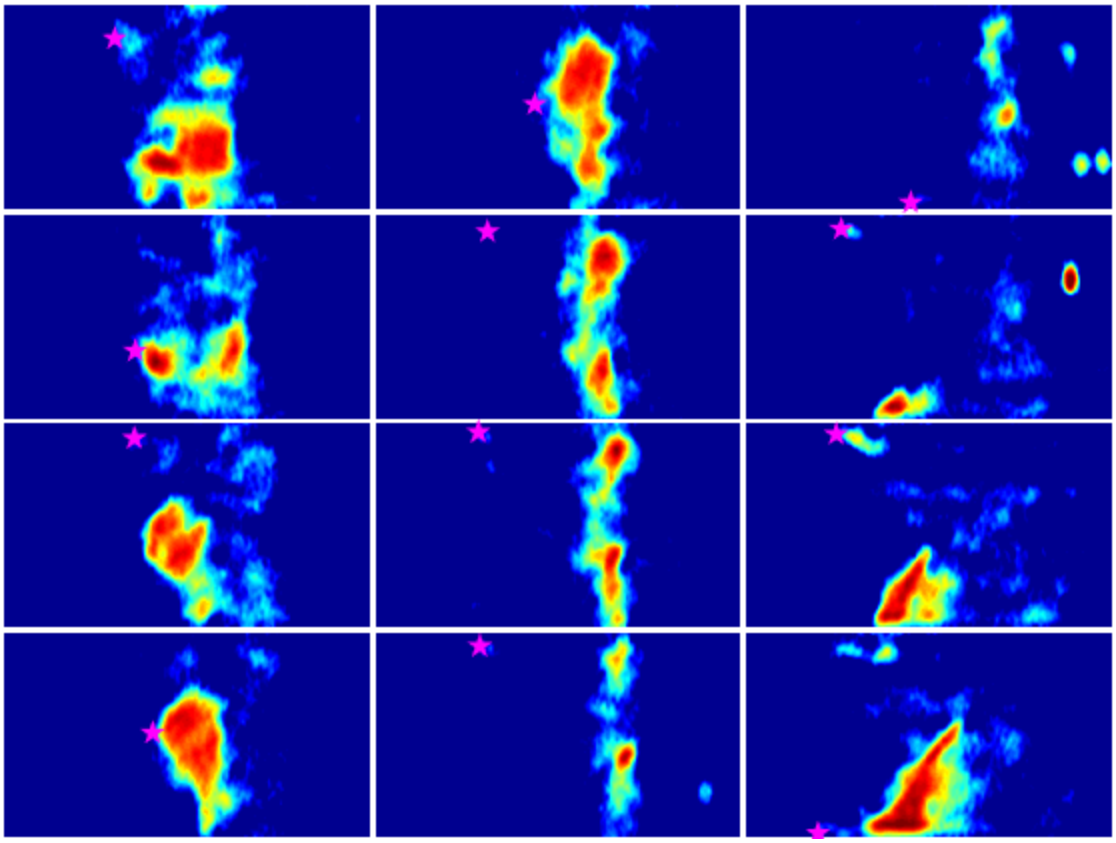

Figure D. 7: Twelve successive CH* chemiluminescence images taken during an LBO precursor event. The star denotes the most upstream spatial location of luminosity. A-2 is burning in these images with an air inlet temperature of 450 K.

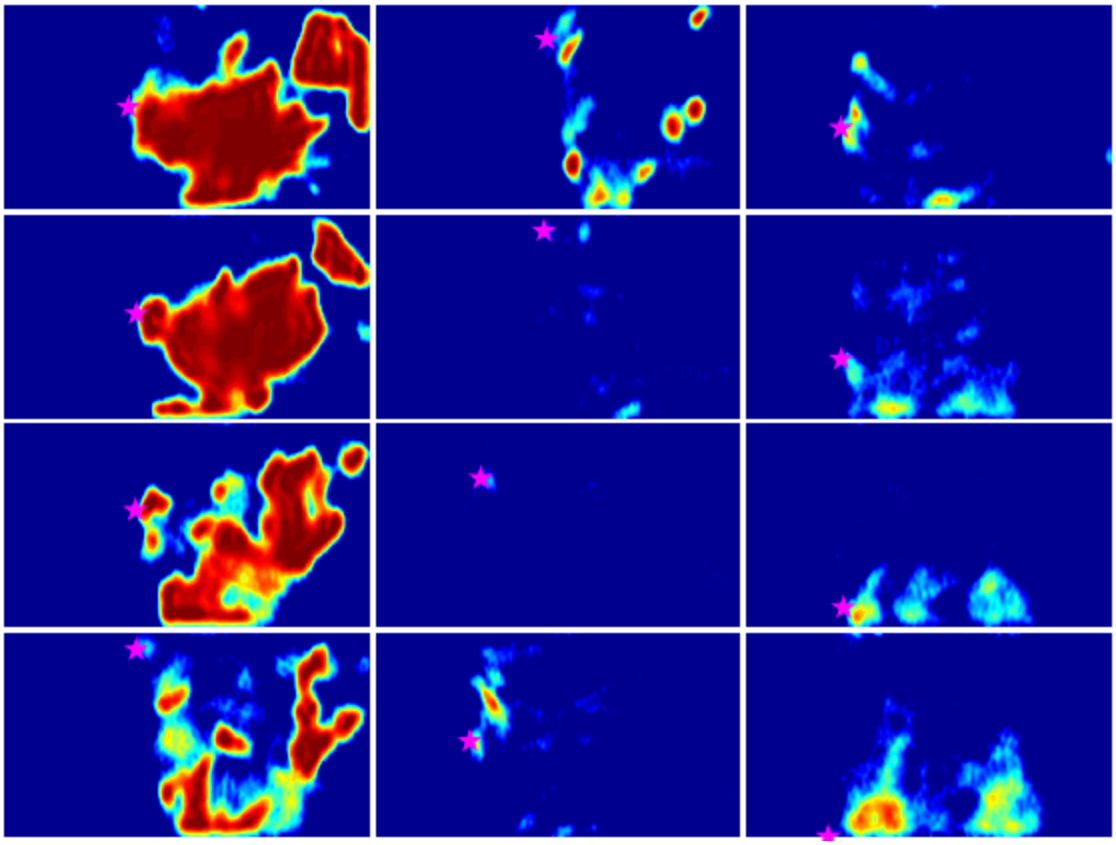

Figure D. 8: Twelve successive CH* chemiluminescence images taken during an LBO precursor event. The star denotes the most upstream spatial location of luminosity. A-2 is burning in these images with an air inlet temperature of 450 K.

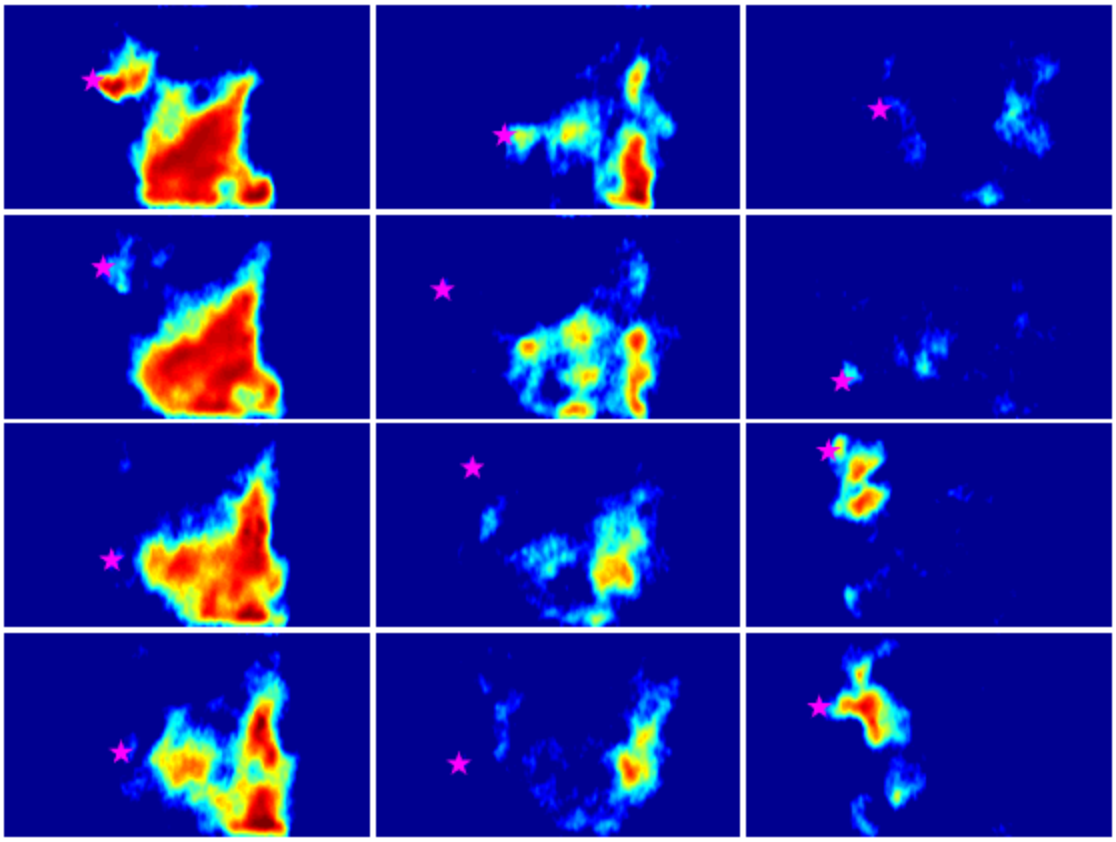

Figure D. 9: Twelve successive CH* chemiluminescence images taken during an LBO precursor event. The star denotes the most upstream spatial location of luminosity. A-2 is burning in these images with an air inlet temperature of 450 K.

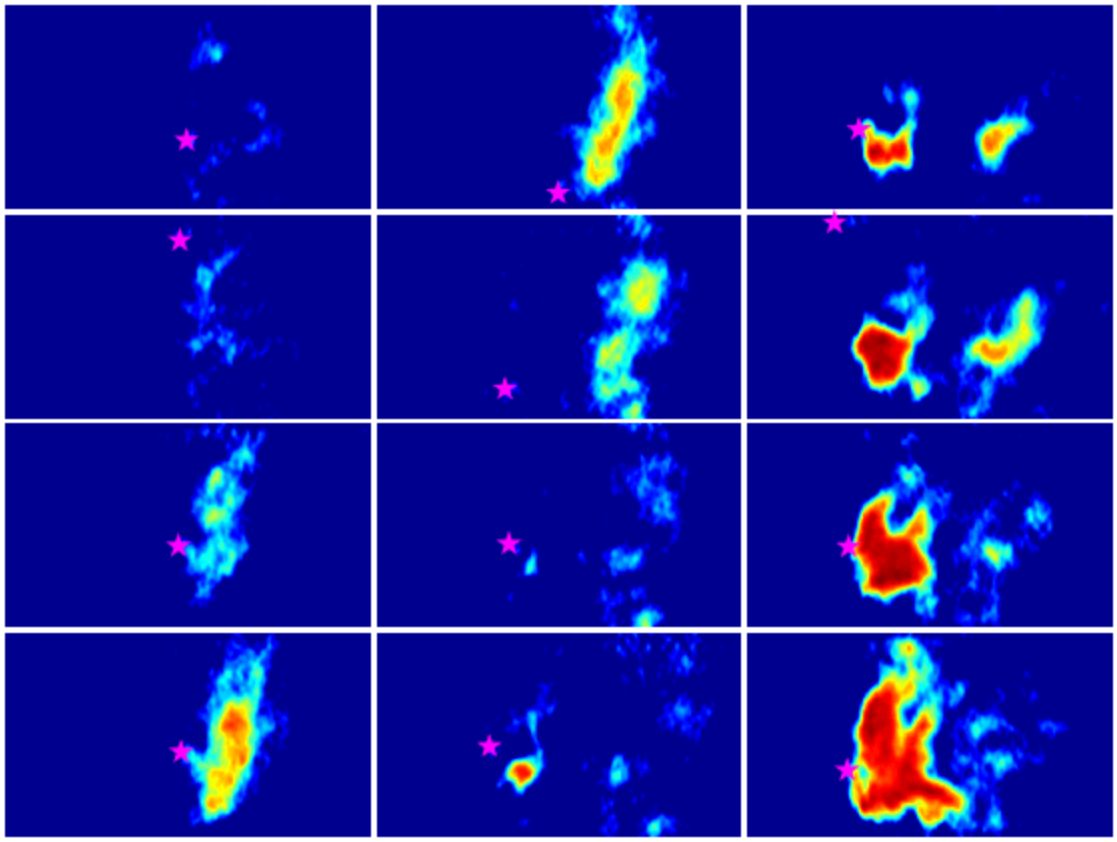

Figure D. 10: Twelve successive CH* chemiluminescence images taken during an LBO precursor event. The star denotes the most upstream spatial location of luminosity. A-2 is burning in these images with an air inlet temperature of 450 K.

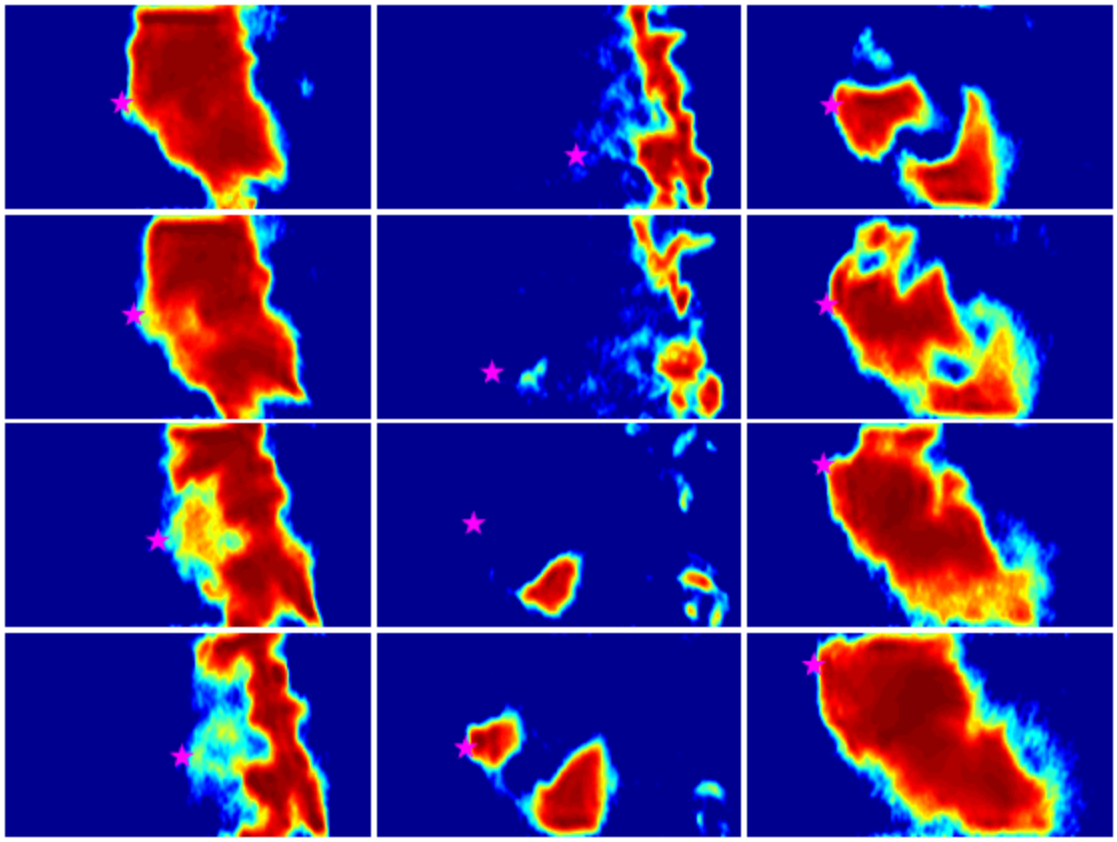

Figure D. 11: Twelve successive CH* chemiluminescence images taken during an LBO precursor event. The star denotes the most upstream spatial location of luminosity. A-2 is burning in these images with an air inlet temperature of 450 K.

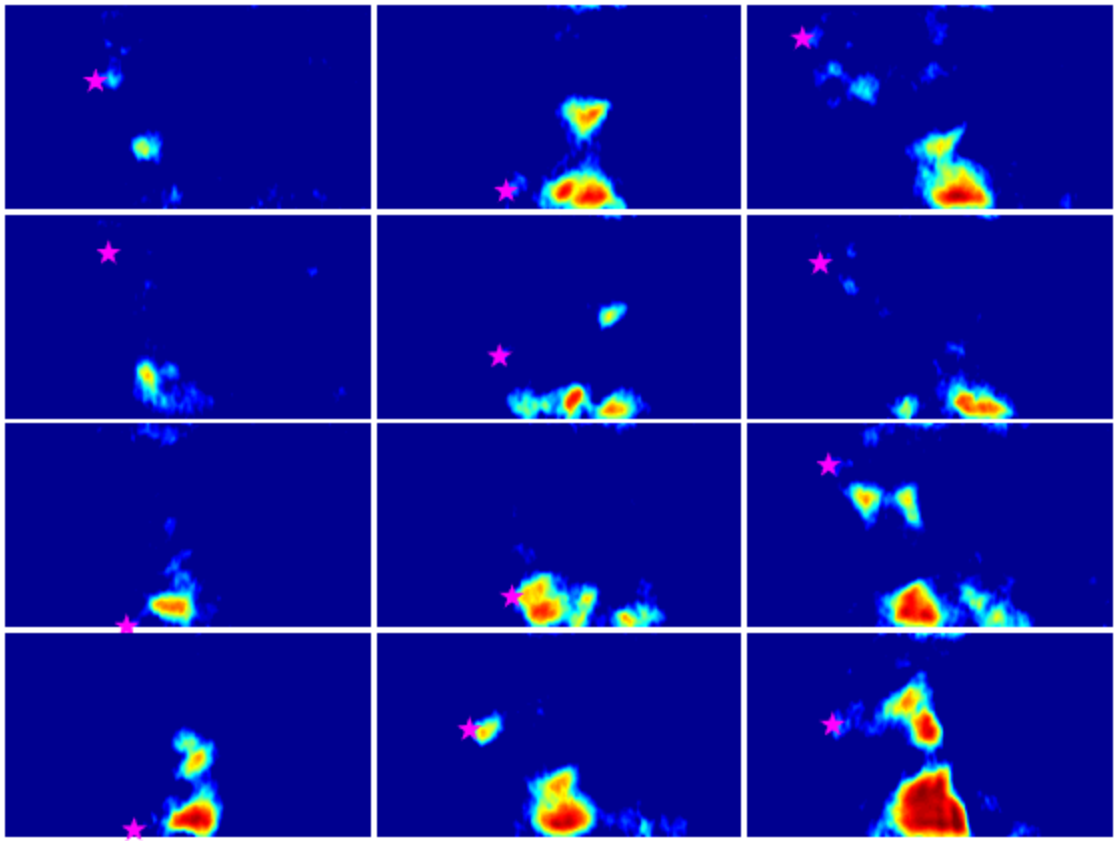

Figure D. 12: Twelve successive CH* chemiluminescence images taken during an LBO precursor event. The star denotes the most upstream spatial location of luminosity. A-2 is burning in these images with an air inlet temperature of 450 K.

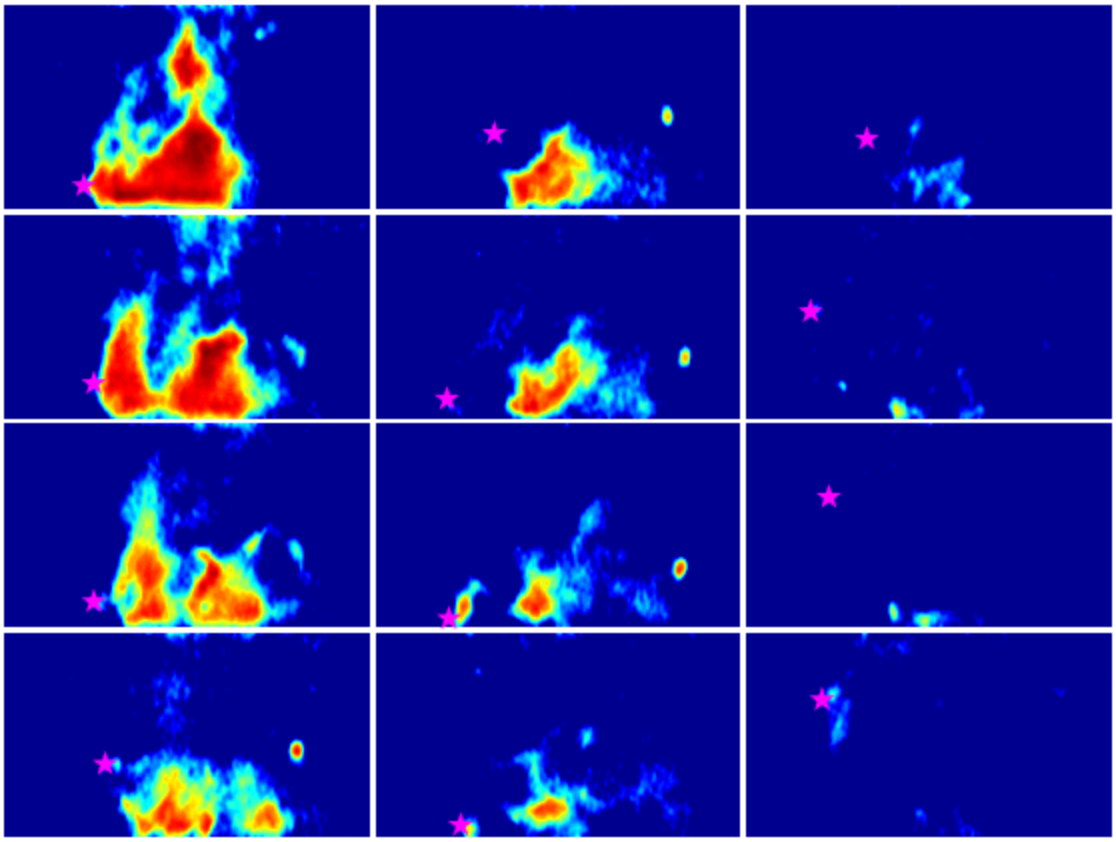

Figure D. 13: Twelve successive CH* chemiluminescence images taken during an LBO precursor event. The star denotes the most upstream spatial location of luminosity. A-2 is burning in these images with an air inlet temperature of 450 K.

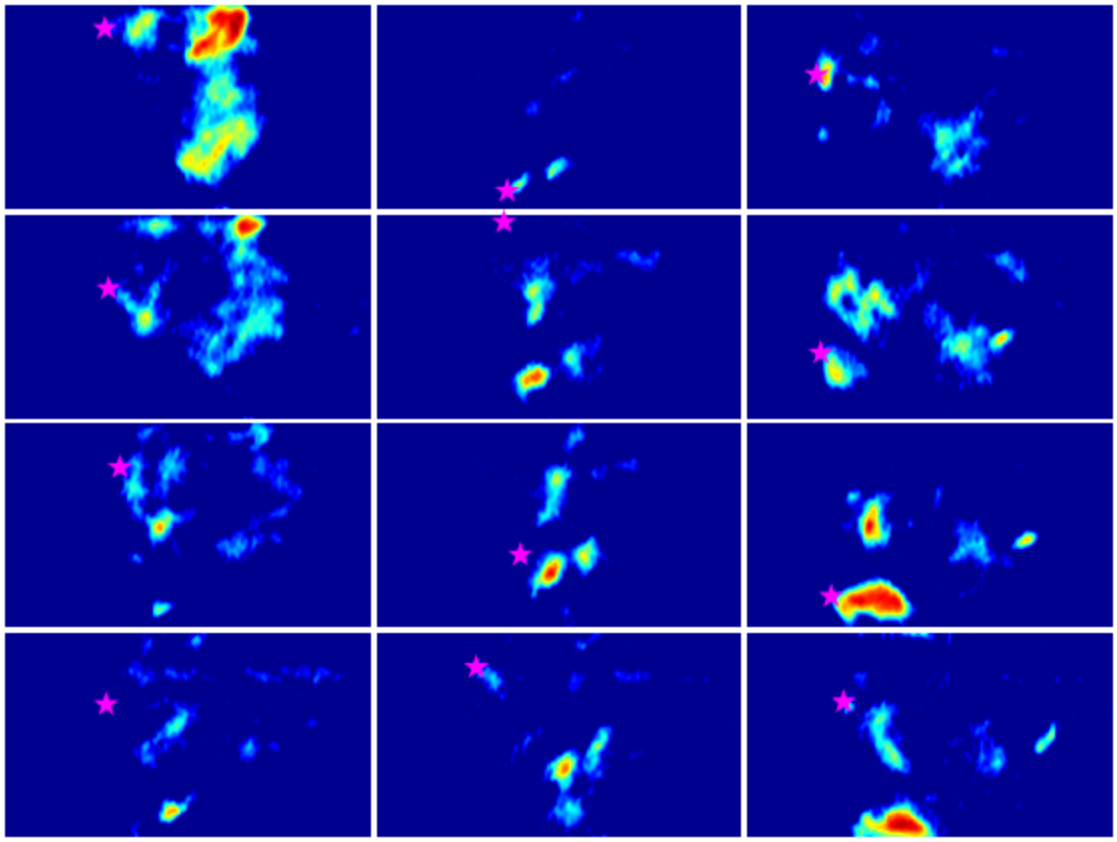

Figure D. 14: Twelve successive CH* chemiluminescence images taken during an LBO precursor event. The star denotes the most upstream spatial location of luminosity. A-2 is burning in these images with an air inlet temperature of 450 K.

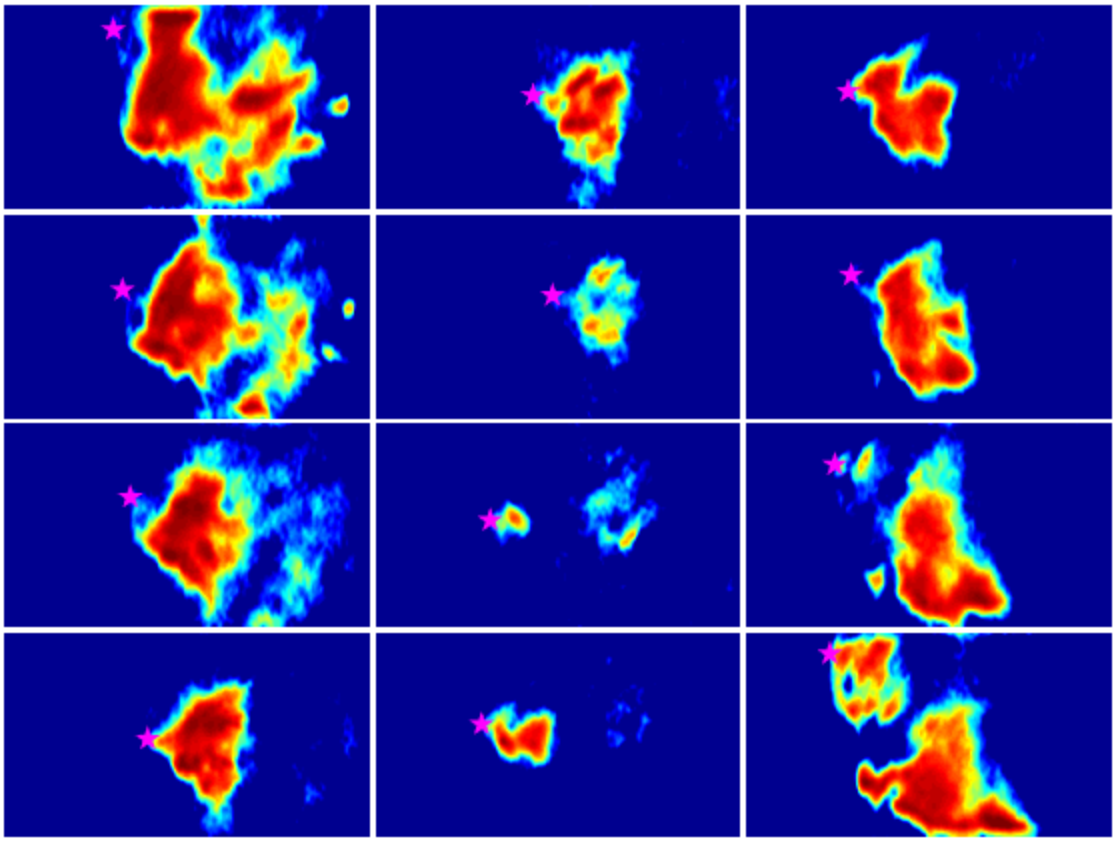

Figure D. 15: Twelve successive CH* chemiluminescence images taken during an LBO precursor event. The star denotes the most upstream spatial location of luminosity. A-2 is burning in these images with an air inlet temperature of 450 K.

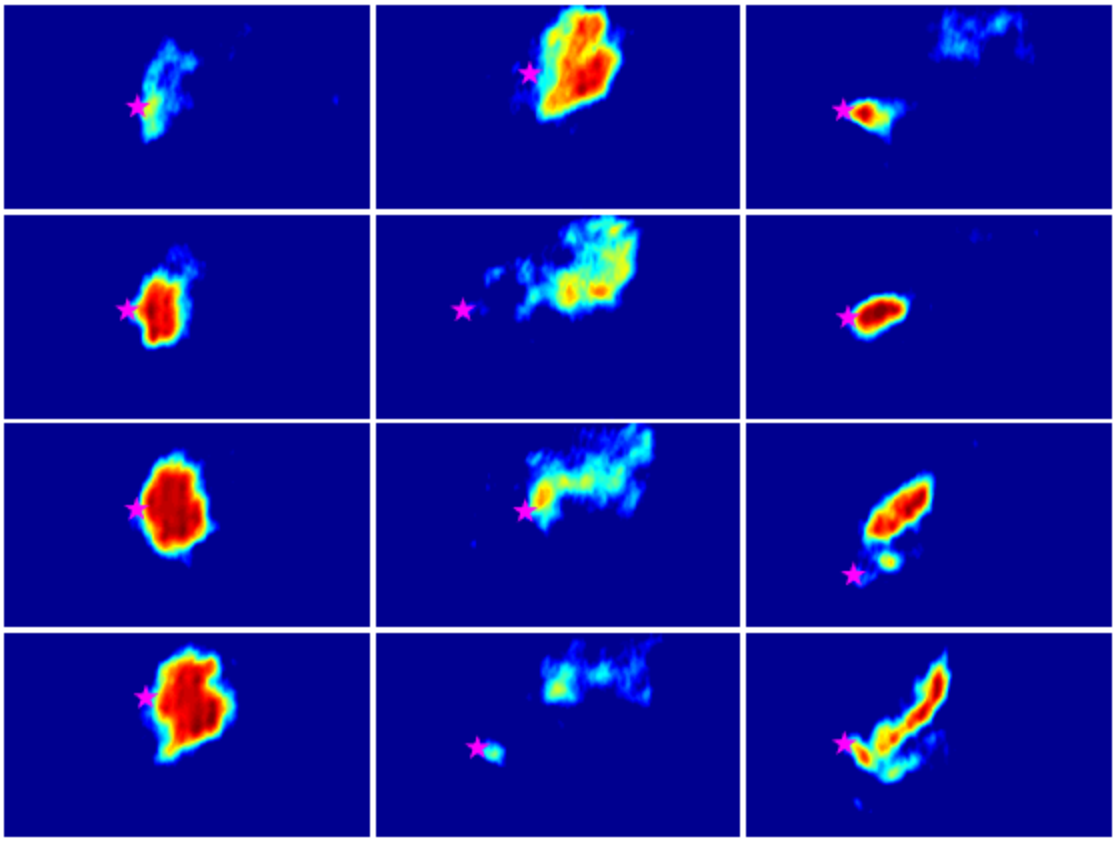

Figure D. 16: Twelve successive CH* chemiluminescence images taken during an LBO precursor event. The star denotes the most upstream spatial location of luminosity. C-1 is burning in these images with an air inlet temperature of 450 K.

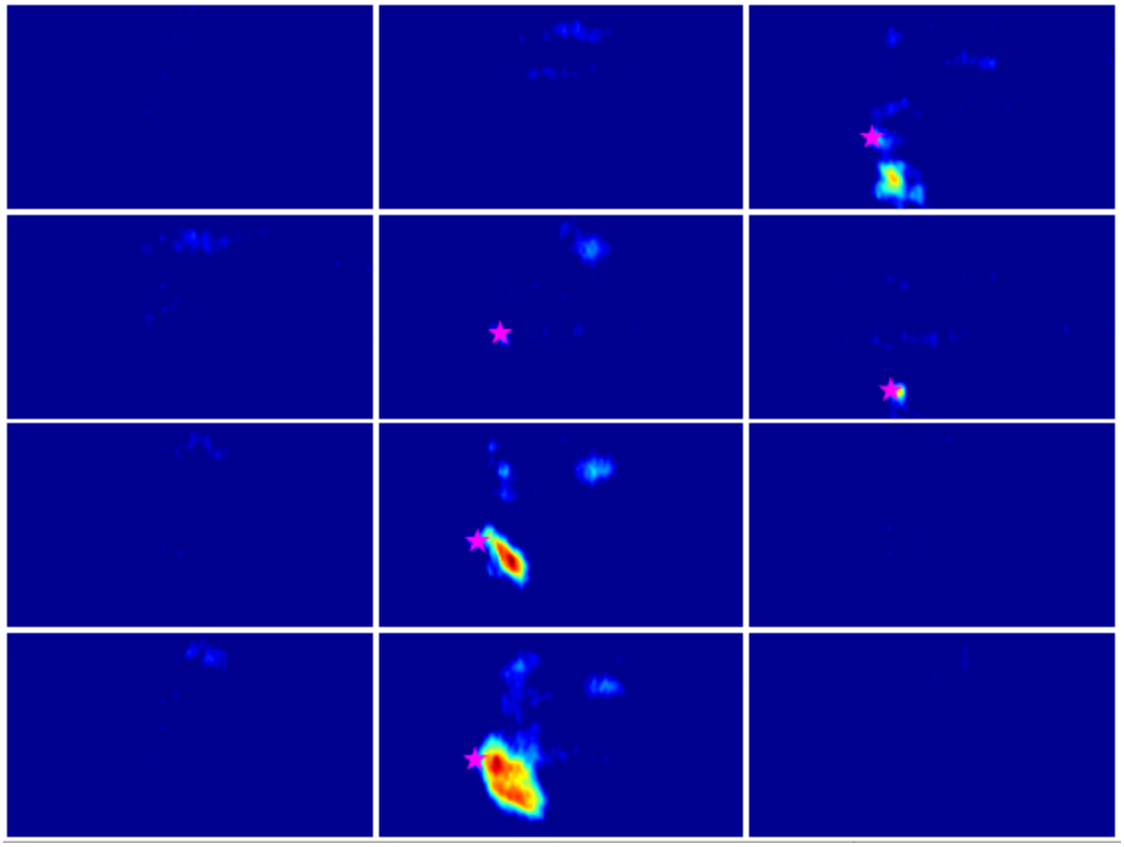

Figure D. 17: Twelve successive CH* chemiluminescence images taken during an LBO precursor event. The star denotes the most upstream spatial location of luminosity. C-1 is burning in these images with an air inlet temperature of 450 K.

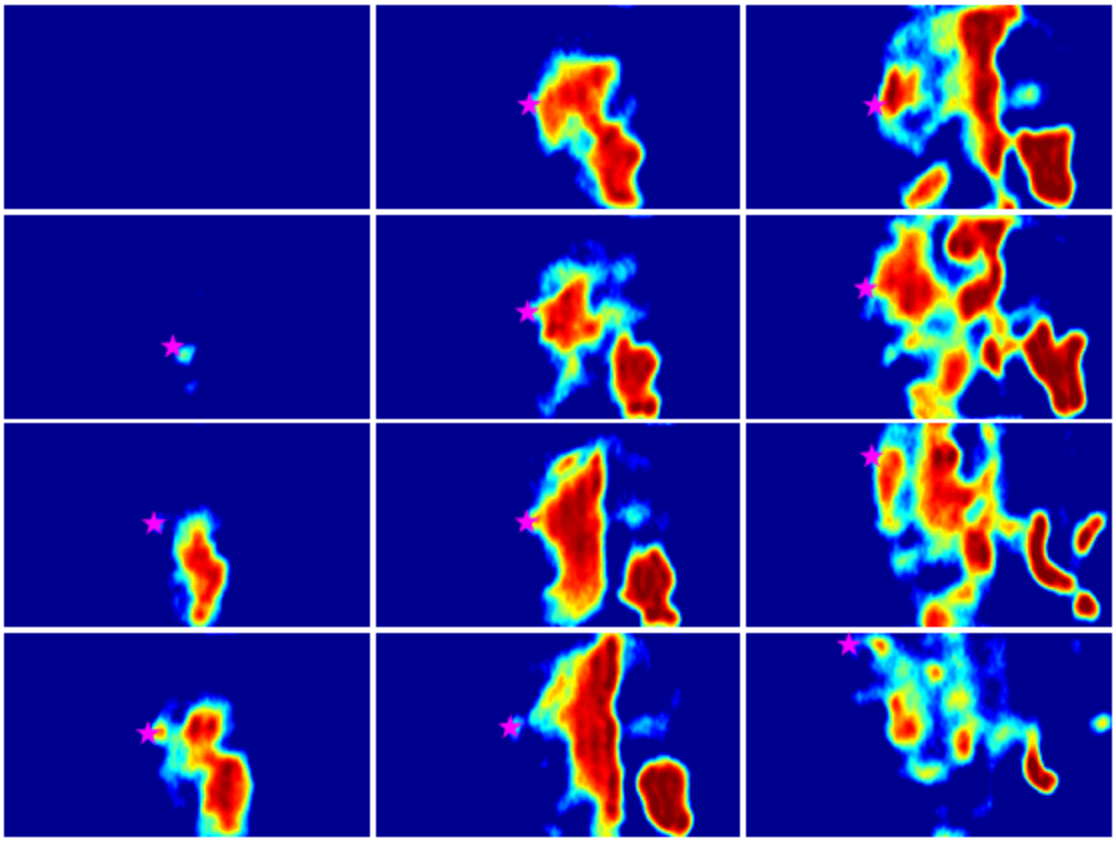

Figure D. 18: Twelve successive CH* chemiluminescence images taken during an LBO precursor event. The star denotes the most upstream spatial location of luminosity. C-1 is burning in these images with an air inlet temperature of 450 K.

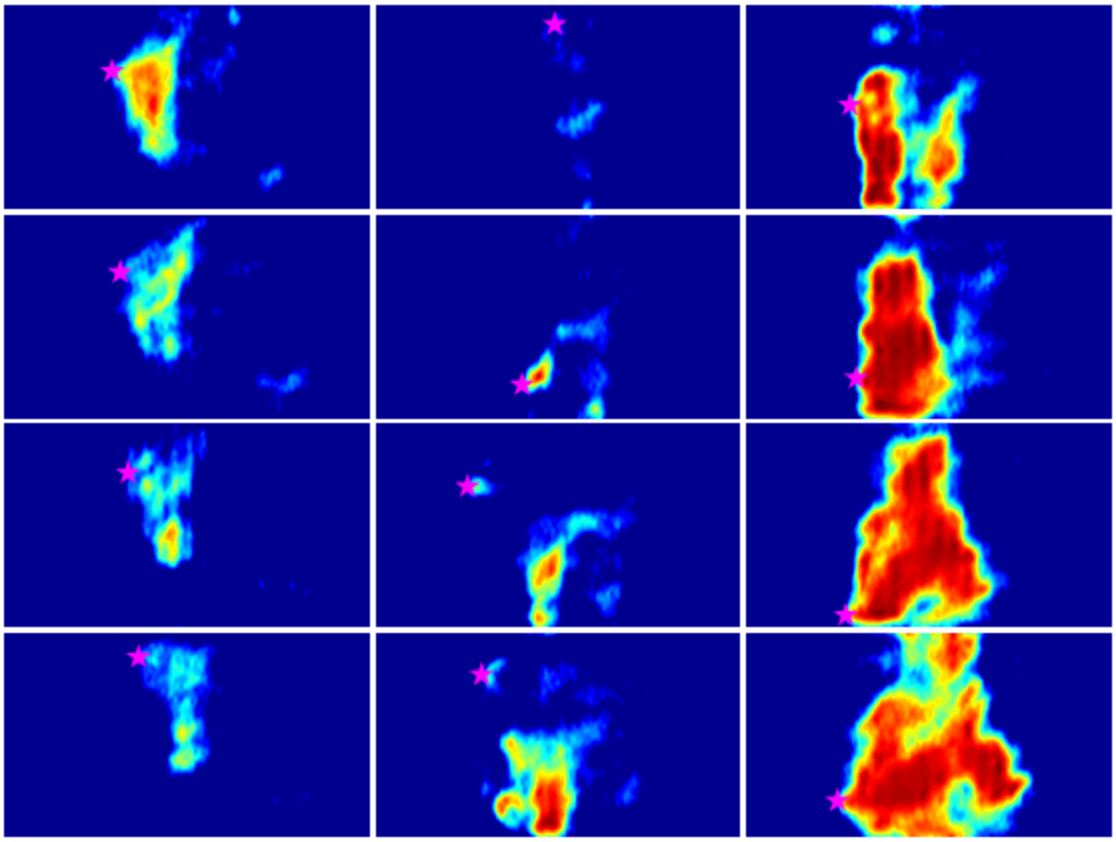

Figure D. 19: Twelve successive CH* chemiluminescence images taken during an LBO precursor event. The star denotes the most upstream spatial location of luminosity. C-1 is burning in these images with an air inlet temperature of 450 K.

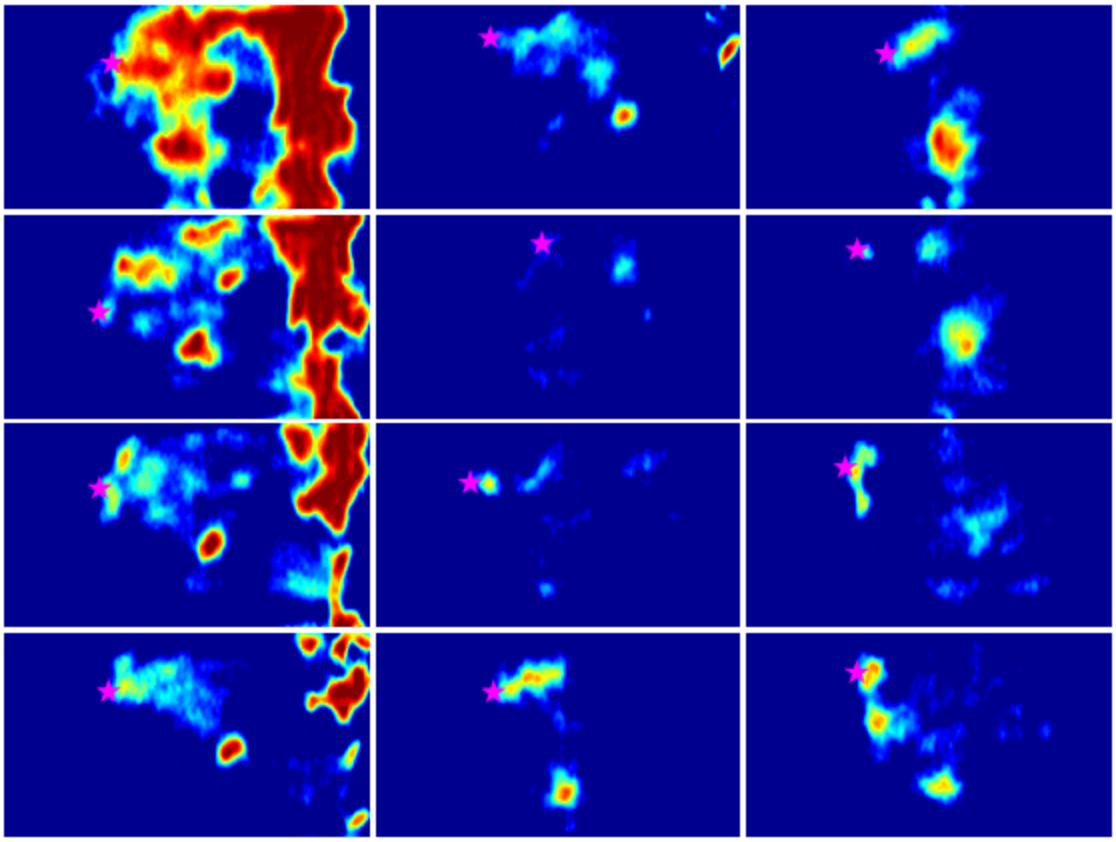

Figure D. 20: Twelve successive CH* chemiluminescence images taken during an LBO precursor event. The star denotes the most upstream spatial location of luminosity. C-1 is burning in these images with an air inlet temperature of 450 K.

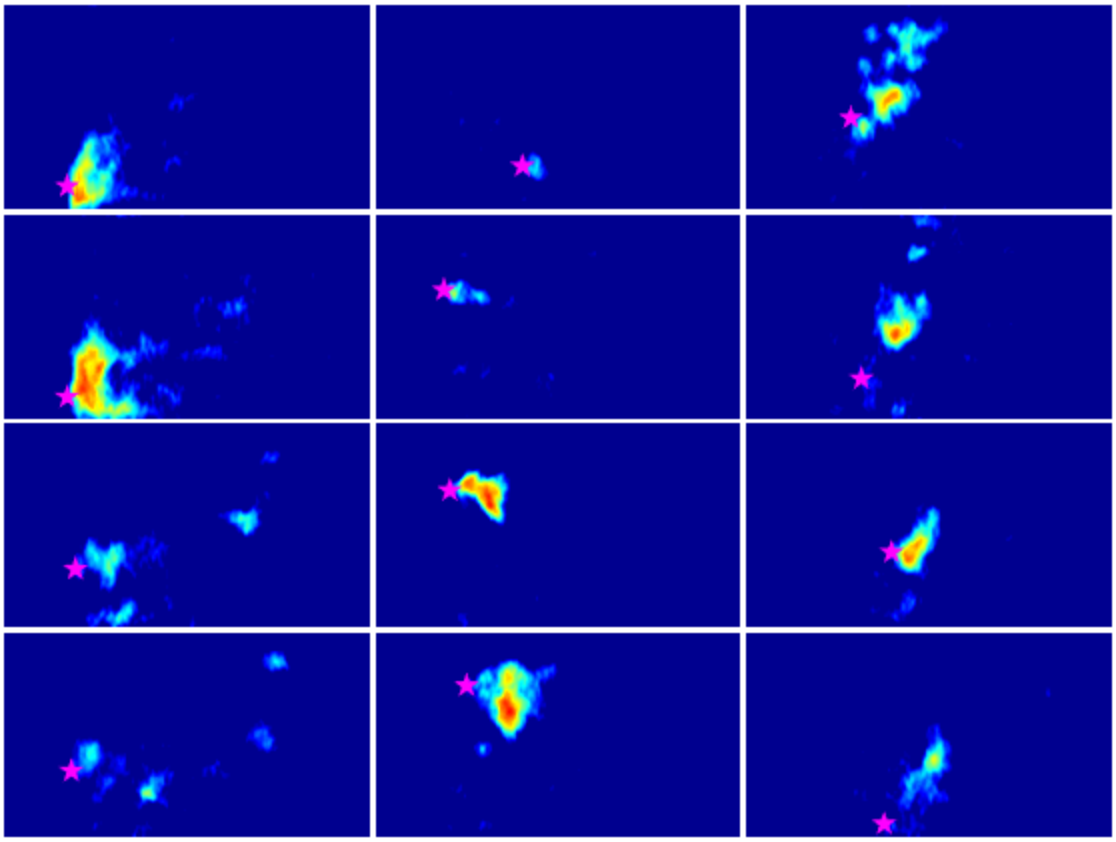

Figure D. 21: Twelve successive CH* chemiluminescence images taken during an LBO precursor event. The star denotes the most upstream spatial location of luminosity. C-1 is burning in these images with an air inlet temperature of 450 K.

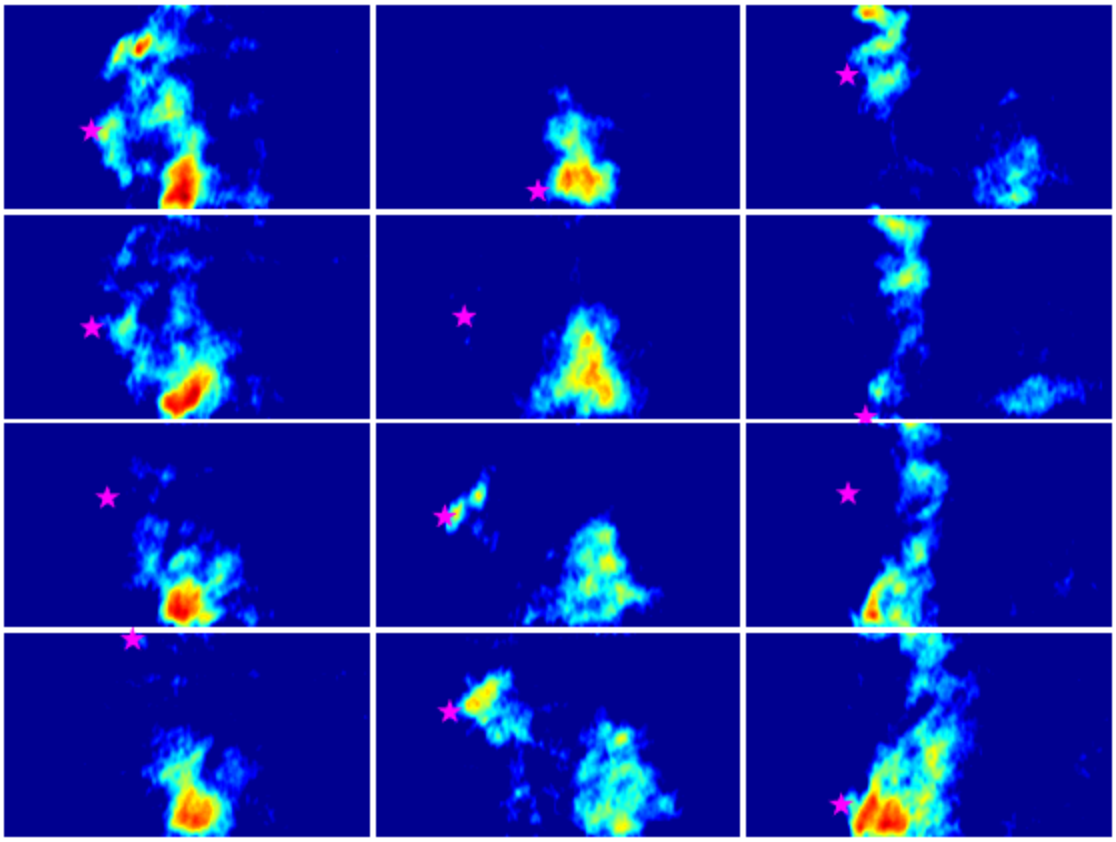

Figure D. 22: Twelve successive CH* chemiluminescence images taken during an LBO precursor event. The star denotes the most upstream spatial location of luminosity. C-1 is burning in these images with an air inlet temperature of 450 K.

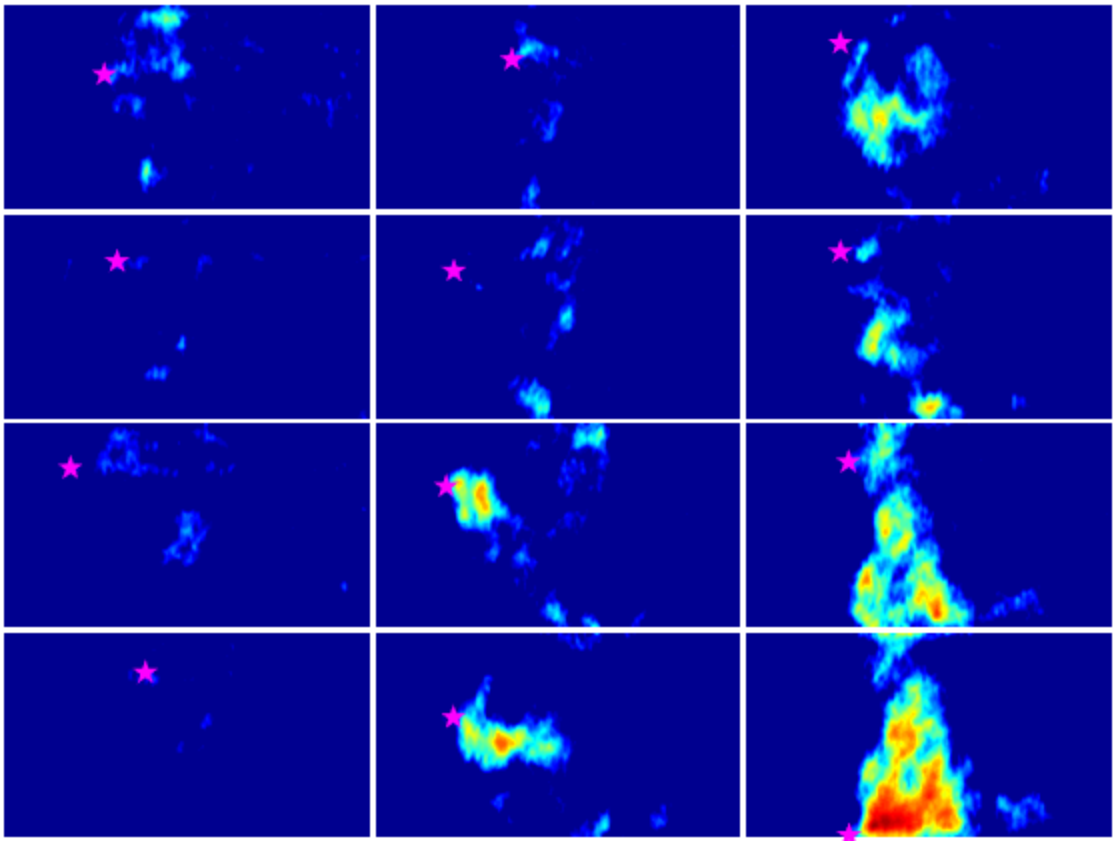

Figure D. 23: Twelve successive CH* chemiluminescence images taken during an LBO precursor event. The star denotes the most upstream spatial location of luminosity. C-1 is burning in these images with an air inlet temperature of 450 K.

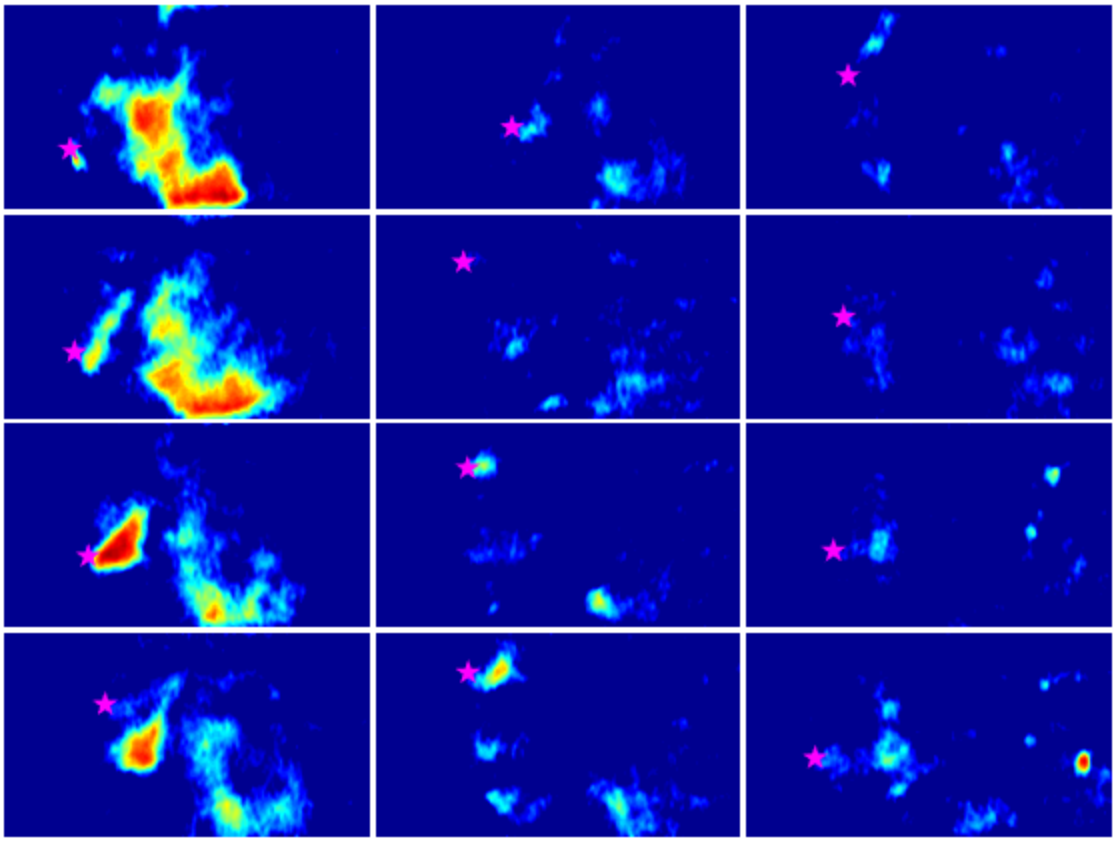

Figure D. 24: Twelve successive CH* chemiluminescence images taken during an LBO precursor event. The star denotes the most upstream spatial location of luminosity. C-1 is burning in these images with an air inlet temperature of 450 K.

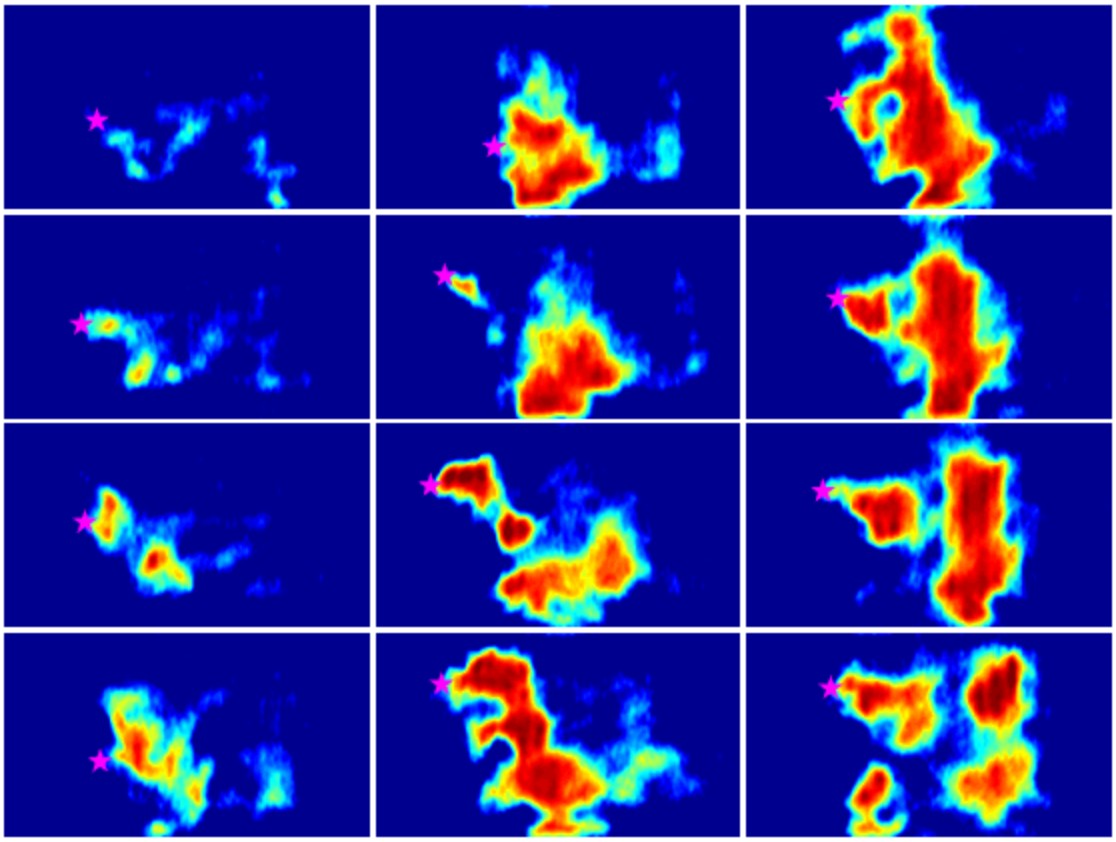

Figure D. 25: Twelve successive CH* chemiluminescence images taken during an LBO precursor event. The star denotes the most upstream spatial location of luminosity. N-dodecane is burning in these images with an air inlet temperature of 450 K.

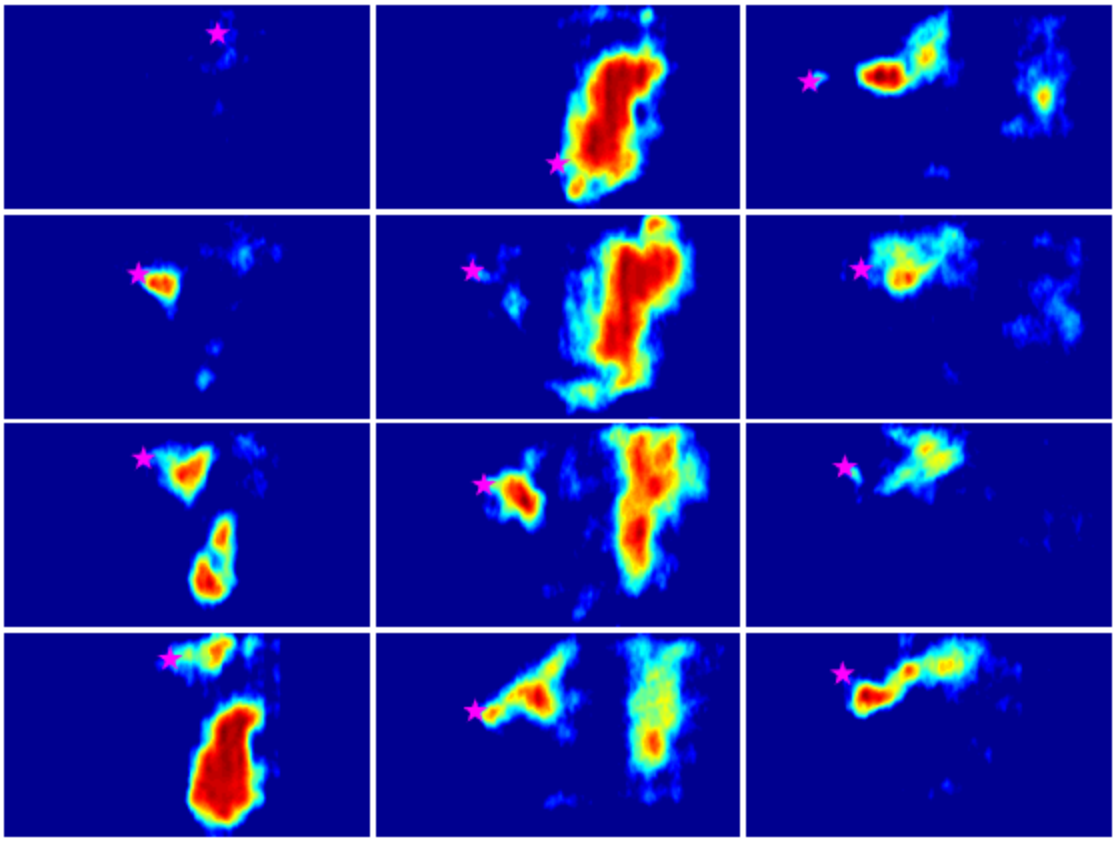

Figure D. 26: Twelve successive CH* chemiluminescence images taken during an LBO precursor event. The star denotes the most upstream spatial location of luminosity. N-dodecane is burning in these images with an air inlet temperature of 450 K.

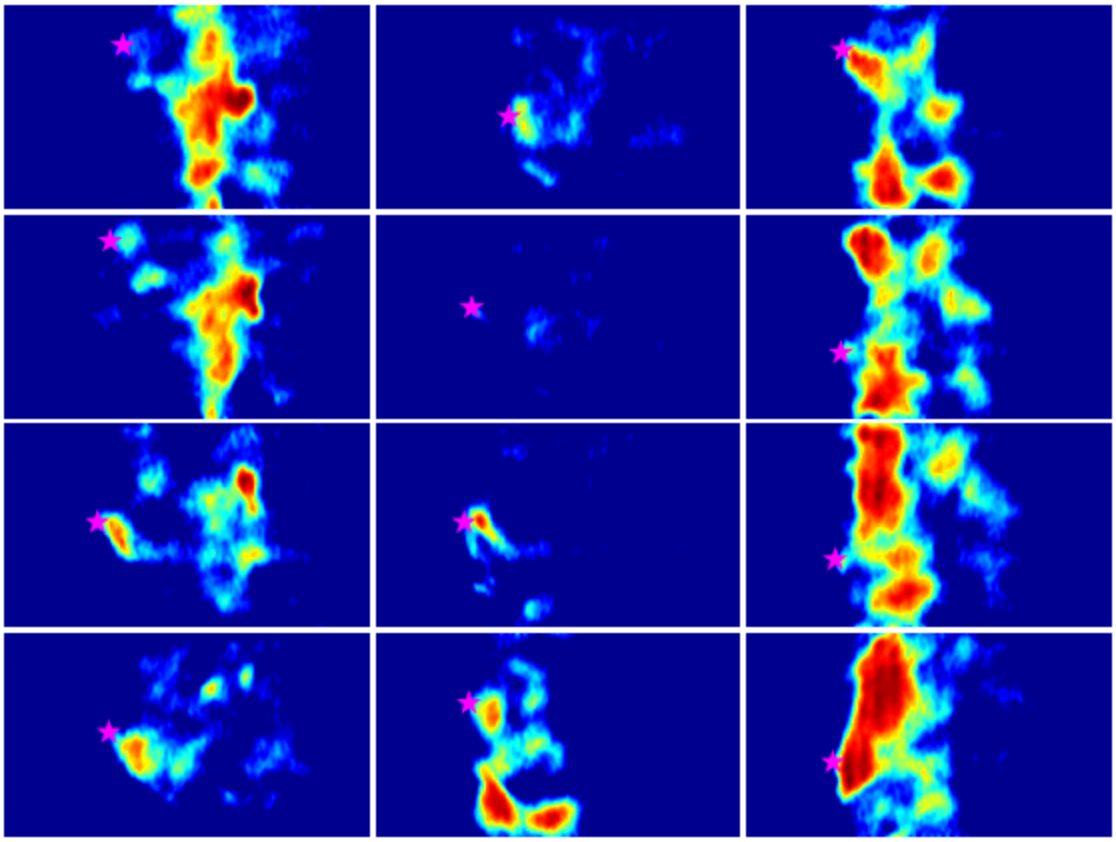

Figure D. 27: Twelve successive CH* chemiluminescence images taken during an LBO precursor event. The star denotes the most upstream spatial location of luminosity. N-dodecane is burning in these images with an air inlet temperature of 450 K.

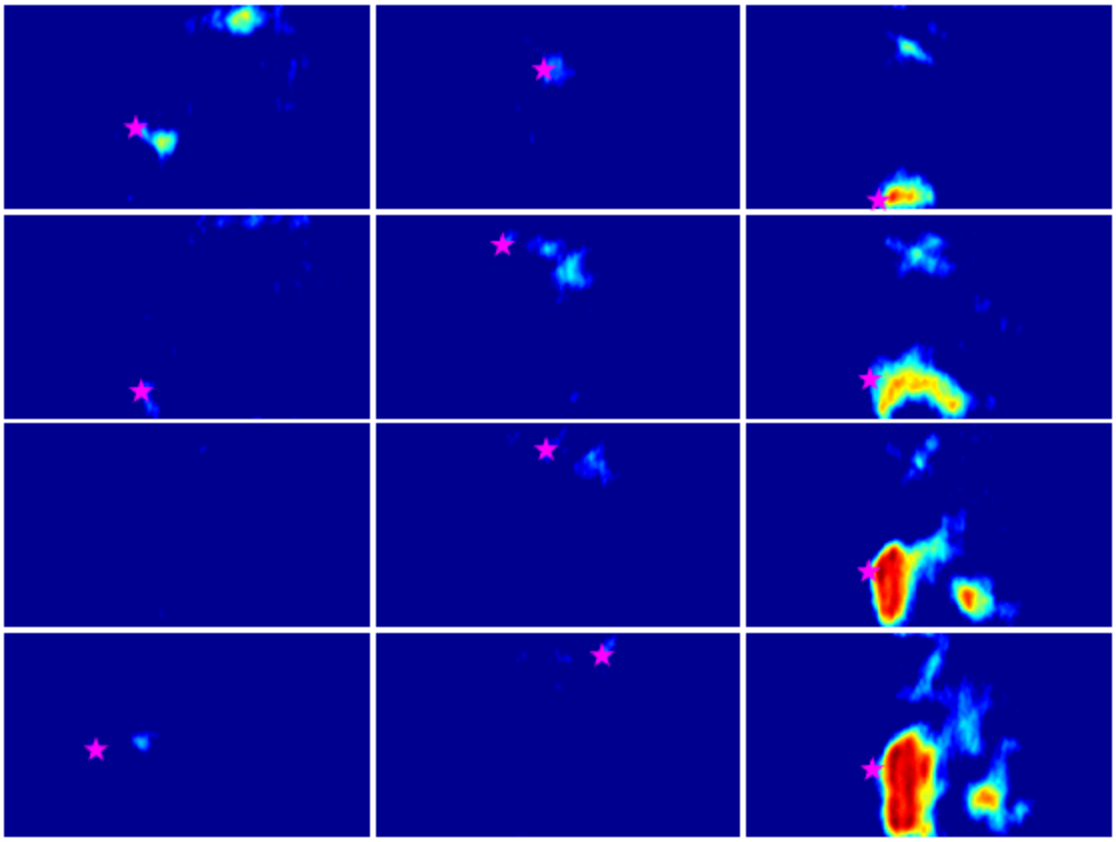

Figure D. 28: Twelve successive CH* chemiluminescence images taken during an LBO precursor event. The star denotes the most upstream spatial location of luminosity. N-dodecane is burning in these images with an air inlet temperature of 450 K.

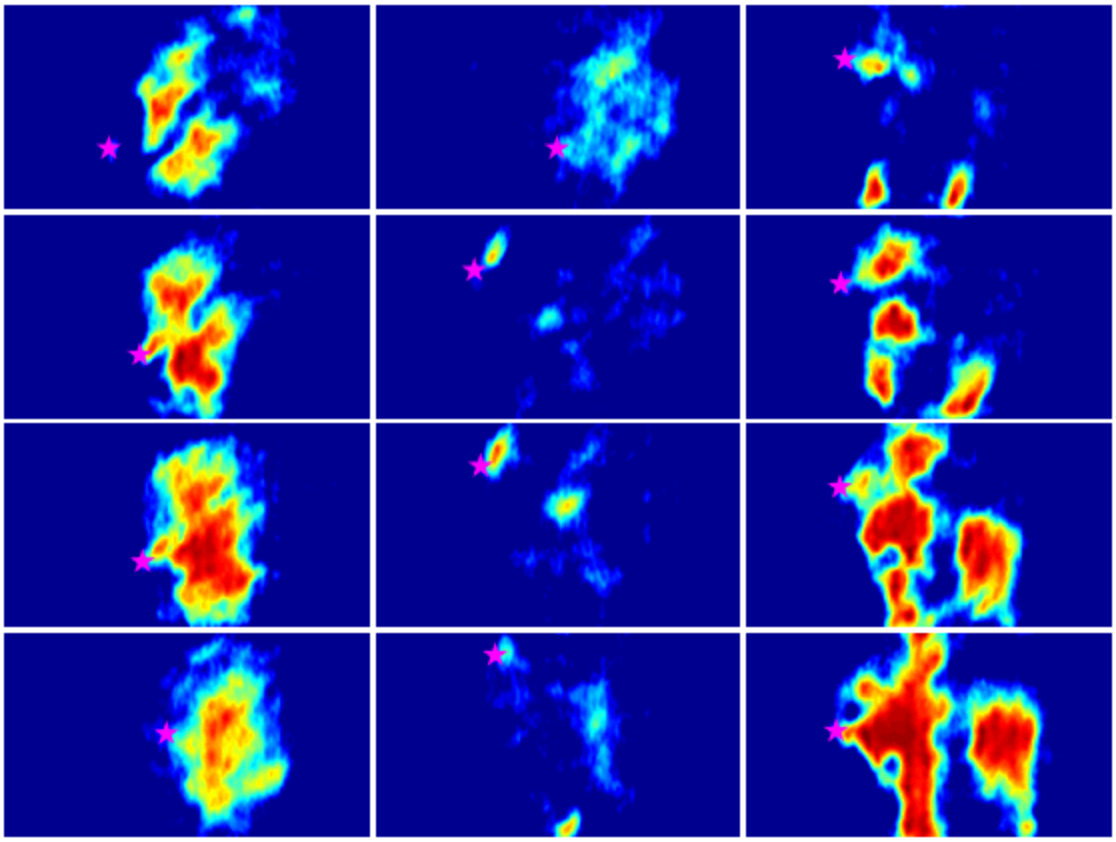

Figure D. 29: Twelve successive CH* chemiluminescence images taken during an LBO precursor event. The star denotes the most upstream spatial location of luminosity. N-dodecane is burning in these images with an air inlet temperature of 450 K.

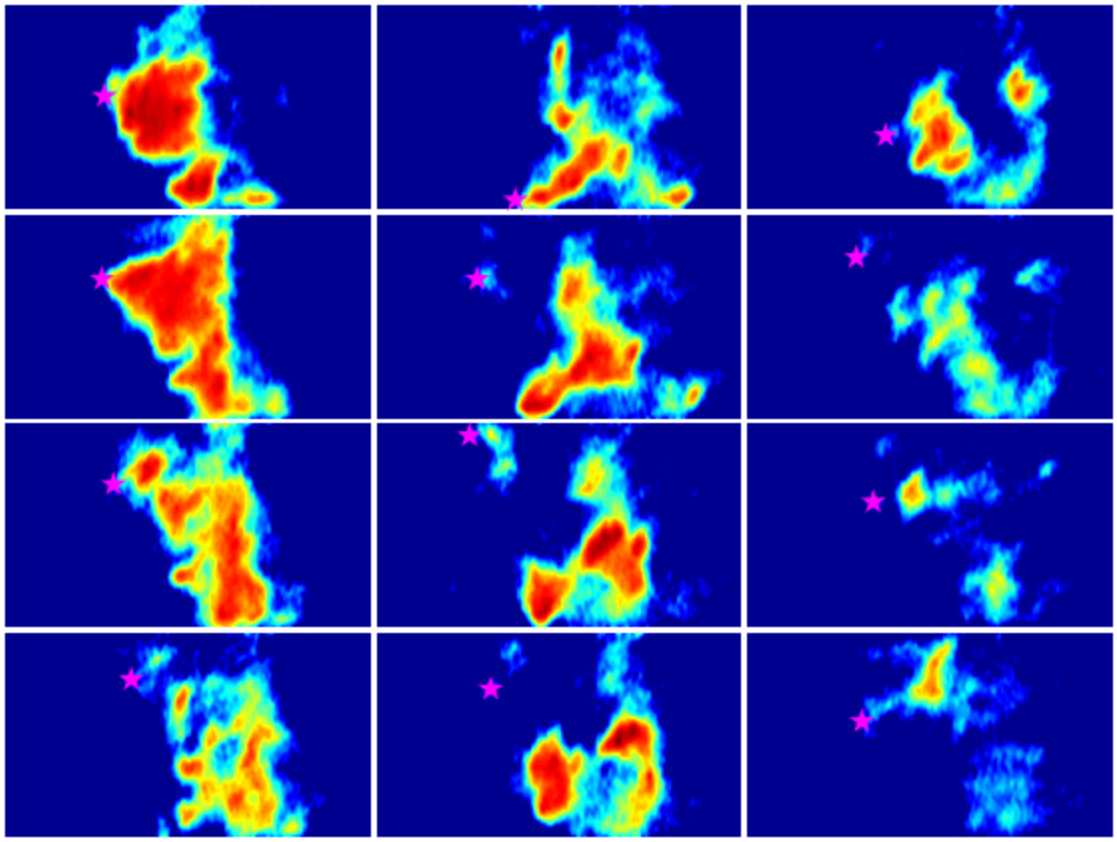

Figure D. 30: Twelve successive CH* chemiluminescence images taken during an LBO precursor event. The star denotes the most upstream spatial location of luminosity. N-dodecane is burning in these images with an air inlet temperature of 450 K.

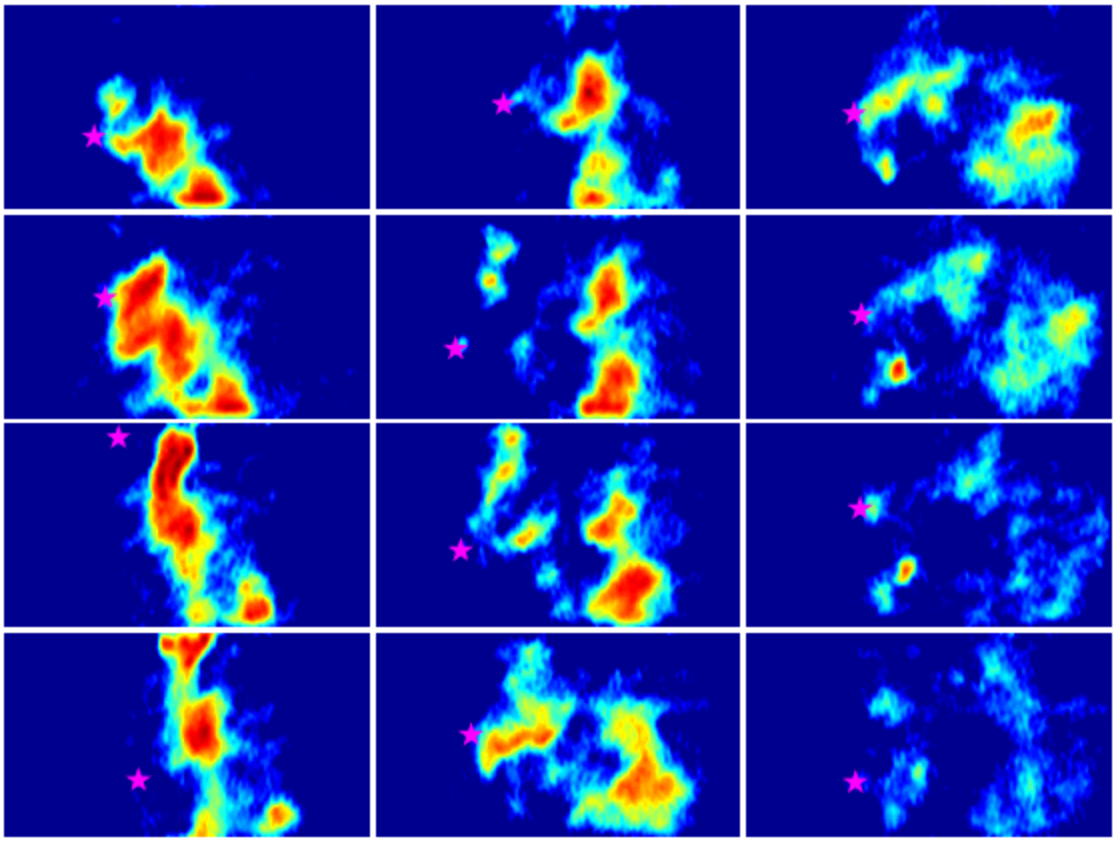

Figure D. 31: Twelve successive CH* chemiluminescence images taken during an LBO precursor event. The star denotes the most upstream spatial location of luminosity. N-dodecane is burning in these images with an air inlet temperature of 450 K.

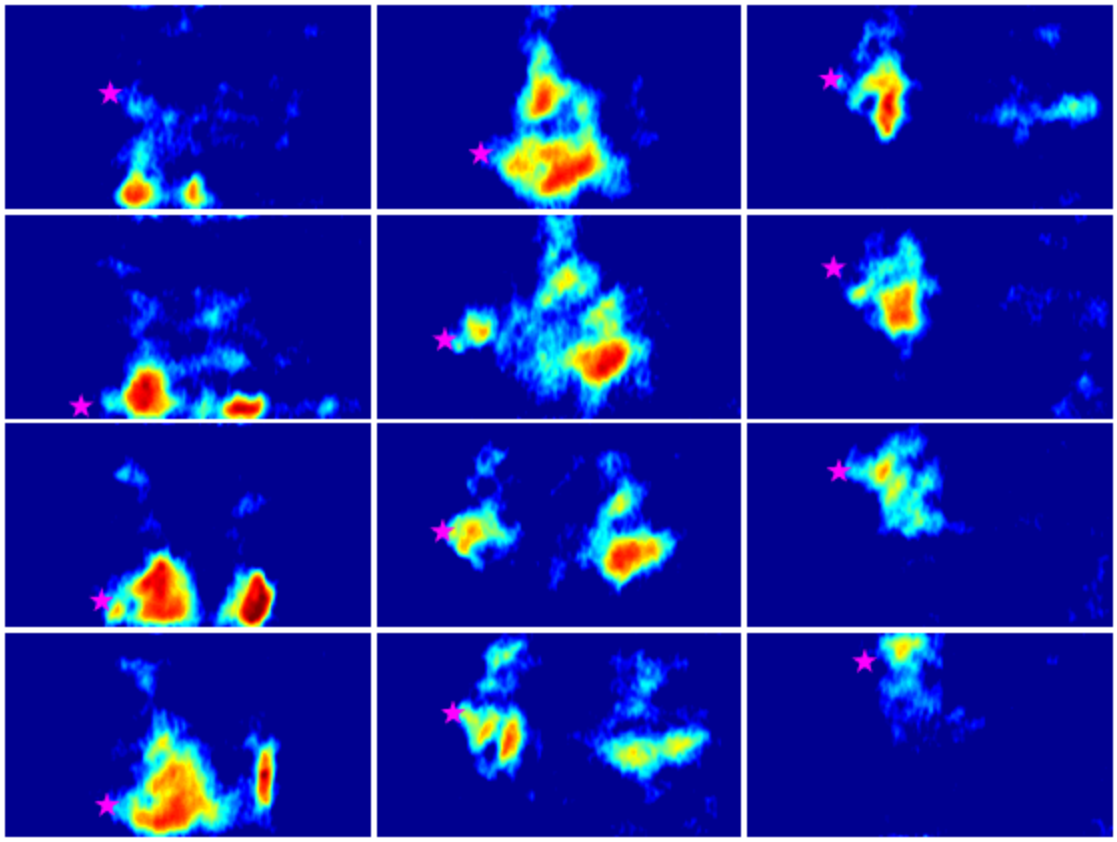

Figure D. 32: Twelve successive CH* chemiluminescence images taken during an LBO precursor event. The star denotes the most upstream spatial location of luminosity. N-dodecane is burning in these images with an air inlet temperature of 450 K.

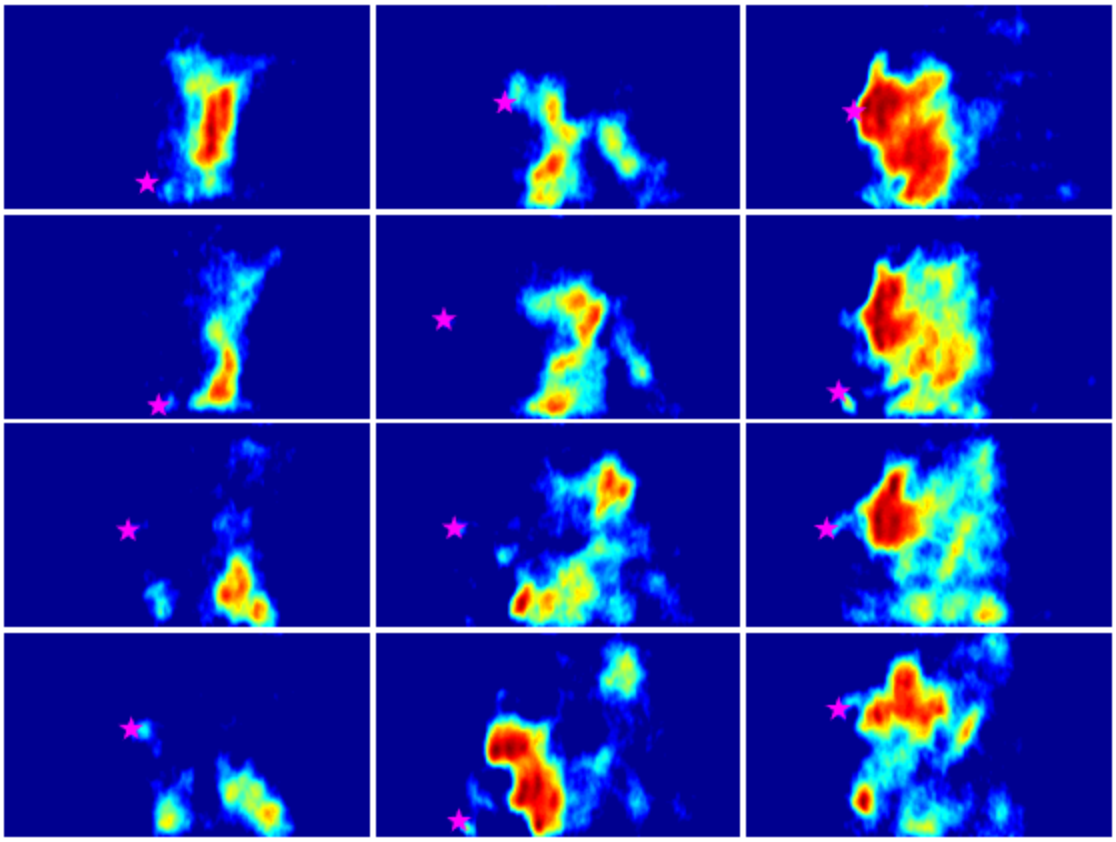

Figure D. 33: Twelve successive CH* chemiluminescence images taken during an LBO precursor event. The star denotes the most upstream spatial location of luminosity. S2 is burning in these images with an air inlet temperature of 450 K.

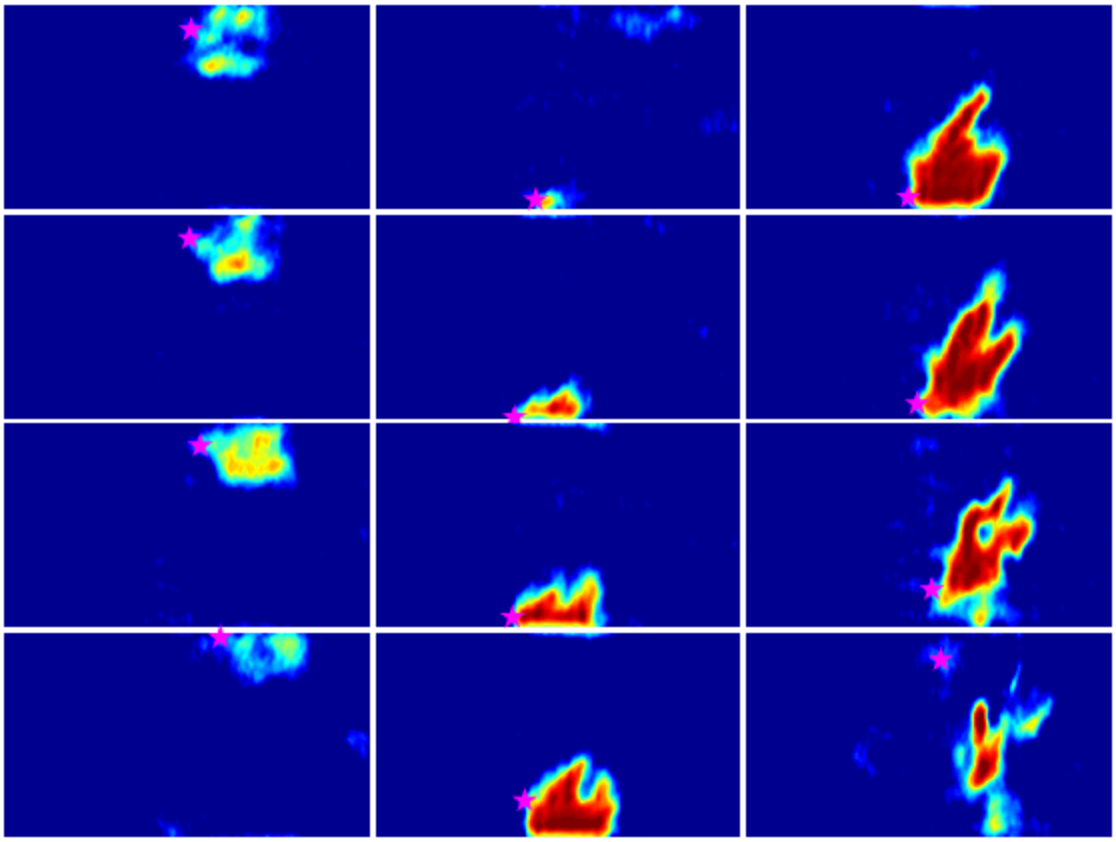

Figure D. 34: Twelve successive CH* chemiluminescence images taken during an LBO precursor event. The star denotes the most upstream spatial location of luminosity. S2 is burning in these images with an air inlet temperature of 450 K.

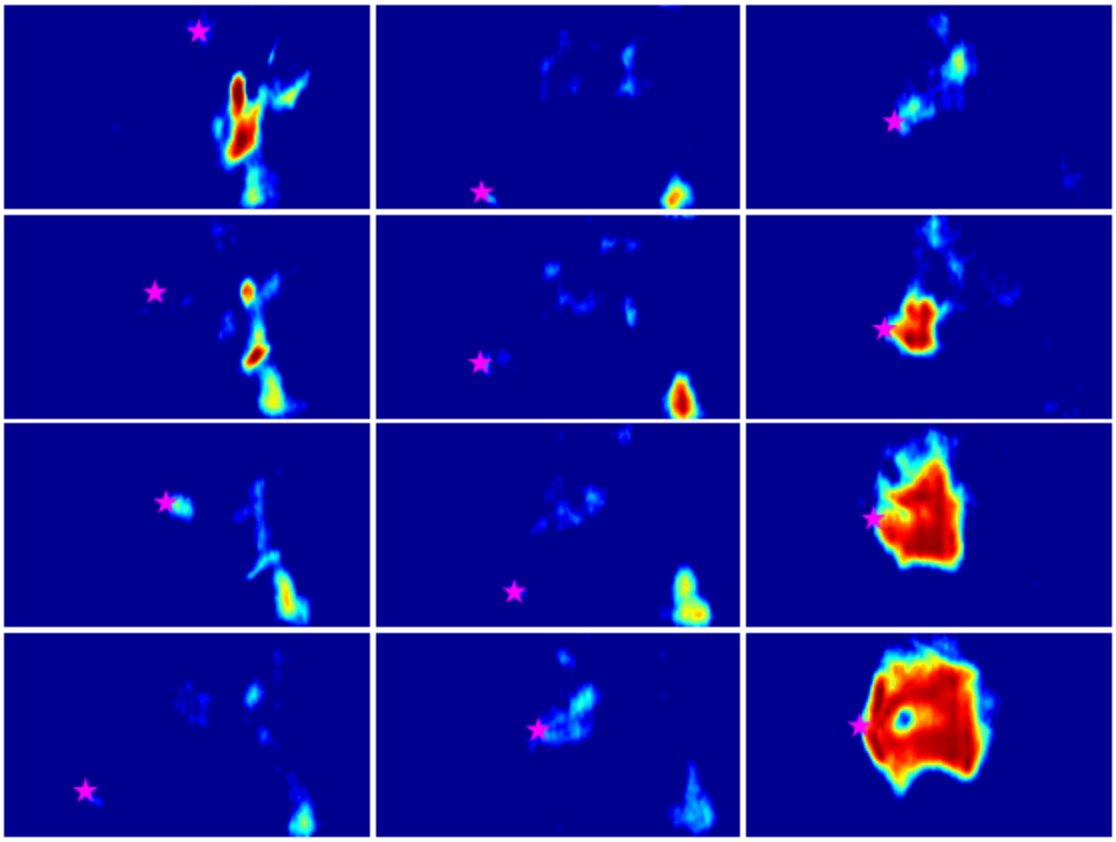

Figure D. 35: Twelve successive CH* chemiluminescence images taken during an LBO precursor event. The star denotes the most upstream spatial location of luminosity. S2 is burning in these images with an air inlet temperature of 450 K.

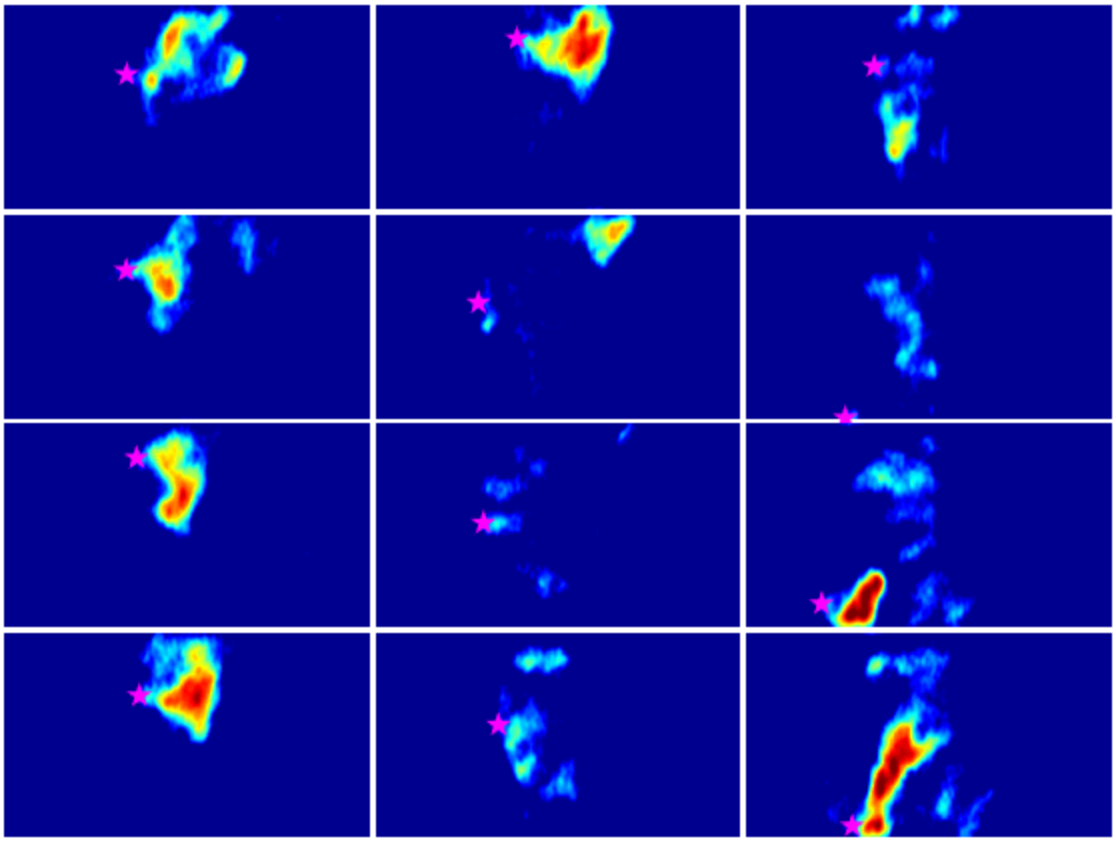

Figure D. 36: Twelve successive CH* chemiluminescence images taken during an LBO precursor event. The star denotes the most upstream spatial location of luminosity. S2 is burning in these images with an air inlet temperature of 450 K.

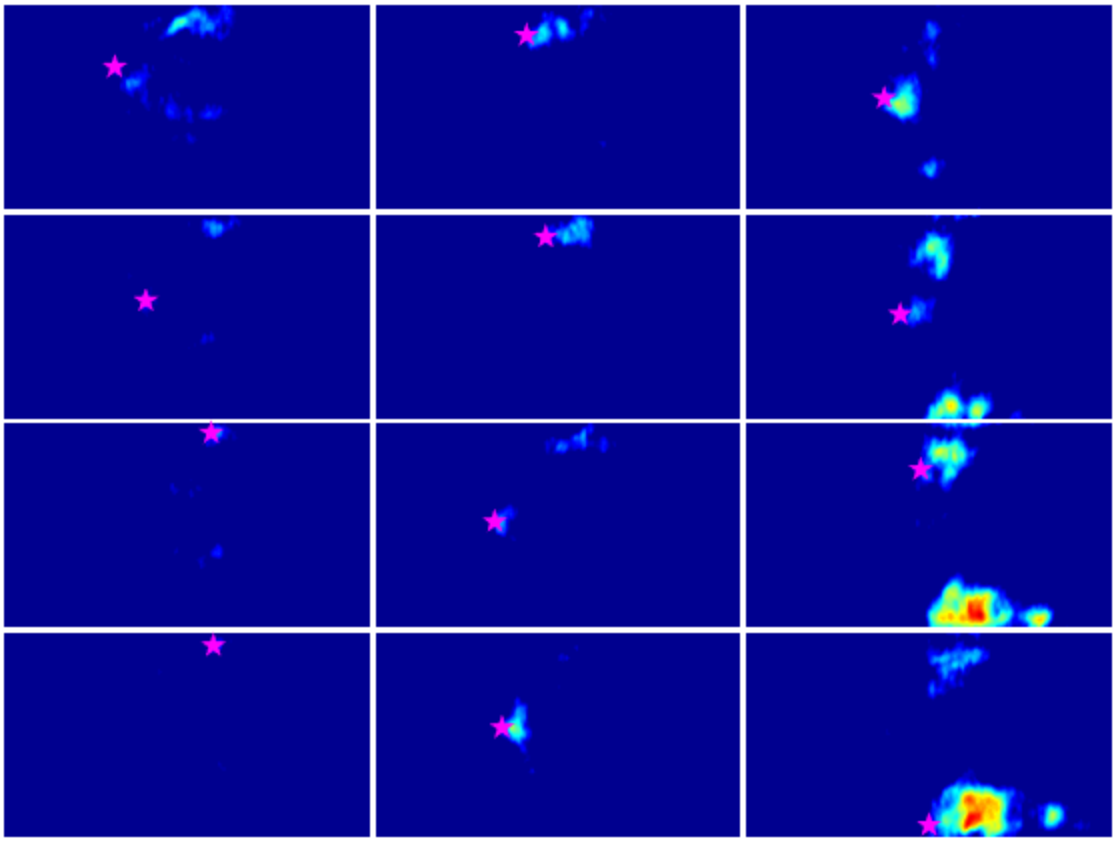

Figure D. 37: Twelve successive CH* chemiluminescence images taken during an LBO precursor event. The star denotes the most upstream spatial location of luminosity. S2 is burning in these images with an air inlet temperature of 450 K.

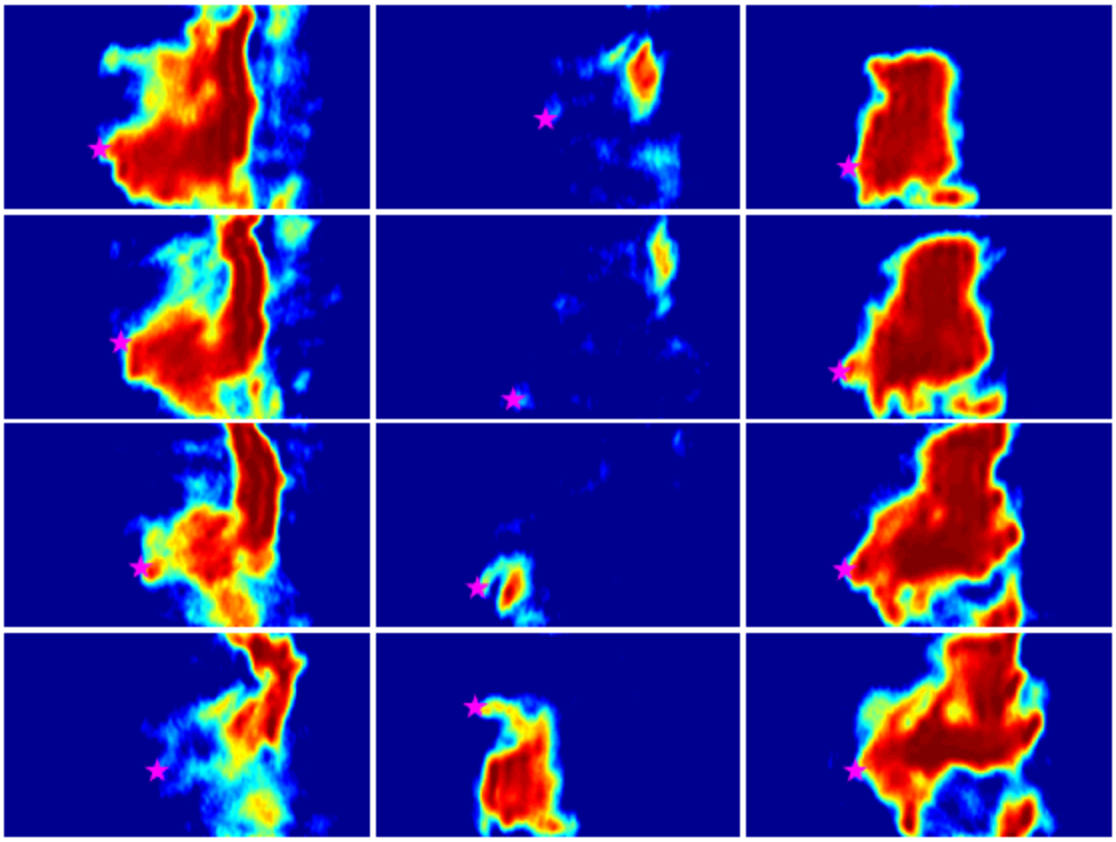

Figure D. 38: Twelve successive CH* chemiluminescence images taken during an LBO precursor event. The star denotes the most upstream spatial location of luminosity. S2 is burning in these images with an air inlet temperature of 450 K.

APPENDIX E. V_{UP} PROBABILITY DENSITY FUNCTIONS

This appendix includes plots of the v_{up} PDFs for the individual runs.

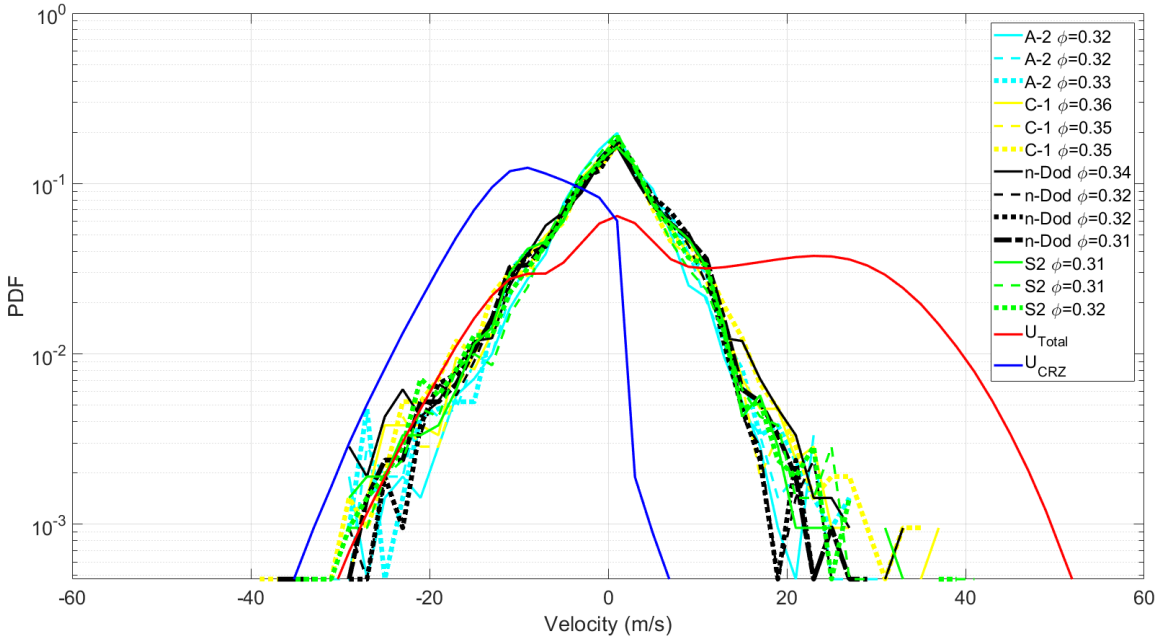

Figure E. 1: PDFs of v_{up} for A-2, C-1, n-dodecane, and S2 at 450 K, taken as ϕ-$\phi_{LBO}\rightarrow$0. The axial flow velocity PDFs U_{Total} and U_{CRZ} are also shown.

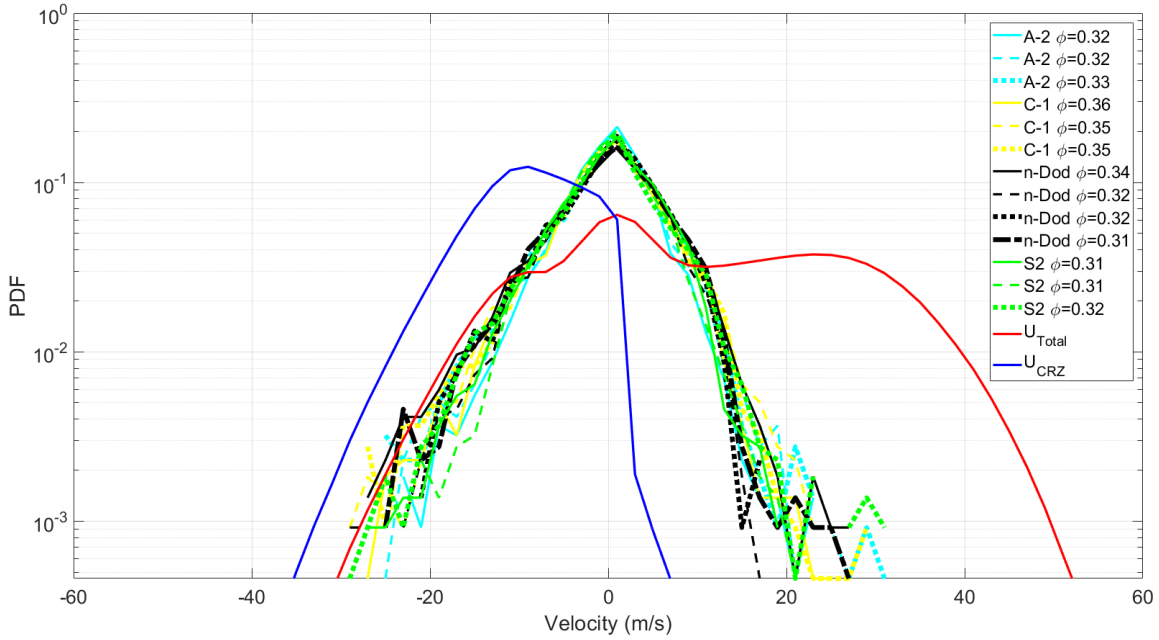

Figure E. 2: PDFs of v_{up} for A-2, C-1, n-dodecane, and S2 at 450 K, taken as ϕ-ϕ_{LBO}≈0.025. The axial flow velocity PDFs U_{Total} and U_{CRZ} are also shown.

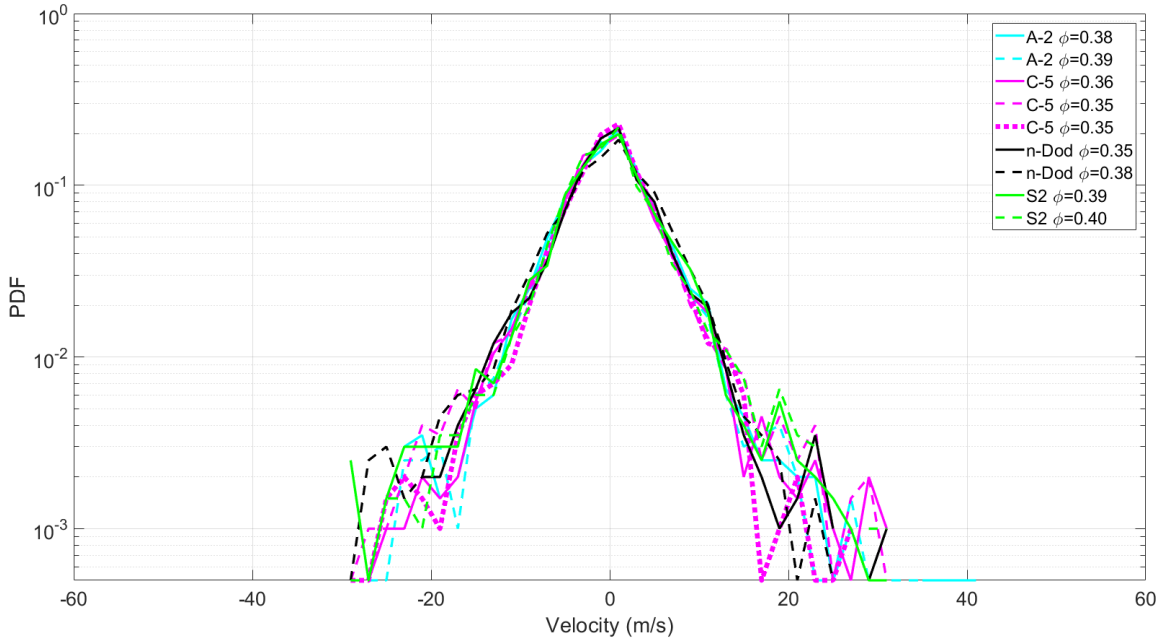

Figure E. 3: PDFs of v_{up} for A-2, C-5, n-dodecane, and S2 at 300 K, taken as ϕ-ϕ_{LBO}→0.

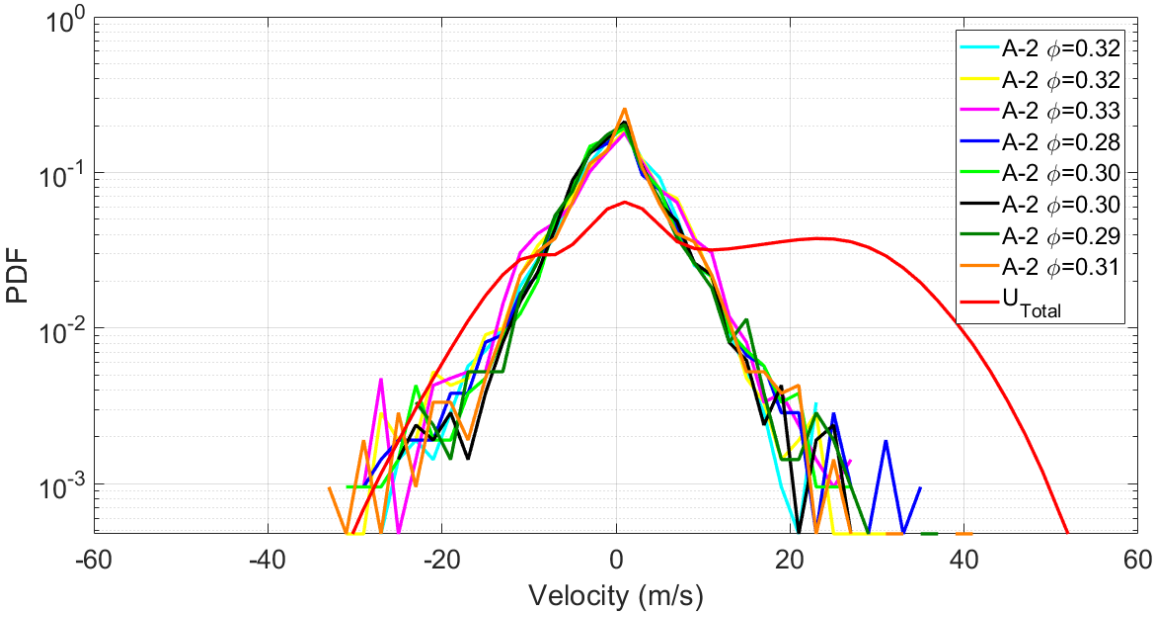

Figure E. 4: PDFs of v_{up} for A-2 at 450 K, taken as ϕ-ϕ_{LBO}→0. The axial flow velocity PDFs U_{Total} are also shown.

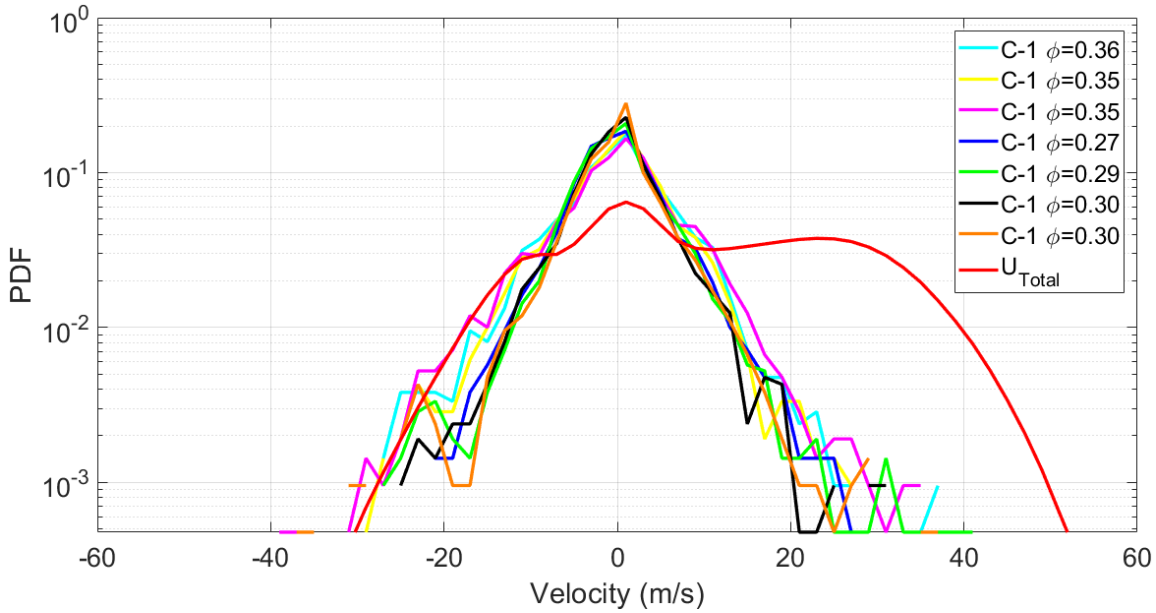

Figure E. 5: PDFs of v_{up} for C-1 at 450 K, taken as ϕ-ϕ_{LBO}→0. The axial flow velocity PDFs U_{Total} are also shown.

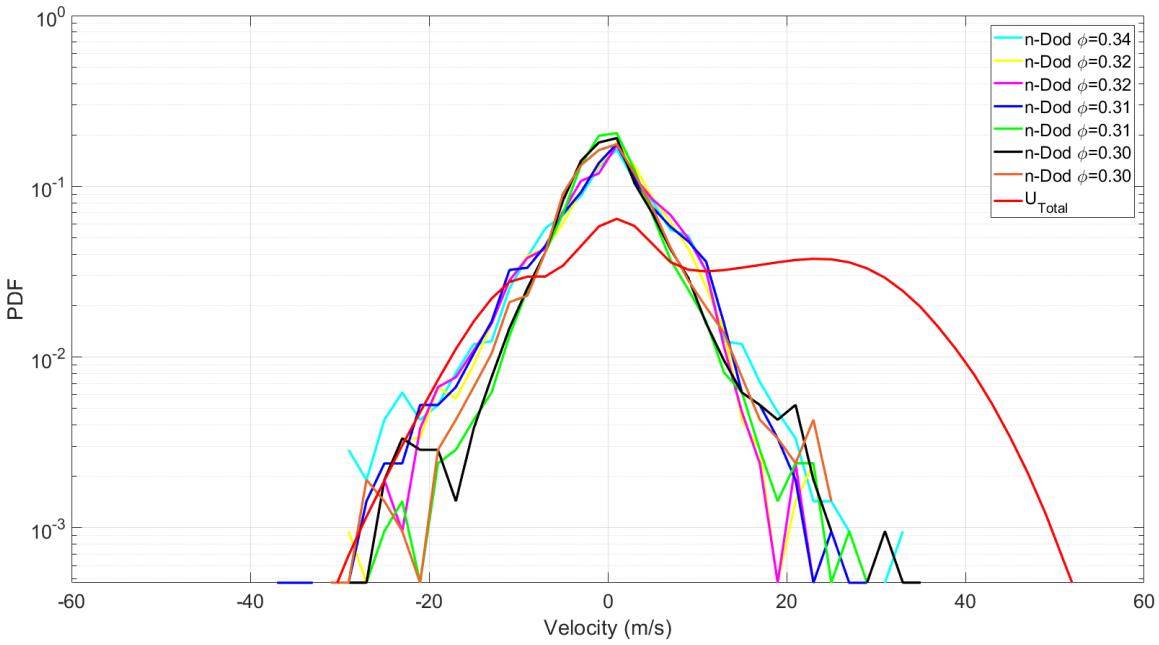

Figure E. 6: PDFs of v_{up} for n-dodecane at 450 K, taken as ϕ-ϕ_{LBO}→0. The axial flow velocity PDFs U_{Total} are also shown.

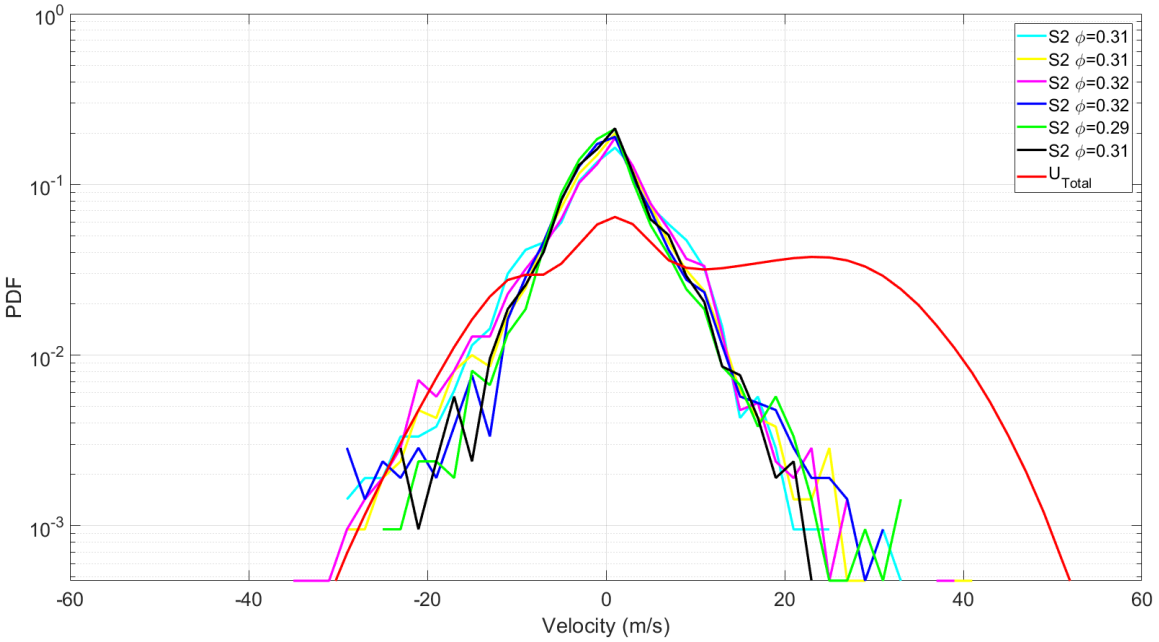

Figure E. 7: PDFs of v_{up} for S2 at 450 K, taken as ϕ-ϕ_{LBO}→0. The axial flow velocity PDFs U_{Total} are also shown.

REFERENCES

1. Edwards, T., *Advancements in gas turbine fuels from 1943 to 2005.* Journal of Engineering for Gas Turbines and Power, 2007. **129**(1): p. 13-20.

2. Smith, J.L., *World oil: market or mayhem?* Journal of Economic Perspectives, 2009. **23**(3): p. 145-64.

3. Law, C.K., *Fuel options for next-generation chemical propulsion.* Aiaa Journal, 2012. **50**(1): p. 19-36.

4. Sorrell, S., R. Miller, R. Bentley, and J. Speirs, *Oil futures: A comparison of global supply forecasts.* Energy Policy, 2010. **38**(9): p. 4990-5003.

5. Aguilera, R.F., R.G. Eggert, G. Lagos CC, and J.E. Tilton, *Depletion and the future availability of petroleum resources.* The Energy Journal, 2009: p. 141-174.

6. Owen, N.A., O.R. Inderwildi, and D.A. King, *The status of conventional world oil reserves—Hype or cause for concern?* Energy policy, 2010. **38**(8): p. 4743-4749.

7. Kuhns, R.J. and G.H. Shaw, *Navigating the Energy Maze: The Transition to a Sustainable Future*. 2018: Springer.

8. Hodges, T. and J. Potter, *Transportation's Role in Reducing US Greenhouse Gas Emissions: Volume 1: Synthesis Report and Volume 2: Technical Report.* 2010.

9. Colket, M., J. Heyne, M. Rumizen, M. Gupta, T. Edwards, W.M. Roquemore, G. Andac, R. Boehm, J. Lovett, and R. Williams, *Overview of the national jet fuels combustion program.* AiAA Journal, 2017: p. 1-18.

10. Kosir, S.T., L. Behnke, J.S. Heyne, R.D. Stachler, G. Flora, S. Zabarnick, A. George, A. Landera, R. Bambha, and R. Denney. *Improvement in Jet Aircraft Operation with the Use of High-Performance Drop-in Fuels*. in *AIAA Scitech 2019 Forum*. 2019.

11. Zhang, C., X. Hui, Y. Lin, and C.-J. Sung, *Recent development in studies of alternative jet fuel combustion: Progress, challenges, and opportunities.* Renewable and Sustainable Energy Reviews, 2016. **54**: p. 120-138.

12. Kärcher, B. and F. Yu, *Role of aircraft soot emissions in contrail formation.* Geophysical Research Letters, 2009. **36**(1).

13. Moses, C.A. and P.N. Roets, *Properties, characteristics, and combustion performance of Sasol fully synthetic jet fuel.* Journal of Engineering for Gas turbines and Power, 2009. **131**(4): p. 041502.

14. Lefebvre, A.H. and D.R. Ballal, *Gas turbine combustion: alternative fuels and emissions*. 2010: CRC press.

15. Bittner, J.D. and J.B. Howard, *Role of aromatics in soot formation.* Alternative Hydrocarbon Fuels: Combustion and Chemical Kinetics, 1978. **62**: p. 335-358.

16. Durbin, M. and D. Ballal, *Studies of lean blowout in a step swirl combustor.* Journal of Engineering for gas Turbines and Power, 1996. **118**(1): p. 72-77.

17. Nair, S. and T. Lieuwen, *Acoustic detection of blowout in premixed flames.* Journal of Propulsion and Power, 2005. **21**(1): p. 32-39.

18. Richards, G., M. McMillian, R. Gemmen, W.A. Rogers, and S. Cully, *Issues for low-emission, fuel-flexible power systems.* Progress in Energy and Combustion Science, 2001. **27**(2): p. 141-169.

19. Burger, V., *The influence of fuel properties on threshold combustion in aviation gas turbine engines*. 2017, University of Cape Town.

20. Rosfjord, T.J. and J.M. Cohen, *Evaluation of the transient operation of advanced gas turbine combustors.* Journal of Propulsion and Power, 1995. **11**(3): p. 497-504.

21. Hodzic, E., M. Jangi, R.-Z. Szasz, C. Duwig, M. Geron, J. Early, L. Fuchs, and X.-S. Bai, *Large Eddy Simulation of Bluff-Body Flame Approaching Blow-Off: A Sensitivity Study.* Combustion Science and Technology, 2018: p. 1-28.

22. DeZubay, E., *Characteristics of disk-controlled flames.* Aero Digest, 1950. **61**(1): p. 54-56.

23. Huelskamp, B., B. Kiel, A. Lynch, S. Kostka, P. Gokulakrishnan, and M. Klassen. *Improved correlation for blowout of bluff body stabilized flames*. in *49th AIAA Aerospace Sciences Meeting including the New Horizons Forum and Aerospace Exposition*. 2011.

24. King, C.R., *A Semiempirical Correlation of Afterburner Combustion Efficiency and Lean-Blowout Fuel-air-ratio Data with Several Afterburner-inlet Variables and Afterburner Lengths.* 1957.

25. Ballal, D.R. and A.H. Lefebvre, *Weak extinction limits of turbulent flowing mixtures.* Journal of Engineering for Power, 1979. **101**(3): p. 343-348.

26. Huelskamp, B.C., B.V. Kiel, and P. Gokulakrishnan. *Influence of Fuel Characteristics in a Correlation to Predict Lean Blowout of Bluff-Body Stabilized Flames*. in *ASME Turbo Expo 2015: Turbine Technical Conference and Exposition*. 2015. American Society of Mechanical Engineers.

27. Zhang, Q., D.R. Noble, and T. Lieuwen, *Characterization of Fuel Composition Effects in H2/ CO/ CH4 Mixtures Upon Lean Blowout.* Journal of engineering for gas turbines and power, 2007. **129**(3): p. 688-694.

28. Longwell, J.P., E.E. Frost, and M.A. Weiss, *Flame Stability in Bluff Body Recirculation Zones.* Industrial and Engineering Chemistry, 1953. **45**(8): p. 1629-1633.

29. Blust, J., D. Ballal, and G. Sturgess, *Fuel effects on lean blowout and emissions from a well-stirred reactor.* Journal of propulsion and power, 1999. **15**(2): p. 216-223.

30. Williams, G., H. Hottel, and A. Scurlock. *Flame stabilization and propagation in high velocity gas streams*. in *Symposium on Combustion and Flame, and Explosion Phenomena*. 1948. Elsevier.

31. Kundu, K., D. Banerjee, and D. Bhaduri, *On flame stabilization by bluff-bodies.* Journal of Engineering for Power, 1980. **102**(1): p. 209-214.

32. Zukoski, E.E., *Flame stabilization on bluff bodies at low and intermediate Reynolds numbers*. 1954, California Institute of Technology.

33. Zukoski, E.E. and F.E. Marble, *Experiments concerning the mechanism of flame blowoff from bluff bodies.* 1983.

34. Shanbhogue, S.J., S. Husain, and T. Lieuwen, *Lean blowoff of bluff body stabilized flames: Scaling and dynamics.* Progress in Energy and Combustion Science, 2009. **35**(1): p. 98-120.

35. Yamaguchi, S., N. Ohiwa, and T. Hasegawa, *Structure and blow-off mechanism of rod-stabilized premixed flame.* Combustion and Flame, 1985. **62**(1): p. 31-41.

36. Karlovitz, B., D. Denniston Jr, D. Knapschaefer, and F. Wells. *Studies on Turbulent flames: A. Flame Propagation Across velocity gradients B. turbulence Measurement in flames*. in *Symposium (international) on combustion*. 1953. Elsevier.

37. Potter Jr, A.E. and E.L. Wong, *Effect of pressure and duct geometry on bluff-body flame stabilization.* 1958.

38. Zhang, Q., S.J. Shanbhogue, and T. Lieuwen, *Dynamics of premixed H2/CH4 flames under near blowoff conditions.* Journal of engineering for gas turbines and power, 2010. **132**(11): p. 111502.

39. Foley, C.W., *Attachment point characteristics and modeling of shear layer stabilized flames in an annular, swirling flowfield*. 2015, Georgia Institute of Technology.

40. Stachler, R.D., J.S. Heyne, S. Stouffer, J.D. Miller, and M. Roquemore. *Investigation of Combustion Emissions from Conventional and Alternative Aviation Fuels in a Well-Stirred Reactor*. in *55th AIAA Aerospace Sciences Meeting*. 2017.

41. Dawson, J., R. Gordon, J. Kariuki, E. Mastorakos, A. Masri, and M. Juddoo, *Visualization of blow-off events in bluff-body stabilized turbulent premixed flames.* Proceedings of the Combustion institute, 2011. **33**(1): p. 1559-1566.

42. Driscoll, J.F., *Turbulent premixed combustion: Flamelet structure and its effect on turbulent burning velocities.* Progress in energy and Combustion Science, 2008. **34**(1): p. 91-134.

43. Pan, J. and D. Ballal. *Chemistry and turbulence effects in bluff-body stabilized flames*. in *30th aerospace sciences meeting and exhibit*. 1992.

44. Lefebvre, A. and R. Stwalley III, *Flame stabilization using large flameholders of irregular shape.* Journal of Propulsion and Power, 1988. **4**(1): p. 4-13.

45. Lieuwen, T.C., *Unsteady combustor physics*. 2012: Cambridge University Press.

46. Nair, S. and T.C. Lieuwen, *Near-blowoff dynamics of a bluff-body stabilized flame.* Journal of Propulsion and power, 2007. **23**(2): p. 421-427.

47. Smith, C., D. Nickolaus, T. Leach, B. Kiel, and K. Garwick. *LES blowout analysis of premixed flow past V-gutter flameholder*. in *45th AIAA Aerospace Sciences Meeting and Exhibit*. 2007.

48. Muruganandam, T., B. Kim, R. Olsen, M. Patel, B. Romig, J. Seitzman, and B. Zinn. *Chemiluminescence based sensors for turbine engines*. in *39th AIAA/ASME/SAE/ASEE Joint Propulsion Conference and Exhibit*. 2003.

49. Muruganandam, T., S. Nair, D. Scarborough, Y. Neumeier, J. Jagoda, T. Lieuwen, J. Seitzman, and B. Zinn, *Active control of lean blowout for turbine engine combustors.* Journal of Propulsion and Power, 2005. **21**(5): p. 807-814.

50. Muruganandam, T., *Sensing and dynamics of lean blowout in a swirl dump combustor.* PhD diss., Georgia Institute of Technology, 2006. **18**: p. 950-960.

51. Prakash, S., Y. Neumeier, and B. Zinn. *Investigation of Mode Shift Dynamics of Lean, Premixed Flames*. in *44th AIAA Aerospace Sciences Meeting and Exhibit*. 2006.

52. Nair, S., R. Rajaram, A. Meyers, T. Lieuwen, L. Tozzi, and K. Benson. *Acoustic and ion sensing of lean blowout in an aircraft combustor simulator*. in *43rd AIAA Aerospace Sciences Meeting and Exhibit*. 2005.

53. Longwell, J.P., E.E. Frost, and M.A. Weiss, *Flame Stability in Bluff Body Recirculation Zones.* Industrial & Engineering Chemistry, 1953. **45**(8): p. 1629-1633.

54. Radhakrishnan, K., J.B. Heywood, and R.J. Tabaczynski, *Premixed turbulent flame blowoff velocity correlation based on coherent structures in turbulent flows.* Combustion and flame, 1981. **42**: p. 19-33.

55. Mellor, A., *Semi-empirical correlations for gas turbine emissions, ignition, and flame stabilization.* Progress in Energy and Combustion Science, 1980. **6**(4): p. 347-358.

56. Kiel, B., K. Garwick, J. Gord, J. Miller, A. Lynch, R. Hill, and S. Phillips. *A detailed investigation of bluff body stabilized flames*. in *45th AIAA Aerospace Sciences Meeting and Exhibit*. 2007.

57. Chaudhuri, S., S. Kostka, S.G. Tuttle, M.W. Renfro, and B.M. Cetegen, *Blowoff mechanism of two dimensional bluff-body stabilized turbulent premixed flames in a prototypical combustor.* Combustion and Flame, 2011. **158**(7): p. 1358-1371.

58. Erickson, R. and M. Soteriou, *The influence of reactant temperature on the dynamics of bluff body stabilized premixed flames.* Combustion and Flame, 2011. **158**(12): p. 2441-2457.

59. Emerson, B., J. O'Connor, M. Juniper, and T. Lieuwen, *Density ratio effects on reacting bluff-body flow field characteristics.* Journal of Fluid Mechanics, 2012. **706**: p. 219-250.

60. Morales, A.J., I.M. Lasky, J. Reyes, K.A. Ahmed, and I.G. Boxx. *Controlling Flame Stability in a High-Speed Combustor through Pressure Gradients*. in *AIAA Scitech 2019 Forum*. 2019.

61. Khosla, S., T. Leach, and C. Smith. *Flame stabilization and role of von karman vortex shedding behind bluff body flameholders*. in *43rd AIAA/ASME/SAE/ASEE Joint Propulsion Conference & Exhibit*. 2007.

62. Kariuki, J., J.R. Dawson, and E. Mastorakos, *Measurements in turbulent premixed bluff body flames close to blow-off.* Combustion and flame, 2012. **159**(8): p. 2589-2607.

63. Fugger, C.A., B. Paxton, J.R. Gord, B.A. Rankin, and A.W. Caswell. *Measurements and Analysis of Flow-Flame Interactions in Bluff-Body-Stabilized Turbulent Premixed Propane-Air Flames*. in *AIAA Scitech 2019 Forum*. 2019.

64. Chowdhury, B.R. and B.M. Cetegen, *Effects of free stream flow turbulence on blowoff characteristics of bluff-body stabilized premixed flames.* Combustion and Flame, 2018. **190**: p. 302-316.

65. Kariuki, J., A. Dowlut, R. Yuan, R. Balachandran, and E. Mastorakos, *Heat release imaging in turbulent premixed methane–air flames close to blow-off.* Proceedings of the Combustion Institute, 2015. **35**(2): p. 1443-1450.

66. Kedia, K.S. and A.F. Ghoniem, *The blow-off mechanism of a bluff-body stabilized laminar premixed flame.* Combustion and Flame, 2015. **162**(4): p. 1304-1315.

67. Kariuki, J., A. Dowlut, R. Balachandran, and E. Mastorakos, *Heat release imaging in turbulent premixed ethylene-air flames near blow-off.* Flow, Turbulence and Combustion, 2016. **96**(4): p. 1039-1051.

68. Law, C.K., *Combustion physics*. 2010: Cambridge university press.

69. Chaudhuri, S., S. Kostka, M.W. Renfro, and B.M. Cetegen, *Blowoff dynamics of bluff body stabilized turbulent premixed flames.* Combustion and flame, 2010. **157**(4): p. 790-802.

70. Chaudhuri, S., S. Kostka, M.W. Renfro, and B.M. Cetegen, *Blowoff mechanism of harmonically forced bluff body stabilized turbulent premixed flames.* Combustion and flame, 2012. **159**(2): p. 638-640.

71. Tuttle, S.G., S. Chaudhuri, S. Kostka Jr, K.M. Kopp-Vaughan, T.R. Jensen, B.M. Cetegen, and M.W. Renfro, *Time-resolved blowoff transition measurements for two-dimensional bluff body-stabilized flames in vitiated flow*. Combustion and Flame, 2012. **159**(1): p. 291-305.

72. Syred, N. and J. Beer, *Combustion in swirling flows: a review.* Combustion and flame, 1974. **23**(2): p. 143-201.

73. Lovett, J.A. and N. Abuaf. *Emissions and stability characteristics of flameholders for lean-premixed combustion*. in *ASME 1992 International Gas Turbine and Aeroengine Congress and Exposition*. 1992. American Society of Mechanical Engineers.

74. Santhosh, R. and S. Basu, *Transitions and blowoff of unconfined non-premixed swirling flame.* Combustion and Flame, 2016. **164**: p. 35-52.

75. Zhang, Q., *Lean blowoff characteristics of swirling H2/CO/CH4 Flames*. 2008, Georgia Institute of Technology.

76. Chterev, I.P., *Flow Characterization of Lifted Flames in Swirling, Reacting Flows*. 2017, Georgia Institute of Technology.

77. Manosh Kumar, R., I. Chterev, D. Stepien, M. Sirignano, B.L. Emerson, T. Yi, N. Jiang, C.A. Fugger, P.S. Hsu, and J. Felver. *Characterization of transient blowout dynamics of a swirl stabilized flame using simultaneous OH and CH2O PLIF*. in *AIAA Scitech 2019 Forum*. 2019.

78. Stöhr, M., I. Boxx, C. Carter, and W. Meier, *Dynamics of lean blowout of a swirl-stabilized flame in a gas turbine model combustor.* Proceedings of the Combustion Institute, 2011. **33**(2): p. 2953-2960.

79. Shih, W.-P., J.G. Lee, and D.A. Santavicca. *Stability and emissions characteristics of a lean premixed gas turbine combustor*. in *Symposium (International) on Combustion*. 1996. Elsevier.

80. Lyons, K.M., *Toward an understanding of the stabilization mechanisms of lifted turbulent jet flames: experiments.* Progress in Energy and Combustion Science, 2007. **33**(2): p. 211-231.

81. Vanquickenborne, L. and A. Van Tiggelen, *The stabilization mechanism of lifted diffusion flames.* Combustion and Flame, 1966. **10**(1): p. 59-69.

82. Kalghatgi, G.T., *Blow-out stability of gaseous jet diffusion flames. Part I: in still air.* Combustion Science and Technology, 1981. **26**(5-6): p. 233-239.

83. Broadwell, J.E., W.J. Dahm, and M.G. Mungal. *Blowout of turbulent diffusion flames*. in *Symposium (international) on combustion*. 1985. Elsevier.

84. Roquemore, W., V. Reddy, P. Hedman, M. Post, and T. Chen. *Experimental and theoretical studies in a gas-fueled research combustor*. in *29th Aerospace Sciences Meeting*. 1991.

85. Driscoll, J.F. and C.C. Rasmussen, *Correlation and analysis of blowout limits of flames in high-speed airflows.* Journal of propulsion and power, 2005. **21**(6): p. 1035-1044.

86. Peters, N. and F.A. Williams, *Liftoff characteristics of turbulent jet diffusion flames.* AIAA journal, 1983. **21**(3): p. 423-429.

87. Starner, S., R. Bilger, M. Long, J. Frank, and D. Marran, *Scalar dissipation measurements in turbulent jet diffusion flames of air diluted methane and hydrogen.* Combustion science and technology, 1997. **129**(1-6): p. 141-163.

88. Sutton, J.A. and J.F. Driscoll, *Imaging of local flame extinction due to the interaction of scalar dissipation layers and the stoichiometric contour in turbulent non-premixed flames.* Proceedings of the Combustion Institute, 2007. **31**(1): p. 1487-1495.

89. Juddoo, M. and A. Masri, *High-speed OH-PLIF imaging of extinction and re-ignition in non-premixed flames with various levels of oxygenation.* Combustion and Flame, 2011. **158**(5): p. 902-914.

90. Hult, J., U. Meier, W. Meier, A. Harvey, and C. Kaminski, *Experimental analysis of local flame extinction in a turbulent jet diffusion flame by high repetition 2-D laser techniques and multi-scalar measurements.* Proceedings of the Combustion Institute, 2005. **30**(1): p. 701-709.

91. Steinberg, A., I. Boxx, C. Arndt, J. Frank, and W. Meier, *Experimental study of flame-hole reignition mechanisms in a turbulent non-premixed jet flame using sustained multi-kHz PIV and crossed-plane OH PLIF*. Proceedings of the Combustion Institute, 2011. **33**(1): p. 1663-1672.

92. Chen, T., L. Goss, D. Talley, and D. Mikolaitis. *Stabilization zone structure in jet diffusion flames from liftoff toblowout*. in *27th Aerospace Sciences Meeting*. 1989.

93. Murugesan, M. and R. Sujith, *Physical mechanisms that cause intermittency that presages combustion instability and blowout in a turbulent lifted jet flame combustor.* Combustion Science and Technology, 2018. **190**(2): p. 312-335.

94. Won, S.H., F.M. Haas, S. Dooley, T. Edwards, and F.L. Dryer, *Reconstruction of chemical structure of real fuel by surrogate formulation based upon combustion property targets.* Combustion and Flame, 2017. **183**: p. 39-49.

95. Lefebvre, A., *Fuel effects on gas turbine combustion—ignition, stability, and combustion efficiency.* Journal of engineering for gas turbines and power, 1985. **107**(1): p. 24-37.

96. Burger, V., A. Yates, and C. Viljoen. *Influence of fuel physical properties and reaction rate on threshold heterogeneous gas turbine combustion*. in *ASME Turbo Expo 2012: Turbine Technical Conference and Exposition*. 2012. American Society of Mechanical Engineers.

97. Burger, V., A. Yates, T. Mosbach, and B. Gunasekaran. *Fuel influence on targeted gas turbine combustion properties: Part II—detailed Results*. in *ASME Turbo Expo 2014: Turbine Technical Conference and Exposition*. 2014. American Society of Mechanical Engineers.

98. Mosbach, T., V. Burger, and B. Gunasekaran. *Fuel composition influence on gas turbine ignition and combustion performance*. in *ASME Turbo Expo 2015: Turbine Technical Conference and Exposition*. 2015. American Society of Mechanical Engineers.

99. Peters, J. *Current gas turbine combustion and fuels research and development*. in *ASME 1987 International Gas Turbine Conference and Exhibition*. 1987. American Society of Mechanical Engineers.

100. Grohmann, J., B. Rauch, T. Kathrotia, W. Meier, and M. Aigner, *Influence of Single-Component Fuels on Gas-Turbine Model Combustor Lean Blowout.* Journal of Propulsion and Power, 2017: p. 1-11.

101. Rock, N., I. Chterev, T. Smith, H. Ek, B. Emerson, D. Noble, J. Seitzman, and T. Lieuwen. *Reacting Pressurized Spray Combustor Dynamics: Part 1—Fuel Sensitivities and Blowoff Characterization*. in *ASME Turbo Expo 2016: Turbomachinery Technical Conference and Exposition*. 2016. American Society of Mechanical Engineers.

102. Rock, N., I. Chterev, B. Emerson, J. Seitzman, and T. Lieuwen. *Blowout Sensitivities in a Liquid Fueled Combustor: Fuel Composition and Preheat Temperature Effects*. in *ASME Turbo Expo 2017: Turbomachinery Technical Conference and Exposition*. 2017. American Society of Mechanical Engineers.

103. Corporan, E., R.Q. Casselberry, C.D. Klingshirn, M. Wagner, M. DeWitt, J.T. Edwards, P. Wrzesinski, S.D. Stouffer, and T.H. Hendershott. *Fuel Effects on the Lean Operational Limits of a T63 Turboshaft Engine*. in *AIAA Scitech 2019 Forum*. 2019.

104. Colket, M., S. Zeppieri, Z. Dai, and D. Hautman. *Fuel research at UTRC*. in *Multi-Agency Coordinating Council for Combustion Research 5th Annual Fuel Research Meeting, Livermore, California, September*. 2012.

105. Stouffer, S., T. Hendershott, J.R. Monfort, J. Diemer, E. Corporan, P. Wrzesinski, and A.W. Caswell. *Lean Blowout and Ignition Characteristics of Conventional and Surrogate Fuels Measured in a Swirl Stabilized Combustor*. in *55th AIAA Aerospace Sciences Meeting*. 2017.

106. Allison, P.M., J.A. Sidey, and E. Mastorakos. *Lean Blowoff Scaling of Swirling, Bluff-Body Stabilized Spray Flames*. in *2018 AIAA Aerospace Sciences Meeting*. 2018.

107. Won, S.H., P.S. Veloo, S. Dooley, J. Santner, F.M. Haas, Y. Ju, and F.L. Dryer, *Predicting the global combustion behaviors of petroleum-derived and alternative jet fuels by simple fuel property measurements.* Fuel, 2016. **168**: p. 34-46.

108. Dooley, S., S.H. Won, M. Chaos, J. Heyne, Y. Ju, F.L. Dryer, K. Kumar, C.-J. Sung, H. Wang, and M.A. Oehlschlaeger, *A jet fuel surrogate formulated by real fuel properties.* Combustion and flame, 2010. **157**(12): p. 2333-2339.

109. Dooley, S., S.H. Won, J. Heyne, T.I. Farouk, Y. Ju, F.L. Dryer, K. Kumar, X. Hui, C.-J. Sung, and H. Wang, *The experimental evaluation of a methodology for surrogate fuel formulation to emulate gas phase combustion kinetic phenomena.* Combustion and Flame, 2012. **159**(4): p. 1444-1466.

110. Dooley, S., S.H. Won, S. Jahangirian, Y. Ju, F.L. Dryer, H. Wang, and M.A. Oehlschlaeger, *The combustion kinetics of a synthetic paraffinic jet aviation fuel and a fundamentally formulated, experimentally validated surrogate fuel.* Combustion and flame, 2012. **159**(10): p. 3014-3020.

111. Kim, D., J. Martz, and A. Violi, *A surrogate for emulating the physical and chemical properties of conventional jet fuel.* Combustion and Flame, 2014. **161**(6): p. 1489-1498.

112. Pitz, W.J. and C.J. Mueller, *Recent progress in the development of diesel surrogate fuels.* Progress in Energy and Combustion Science, 2011. **37**(3): p. 330-350.

113. Yuan, R., J. Kariuki, A. Dowlut, R. Balachandran, and E. Mastorakos, *Reaction zone visualisation in swirling spray n-heptane flames.* Proceedings of the Combustion Institute, 2015. **35**(2): p. 1649-1656.

114. Evans, M., J. Sidey, J. Ye, P. Medwell, B. Dally, and E. Mastorakos, *Temperature and reaction zone imaging in turbulent swirling dual-fuel flames.* Proceedings of the Combustion Institute, 2018.

115. Verdier, A., J.M. Santiago, A. Vandel, G. Godard, G. Cabot, and B. Renou, *Local extinction mechanisms analysis of spray jet flame using high speed diagnostics.* Combustion and Flame, 2018. **193**: p. 440-452.

116. Yuan, R., J. Kariuki, and E. Mastorakos, *Measurements in swirling spray flames at blow-off.* International Journal of Spray and Combustion Dynamics, 2018: p. 1756827718763559.

117. Esclapez, L., P. Ma, and M. Ihme, *Large-eddy simulation of fuel effect on lean blow-out in gas turbines.* Stanford Center for Turbulence Research, Annual Research Briefs, 2015.

118. Giusti, A. and E. Mastorakos, *Detailed chemistry LES/CMC simulation of a swirling ethanol spray flame approaching blow-off.* Proceedings of the Combustion Institute, 2017. **36**(2): p. 2625-2632.

119. Esclapez, L., P.C. Ma, E. Mayhew, R. Xu, S. Stouffer, T. Lee, H. Wang, and M. Ihme, *Fuel effects on lean blow-out in a realistic gas turbine combustor.* Combustion and Flame, 2017. **181**: p. 82-99.

120. Hasti, V.R., P. Kundu, G. Kumar, S.A. Drennan, S. Som, and J.P. Gore. *A Numerical Study of Flame Characteristics during Lean Blow-Out in a Gas Turbine Combustor*. in *2018 Joint Propulsion Conference*. 2018.

121. Cohen, J. and T. Rosfjord, *Influences on the Sprays Formed by High-Shear Fuel Nozzle/S wirler Assemblies.* Journal of Propulsion and Power, 1993. **9**(1): p. 16-27.

122. Bokhart, A., D. Shin, R.M. Gejji, P. Sojka, J.P. Gore, R.P. Lucht, S.V. Naik, and T. Buschhagen. *Spray Measurements at Elevated Pressures and Temperatures Using Phase Doppler Anemometry*. in *55th AIAA Aerospace Sciences Meeting*. 2017.

123. Foley, C., I. Chterev, B. Noble, J. Seitzman, and T. Lieuwen, *Shear layer flame stabilization sensitivities in a swirling flow.* International Journal of Spray and Combustion Dynamics, 2017. **9**(1): p. 3-18.

124. Bokhart, A., D. Shin, N.S. Rodrigues, P. Sojka, J.P. Gore, and R.P. Lucht. *Spray Characteristics of a Hybrid Airblast Pressure-Swirl Atomizer at Near Lean Blowout Conditions using Phase Doppler Anemometry*. in *2018 AIAA Aerospace Sciences Meeting*. 2018.

125. Shin, D., A.J. Bokhart, N.S. Rodrigues, P. Sojka, J.P. Gore, and R.P. Lucht. *Experimental Study of Spray Characteristics at Cold Start and Elevated Ambient Pressure using Hybrid Airblast Pressure-Swirl Atomizer*. in *AIAA Scitech 2019 Forum*. 2019.

126. Sazhin, S.S., *Modelling of fuel droplet heating and evaporation: Recent results and unsolved problems.* Fuel, 2017. **196**: p. 69-101.

127. Al Qubeissi, M., N. Al-Esawi, S.S. Sazhin, and M. Ghaleeh, *Ethanol/gasoline droplet heating and evaporation: effects of fuel blends and ambient conditions.* Energy & fuels, 2018. **32**(6): p. 6498-6506.

128. Knothe, G., A.C. Matheaus, and T.W. Ryan III, *Cetane numbers of branched and straight-chain fatty esters determined in an ignition quality tester☆.* Fuel, 2003. **82**(8): p. 971-975.

129. Edwards, J.T. *Reference jet fuels for combustion testing*. in *55th AIAA Aerospace Sciences Meeting*. 2017.

130. Heyne, J.S., M.B. Colket, M. Gupta, A. Jardines, J.P. Moder, J.T. Edwards, M. Roquemore, C. Li, and M. Rumizen. *Year 2 of the National Jet Fuels Combustion Program: Towards a Streamlined Alternative Jet Fuels Certification Process*. in *55th AIAA Aerospace Sciences Meeting*. 2017.

131. Heyne, J.S., E. Peiffer, M.B. Colket, A. Jardines, C. Shaw, J.P. Moder, W.M. Roquemore, J.T. Edwards, C. Li, and M. Rumizen. *Year 3 of the National Jet Fuels Combustion Program: Practical and Scientific Impacts of Alternative Jet Fuel Research*. in *2018 AIAA Aerospace Sciences Meeting*. 2018.

132. Luning Prak, D.J., M.H. Jones, P. Trulove, A.M. McDaniel, T. Dickerson, and J.S. Cowart, *Physical and chemical analysis of Alcohol-to-Jet (ATJ) fuel and development of surrogate fuel mixtures.* Energy & Fuels, 2015. **29**(6): p. 3760-3769.

133. Dooley, S., J. Heyne, S.H. Won, P. Dievart, Y. Ju, and F.L. Dryer, *Importance of a Cycloalkane Functionality in the Oxidation of a Real Fuel.* Energy & Fuels, 2014. **28**(12): p. 7649-7661.

134. Mensch, A., R.J. Santoro, T.A. Litzinger, and S.-Y. Lee, *Sooting characteristics of surrogates for jet fuels.* Combustion and flame, 2010. **157**(6): p. 1097-1105.

135. Mensch, A., *A study on the sooting tendency of jet fuel surrogates using the threshold soot index.* 2009.

136. Haas, F.M., A. Qin, and F.L. Dryer. *"Virtual" Smoke Point Determination of Alternative Aviation Kerosenes by Threshold Sooting Index TSI) Methods*. in *50th AIAA/ASME/SAE/ASEE Joint Propulsion Conference*. 2014.

137. Opacich, K.C., J.S. Heyne, E. Peiffer, and S.D. Stouffer. *Analyzing the Relative Impact of Spray and Volatile Fuel Properties on Gas Turbine Combustor Ignition in Multiple Rig Geometries*. in *AIAA Scitech 2019 Forum*. 2019.

138. *ASTM D86-16a, Standard Test Method for Distillation of Petroleum Products and Liquid Fuels at Atmospheric Pressure*, in *ASTM International*. 2016.

139. *ASTM D6890, Test Method for Determination of Ignition Delay and Derived Cetane Number (DCN) of Diesel Fuel Oils by Combustion in a Constant Volume Chamber*, in *ASTM International*. 2012.

140. Bruno, T.J., *Improvements in the measurement of distillation curves. 1. A composition-explicit approach.* Industrial & engineering chemistry research, 2006. **45**(12): p. 4371-4380.

141. Bruno, T.J., L.S. Ott, B.L. Smith, and T.M. Lovestead, *Complex fluid analysis with the advanced distillation curve approach*. 2009, ACS Publications.

142. Govindaraju, P.B. and M. Ihme, *Group contribution method for multicomponent evaporation with application to transportation fuels.* International Journal of Heat and Mass Transfer, 2016. **102**: p. 833-845.

143. Smith, T.E., *Experimental Investigation of Transverse Acoustic Instabilities*. 2017, Georgia Institute of Technology.

144. Chterev, I., N. Rock, H. Ek, T. Smith, B. Emerson, D. Noble, E. Mayhew, T. Lee, N. Jiang, and S. Roy. *Reacting Pressurized Spray Combustor Dynamics: Part 2—High Speed Planar Measurements*. in *ASME Turbo Expo 2016: Turbomachinery Technical Conference and Exposition*. 2016. American Society of Mechanical Engineers.

145. Chterev, I., N. Rock, H. Ek, B. Emerson, J. Seitzman, N. Jiang, S. Roy, T. Lee, J. Gord, and T. Lieuwen, *Simultaneous imaging of fuel, OH, and three component velocity fields in high pressure, liquid fueled, swirl stabilized flames at 5 kHz.* Combustion and Flame, 2017. **186**: p. 150-165.

146. Paynabar, K., J. Jin, and M.P. Reed, *Informative sensor and feature selection via hierarchical nonnegative garrote.* Technometrics, 2015. **57**(4): p. 514-523.

147. Breiman, L., *Better subset regression using the nonnegative garrote.* Technometrics, 1995. **37**(4): p. 373-384.

148. Tibshirani, R., *Regression shrinkage and selection via the lasso.* Journal of the Royal Statistical Society: Series B (Methodological), 1996. **58**(1): p. 267-288.

149. Efron, B., T. Hastie, I. Johnstone, and R. Tibshirani, *Least angle regression.* The Annals of statistics, 2004. **32**(2): p. 407-499.

150. Yuan, M. and Y. Lin, *On the non-negative garrotte estimator.* Journal of the Royal Statistical Society: Series B (Statistical Methodology), 2007. **69**(2): p. 143-161.

151. Friedman, J., T. Hastie, and R. Tibshirani, *The elements of statistical learning*. Vol. 1. 2001: Springer series in statistics New York.

152. Yuan, M. and Y. Lin, *Model selection and estimation in regression with grouped variables.* Journal of the Royal Statistical Society: Series B (Statistical Methodology), 2006. **68**(1): p. 49-67.

153. Grant, M. and S. Boyd, *CVX: Matlab software for disciplined convex programming, version 2.1*. 2014.

154. Grant, M.C. and S.P. Boyd, *Graph implementations for nonsmooth convex programs*, in *Recent advances in learning and control*. 2008, Springer. p. 95-110.

155. Sur, F. and M. Grediac, *Automated removal of quasiperiodic noise using frequency domain statistics.* Journal of Electronic Imaging, 2015. **24**(1): p. 013003.

156. Otsu, N., *A threshold selection method from gray-level histograms.* IEEE transactions on systems, man, and cybernetics, 1979. **9**(1): p. 62-66.

157. Buschhagen, T., R.Z. Zhang, A.J. Bokhart, R.M. Gejji, S.V. Naik, R.P. Lucht, J.P. Gore, P.E. Sojka, C.D. Slabaugh, and S. Meyer. *Effect of Aviation Fuel Type and Fuel Injection Conditions on Non-reacting Spray Characteristics of a Hybrid Airblast Fuel Injector*. in *54th AIAA Aerospace Sciences Meeting*. 2016.

158. Tyliszczak, A., D.E. Cavaliere, and E. Mastorakos, *LES/CMC of blow-off in a liquid fueled swirl burner.* Flow, Turbulence and Combustion, 2014. **92**(1-2): p. 237-267.

159. Won, S.H., S. Dooley, F.L. Dryer, and Y. Ju, *A radical index for the determination of the chemical kinetic contribution to diffusion flame extinction of large hydrocarbon fuels.* Combustion and Flame, 2012. **159**(2): p. 541-551.

160. Ek, H., I. Chterev, N. Rock, B. Emerson, J. Seitzman, T. Lieuwen, N. Jiang, and W. Proscia. *Feature Extraction From Time Resolved Reacting Flow Data Sets*. in *ASME Turbo Expo 2018: Turbomachinery Technical Conference and Exposition*. 2018. American Society of Mechanical Engineers.

161. Chterev, I., G. Sundararajan, B. Emerson, J. Seitzman, and T. Lieuwen, *Precession effects on the relationship between time-averaged and instantaneous reacting flow characteristics.* Combustion Science and Technology, 2017. **189**(2): p. 248-265.

162. Unni, V.R. and R. Sujith, *Multifractal characteristics of combustor dynamics close to lean blowout.* Journal of Fluid Mechanics, 2015. **784**: p. 30-50.

163. Do Lee, U., C.S. Yoo, J.H. Chen, and J.H. Frank, *Effects of H2O and NO on extinction and re-ignition of vortex-perturbed hydrogen counterflow flames.* Proceedings of the Combustion Institute, 2009. **32**(1): p. 1059-1066.

164. Wang, H. and S.B. Pope, *Lagrangian investigation of local extinction, re-ignition and auto-ignition in turbulent flames.* Combustion Theory and Modelling, 2008. **12**(5): p. 857-882.

165. Sripakagorn, P., S. Mitarai, G. Kosály, and H. Pitsch, *Extinction and reignition in a diffusion flame: a direct numerical simulation study.* Journal of Fluid Mechanics, 2004. **518**: p. 231-259.

166. Edwards, T. and J.V. Atria. *Thermal stability of high temperature fuels*. in *ASME 1997 International Gas Turbine and Aeroengine Congress and Exhibition*. 1997. American Society of Mechanical Engineers.

167. Zeuthen, E.D. and D.L. Blunck, *Radiation Emissions from Turbulent Diffusion Flames Burning Vaporized Jet and Jet-like Fuels.* Energy & Fuels, 2017. **31**(12): p. 14150-14160.